

From stressed satellite cells to mouse and human gastruloids

Applications of single-cell and spatial
transcriptomics

Susanne Carina van den Brink

Colophon

The work described in this thesis was performed at the Hubrecht Institute for Developmental Biology and Stem Cell Research (the Royal Netherlands Academy of Arts and Sciences, KNAW) within the framework of the research school Cancer Stem cells & Developmental biology (CS&D), which is part of the Utrecht Graduate School of Life Sciences (Utrecht University).

Cover: Confocal image of a mouse gastruloid (embryo-like structure generated in vitro from embryonic stem cells) that is embedded in Matrigel at 96 hours and imaged at 120 hours after aggregation. Matrigel-embedding induces the formation of somite-like structures, blocks of tissue that contain the precursors of the vertebrae and skeletal muscles, in these gastruloids. Cyan stripes represent expression pattern of *Uncx4.1*, which marks the posterior halves of somites. Credit: Vincent van Batenburg. Background: DNA string (Credit: polesnoy/Alamy Stock Photo) and bright field image of mouse embryonic stem cells in regular 2D culture conditions. Credit: Susanne van den Brink.

Artwork Ch. 2: Confocal image of a dissociated piece of tibialis anterior muscle tissue, stained for the stress-response gene *Fos* (green), which is induced during tissue dissociation procedures. Blue, DAPI (nucleus); red, auto-fluorescent cells. Credit: Susanne van den Brink. **Ch. 3:** Gastruloid embedded in Matrigel; see cover artwork description for details. **Ch. 4:** Wide-field microscopy picture of a human gastruloid. Blue, BRACHYURY (mesoderm); red, SOX17 (endoderm); green, SOX2 (neuroectoderm). Credit: Naomi Moris. **Addendum:** Parts of this thesis were written during the 2020 COVID-19 pandemic. Picture: sunset view from studio on Utrecht University campus during thesis-writing in lock-down, with in the background the RIVM (Rijksinstituut voor Volksgezondheid en Milieu | National Institute for Public Health and Environment). Credit: Susanne van den Brink.

Supplementary files associated with this thesis are available online at <https://bit.ly/3eyS6ZY>. All scRNA-seq and tomo-seq data associated with Ch. 3 can be explored online at <https://avolab.hubrecht.eu/MouseGastruloids2020>.

| | |
|------------|---|
| Layout by | Melanie Fremery |
| Printed by | Ridderprint, www.ridderprint.nl |
| ISBN | 978-94-6375-898-7 |

Copyright © 2020 by Susanne Carina van den Brink. All rights reserved. No part of this book may be reproduced, stored in a retrieval system or transmitted in any form or by any means, without prior permission of the author.

Printing of this thesis was financially supported by Greiner Bio-One, Takara Bio and the Hubrecht Institute.

From stressed satellite cells to mouse and human gastruloids

Applications of single-cell and spatial
transcriptomics

**Van gestreste spierstamcellen
tot muizen en humane gastruloïden**

Toepassingen van single-cell en spatiële RNA sequencing methodes
(met een samenvatting in het Nederlands)

Proefschrift

ter verkrijging van de graad van doctor aan de Universiteit Utrecht
op gezag van de rector magnificus, prof.dr. H.R.B.M. Kummeling,
ingevolge het besluit van het college voor promoties
in het openbaar te verdedigen op

vrijdag 27 november 2020
des middags te 4.15 uur

door

Susanne Carina van den Brink

geboren op 3 juli 1989
te Vleuten-De Meern

Promotor:

Prof. dr. ir. A. van Oudenaarden

Table of contents

| | | |
|---------------------------------|--|-----|
| Outline and scope of the thesis | | 6 |
| Chapter 1 | Introduction Single-cell and spatial transcriptomics: applications for satellite cells and gastruloids | 9 |
| Chapter 2 | Single-cell sequencing reveals dissociation-induced gene expression in tissue subpopulations | 31 |
| Chapter 3 | Single-cell and spatial transcriptomics reveal somitogenesis in gastruloids | 61 |
| Chapter 4 | An in vitro model for early anteroposterior organization during human development | 101 |
| Chapter 5 | Discussion | 133 |
| Addendum | | 147 |
| | Samenvatting in het Nederlands | 149 |
| | Dankwoord | 157 |
| | List of publications | 166 |
| | Curriculum Vitae | 167 |

Outline and scope of the thesis

The first part of this thesis describes how the widely-used tissue dissociation protocols that are often required prior to single-cell RNA sequencing procedures can alter the transcriptome of cells. These findings highlight that results obtained with single-cell RNA sequencing methods require validation with microscopy-based spatial transcriptomics technologies. The second part of this thesis describes how single-cell RNA sequencing and spatial transcriptomics technologies can aid in the characterization and improvement of gastruloid models, which can be used to study mouse and human early post-implantation development in vitro.

Chapter 1 provides an introduction into embryology, muscles, satellite cells, stem cells, and stem-cell based in vitro models for embryology, with a focus on gastruloids. Gastruloids are aggregates of embryonic stem cells that model early post-implantation embryonic development in vitro. Chapter 1 describes the historical context of gastruloids and other stem-cell based embryo models, and explains why such in vitro models are useful additions to the toolbox of modern-day embryologists. This chapter also summarizes the advantages and current limitations of the gastruloids system, and describes what aspects of this model system still need to be (further) developed. Chapter 1 also provides a brief introduction into single-cell RNA sequencing spatial transcriptomics technologies, and describes how these technologies can be used to characterize in vitro models for embryology, and thereby aid the development of improved versions of such models.

Chapter 2 describes an important limitation of single-cell RNA sequencing and other RNA sequencing technologies for which tissue dissociation procedures are required. This chapter shows that such dissociation procedures, which cannot easily be avoided, can induce a stress response in a subpopulation of the cells. This chapter shows that satellite cells (muscle stem cells) are particularly sensitive to such a dissociation-induced stress response. This chapter also provides experimental and computational solutions that can be used to remove dissociation-affected subpopulations.

The first part of **Chapter 3** provides a detailed single-cell and spatial transcriptomics-based characterization of mouse gastruloids. In addition, this chapter provides a detailed comparison between mouse gastruloids and mouse embryos. This comparison reveals that most embryonic cell types are present in gastruloids, and shows that, while such gastruloids are unable to generate somites, they still express key markers of somitogenesis in the correct spatial location. We follow up on these observations in the second part of Chapter 3, which describes how live-imaging experiments revealed that the somitogenesis clock is active in gastruloids. We then perform a small drug screening study to perturb the somitogenesis clock in gastruloids, which exemplifies how gastruloids, which can easily be generated in large numbers, can be used to perform large-scale drug screening procedures. In addition, this chapter describes the discovery that the addition of a small amount of Matrigel can induce the formation of somite-like structures in mouse gastruloids, and thus results in gastruloids

that more accurately resemble mouse embryos.

Chapter 4 describes the development and characterization of the first human gastruloids model. This human version of the gastruloids system can be used to study human early post-implantation development, in particular events associated with gastrulation and anterior-posterior axis formation, in vitro. In this chapter, this new human gastruloids system is characterized and compared to mouse gastruloids with spatial transcriptomics. In addition, this chapter describes how various teratogens and inhibitors affect the development of these human gastruloids, revealing that this system can be used to study how environmental factors affect human development.

Chapter 5 contains a discussion of the work described in this thesis. This chapter describes alternative tissue dissociation protocols that have been developed by other groups that followed up on our results described in Chapter 2. In addition, Chapter 5 provides an extensive overview of the current challenges, ethical considerations and potential future perspectives of the (human) gastruloid field.



*"Invention, it must be humbly admitted,
does not consist in creating out of void but out of chaos."
(M. Shelly)*

1

Introduction

Single-cell and spatial transcriptomics: applications for satellite cells and gastruloids

Some parts of this chapter are based on sections from the following publications:

Generating gastruloids with somite-like structures from mouse embryonic stem cells.

Vincent van Batenburg, Susanne van den Brink[§], Marloes Blotenburg, Anna Alemany, Naomi Moris, Peter Baillie-Johnson, Yasmine el Azhar, Katharina F. Sonnen, Alfonso Martinez Arias & Alexander van Oudenaarden[§].

Protocol Exchange (2020)

Debate ethics of embryo models from stem cells.

Nicolas Rivron^{*§}, Martin Pera^{*§}, Janet Rossant, Alfonso Martinez Arias, Magdalena Zernicka-Goetz, Jianping Fu, Susanne van den Brink, Annelien Bredenoord, Wybo Dondorp, Guido de Wert, Insoo Hyun, Megan Munsie & Rosario Isasi.

Nature (2018)

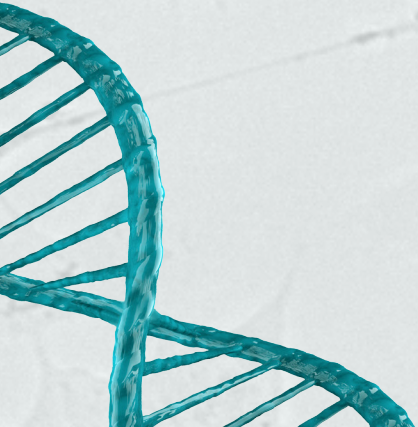
Modelling human embryogenesis: embryo-like structures spark ethical and policy debate.

Ana Pereira Daoud^{*}, Mina Popovic^{*}, Wybo Dondorp, Marc Trani Bustos, Annelien Bredenoord, Susana M. Chuva de Sousa Lopes, Susanne C. van den Brink, Bernard A.J. Roelen, Guido de Wert, Björn Heindryckx[§].

Human Reproduction Update (2020)

* Equal contribution

§ Corresponding author(s)



During embryonic development, cellular interactions coordinate the transformation of a small, uniform cluster of cells into a complex 3-dimensional (3D) multicellular organism. The morphogenetic processes that shape the embryo are complex and still not well understood, and many questions about the processes that regulate embryonic development remain unanswered. Studies that probe into the mechanisms that regulate embryonic development are not only hampered by the complexity of embryonic development itself, but also by the technical, ethical and legal limitations that surround experimentation with embryos. Especially studies that probe into human development are limited by the scarcity of human research material and by the legal restrictions surrounding experimentation with human embryos. The “14-day rule” that prohibits experimentation with > 14 days post fertilization (dpf) human embryos in most jurisdictions is an important example of such a legal restriction. To circumvent the technical and legal restrictions that surround research with human embryos, embryological studies often rely on animal models, such as mice. Results obtained with such animal models are however not always relevant for human development, as many important differences between mouse and human embryos have been reported^{1,2}. Additionally, such animal experiments are not free of technical, legal and ethical considerations either; and many animal species cannot easily be obtained in large numbers, limiting their use in large-scale genetic or drug screening procedures.

The discovery that embryonic cells derived from mouse and human embryos can be propagated in a pluripotent state *in vitro* circumvented some of the abovementioned challenges and provided scientists with the possibility to study the processes that direct embryonic development *in vitro* in a high-throughput manner. The 2-dimensional (2D) and 3D embryonic stem (ES) cell culture systems that were developed in the first decades following this discovery did however not accurately capture the complex 3D morphology of the embryo. These culture systems could therefore not be used to address questions regarding for example 3D interactions between the embryonic and extra-embryonic lineages, the coordinated 3D cellular morphogenetic rearrangements that are associated with gastrulation, or the processes that ensure that the embryonic organs appear in the correct position along the body axes of the embryo. The recent discovery that stem cells can be coaxed into 3D structures (referred to as “stem cell-based embryo-like structures” or “embryo models” throughout this thesis) that more accurately resemble the 3D morphology of embryos³⁻¹³ is now starting to provide scientists with the possibility to study the more complex 3D aspects of embryonic development *in vitro*.

Most of the currently available protocols to generate such embryo-like structures from ES cells are still very new, and some of these models have not yet been characterized and compared to embryos in detail. Additionally, these new protocols are often suboptimal and require validation and optimization. Importantly, most of the currently available embryo model systems are generated with mouse ES cells, and human versions of these models will have to be developed before these models can be used to study human embryonic development *in vitro*.

Mouse and human development, from fertilization to early organogenesis

Embryonic development in mammals starts with the fertilization of the oocyte. In the days that follow fertilization, mitotic divisions result in the formation of a multicellular structure referred to as a “morula”^{14,15} (Fig. 1). The cells in the morula segregate into an outer trophoblast layer that will later give rise to extra-embryonic tissues, and an inner cell mass lineage from which the embryo will develop. Next, the conceptus* starts to absorb fluids, which results in the formation of a fluid-filled cavity (the “blastocoel”). The inner cell mass cells are positioned on one side of the blastocoel (Fig. 1) and further specialize towards either the hypoblast (primitive endoderm) or the epiblast lineage. The hypoblast layer faces the blastocoel and mainly contributes to the yolk sac, while the epiblast lineage generates the embryonic lineages of the conceptus. The conceptus, which is now in the “blastocyst” stage of development, subsequently implants into the uterus of the mother (~day 4.5 in mouse embryos; ~day 7 in human embryos). In mice, the epiblast elongates in proximal-distal direction after implantation, resulting in the formation of a cup-shaped post-implantation epiblast (blue cells in Carnegie stages 5 and 6 mouse embryo in Fig. 1a) that will give rise to the embryo proper. In primates in contrast, the post-implantation epiblast is flat and referred to as the “embryonic disk” (Fig. 1b).

At day 6.5 in mouse and ~day 16 in human embryos, a process referred to as “gastrulation” starts. This process starts with the formation of a primitive streak in the posterior part of the epiblast (Fig. 1-3) and shapes the body plan of the embryo^{14,15}. During gastrulation, the primitive streak coordinates extensive cell rearrangements that transform the monolayered epiblast into a three-layered structure that contains three germ layers (endoderm, mesoderm and ectoderm) (Fig. 2-3). These germ layers are organized relative to a coordinate system (anterior-posterior, dorsal-ventral and left-right axis) that acts as a reference for the development of tissues and organs. Gastrulation is shortly followed by cardiogenesis (formation of the heart tube and initiation of a heart beat at day 22 in human and E8.0-8.5 in mice), neurulation (neural plate formation and neural tube closure at day 26 in human and E10.5 in mice) (Fig. 4a) and initiation of somitogenesis, a process by which two longitudinal rows of mesoderm flanking the neural groove condense into two strings of blocks (day 21 in human and E8.0 in mouse) (Fig. 4a-b). These “blocks”, which are referred to as “somites”, will later form the cartilage, tendons, dermis and skeletal muscles of the embryo.

* To avoid confusion, we will in this thesis use the terms “conceptus” to refer to the ensemble of the embryo with its extra-embryonic tissues, and the term “embryo” to refer to the embryo proper only, without its extra-embryonic tissues.

Fig. 1 | Rodent (a) and primate (b) early embryonic development, from fertilization to initiation of gastrulation. Blue shading, embryonic lineages; red shading, extra-embryonic lineages; grey shading, endometrium (inner lining of uterus of the mother). Names of tissues that are marked in red in both panels highlight those that display significant differences between rodents and humans (for details, see Boroviak et al., 2017 (ref. ²⁶)). Orange arrows indicate lineages that are recapitulated in vitro with mouse ES cells, conventional (“primed”) human ES cells and naïve human ES cells and with mouse TS cells and mouse XEN-cells. Adapted with permission from Boroviak et al., “Primate embryogenesis predicts the hallmarks of human naïve pluripotency” (*Development*, Copyright © 2017 (ref. ²⁶)).

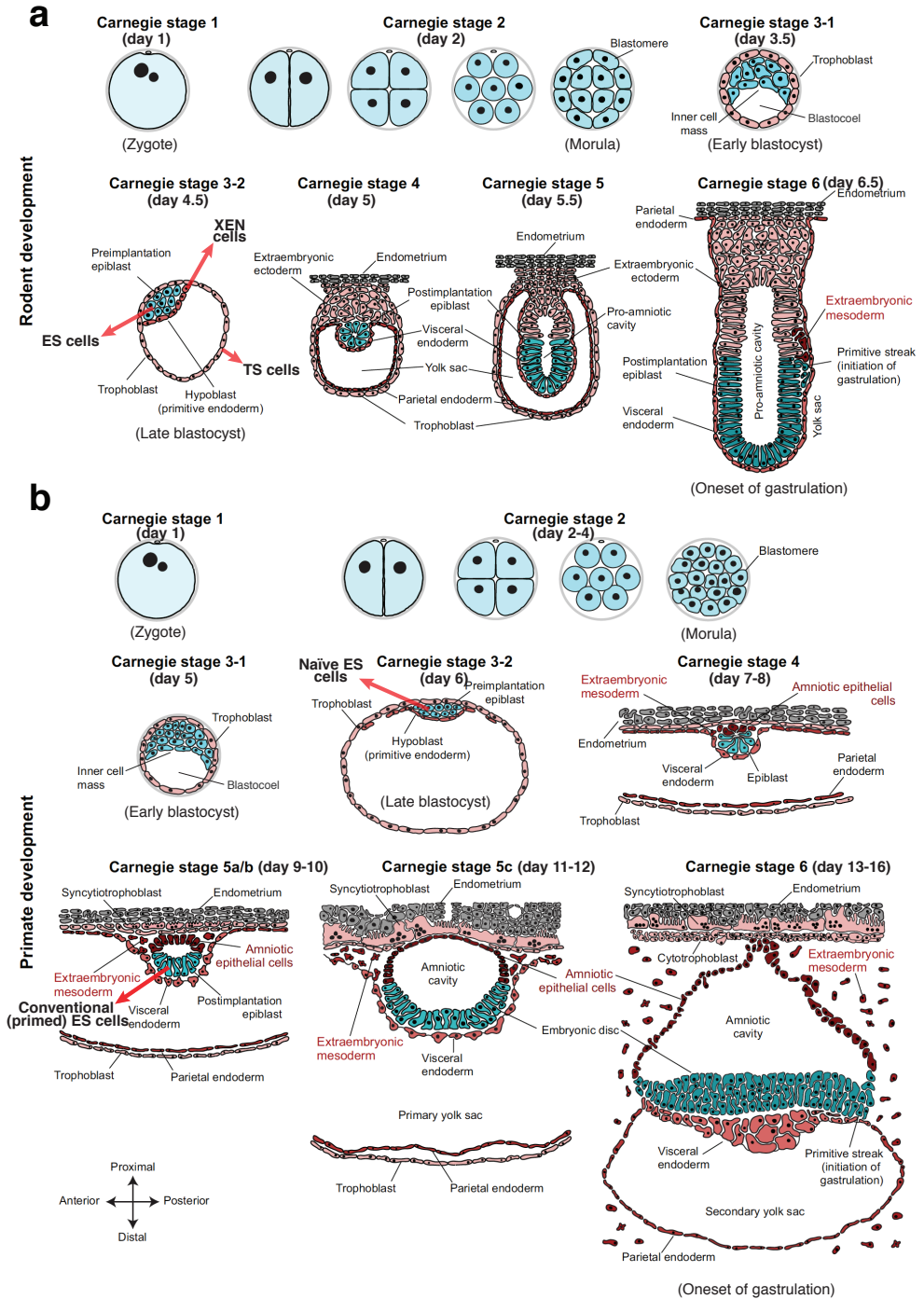


Fig. 1 | See previous page for caption. Adapted with permission from Boroviak et al., "Primate embryogenesis predicts the hallmarks of human naïve pluripotency" (*Development*, Copyright © 2017 (ref. ²⁶)).

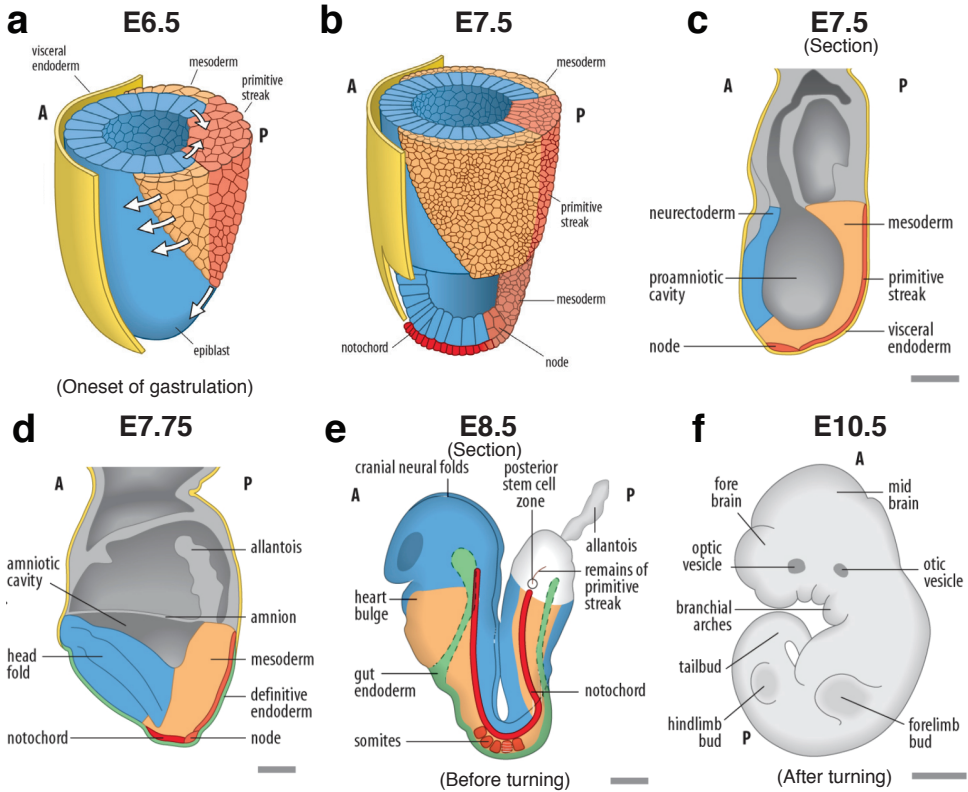


Fig. 2 | Gastrulation in mouse embryos. a, Gastrulation starts with the formation of the primitive streak, which appears in the posterior part of the cup-shaped epiblast (blue) and extends in anterior direction over time (bottom white arrow). During gastrulation, cells ingress through the primitive streak (dark orange) to form the mesodermal (light orange) and endodermal germ layers (white arrows). b-d, At E7.75, the primitive streak has reached its most anterior position and starts to regress in posterior direction, laying down the notochord in its wake. e, During the later stages of gastrulation, the remains of the primitive streak are positioned in the tail bud, which grows and extends in posterior direction by proliferation of cells in the posterior stem cell zone. f, Organs and limb buds appear with reference to the main body plan that is laid down during gastrulation. A, anterior; P, posterior. Scale bars: 100 μm for c-e, and 75 μm for f. Copyright © Oxford University Press 2015. Adapted from Wolpert, Tickle and Martinez Arias., "Principles of Development" (5th edition; ref. 14). Reproduced with permission of the Licensor through PLSclear.

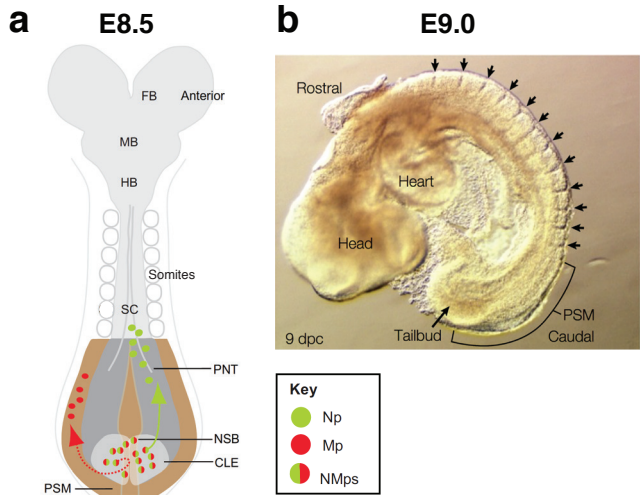
(This figure is only available in the password-protected version of this document due to copyrights. For password information, please contact the author of this document)

Fig. 3 | Gastrulation in human embryos. Gastrulation in humans also starts with the formation of a primitive streak in the posterior part of the epiblast (1) that extends in anterior direction (2) and then regresses in posterior direction (not shown). During gastrulation, cells form the epiblast ingress through the primitive streak (red arrows) to form the mesodermal and endodermal germ layers. During gastrulation, the monolayered epiblast is thus transformed into an axially organized, three-layered structure that contains the ectodermal (blue; top layer), mesodermal (red; middle layer) and endodermal (yellow; bottom layer) germ layers. A, anterior; P, posterior. Marieb, Elaine N.; Brady, Patricia M.; Mallatt, Jon B., Human Anatomy, 9th, © 2020. Reprinted by permission of Pearson Education, Inc., New York, New York.

Fig. 4 | Posterior elongation, somitogenesis and spinal cord formation in mouse embryos.

a, Schematic illustration of E8.5 mouse embryo, dorsal view. During the second phase of gastrulation, the embryo grows and extends in posterior direction. During this elongation process, neuromesodermal progenitors (NMps; red and green), which are localized in the caudal lateral epiblast (CLE), divide and give rise to mesoderm progenitors (Mp; red) and neural progenitors (Np; green). The Mps give rise to the mesoderm that condenses into somites in anterior to posterior direction while the embryo extends posteriorly; in mice, a new pair of somites is formed every 90-120 minutes⁵⁸. Nps give rise to the posterior part of the spinal cord (SC);

the anterior part of the spinal cord (which gives rise to the forebrain (FB), midbrain (MB) and hindbrain (HB)) is not derived from these cells. PSM, presomitic mesoderm; NSB, node-streak border; PNT, preneural tube; PS, remains of primitive streak. **b**, E9.0 mouse embryo. Arrows indicate somite borders. Dpc, days post-coitum. Adapted with permission from Henrique et al., "Neuromesodermal progenitors and the making of the spinal cord" (*Development* 142, 2864-2875, Copyright © 2015) (a). Reprinted by permission from Springer Nature Customer Service Centre GmbH: Springer Nature, *Nature Reviews Genetics*, "The making of the somite: molecular events in vertebrate segmentation", Saga and Takeda, Copyright © Macmillan Magazines Ltd (2001) (b).



Satellite cells: quiescent muscle stem cells that are activated by muscle injury

The skeletal muscles that are derived from the embryonic somites control the voluntary movements of vertebrates. Most skeletal muscles are directly connected to and control the movements of the skeleton via tendons (Fig. 5). Skeletal muscles consist of myofibres: long, multinucleated cells that contain the contractile myofibrils¹⁶. The myofibres of adult muscles are maintained by muscle stem cells ("satellite cells"). These cells can be identified by the expression of the satellite cell marker gene *Pax7*, and are located in between the plasmalemma and basement membrane of the myofibres (Fig. 5). Satellite cells are quiescent (inactive/dormant) in uninjured muscles and are activated upon muscle injury. Upon activation, these cells increase their size and their metabolic, proliferative and migratory activity, and ultimately differentiate to myoblasts that fuse with and thereby repair the damaged myofibres.

The quiescent satellite cell population has previously been reported to be heterogeneous and consist of various subpopulations of which some are more dormant ("stem-cell like") than others^{17,18}. One prominent study that probed into the heterogeneity of the quiescent satellite cell population found that satellite cells extracted from the tibialis anterior muscle of adult *Pax7nGFP* mice display variable expression levels of *Pax7* (ref. ¹⁷). Follow-up experiments on this observation revealed that satellite cells with high *Pax7* expression levels are metabolically less active, take longer to divide in culture following isolation from their in vivo environment, and are more quiescent than satellite cells with lower *Pax7* expression levels, which are transcriptionally more primed for commitment towards myogenic differentiation. These

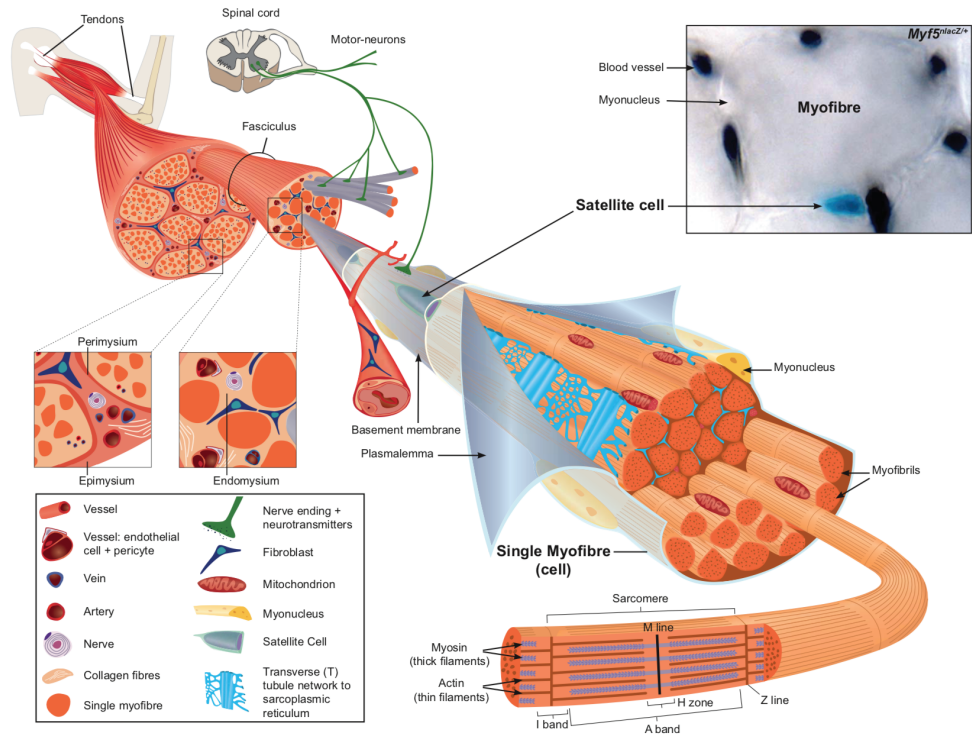


Fig. 5 | Anatomy of skeletal muscles, and location of satellite cells within these muscles. Upper right inset: section of the tibialis anterior muscle of an adult *Myf5^{lacZ}* mouse that was perfused with India ink to label the vasculature, and stained with X-gal to reveal satellite cells. Used with permission from Tajbaksh, "Skeletal muscle stem cells in developmental versus regenerative myogenesis" (*Journ. Intern. Medicine* 266, 372-389; 2009 (ref. ¹⁶)); Copyright © Blackwell publishing LTD. Reproduced with permission of the Licensor John Wiley and Sons.

observations thus suggested that the quiescent satellite cell population is heterogeneous and consists of at least two functionally distinct subpopulations. The full heterogeneity of this population was however still unknown at the start of this PhD trajectory (in June 2014), and had not yet been explored with the at the time still very new single-cell RNA sequencing (scRNA-seq) technology. For these reasons, we decided to apply scRNA-seq to satellite cells extracted from the tibialis anterior muscle of *Pax7nGFP* mice. The results of these experiments are presented in Chapter 2.

Modelling embryonic development in vitro with stem cells

In the last decades, scientists have started to develop 2D and 3D stem cell-based culture systems that can be used to study various aspects of embryonic development in vitro. Even though it is important to keep in mind that results obtained with such in vitro systems may require validation with *in vivo* (animal-based) studies, these culture systems have greatly expanded the toolbox of embryologists. One of the most important advantages of model systems is that they provide the opportunity to study human-specific embryological processes that cannot be studied with human embryos due to the technical, legal and ethical restrictions that surround research with human embryos. Another useful property of stem cells is that

they can be expanded almost infinitely in vitro and that it is therefore easy to generate large amounts of genetically identical embryo-like structures from stem cells. As a result, such in vitro models for embryology are particularly useful for studies that require large-scale screening procedures, which cannot easily be performed with (human) embryos. Another advantage of such in vitro embryo models is that they can more easily be genetically modified than in vivo embryos, as they are generated directly from stem cells and thus bypass the need for the creation of genetically modified animal lines. Interestingly, attempts to build embryo-like structures from stem cells can provide a new, bottom-up view on embryology that can result in new insights that could not easily have been obtained with animal studies (see Discussion in Chapter 5 for examples and details). Lastly, stem cells provide an opportunity to reduce the need for animals in research and may provide a morally favourable alternative for experimentation with animals.

Mouse ES cells were for the first time derived from blastocyst-stage mouse embryos in 1981 (ref. ^{19,20}), and the first human ES cell line** was reported in 1998 (ref. ²¹) (Fig. 1). Important properties of both mouse and human ES cells include that they can be expanded and kept in a pluripotent state in vitro, and that they have the potential to contribute towards all embryonic derivatives, but not to the extra-embryonic tissues***. In mouse, the developmental potency of the extra-embryonic primitive endoderm and trophoblast lineages can be captured with extra-embryonic endoderm (XEN) cells²² and trophoblast stem (TS) cells²³, respectively (Fig. 1). More recently, it was discovered that mouse²⁴ and human²⁵ somatic cells can be reprogrammed into induced pluripotent stem cells (iPSCs) that resemble embryonic stem cells in terms of their differentiation potential. This technological advance opened up many new opportunities for the development of patient-specific applications.

The discovery that embryonic cells can be propagated and kept in a pluripotent state in vitro resulted in the development of 2D and 3D culture systems that can be used to study various aspects of embryonic development in vitro. In conventional 2D stem-cell cultures, cells are cultured in a monolayer on the flat surface of a dish that is coated with for example gelatin or vitronectin, which allows the cells to attach to the bottom of the dish. While such conventional 2D cultures have been proven useful for studies that probe into the molecular mechanisms and signalling requirements of cell lineage specification events during embryonic development, they fail to capture the 3D organization and morphology of embryos. It has recently been shown that more organized 2D cultures can be obtained by geometrically

** Note that conventional (“primed”) human ES cells are derived from pre-implantation human embryos but represent cells in the human ~Carnegie stage 5 post-implantation epiblast. This has been suggested to be the result of the culturing conditions for human ES cells, which seem to fail to keep these cells in a pre-implantation epiblast state²⁶. Recently, various protocols that “reset” conventional human ES cells into a more naive state (referred to as “Naïve ES cells”) have been developed; see Boroviak et al., 2017 (ref. ²⁶) for details. For the human gastruloids protocol that we describe in Chapter 4, conventional human ES cells were used.

*** Note though that this idea has been challenged for human ES cells recently in studies that showed that it is possible to generate human embryo-like structures from human ES cells that generate both an epiblast-like and an amniotic ectoderm-like compartment^{11,12}.

confining ES cells to micropatterns. In such micropattern culture systems, cells are plated in a dish that is coated with (usually circular-shaped) micropatterns to which the cells can attach. Using this method, Warmflash et al. (2014) (ref. ²⁷) demonstrated that micropatterned colonies of human ES cells cultured in the presence of BMP4 acquire fates of all three germ layers and the trophectoderm in a radially organized manner, with trophectoderm, endoderm, mesoderm and ectoderm forming from the edges inwards, respectively. While such micropatterned monolayer cultures are more organized than conventional 2D culture systems, they do not capture the 3D morphology of the embryo, which is during gastrulation reshaped into an axially organized three-layered structure in which the three germ layers are positioned on top of each other (Fig. 2-4). While these micropattern cultures have many interesting applications²⁷⁻²⁹, they can thus not be used to study the 3D morphological changes and axial elongation processes that are associated with gastrulation in *in vivo* embryos.

Aggregates of stem cells referred to as “embryoid bodies” (EBs), which are able to differentiate spontaneously into all three germ layers *in vitro*^{30,31}, have long served as a valuable tool to study differentiation in a 3D context. In contrast to embryos, such EBs are however disorganized both in space and in time. Importantly, EBs usually lack the axial organization of mammalian embryos (with the exception of the more organized EB culture system that was developed by ten Berge et al in 2008 (ref. ³)), and can thus not be used to study embryonic development in an axially organized context. For these reasons, many groups have recently invested efforts into the development of 3D stem cell-based embryo models, such as blastoids¹³, ETS- and ETX-embryos^{7,9}, embryonic sac models^{11,12} and gastruloids^{5,6,8}, that more accurately recapitulate the 3D morphology of embryos.

The 3D embryo models that have been developed in the last decade model different stages and different parts of the early mammalian embryo. Blastoids, for example, which are generated by the aggregation of mouse ES cells and mouse TS cells, model the blastocyst-stage mouse conceptus¹³. This model system can be used to study many aspects of blastocyst formation, such as the formation of the blastocoel cavity and the role of the interactions between the embryonic and extra-embryonic lineages therein, *in vitro*. Blastoids can induce decidualization**** upon introduction into the uterus of pseudo-pregnant mice, but they poorly develop into post-implantation structures both *in vivo* and *in vitro*. As such, these structures are not viable and can currently not be used to study post-implantation development¹³. ETS-embryos⁷ and ETX-embryos⁹ model a slightly later stage in mouse embryonic development. These structures, which are generated by the aggregation of mouse ES cells and mouse TS cells (for ETS-embryos) or by the aggregation of mouse ES cells, mouse TS cells and mouse XEN-cells (for ETX-embryos), can be used to study post-implantation mouse development and the early stages of gastrulation *in vitro*. In a recent publication, Zheng et al¹¹ managed to generate structures from human ES cells that recapitulate human epiblast and human amniotic ectoderm development prior to and during the early

**** Decidualization: changes in the endometrium (inner lining of the uterus) in preparation for, and during, pregnancy.

phases of human gastrulation. The culture system used in this study is based on the “post-implantation amniotic sac embryoid” (PASE) model developed earlier by the same group¹² and uses microfluidics to generate such human embryo-like structures in a more controlled and reproducible manner. Gastruloids, which are generated from mouse ES cells and do not contain any extra-embryonic cell types, model a later stage of embryonic development than any of the other currently available embryo model systems^{5,6,8}. These structures recapitulate the later stages of gastrulation and the early stages of organogenesis *in vitro* in an axially organized manner.

The field of stem cell-based embryo models is still in its infancy, and it is not unlikely that improved versions of such embryo models will be developed in the coming years. Importantly, most of these currently available embryo models (which are all listed and reviewed in detail elsewhere³²) are based on mouse ES cells, and do thus not allow the study of development in a human context. In this thesis, we focus on gastruloids^{5,6,8}, and aim to develop both an improved version of the mouse gastruloids system (Chapter 3) and a first human version of this system (Chapter 4).

Gastruloids: modelling mammalian early post-implantation development with stem cells

In 2009, Marikawa et al.⁴ reported that 3D aggregates of embryocarcinoma cells could undergo morphogenetic movements associated with early mesodermal differentiation. Following this study, we developed a mouse ES cell-based protocol through which 3D post-implantation embryo-like structures could be generated in 2014 (ref. ^{5,33}) (Fig. 6). In this protocol, mouse ES cells obtained from 2D cultures that are maintained in serum-supplemented medium are aggregated by plating ~300 cells in each well of a low-attachment U-bottomed 96-well plate in neural differentiation medium³³ (Fig. 6a). During the 2 days following plating, these cells sink to the bottom of the well and attach to each other to form one small, spherical aggregate per well. Upon treatment with the WNT-agonist Chiron (CHIR99021) for 24h on day 3, these aggregates break their symmetry, resulting in the formation of an elongating structure at 4-5 days after aggregation^{5,33} (Fig. 6b-d). Analysis of the resulting elongating structures revealed that they generated the three germ layers with reference to the three body axes, and elongated in posterior direction over time. As these processes are the consequences of gastrulation, we termed the structures “gastruloids”. A subsequent study extended gastruloid development to 7 days in a dish and showed that during this period gastruloids recapitulate key aspects of mouse development between E5.5 and E9.5 (ref. ^{8,34}). Beccari et al.⁸ also revealed that gastruloids recapitulate the spatial and temporal patterns of *Hox* gene expression that determine the anteroposterior organization of the embryo. Remarkably, the Lütolf lab in Switzerland posted a preprint on bioRxiv few months ago showing that gastruloids can be engaged in organogenesis and can generate an anterior beating heart-like structure that is very similar to the *in vivo* mouse embryonic heart³⁵. Overall, these studies show that gastruloids can be used to study gastrulation, body axes establishment and the early phases of organogenesis in a high-throughput manner *in vitro* (for extensive discussion on applications, advantages and disadvantages of this system, see Discussion in Chapter 5).

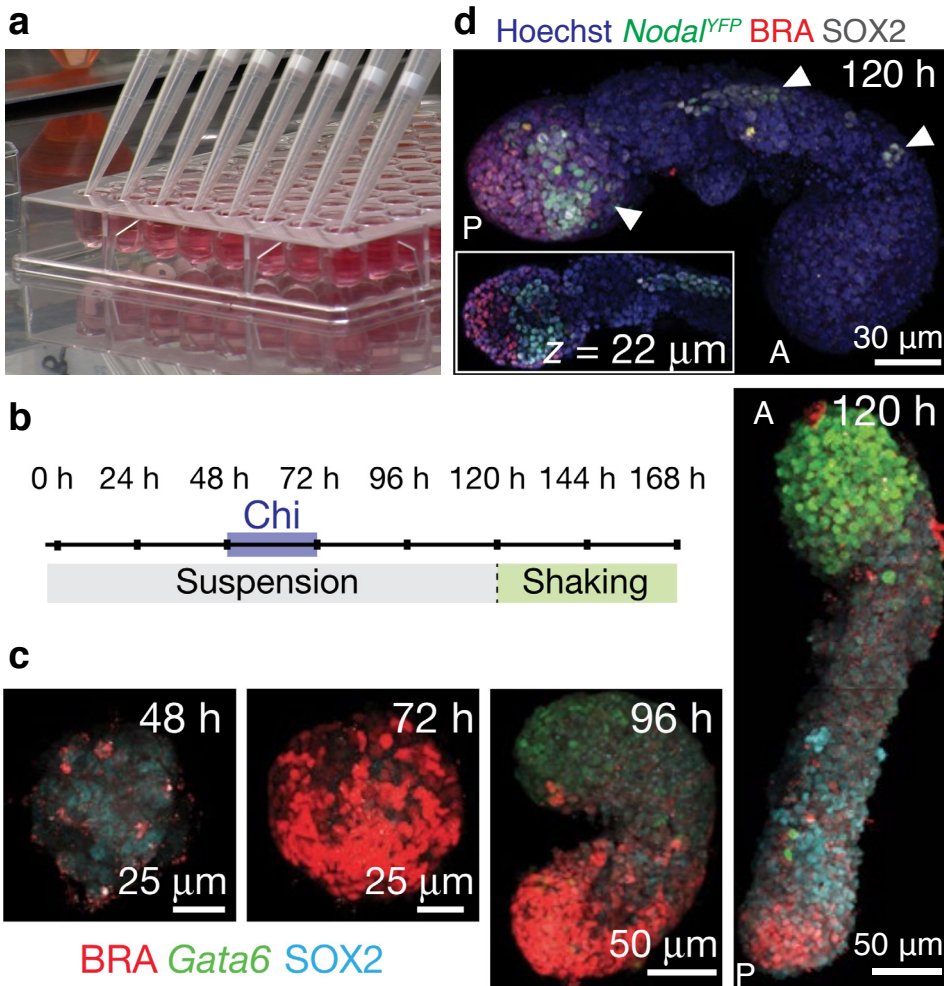


Fig. 6 | Gastruloids: aggregates of mouse ES cells that model body axis formation and germ layer specification in 3D *in vitro*. **a**, U-bottomed 96-well plate used for the generation of gastruloids. To generate gastruloids, ~300 mouse ES cells are added to each well with a multichannel pipette. In the two days that follow plating, the individual cells sink to the bottom of the wells, resulting in the formation of one coherent aggregate per well. **b**, Timeline of gastruloid culture protocol. Cells are aggregated in N2B27 (neural differentiation medium) for 48 hours. The WNT agonist CHIR99201 (Chi) is added at 48 hours after aggregation (48 h) and washed away at 72 h. At 120 h, the aggregates are transferred to a flat bottomed 24-well plate that is placed on an incubator-compatible shaker to prevent them from attaching to the bottom of the 96-well plate. **c**, 3D projections of *Gata6^{H2B-Venus}* (green; anterior cardiac crescent) gastruloids stained for *BRA* (*Brachyury*, red; posterior embryonic tail bud) and *SOX2* (blue), imaged at the indicated timepoints, revealing the elongation process that results in the formation of a clear anterior-posterior axis in gastruloids. **d**, 3D rendering of a 120 h *Nodal^{YFP}* (green) gastruloid stained for *BRA* (red) and *SOX2* (grey). Ventral view. Inset shows a section of the posterior region. Left arrowhead: *Nodal* expression in the posterior region, suggesting the presence of a node-like structure. Middle and left arrowheads, asymmetric *Nodal* expression indicating the presence of left-right asymmetry. For stainings of dorsal-ventral axis formation and additional details, see van den Brink et al., *Development* 2014 (ref. ⁵), Turner et al., *bioRxiv* 2016 (ref. ⁵⁹) and Beccari et al., *Nature* (2018)³³. A, Anterior; P, Posterior. Adapted with permission from "Generation of aggregates of mouse embryonic stem cells that show symmetry Breaking, polarization and emergent collective behaviour *in vitro*" (*J. Vis. Exp.*, 2015; ref. ³³) (a). Reprinted by permission from Springer Nature Customer Service Centre GmbH: Springer Nature, *Nature*, "Multi-axial self-organization properties of mouse embryonic stem cells into gastruloids" (ref. ⁸), Beccari et al., Copyright © (2018) (b-d).

The first versions of the gastruloid culture protocol^{5,6,8,33,34} result in structures that recapitulate the developmental trajectory of the E5.5-E9.5 mouse embryonic epiblast (dark blue cells in Fig. 1a). Gastruloids do however not generate anterior neural (brain) or any extra-embryonic tissues, and as a result are not able to implant *in utero*, ultimately lacking full organismal potential. Another important feature of gastruloids is that they resemble embryos in terms of their overall body plan organization, but that more detailed morphological embryonic structures are not formed properly. This feature is most clearly seen in the processes of somitogenesis: even though the somitic mesoderm is present in the correct location in gastruloids, gastruloids generated with previously published protocols^{33,34} do not form somites^{5,8} (Fig. 7a). Similarly, gastruloids generated with previously published protocols do not generate a properly shaped neural tube-like or notochord-like structure (Fig. 7b).

The mouse gastruloid system is still relatively new, and has so far mostly been characterized with microscopy-based approaches with which the expression patterns of only a limited number of genes have been explored^{5,6,8}. This system has not yet been characterized with scRNA-seq and spatial transcriptomics, and we therefore currently do not know to what extent the cell type composition and genome-wide spatial gene expression patterns in gastruloids resemble those in mouse embryos. To address this issue, we applied a combination of scRNA-seq and spatial transcriptomics to mouse gastruloids, and made a detailed comparison with mouse embryos (Chapter 3). Furthermore, we currently do not know why gastruloids are unable to generate neural tube-like, notochord-like and somite-like structures. It would be interesting to try to address this and develop modified protocols that results in gastruloids

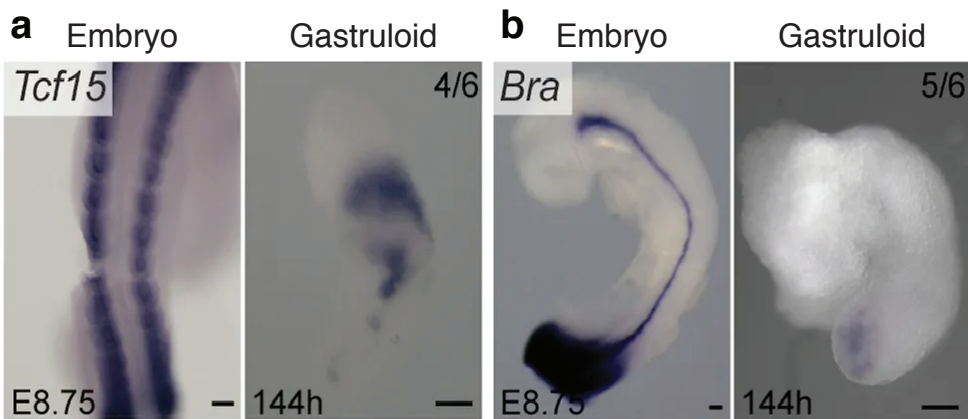


Fig. 7 | Gastruloids generated with previously published protocols^{5,8,33,34} do not generate somites and lack a notochord. **a**, *Tcf15* (somitic mesoderm) ISH staining in an E8.75 mouse embryo (left) and a 144 h after aggregation mouse gastruloid (right). At 144 h, gastruloids resemble E8.75 mouse embryos in terms of their body plan organization, but such gastruloids do not generate somites. **b**, *Brachyury* (*Bra*) ISH staining in E8.75 mouse embryo (left) and in a 144h gastruloid (right), revealing that the *Brachyury*-expressing posterior mesoderm is present, but also revealing that the *Brachyury*-expressing notochord (thin line) is missing in gastruloids. In addition to these differences between gastruloids and embryos, gastruloids are also unable to generate anterior neural (brain) and extra-embryonic structures. Scale bar: 100 μ m. Reprinted by permission from Springer Nature Customer Service Centre GmbH: Springer Nature, *Nature*, "Multi-axial self-organization properties of mouse embryonic stem cells into gastruloids" (ref. ⁸), Beccari et al., Copyright © (2018).

that resemble embryos with higher accuracy, something we partly achieve in Chapter 3. Importantly, a human version of the gastruloids system, which may allow the evaluation of human-specific aspects of gastrulation, does not yet exist. To address this, we develop a first human version of the gastruloids system, which we compare to mouse gastruloids with spatial transcriptomics in Chapter 4.

Single-cell transcriptomics: measuring gene expression in individual cells

The technological advances of the last decade have resulted in advanced scRNA-seq technologies with which the mRNA content of thousands of individual, single cells can be analysed in an automated and high-throughput manner. At the start of this PhD trajectory, in June 2014, scRNA-seq was not yet as automated and high-throughput as it is now, in 2020. In 2014, scRNA-seq was very novel, and only very few tissues had been analysed using this technology.

The first single-cell RNA seq protocol, which was published in 2009 (ref. ³⁶), was particularly cumbersome and labour-intensive. Cells analysed with this protocol could not be pooled and had to be kept in individual tubes throughout the whole protocol, which as a result was very labour-intensive, low-throughput and expensive. In the years that followed this first publication, many more advanced scRNA-seq protocols that allowed the analysis of larger numbers of cells, such as STRT-seq³⁷, SMART-seq³⁸, CEL-seq1 (ref. ³⁹) and CEL-seq2 (ref. ⁴⁰) (Fig. 8a) were developed. One major improvement of these new protocols entailed the implementation of cell-specific barcodes into the primers used to convert the mRNA content of individual cells into cDNA (step 1 in Fig. 8a). These barcodes allowed multiplexing (pooling; step 3 in Fig. 8a) of multiple cells into one sequencing library. As a result of this pooling step, a large part of these newer protocols could be performed in just one tube, which enormously increased the number of cells that could be processed in one day. Even though the development of such barcoded protocols did greatly improve the number of cells that could be processed simultaneously, these scRNA-seq protocols were still relatively labour-intensive. Especially the first steps of the protocol, in which cells were not yet pooled and had to be processed manually one by one, were cumbersome. In the modified version of the CEL-seq1 protocol that our laboratory implemented in 2013, individual cells were FACS-sorted into the individual wells of 96-well plates that were pre-filled with TRIzol. Subsequently, the content of these plates was transferred to 96 individual 0.5 ml tubes, after which manual and labour-intensive TRIzol extractions were performed on each of these tubes. In 2016, an improved version of the CEL-seq1 protocol (CEL-seq2 (ref. ⁴⁰)) was published, and in 2016, our laboratory implemented and published a robotized version of this protocol, referred to as “sorting and robot-assisted transcriptome sequencing”, or “SORT-seq”⁴¹). In SORT-seq, cells are sorted into the individual wells of 384-well plates that are pre-filled with oil and barcoded primers. Subsequently, cells are heat-lysed, after which the reagents required for first and second strand synthesis (Fig. 8a) are added with a robot. As multiple (~8) plates could be processed simultaneously with this robotized protocol, these developments enormously increased the number of cells that could be analysed per week. More recently, microfluidics-

based scRNA-seq approaches that allow even larger numbers of cells to be processed simultaneously, such as inDrop⁴², Drop-seq⁴³ and 10x Genomics Chromium⁴⁴ have been developed. The microfluidics devices that are used in these methods encapsulate individual

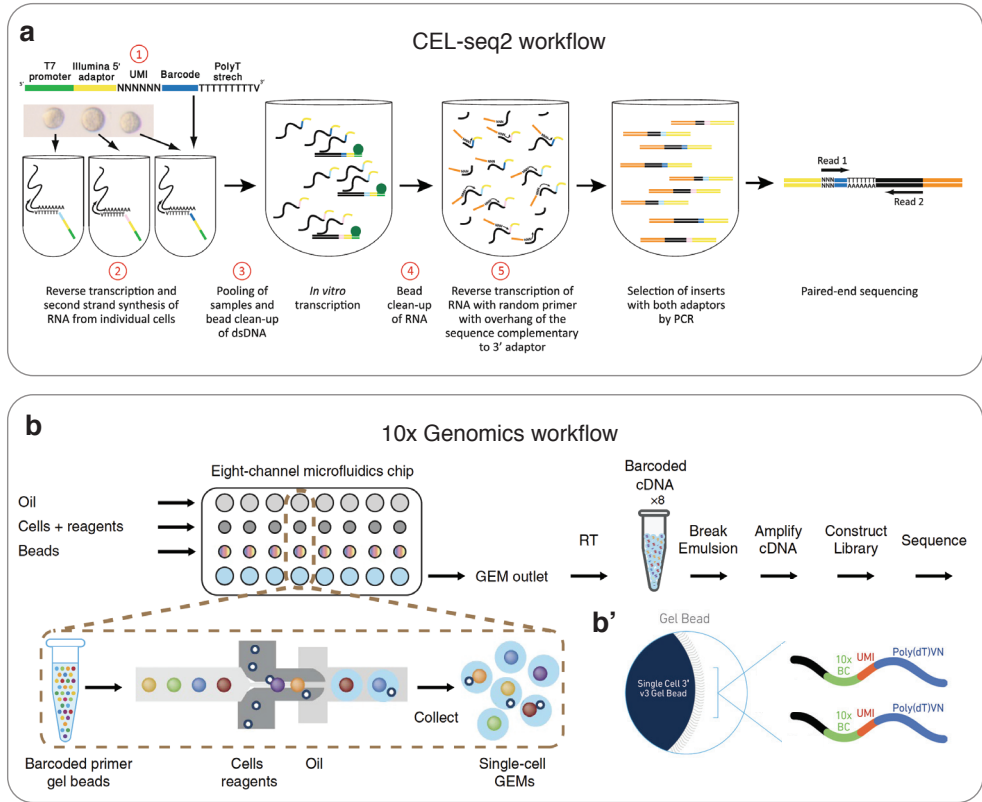


Fig. 8 | Examples of scRNA-seq methods: CEL-seq2 and 10x Genomics. a, CEL-seq2 workflow. Individual cells are sorted into individual tubes that contain barcoded primers. These primers contain a polyT stretch that hybridizes to the polyA tail of mRNA molecules, and a barcode that is unique for every tube. After lysis of the cells, the mRNA is reverse transcribed into DNA using reverse transcription and second strand synthesis. Next, all barcoded DNA molecules in the individual tubes are pooled into one Eppendorf tube, after which they are amplified using in vitro transcription (IVT). After IVT, the RNA is reverse-transcribed into DNA molecules that are amplified with PCR and sequenced. After sequencing, Read 1 (barcode read) can be used to determine to which cell this particular molecule belonged, and Read 2 is mapped to a reference transcriptome file to determine from what gene the original RNA molecule was derived. In our lab, we use a 384-well plate-based version of this protocol named “SORT-seq”⁴¹. In SORT-seq, cells are sorted into the individual wells of 384-well plates that are pre-filled with oil (to prevent evaporation) and uniquely barcoded primers. In SORT-seq, the reverse transcription and second strand synthesis reaction mixes are added with a Nanodrop robot, and plates are pooled into one Eppendorf tube by spinning them upside-down. b, 10x Genomics workflow. Thousands of cells are FACS-sorted into one Eppendorf tube. Next, the cells are added to a microfluidics chip, which is also loaded with oil and barcoded primer gel beads. The chip is then loaded into the 10x Genomics machine, after which the beads and cells will flow through miniature channels in the chip, which results in the formation of oil droplets (GEMs) that contain individual cells and barcoded beads (see also b’). These GEMs can subsequently be collected from the outflow well (blue well) of the chip. Next, the mRNA inside the GEMs is reverse transcribed into barcoded cDNA, after which the droplets are broken to pool the cDNA. The subsequent cDNA amplification and library construction steps result in the formation of sequencable DNA molecules. b’, Design of barcoded beads used in 10x Genomics. Adapted from “CEL-seq2: sensitive highly-multiplexed single-cell RNA-seq” (*Genome Biology*, Copyright © 2016) (a) and “Massively parallel digital transcriptional profiling of single cells” (*Nature Communications*, Copyright © 2017) (b).

1 cells into oil droplets that contain barcoded beads (Fig. 8b). With the development of such microfluidics-based technologies, which made it possible to measure the mRNA content of thousands of individual cells in an automated manner in just a few days, scRNA-seq became a standard technology in biology.

In this thesis, we have used scRNA-seq to characterize satellite cells (Chapter 2) and to analyse the cell type composition of mouse gastruloids (Chapter 3). The “evolution” of the scRNA-seq field can be observed throughout these two chapters. The first datasets from Chapter 2 were generated in 2014-2016 with the at the time still very new manual CEL-seq1 (ref. ³⁹) protocol. The data presented in the second part of Chapter 2 has been obtained in 2017 with SORT-seq⁴¹. The scRNA-seq mouse gastruloid dataset presented in Chapter 3 has been generated with a combination of SORT-seq (for cells analysed in 2018) and 10x Genomics Chromium⁴⁴ (for cells analysed in 2019).

Microscopy-based or sequencing-based spatial gene expression technologies complement scRNA-seq studies

Prior to scRNA-seq, tissues have to be dissociated into a single-cell suspension, which unavoidably comes together with a loss of spatial information. As such, scRNA-seq cannot be used to measure spatial gene expression patterns. In order to recover spatial gene expression patterns, alternative, spatial transcriptomics methods are required. Such spatial transcriptomics methods can be either microscopy- or sequencing-based. Microscopy-based spatial transcriptomics technologies, such as *in situ* hybridization (ISH)⁴⁵, single-molecule fluorescent ISH (smFISH⁴⁶⁻⁴⁸) and hybridization chain reaction (HCR⁴⁹) technologies, rely on the basic concept that a labelled DNA probes with a sequence that is complementary to the sequence of a transcript of interest can hybridize to, and hence label, this transcript directly in the tissue of interest. In conventional ISH protocols these probes contain DIG-labelled uridine nucleotides that can be detected with an antibody that is coupled to an alkaline phosphatase. This phosphatase converts a colourless dye to a purple dye that is deposited nearby the location of the transcript of interest. While conventional ISH can be used to visualize gene expression patterns in whole-mount samples, this method does not provide single molecule resolution and is thus not quantitative. In the more recently developed ISH-based smFISH⁴⁶⁻⁴⁸ protocol, transcripts are labelled with multiple (50-100) short (~20 nucleotide) fluorescently-labelled probes. The added-up fluorescent signal of these individual probes results in a signal that is strong enough to be detected with microscopy. As such, smFISH provides single-molecule resolution information on gene expression patterns in tissue sections. The fluorescent signal in smFISH is however not strong enough to detect RNA molecules at single-molecule resolution in whole-mount imaged samples. In order to detect single molecules in whole-mount samples, more advanced staining protocols such as HCR⁴⁹ that attach even more fluorophores to each RNA molecule of interest are required. In HCR, RNA transcripts are labelled with many small probes that are each linked to a long chain of fluorescently labelled molecules. During the HCR staining protocol, each individual RNA molecule is labelled with hundreds to thousands of fluorophores that together emit fluorescent signals so bright that

it can even be detected in whole-mount imaged embryos⁴⁹.

One of the most important limitations of smFISH and HCR technologies is that they only allow a maximum of ~5-6 transcripts of interest to be stained simultaneously. This limitation is linked to the maximum number of colours that can be discriminated with fluorescence microscopy. Recently, cyclic smFISH methods, such as osmFISH⁵⁰, seqFISH^{51,52} or merFISH⁵³ have been developed. These methods rely on the cyclic removal and re-staining of the same tissue section, and can be used to stain hundreds of genes simultaneously in the same tissue section. Simultaneously, various groups have also developed sequencing-based spatial transcriptomics methods that can be used to quantify the expression pattern of thousands of genes simultaneously without the need for cumbersome cyclic microscopy procedures. Examples of such methods include GEO-seq⁵⁴ (which combines laser capture microdissection with RNA sequencing), glass slide-based spatial transcriptomics-seq^{55,56} and tomo-seq (cryosectioning-based RNA tomography)⁵⁷. In tomo-seq, samples are sectioned into thin (~8-20 μm) sections along an axis of interest with a cryotome (Fig. 9). The sequential sections are subsequently processed either manually (first version of this protocol⁵⁷) or collected into the wells of a 96-well plate so that the mRNA content of the wells can be extracted and sequenced with a robotized, SORT-seq based version of tomo-seq (developed in Chapter 3 of this thesis) (Fig. 8a).

In this thesis, we have used smFISH to validate our scRNA-seq based findings regarding the heterogeneity of quiescent satellite cells (Chapter 2). In addition, we used both ISH and HCR to develop an improved version of the mouse gastruloids protocol (Chapter 3). Lastly, we

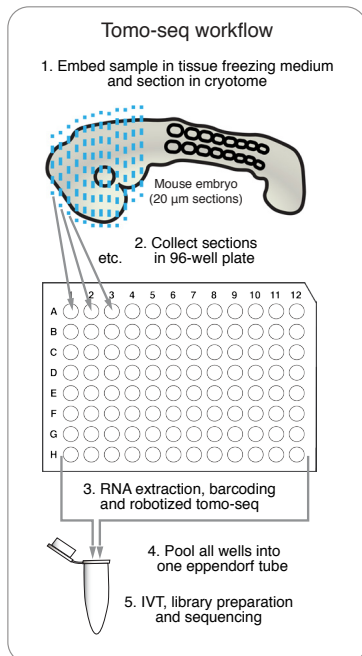


Fig. 9 | Robotized tomo-seq can be used to measure gene expression patterns along an axis of interest. In tomo-seq experiments, samples (for example mouse embryos) are embedded in tissue freezing medium and sectioned (~8-20 μm per section) along an axis of interest with a cryotome (step 1). The resulting sections are collected into the sequential wells of a 96-well plate; these wells are pre-filled with barcoded primers and mineral oil (step 2). Next, the RNA content of each well is amplified and converted to cDNA with a modified version of the SORT-seq protocol⁴¹, which is based on the CEL-seq2 (ref. ⁴⁰) protocol explained in Fig. 7a. To this end, the RNA is first barcoded and reverse transcribed into cDNA (step 3). After pooling all wells into one Eppendorf tube (step 4), the cDNA is converted into amplified RNA (aRNA) during an overnight in vitro transcription step (IVT; step 5). The next day, aRNA is converted to cDNA with reverse transcription, amplified with PCR and sequenced. Note: the original tomo-seq protocol⁵⁷ is manual and based on the CEL-seq1 protocol; this figure displays the workflow of the robotized and CEL-seq2-based version of this tomo-seq protocol that we have developed in Chapters 3 and used in Chapters 3 & 4 of this thesis.

used tomo-seq to compare spatial gene expression patterns between mouse gastruloids and mouse embryos (Chapter 3), to characterize and investigate the effect of Nodal inhibition on human gastruloids, and to compare mouse and human gastruloids (Chapter 4).

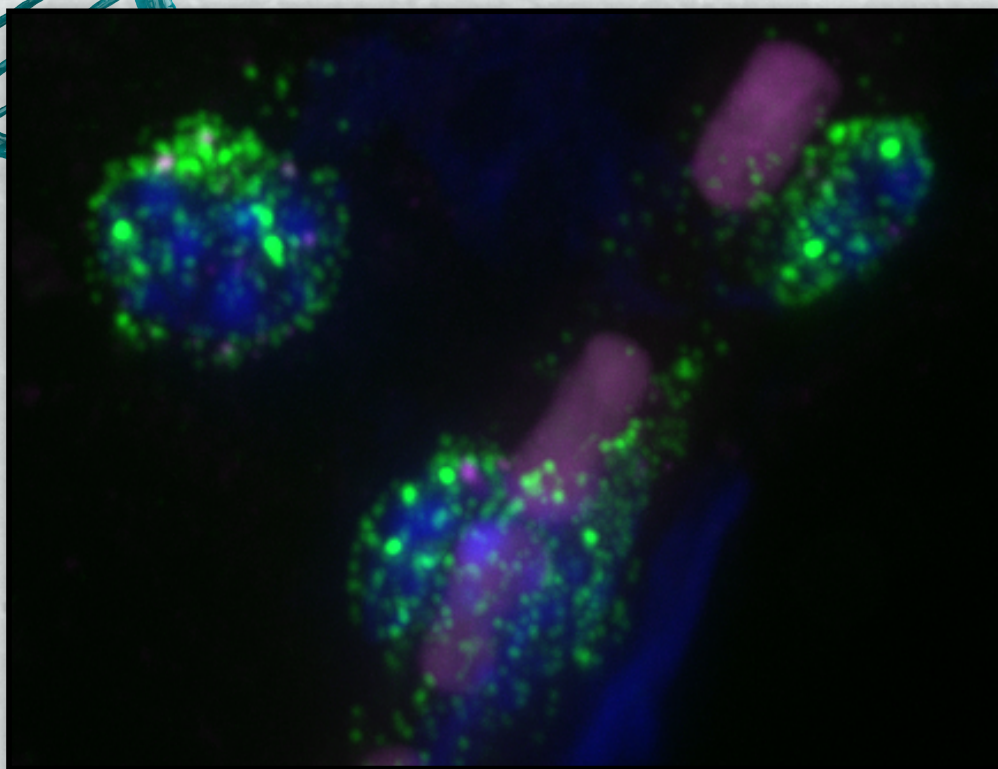
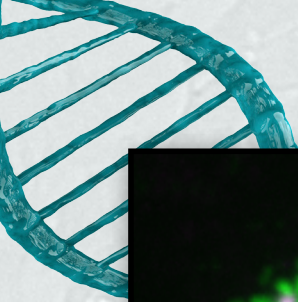
Aims of this thesis

The first aim of this thesis is to characterize the heterogeneity of quiescent satellite cells in more detail. To this end, we apply scRNA-seq to satellite cells extracted from uninjured muscles of Pax7nGFP mice, and validate our findings with smFISH. The results of these experiments are described in Chapter 2. The second aim of this thesis is to develop an improved version of the mouse gastruloids system that more accurately resembles post-implantation mouse embryos. In order to achieve this, we first characterize mouse gastruloids and compare them to mouse embryos in more detail than has been done previously. To this end, we apply a combination of scRNA-seq and tomo-seq to gastruloids, and the resulting datasets are compared to similar datasets generated for mouse embryos. This comparison is then used as a guide towards the development of an improved version of the mouse gastruloids culture protocol, for which we use a combination of live-imaging, ISH and HCR stainings. The results of these experiments are described in Chapter 3. Lastly, we aim to extrapolate our earlier findings with mouse gastruloids⁵ to human ES cells. To this end, we use a combination of immunostainings, (live) imaging and tomo-seq to develop a protocol for the generation of human gastruloids. We then compare such human gastruloids, which cannot easily be compared to human embryos due to legal and technical restrictions, to mouse gastruloids. Lastly, we use microscopy and tomo-seq to explore the effect of various teratogens on the developmental trajectory of these human gastruloids. The results of these experiments with human ES cells are described in Chapter 4.

References

1. Rossant, J. & Tam, P. P. L. New insights into early human development: lessons for stem cell derivation and differentiation. *Cell Stem Cell* **20**, 18–28 (2017).
2. Rossant, J. & Tam, P. P. L. Exploring early human embryo development. *Science* **360**, 1075–1076 (2018).
3. ten Berge, D. et al. Wnt signaling mediates self-organization and axis formation in embryoid bodies. *Cell Stem Cell* **3**, 508–518 (2008).
4. Marikawa, Y., Tamashiro, D. A. A., Fujita, T. C. & Alarcón, V. B. Aggregated P19 mouse embryonal carcinoma cells as a simple in vitro model to study the molecular regulations of mesoderm formation and axial elongation morphogenesis. *Genesis* **47**, 93–106 (2009).
5. van den Brink, S. C. et al. Symmetry breaking, germ layer specification and axial organisation in aggregates of mouse embryonic stem cells. *Development* **141**, 4231–4242 (2014).
6. Turner, D. A. et al. Anteroposterior polarity and elongation in the absence of extra-embryonic tissues and of spatially localised signalling in gastruloids: mammalian embryonic organoids. *Development* **144**, 3894–3906 (2017).
7. Harrison, S. E., Sozen, B., Christodoulou, N., Kyprianou, C. & Zernicka-Goetz, M. Assembly of embryonic and extraembryonic stem cells to mimic embryogenesis in vitro. *Science* **356**, (2017).
8. Beccari, L. et al. Multi-axial self-organization properties of mouse embryonic stem cells into gastruloids. *Nature* **562**, 272–276 (2018).
9. Sozen, B. et al. Self-assembly of embryonic and two extra-embryonic stem cell types into gastrulating embryo-like structures. *Nat. Cell Biol.* **20**, 979–989 (2018).
10. Simunovic, M. et al. A 3D model of a human epiblast reveals BMP4-driven symmetry breaking. *Nat. Cell Biol.* **21**, 900–910 (2019).
11. Zheng, Y. et al. Controlled modelling of human epiblast and amnion development using stem cells. *Nature* **573**, 421–425 (2019).
12. Shao, Y. et al. A pluripotent stem cell-based model for post-implantation human amniotic sac development. *Nat. Commun.* **8**, 208 (2017).
13. Rivron, N. C. et al. Blastocyst-like structures generated solely from stem cells. *Nature* **557**, 106–111 (2018).
14. Wolpert, L., Tickle, C. & Arias, A. M. *Principles of Development*. (Oxford University Press, USA, 2015).
15. Wamaitha, S. E. & Niakan, K. K. Human pre-gastrulation development. *Curr. Top. Dev. Biol.* **128**, 295–338 (2018).
16. Tajbakhsh, S. Skeletal muscle stem cells in developmental versus regenerative myogenesis. *J. Intern. Med.* **266**, 372–389 (2009).
17. Rocheteau, P., Gayraud-Morel, B., Siegl-Cachedenier, I., Blasco, M. A. & Tajbakhsh, S. A subpopulation of adult skeletal muscle stem cells retains all template DNA strands after cell division. *Cell* **148**, 112–125 (2012).
18. Tierney, M. T. & Sacco, A. Satellite cell heterogeneity in skeletal muscle homeostasis. *Trends Cell Biol.* **26**, 434–444 (2016).
19. Evans, M. J. & Kaufman, M. H. Establishment in culture of pluripotential cells from mouse embryos. *Nature* **292**, 154–156 (1981).
20. Martin, G. R. Isolation of a pluripotent cell line from early mouse embryos cultured in medium conditioned by teratocarcinoma stem cells. *Proc. Natl. Acad. Sci. USA* **78**, 7634–7638 (1981).
21. Thomson, J. A. et al. Embryonic stem cell lines derived from human blastocysts. *Science* **282**, 1145–1147 (1998).
22. Kunath, T. et al. Imprinted X-inactivation in extra-embryonic endoderm cell lines from mouse blastocysts. *Development* **132**, 1649–1661 (2005).
23. Tanaka, S., Kunath, T., Hadjantonakis, A. K., Nagy, A. & Rossant, J. Promotion of trophoblast stem cell proliferation by FGF4. *Science* **282**, 2072–2075 (1998).
24. Takahashi, K. & Yamanaka, S. Induction of pluripotent stem cells from mouse embryonic and adult fibroblast cultures by defined factors. *Cell* **126**, 663–676 (2006).
25. Takahashi, K. et al. Induction of pluripotent stem cells from adult human fibroblasts by defined factors. *Cell* **131**, 861–872 (2007).
26. Boroviak, T. & Nichols, J. Primate embryogenesis predicts the hallmarks of human naïve pluripotency. *Development* **144**, 175–186 (2017).
27. Warmflash, A., Sorre, B., Etoc, F., Siggia, E. D. & Brivanlou, A. H. A method to recapitulate early embryonic spatial patterning in human embryonic stem cells. *Nat. Methods* **11**, 847–854 (2014).
28. Etoc, F. et al. A balance between secreted inhibitors and edge sensing controls gastruloid self-organization. *Dev. Cell* **39**, 302–315 (2016).
29. Martyn, I., Siggia, E. D. & Brivanlou, A. H. Mapping cell migrations and fates in a gastruloid model to the human primitive streak. *Development* **146**, (2019).

30. Desbaillets, I., Ziegler, U., Groscurth, P. & Gassmann, M. Embryoid bodies: an in vitro model of mouse embryogenesis. *Exp. Physiol.* **85**, 645–651 (2000).
31. Itskovitz-Eldor, J. et al. Differentiation of human embryonic stem cells into embryoid bodies comprising the three embryonic germ layers. *Molecular Medicine* **6**, 88–95 (2000).
32. Pereira Daoud, A. et al. Modelling human embryogenesis: embryo-like structures spark ethical and policy debate. *Hum. Repr. Update* - submitted.
33. Baillie-Johnson, P., van den Brink, S. C., Balayo, T., Turner, D. A. & Arias, A. M. Generation of aggregates of mouse embryonic stem cells that show symmetry breaking, polarization and emergent collective behaviour in vitro. *J. Vis. Exp.* **105**, e53232 (2015).
34. Girgin, M. et al. Generating gastruloids from mouse embryonic stem cells. *Protoc. Exch.* (2018) doi:10.1038/protex.2018.094.
35. Rossi, G. et al. Embryonic organoids recapitulate early heart organogenesis. *bioRxiv* (2019) doi:10.1101/802181.
36. Tang, F. et al. mRNA-seq whole-transcriptome analysis of a single cell. *Nat. Methods* **6**, 377–382 (2009).
37. Islam, S. et al. Highly multiplexed and strand-specific single-cell RNA 5' end sequencing. *Nat. Prot.* **7**, 813–828 (2012).
38. Ramsköld, D. et al. Full-length mRNA-seq from single-cell levels of RNA and individual circulating tumor cells. *Nat. Biotechnol.* **30**, 777–782 (2012).
39. Hashimshony, T., Wagner, F., Sher, N. & Yanai, I. CEL-seq: single-cell RNA-seq by multiplexed linear amplification. *Cell Rep.* **2**, 666–673 (2012).
40. Hashimshony, T. et al. CEL-seq2: sensitive highly-multiplexed single-cell RNA-seq. *Genome Biol.* **17**, 77 (2016).
41. Muraro, M. J. et al. A single-cell transcriptome atlas of the human pancreas. *Cell Syst* **3**, 385–394.e3 (2016).
42. Klein, A. M. et al. Droplet barcoding for single-cell transcriptomics applied to embryonic stem cells. *Cell* **161**, 1187–1201 (2015).
43. Macosko, E. Z. et al. Highly parallel genome-wide expression profiling of individual cells using nanoliter droplets. *Cell* **161**, 1202–1214 (2015).
44. Zheng, G. X. Y. et al. Massively parallel digital transcriptional profiling of single cells. *Nat. Commun.* **8**, 14049 (2017).
45. Jin, L. & Lloyd, R. V. In situ hybridization: methods and applications. *J. Clin. Lab. Anal.* **11**, 2–9 (1997).
46. Femino, A. M., Fay, F. S., Fogarty, K. & Singer, R. H. Visualization of single RNA transcripts in situ. *Science* **280**, 585–590 (1998).
47. Raj, A., van den Bogaard, P., Rifkin, S. A., van Oudenaarden, A. & Tyagi, S. Imaging individual mRNA molecules using multiple singly labeled probes. *Nat. Methods* **5**, 877–879 (2008).
48. Lyubimova, A. et al. Single-molecule mRNA detection and counting in mammalian tissue. *Nat. Protoc.* **8**, 1743–1758 (2013).
49. Choi, H. M. T. et al. Third-generation hybridization chain reaction: multiplexed, quantitative, sensitive, versatile, robust. *Development* **145**, (2018).
50. Codeluppi, S. et al. Spatial organization of the somatosensory cortex revealed by osmFISH. *Nat. Methods* **15**, 932–935 (2018).
51. Lubeck, E., Coskun, A. F., Zhiyentayev, T., Ahmad, M. & Cai, L. Single-cell in situ RNA profiling by sequential hybridization. *Nat. Methods* **11**, 360–361 (2014).
52. Eng, C.-H. L. et al. Transcriptome-scale super-resolved imaging in tissues by RNA seqFISH. *Nature* **568**, 235–239 (2019).
53. Chen, K. H., Boettiger, A. N., Moffitt, J. R., Wang, S. & Zhuang, X. RNA imaging. Spatially resolved, highly multiplexed RNA profiling in single cells. *Science* **348**, aaa6090 (2015).
54. Chen, J. et al. Spatial transcriptomic analysis of cryosectioned tissue samples with Geo-seq. *Nat. Protoc.* **12**, 566–580 (2017).
55. Ståhl, P. L. et al. Visualization and analysis of gene expression in tissue sections by spatial transcriptomics. *Science* **353**, 78–82 (2016).
56. Rodriques, S. G. et al. Slide-seq: A scalable technology for measuring genome-wide expression at high spatial resolution. *Science* **363**, 1463–1467 (2019).
57. Junker, J. P. et al. Genome-wide RNA tomography in the zebrafish embryo. *Cell* **159**, 662–675 (2014).
58. Chal, J. & Pourqu  , O. Making muscle: skeletal myogenesis in vivo and in vitro. *Development* **144**, 2104–2122 (2017).
59. Turner, D. A. et al. Interactions between Nodal and Wnt signalling drive robust symmetry-breaking and axial organisation in gastruloids (embryonic organoids). *bioRxiv* (2016) doi:10.1101/051722.



*"It is through science that we prove,
but through intuition that we discover."
(H. Poincare)*

2

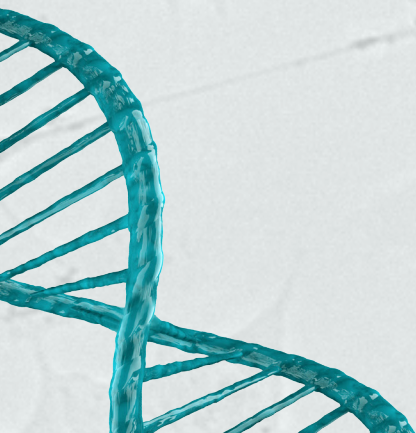
Single-cell sequencing reveals dissociation-induced gene expression in tissue subpopulations

Susanne C. van den Brink^{*}, Fanny Sage^{*}, Ábel Vértesy, Bastiaan Spanjaard, Josi Peterson-Maduro, Chloé S. Baron, Catherine Robin & Alexander van Oudenaarden[§]

^{*} Equal contribution

[§] Corresponding author

Nature Methods (2017)



2

In many gene expression studies, cells are extracted by tissue dissociation and fluorescence-activated cell sorting (FACS), but the effect of these protocols on cellular transcriptomes is not well characterized and is often ignored. Here, we applied single-cell mRNA sequencing (scRNA-seq) to muscle stem cells, and we found a subpopulation that is strongly affected by the widely used dissociation protocol that we employed. One implication of this finding is that several published transcriptomics studies may need to be reinterpreted. Importantly, we detected similar subpopulations in other single-cell data sets, suggesting that cells from other tissues may be affected by this artifact as well.

Regeneration of skeletal muscles in adults depends on the activation of otherwise quiescent muscle stem cells, the satellite cells (SCs)¹. The quiescent SC population is considered to be heterogeneous^{1,2}. We sequenced single SCs that we extracted from uninjured tibialis anterior (TA) muscles of Pax7nGFP mice with a widely used²⁻⁴ dissociation protocol to characterize their heterogeneity in more detail (Supplementary Fig. 1a–e and Supplementary Methods). After dissociation and FACS, we applied scRNA-seq (CEL-seq)⁵, and we identified two subpopulations in the data (Fig. 1a and Supplementary Fig. 1f,g). The cells assigned to subpopulation 2 expressed high levels of immediate early genes (IEGs, including *Fos*, *Jun* and other activating protein 1 complex genes), *Socs3* and heat-shock proteins (HSPs) (Fig. 1a, Supplementary Fig. 2 and Supplementary Table 1). Interestingly, these genes have been described in several satellite cell studies^{3,4,6} (Supplementary Fig. 1h), which suggests that we identified two functionally distinct subpopulations of SCs.

To validate the existence of the two subpopulations, we performed single-molecule RNA fluorescence in situ hybridization (smFISH) on cryosections of Pax7nGFP muscles using probes designed against the subpopulation-2-specific genes *Fos* and *Socs3* (Supplementary Table 2). We could not detect expression of *Fos* and *Socs3* in cryosections; however, we could detect *Fos* in SCs that had undergone dissociation or both dissociation and FACS, which demonstrated that the SC isolation procedure induces *Fos* expression in a subpopulation of the SCs (Fig. 1b and Supplementary Fig. 3). Additional experiments revealed that the duration of the dissociation protocol affects the detected bulk expression levels of the genes that are unique to subpopulation 2 (Fig. 1c, Supplementary Note 1, Supplementary Figs. 4 and 5, and Supplementary Tables 3 and 4), and this confirmed that the dissociation protocol affects the transcriptome of SCs. Our observations thus suggest that subpopulation 2 might not exist in vivo in uninjured muscles and that, in contrast to the current consensus^{1,2}, the quiescent satellite cell population might be relatively homogenous in vivo.

Next, we developed computational and experimental strategies to remove the dissociation-affected subpopulation of SCs. The computational solution entails the in silico removal of dissociation-affected cells from single-cell data sets (Supplementary Note 2, Supplementary Fig. 6 and Supplementary Table 5). The experimental solution combines indexed FACS and robot-assisted transcriptome sequencing (SORT-seq)⁷ on SCs that are stained for mitochondrial activity (Supplementary Note 3) in order to effectively identify and remove

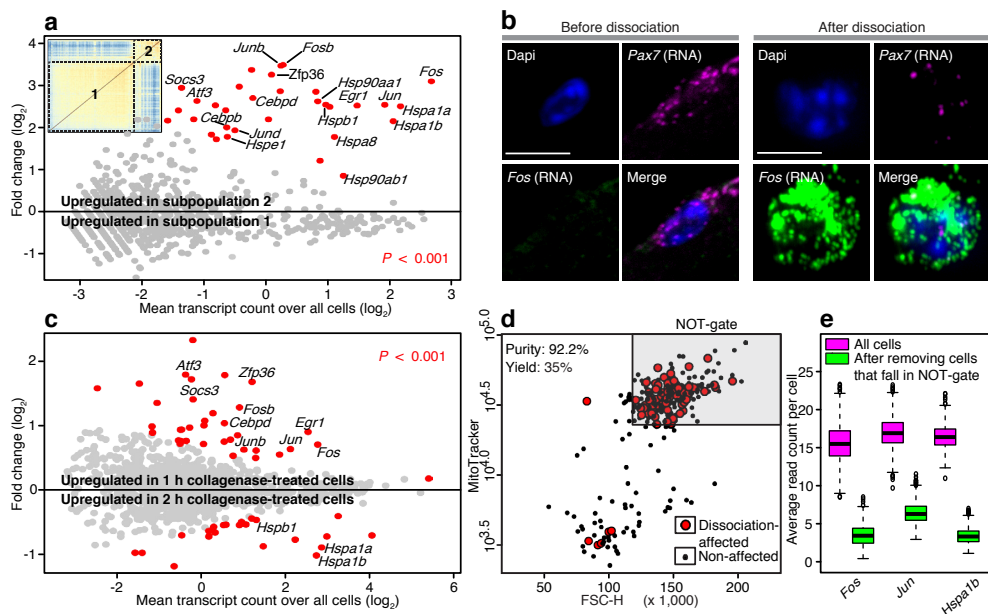


Figure 1 | Widely used tissue dissociation protocol induces transcriptional changes in a subpopulation of satellite cells. **a**, Heatmap (inset) showing transcriptome correlations of 235 freshly isolated single-cell sequenced SCs and scatterplot showing genes that are differentially expressed between the two identified subpopulations. Significant genes are labelled in red ($P < 0.001$); P values were calculated using negative binomial distribution as previously described (Supplementary Methods) and were corrected for multiple testing by the Benjamini-Hochberg method; $n = 178$ and 57 cells for cluster 1 and 2, respectively. Red and blue colours in heatmap represent 1 – Pearson correlation values of 0 and 1, respectively. **b**, Cryosection of SC in intact (all *Fos* negative; $n = 80$) and dissociated (right; *Fos* detected in 27 out of the 75 SCs) muscles that were stained for *Fos* (green) and *Pax7* (magenta) RNA using smFISH. Blue, nuclei, DAPI; scale bar, 5 μm . **c**, Genes that are differentially expressed between 1-h and 2-h collagenase-treated SCs. P values calculated as in **a**, with $n = 272$ and 223 cells for 1-h and 2-h collagenase-treated cells, respectively. **d**, MitoTracker and FSC-H levels of 284 MitoTracker-stained SCs. Dissociation-affected cells (red) were identified by SORT-seq; NOT-gate (gray) was designed based on a pilot study (Supplementary Fig. 7). **e**, Average expression levels of *Fos*, *Jun* and *Hspa1b* in all cells (magenta) and after removing the cells that fall in the NOT-gate (green). Box plots: center line, median; box limits, upper and lower quartiles; whiskers, 1.5x interquartile range; points, outliers.

dissociation-affected cells during FACS (Fig. 1d,e, Supplementary Note 3, and Supplementary Figs. 7 and 8).

Our results show that the SC isolation procedure induces transcriptome-wide changes in a subpopulation of these cells. Even though the dissociation-affected subpopulation can be relatively small, it causes a strong contaminating signal in bulk studies because of the high expression levels of the induced IEG and HSP genes. Interestingly, the genes that are induced by dissociation are also induced by muscle injury⁵, which suggests that the dissociation protocol activated some of the satellite cells (Supplementary Note 4). Our findings thus show that what was previously considered to be a purely quiescent subpopulation of SCs is in fact contaminated with a dissociation-affected subpopulation that might reflect activated SCs. Therefore, the results of several previous bulk studies where similar dissociation protocols have been used to study ‘quiescent’ SCs^{2–4} warrant reinterpretation (Supplementary Note 4).

Since similar dissociation procedures are also used to isolate cells from other tissues, our findings may be more broadly relevant. For example, a similar IEG- and HSP-expressing subpopulation that was not validated by microscopy has been described in a recent single-cell study of mouse acinar cells⁸ (Supplementary Fig. 9a and Supplementary Table 6). We also identified subpopulations with high IEG and HSP expression in other single-cell data sets from our lab, including a subpopulation of osteoblast cells in a zebrafish fin data set that is highly similar to the dissociation-affected subpopulation of satellite cells (Supplementary Fig. 9b– and Supplementary Table 7). The overlap between our satellite cell data and other data sets suggests that dissociation protocols might induce similar problems across tissues and even across species. Taken together, our results highlight the importance of single-cell resolved experiments and validation by orthogonal methods.

Acknowledgements

We thank M. Muraro and A. Lyubimova for experimental advice. We also thank the Hubrecht FACS facility, the Hubrecht Single Cell facility, the Hubrecht Imaging facility and the Utrecht Sequencing Facility (USF). This work was supported by a Nederlandse Organisatie voor Wetenschappelijk Onderzoek (NWO) TOP award (NWO-CW 714.016.001) to A.v.O. and by an European Research Council grant (ERC 220-H75001EU/HSCOrigin-309361) and the UMC Utrecht “Regenerative Medicine & Stem Cells” priority research program to C.R. Pax7nGFP mice were kindly provided by S. Tajbakhsh (Institut Pasteur, Paris, France).

Author contributions

S.C.v.d.B. and A.v.O. conceived and designed the project. S.C.v.d.B. and F.S. performed experiments. S.C.v.d.B., A.V. and B.S. analysed the data. The zebrafish fin experiments were performed by J.P.-M. and analysed by J.P.-M. and C.S.B. S.C.v.d.B. and F.S. wrote the manuscript with support from all other authors. C.R. and A.v.O. guided the project.

Data availability

Sequencing data and FACS index data produced in this study are deposited under accession number GSE85755. Source data for Fig. 1 is available online at <https://bit.ly/3eyS6ZY>.

Code availability

All custom-made code for this study is available in the Supplementary Methods (“in silico purification” section).

Supplementary Information for Chapter 2

Supplementary Notes

Supplementary Note 1 | Dissociation time experiment confirms that the dissociation procedure influences the transcriptome of SCs.

Our microscopy validation experiments show that the expression of *Fos* and *Socs3* is induced by the muscle dissociation protocol (Fig. 1b and Supplementary Fig. 3). To further demonstrate that the dissociation protocol affects the transcriptome of a subpopulation of SCs, we applied SORTing and Robot-assisted Transcriptome SEQuencing (SORT-seq)⁸, a robotized version of the CEL-seq2 protocol⁹ to SCs that experienced 1-hour and 2-hours of enzymatic dissociation (Supplementary Fig. 4a-d). After mapping and filtering, 495 cells were clustered using Rare cell type Identification 2 (RaceID2 (ref. ¹⁰)), and 5 clusters were detected (Supplementary Fig. 4e-f). Cells in clusters 1 and 4 express Activating Protein 1 (AP-1) complex genes (including *Fos*), *Socs3* and HSPs (Supplementary Table 3 and Supplementary Fig. 5), indicating that these clusters contain cells that are affected by the dissociation procedure. Clusters 2, 3 and 5 are very similar to each other and might represent only 1 biologically relevant cluster of SCs that are not affected by the dissociation procedure (Supplementary Table 3). Cluster 1 is very similar to the cluster 2 that was detected in our initial experiments (Supplementary Tables 1 and 3), the only difference being that the SORT-seq protocol allowed us to detect a larger number of differentially expressed genes. Cluster 1 mostly consists of 1-hour collagenase-treated cells (Supplementary Fig. 4g-h) and has higher expression of AP-1 complex genes than cluster 4, where HSPs are more prominent (Supplementary Fig. 4i and Supplementary Fig. 5). Cluster 1-cells are less abundant after 2 hours of enzymatic dissociation (Supplementary Fig. 4h), which may suggest that these cells either die or change their transcriptional profile towards one of the other clusters during the dissociation procedure. Alternatively, these observations might be explained by the sequential release of pre-existing subpopulations that respond to the dissociation procedure in different ways.

Most importantly, this dissociation time course experiment shows that the detected expression levels of cluster 2-specific genes in bulk experiments depend on the duration of the dissociation procedure (Fig. 1c), confirming that the transcriptome of SCs changes during the dissociation procedure. Our observations are therefore suggesting that the IEGs and HSPs expressing subpopulation might not exist in vivo in uninjured muscles and that, in contrast to what was previously believed^{1,2}, the quiescent satellite cell population might be relatively homogenous in vivo (see also Supplementary Note 4 for detailed discussion on SC heterogeneity).

Supplementary note 2 | In silico purification can be used to identify and remove dissociation-affected cells from single-cell datasets.

Here, we have shown that a widely-used SC purification protocol induces transcriptional changes in a subpopulation of the cells. The contamination with dissociation-affected cells is more problematic for bulk expression studies than for single-cell studies, as for single-cell studies this issue can be resolved by in silico removing cells of which the existence cannot be validated in situ. For our datasets, such a purification could be performed by simply removing the clusters with high IEG and HSP expression. However, we decided to instead develop a more generally applicable in silico purification method to remove dissociation-affected cells that does not depend on computational clustering and that can more easily be applied to other datasets (Supplementary Methods). This method was developed using our SORT-seq dataset (Supplementary Fig. 4-5) and validated with our first CEL-seq dataset (Supplementary Fig. 1-2). Using our SORT-seq dataset, we found that dissociation-affected cells (cells in clusters 1 and 4 of Supplementary Fig. 4f) and non-dissociation-affected cells (cells in clusters 2, 3 and 5 of Supplementary Fig. 4f) can be separated by the percentage of reads that map to dissociation-affected genes (Supplementary Methods). The distribution of this metric has a long tail in which the vast majority of the dissociation affected cells reside (Supplementary Fig. 6a). By setting a threshold at 5.75% (red dotted line in Supplementary Fig. 6a), we can remove all dissociation-affected cells while removing only 6% of the non-dissociation affected cells (Supplementary Fig. 6b-d). This in silico purification method was next successfully applied to our first CEL-seq dataset, demonstrating the robustness of this strategy (Supplementary Fig. 6e-g).

Supplementary Note 3 | Experimental strategy to remove dissociation-affected cells during FACS.

Above, we have shown that dissociation-affected cells can be computationally removed from single-cell datasets using in silico purification (Supplementary Note 2). As for some experiments it might be very challenging to obtain single-cell resolution, or it might be required to work with live cells, we also developed a method that can be used to experimentally remove dissociation-affected cells that keeps the cells alive. For this, we hypothesized that dissociation-affected cells may represent stressed cells, which might display a higher metabolic activity. We therefore

stained extracted SCs for mitochondrial activity using MitoTracker Red. This dye accumulates in active mitochondria and may therefore stain dissociation-affected (stressed) cells. We then sorted MitoTracker-stained single Pax7nGFP cells into 384-wells plates using indexed FACS (Supplementary Methods and Supplementary Fig. 7a-b) and noticed that some Pax7nGFP cells stained higher for mitochondrial activity (Supplementary Fig. 7b). After cell sorting, we performed SORT-seq to determine which wells contained dissociation-affected cells. Dissociation-affected cells were defined as cells of which more than 5% of the transcriptome mapped to dissociation-affected genes (using our *in silico* purification method, which is described in Supplementary Note 2), and we identified 14 dissociation-affected cells (Supplementary Fig. 7c). We then analysed the FACS index-data (Supplementary Methods) and found that affected cells stain high for MitoTracker and display high forward scatter values (Supplementary Fig. 7d-e). Based on this information we designed a NOT-gate that can be used to remove cells with high forward scatter and high mitochondrial activity (Supplementary Methods). This NOT-gate allows the removal of 12 of the 14 dissociation-affected cells (Supplementary Fig. 7f).

Next, we validated this gate using a larger number of MitoTracker labelled cells. We sorted all Pax7nGFP-positive cells, including cells inside the NOT-gate (Supplementary Fig. 8a-b), and performed SORT-seq. We identified 80 dissociation-affected cells (Supplementary Fig. 8c). 74 out of the 80 dissociation-affected cells fell in the NOT-gate (Fig. 1d) that was pre-designed based on our pilot study (Supplementary Fig. 7f), reducing the number of dissociation-affected cells by more than one order of magnitude. This gating strategy successfully decreased the bulk expression levels of *Fos* and other HSP and IEG genes (Fig. 1e and Supplementary Fig. 8d). Importantly, this strategy is compatible with live SCs opening the possibility of functional follow-up studies.

Supplementary Note 4 | Extended discussion: dissociation-response is similar to the response to muscle injury, and reinterpretation of existing satellite cell literature.

Here, we show that a widely-used SC purification protocol induces transcriptional changes in a subpopulation of the cells. The genes that are specifically expressed in the dissociation-affected subpopulation (Fig. 1a and Supplementary Table 1) are well known stress-response genes^{11,12}, suggesting that the dissociation protocol induced a stress-response in some of the cells. These genes are also induced in muscles upon injury, as has been shown in a study where the transcriptome of injured muscles was compared with that of uninjured muscles⁶. As the muscles used in this injury study were not dissociated, the genes identified in this injury study are most likely not affected by any experimental procedures. Additionally, another study using *in situ* hybridizations on cryosections of non-dissociated tissues demonstrated that *Fos* and *Jun* are indeed induced upon injury¹³. The overlap between the list of injury-induced genes from the injury microarray analysis study⁶ and our list of genes that are upregulated in dissociation-affected cells (Fig 1h, bottom two bars) suggests that the dissociation protocol might have induced an injury-like response in some of the SCs. Activated SCs are known to have a higher metabolic activity and cell size compared to quiescent SCs¹⁴, consistent with our MitoTracker staining experiments (Supplementary Note 3).

Our findings thus show that what was previously believed to be a purely quiescent subpopulation of SCs is contaminated with a dissociation-affected subpopulation of SCs that might represent activated SCs. Therefore, the results of several previous bulk studies where similar dissociation protocols have been used to study “quiescent” SCs warrant reinterpretation. For example, in an aging study it was shown that *Fos*, *Socs3* and other genes that we found to be specifically expressed in dissociation-affected cells, are lowly expressed in SCs of 3-weeks old mice, expressed at intermediate levels in SCs of 3-months old mice, and expressed at high levels in SCs of 18-months old mice³. From these observations, the authors conclude that *Fos*, *Socs3* and several other genes are higher expressed in quiescent SCs of older mice. This conclusion was based on microarray data of extracted SCs and was not validated *in situ*. Our smFISH experiments show that *Fos* and *Socs3* are not expressed in quiescent SCs of 6-months old mice. The observations from this ageing study do thus likely not reflect differences between young and old quiescent SCs, but might instead reflect differences in the dissociation protocol. For example, old muscles are stiffer¹⁵ and might therefore be harder to dissociate than young muscles, which may result in a stronger *ex vivo* stress response in SCs isolated from older muscles. Alternatively, the results from the ageing study might reflect age-dependent differences in the response to injury/dissociation. In another SC bulk transcriptome analysis study, it was shown that *Fos*, *Socs3* and other genes that are specifically expressed in our dissociation-affected clusters are higher expressed in quiescent (freshly isolated) SCs than in SCs that have been cultured for 4 days⁴. From these observations, the authors conclude that *Fos* and *Socs3* are only expressed in quiescent SCs. These conclusions were however not validated *in situ*. In contrast, we suggest that the expression of *Fos* and *Socs3* is not linked to the quiescence of SCs, but rather to the recent isolation (activation) of the cells.

In our study, we have shown that the dissociation protocol induces the expression of IEGs and HSPs in a subpopulation of the SCs. It is currently not known why these genes are induced in only some of the cells. This heterogeneity in the response to dissociation could reflect the presence of two *in vivo* subpopulations that respond

2

to the dissociation protocol in different ways. Alternatively, this heterogeneity might be explained by heterogeneity in the exact treatment that individual cells receive during the dissociation protocol. For example, in the initial step of the dissociation protocol the muscles are chopped into small pieces with a razor blade, and the cells that upregulate *Fos* expression during the treatment might be hit by the razor blade during this initial step, while the other cells might not be damaged by the razor blade. If the latter explanation is what explains the heterogeneity in our dataset, then the satellite cell population might be relatively homogenous in vivo in uninjured muscles. Most studies on the heterogeneity of quiescent SCs have also been performed on freshly isolated SCs^{1,2}, however, the results of some of these studies are not validated in non-dissociated muscles. In one important SC heterogeneity study², SCs are extracted from tibialis anterior muscles of Pax7nGFP mice using an extraction protocol that is very similar to our SC extraction protocol². After SC extraction, the authors show that there are at least two subpopulations of SCs. One of these subpopulations (the Pax7nGFP^{hi} population) is by the authors described as a more dormant population, while the other subpopulation (the Pax7nGFP^{lo} population) is described as a population that is more primed for activation². The authors however also show that the Pax7nGFP^{lo} population has a higher metabolic activity and stains higher for MitoTracker than the Pax7nGFP^{hi} population (Fig. 2c in Rocheteau et al., 2012 (ref. ²)). In our experiments, we have shown that MitoTracker staining levels are higher in SCs that are affected by the dissociation protocol (Fig. 1d, Supplementary Note 3 and Supplementary Figs. 7-8). Therefore, the Pax7nGFP^{lo} population form this previously published heterogeneity study might represent SCs that are affected by the dissociation protocol. Both the Pax7nGFP^{lo} population and our dissociation-affected subpopulations of SCs might reflect a subpopulation that interpreted the muscle dissociation protocol as muscle injury and that became activated during the protocol. Therefore, the interpretation of the results on the Pax7nGFP^{lo} population might be slightly different as previously thought, as the events that are described in this previous heterogeneity publication might not reflect the in vivo uninjured situation. Instead, these events might only happen in dissociated/injured muscles, and the Pax7nGFP^{lo} population might not exist in vivo in uninjured muscles.

Taken together, one major implication of our work is that several previously published studies in the SC field will need to be reinterpreted. The main heterogeneity that we detect in our dataset is most likely induced by the dissociation procedure, suggesting that in contrast to what is currently the main consensus in the SC field¹, the quiescent SC population in uninjured TA muscles might be relatively homogenous in vivo.

Supplementary Methods

Mice and zebrafish

The following mouse strains were used for experiments: C57BL/6 and Pax7nGFP (ref. ¹⁶) (kindly provided by Dr. S. Tajbakhsh, Pasteur Institute Paris, France). All mice were housed according to the Hubrecht Institute guideline, which includes access to food and water ad libitum. All animal experiments were carried out in compliance with Standards for Care and Use of Laboratory Animals, with approval from the Dutch Animal Experiment Committee of the Koninklijke Nederlandse Akademie van Wetenschappen (KNAW). All Pax7nGFP mice used for microscopy and sequencing of non-MitoTracker stained cells were male, all Pax7nGFP mice used for MitoTracker staining experiments were female; all mice were between 4.7 and 7 months old at time of sacrifice. For our CEL-seq experiments (Fig. 1a, Supplementary Figs. 1-2 and Supplementary Table 1), 6 TA muscles were dissected from 3 mice; the muscles from the last 2 mice were processed in parallel on the same experimental day. For our SORT-seq collagenase-treatment duration experiment, 8 TA muscles dissected from 4 mice were pooled. The sample was split in two before the collagenase treatment was started. For our first series of microscopy experiments (validation experiments were cryosections of an intact muscle were stained for *Fos*, *Socs3* and *Pax7*; Supplementary Fig. 3a-b), 1 TA of 1 mouse was used. For both replicates of the dissociation experiment (where smFISH was applied to dissociated and sorted SCs; Fig. 1b and Supplementary Fig. 3c-g), two animals were sacrificed. For mouse 1, the right TA was fixed intact and the left muscle was dissociated. For mouse 2, the left TA was fixed intact and the right muscle was dissociated. The two muscles that were dissociated were pooled, dissociated and sorted together; both intact muscles were stained as controls. The two dissociation-smFISH experiments were performed on different, independent experimental days. For the first MitoTracker staining experiment (Supplementary Fig. 7), SCs were extracted from both TA's of a 4.7 months old female Pax7nGFP mouse. For the second MitoTracker staining experiment (Supplementary Fig. 8), SCs were extracted from 6 TA muscles from 3 female 6-months old Pax7nGFP mice. For the zebrafish fin dataset, we used the fin of two 18-months old fish that were housed according to standard laboratory guidelines at the Hubrecht Institute, Utrecht, The Netherlands according to local guidelines and policies in compliance with national and European law. The amputation and dissociation of the fin of both fish was performed on two independent experimental days.

Isolation of SCs using dissociation and FACS

SCs can be identified based on the expression of *Pax7* (ref. ^{1,17,18}). To characterize the heterogeneity of quiescent SCs in detail, we isolated SCs from uninjured tibialis anterior (TA) muscles of 6-month-old male Pax7nGFP mice¹⁶. The muscle dissociation protocol, which is necessary for the isolation of SCs, takes about 2.5 hours and combines mechanical and enzymatic dissociation (Supplementary Fig. 1a). After dissection, the muscles were dissociated to obtain a muscle single cell suspension from which single SCs could be extracted. Our dissociation procedure was based on previous SC isolation protocols^{17,18}. In the first step of the dissociation protocol, the muscle was chopped into small pieces with a razor blade in a 6 cm petri dish. Next, muscle pieces were transferred to 50 ml falcon tube and incubated in a collagenase type II (2 mg/ml Gibco, 17101015)/phosphate-buffered saline (PBS, Lonza, 17-516F) solution placed in a water bath set at 37 °C for 1 hour to degrade the extracellular matrix and release cells from their niche (Supplementary Fig. 1a, step 2). A volume of 10 ml of the collagenase solution was used per TA. The rest of the process was performed in PBS supplemented with 5% Fetal Bovine Serum (FBS, Sigma, F7524). After this enzymatic dissociation step, the volume in the falcon tube was readjusted to 50 ml with PBS/FBS and spun down (5 min, 300 rcf, 4 °C) to stop digestion by removing the enzyme. Next, the supernatant was aspirated and the pellet was resuspended in 10 ml of PBS/FBS. The digested tissue was then further dissociated using a p1000 pipette from which the tip extremity was cut off. The tissues were then further dissociated by passing the material 5 times through a 10 ml syringe associated with a 20 G needle. The Falcon was then filled up with PBS/FBS and spun down to wash away all the debris. After supernatant removal, the pellet was resuspended in 10 ml of PBS/FBS. The solution was then filtered with a cell strainer (Falcon 40 µm, 08-771-1) spun down and resuspended in 2 ml of FBS/PBS. Cells were then stored on ice for a maximum of 30 minutes before FACS was started. Just prior the sort, Hoechst 33258 (Molecular Probes, H3569; stock solution 10 mg/ml used 1/40,000) was added to the cell suspension.

Cell sorting was performed using a BD FACSAria II SORP Cell Sorter (BD Biosciences) that was equipped with Aria de DiVa software (version 8.0.1). For all sorts, we used a 100 µm nozzle, pressure of 20 psi, drop frequency of 27.1 kHz and a sample speed of 2,000 events/second. Single cells were selected by gating on forward scatter height, forward scatter width, side scatter height and side scatter width. Dead cells were excluded by gating on Hoechst negative cells using a 407 nm-laser and 450/50 emission filter and forward scatter area (Supplementary Fig. 1b and Supplementary Fig. 4a). nGFP expressing cells were selected using a 488 nm-laser and a 525/50 emission filter; sorting gates were defined based on negative control wildtype (C57Bl/6) muscle suspensions. Sort precision: yield mask = 0, purity mask = 16, phase mask = 8, single cell mode. An extra sample was sorted to check the purity. The purity for all the experiment was calculated to be between 85-95%.

Isolation of zebrafish fin cells using dissociation and FACS

Caudal fin collections were performed as previously described¹⁹. Once isolated, this tissue was immediately dissociated by moderately shaking at 30 °C for 1 h, with gentle trituration performed every 10 min with a p200 pipette, in a solution of 2 mg/ml collagenase A (Sigma-Aldrich) and 0.3 mg/ml protease (type XIV, Sigma-Aldrich) in Hanks solution. After 1 h, the solution was incubated for 5 min in 0.05% trypsin in PBS. The solution was strained using 70 µm and 40 µm cell strainers (Corning) and cells were washed in 2% FBS in Hanks solution. Before flow cytometry, cells were centrifuged and resuspended in PBS/FBS supplemented with DAPI (Thermo Fisher) to assess cell viability. Cell sorting was performed using a BD FACSJazz Cell Sorter (BD Biosciences) that was equipped with BD FACS software (version 1.2.0.124).

MitoTracker staining and indexed FACS of MitoTracker stained SCs

For the MitoTracker experiment, the extracted SCs were stained with MitoTracker Red CMXRos (ThermoFisher Scientific, M7512) at a concentration of 1/4,000 in PBS/FCS for 10 minutes at 37 °C. A small aliquot of the SC suspension was not stained and used as a negative control during FACS. A C75Bl/6 (wildtype) sample was used for compensation settings. During FACS, index files were generated. Index-files are spreadsheets in which all FACS information of a cell that is sorted into a specific well of our 384 wells plate is stored. FACS was performed as described above. MitoTracker staining levels of the nGFP expressing cells were recorded using a 532 nm-laser and 610/20 emission filter.

CEL-seq and library preparation

For CEL-seq⁵ experiments (Fig. 1a, Supplementary Figs. 1-2 and Supplementary Table 1), 94 single cells were sorted in 96-wells skirted qPCR plates (Greiner) that were pre-filled with 100 µl TRIzol Reagent (Ambion, Life Technologies, REF15596018) mixed with synthetic ERCC Spike-in RNA molecules (1:25x10⁷, Ambion, 4456740) per well²⁰. In the first and last well, we sorted 300 cells. After sorting, plates were snap-frozen on dry-ice and stored at -80 °C. Prior to CEL-seq, the content of each well was transferred to a 0.5 ml DNA-LoBind tube (VWR, 525-0129), after which a TRIzol RNA extraction was performed as described by the manufacturer, with two modifications. First, 0.25 µl of GlycoBlue reagent (1.25 µg/µl, Ambion, AM9515) was added to each sample before isopropanol was added to

2 facilitate RNA precipitation and to make pellets visible for later ethanol-washes. Second, the samples were incubated in isopropanol overnight. After precipitation, the RNA pellets were washed with 75% ethanol two times, air dried and resuspended in 1 μ l 5 ng/ μ l barcoded CEL-seq primers. Subsequently, CEL-seq was performed as described before⁵. The CEL-seq primers used here were modified to include unique molecular identifier (UMI)-barcodes, allowing us to count unique transcripts after sequencing^{21,22}. Because SCs are small and have very little RNA content, pooling material of 94 single SCs did not result in a sufficient amount of aRNA. Therefore, we also extracted the RNA from one bulk (300 cells) sample, of which the pellet was resuspended in 1 μ l of CEL-seq primer (barcode number 95). After first and second strand synthesis, the cDNA of this bulk sample was pooled with that of the single cells in order to get sufficient cDNA concentrations. Reads coming from this bulk sample could be identified after sequencing based on their barcode, and were removed from all datasets before data-analysis was started. After in vitro transcription (IVT), a library was prepared with TruSeq small RNA primers (Illumina) as described before⁵ with the following modifications: phosphatase-treatment, PNK-treatment and second column cleanup were skipped. For library preparation, 15 PCR cycles were applied.

For SORT-seq⁷ experiments, single cells were sorted in hard-shell 384-wells plates (Biorad, HSP3801). Wells O20-24 and P20-24 were left empty as an internal negative control. For the dissociation time course experiments (Fig. 1c and Supplementary Figs. 4-5), the plates were pre-filled with 6 μ l of Vapor-Lock oil (Qiagen, 981611), 100 nl of 7.5 ng/ μ l CEL-seq primers⁵ (that were modified to include UMI-barcodes as previously described previously^{21,22}), Spike-ins and dNTPs. As we only had 96 differently barcoded CEL-seq primers, every primer was used in 4 wells, so 4 libraries each containing reads from 94 single SCs were obtained from each plate (primers 95 and 96 were used for the empty wells). For the SORT-seq on MitoTracker stained SCs (Fig. 1d-e and Supplementary Figs. 7-8), we used 384 differently barcoded primers. After the sort, the plates were centrifuged for 1 minute at 400 rcf, after which they were snap-frozen on dry-ice and stored at -80 °C. Prior to SORT-seq, cells were lysed by heating the 384-wells plate to 65 °C 2x for 2.5 minutes, after which SORT-seq⁷, a modified version of the CEL-seq2 protocol⁹ was applied. For 1st cDNA strand synthesis, 150 nl of reverse transcription mix was added to the wells using a pipetting robot (Nanodrop II liquid handling system) and for 2nd strand synthesis, 1,920 nl of second strand mix was added to the wells using the robot (for contents of mix, see CEL-seq2 protocol⁹). After first and second strand synthesis, the cDNA was pooled. Tubes were then centrifuged at maximum speed for 1 minute, after which the aqueous phase was extracted from the oil. Next, aRNA was generated via IVT and library preparation was performed as described in the CEL-seq2 protocol, the only modification being that reagents were ordered from Thermo Fisher Scientific. Because of the higher efficiency of the SORT-seq protocol, we did not co-sequence a bulk sample in our SORT-seq experiments. Also, during library prep, only 12 (dissociation time course) or 13 (MitoTracker staining experiments) PCR cycles were applied. For SORT-seq experiments of MitoTracker stained SCs and for SORT-seq of zebrafish fin cells, the volumes of all reagents used during the SORT-seq protocol were half that of the volumes mentioned above.

Sequencing

Paired end (75 bp) sequencing was performed on the Illumina Next-seq sequencing platform. For CEL-seq experiments, we sequenced in total 7 libraries (4 libraries containing cells from mouse 1, 2 libraries containing cells from mouse 2 and 1 library containing cells from mouse 3). Cells processed with CEL-seq were sequenced at an average depth of 75,000 (mouse 1, first two libraries), 38,000 (mouse 1, last 2 libraries) and 25,000 (mice 2 and 3) reads per cell. For the SORT-seq dissociation time course experiments, we sequenced in total 8 libraries (each library containing cells from 94 wells), and all cells processed with SORT-seq were sequenced at an average depth of 156,000 reads per cell. For the first (pilot) SORT-seq experiment of MitoTracker stained cells, we sequenced 1 library (containing cells from 376 wells) with an average dept of 110,000 reads per cell. For the second MitoTracker SORT-seq experiment, we sequenced 4 libraries (376 wells per library) with an average dept of 110,000 reads/cell.

Mapping and generation of sequencing statistics plots

Mapping was performed as described previously²³. Briefly, fastq files were mapped to the mus musculus mm10 reference transcriptome (created from the mm10 genome downloaded from the UCSC genome browser; ERCC Spike-in sequences were added) using bwa (Li, H. & Durbin, R. Fast and accurate short read alignment with Burrows-Wheeler transform. *Bioinformatics* 25, 1754-1760 (2009)) with default parameters. Reads 2 were mapped to this reference transcriptome, and reads 1 were used to extract the cell-barcode sequences and UMIs as described before²³. Reads mapping to multiple loci in the transcriptome were discarded. For CEL-seq experiments, 23% (mouse 1, same result for all libraries), 20% (mouse 2, library 1), 5% (mouse 2, library 2) and 15% (mouse 3) of the reads sequenced mapped with a valid cell-specific barcode. For SORT-seq dissociation time course experiments, 23% of the sequenced reads were mapped with a valid barcode. For first (pilot) MitoTracker sequencing experiments, we used an optimized mapping script and a reference transcriptome that included mitochondrial genes (which were excluded during the initial data-analysis steps), the mappability was 90%. For the second MitoTracker experiment, which was mapped using the same script as the MitoTracker pilot experiment, the mappability was on average 88.5%. Zebrafish

data was also mapped with this optimized mapping script, and also here mitochondrial genes were removed prior to RaceID2-analysis.

After mapping, a UMI-correction was applied to the read and barcode counts files as described before²¹ to generate unique transcript count tables. From these tables, bulk samples (only for CEL-seq data), mitochondrial reads (only for SORT-Seq experiments of MitoTracker stained cells) and Spike-in reads were removed. Next, histograms showing the number of unique transcripts and number of genes detected per cell (Supplementary Fig. 1c-d and Supplementary Fig. 4b-c) were generated in R studio (version 0.98.953). Oversequencing histograms (Supplementary Fig. 1e and Supplementary Fig. 4d) were generated by dividing raw read counts by UMI-barcode counts for each gene in each cell detected. For all histograms, medians were calculated and plotted as red lines.

Clustering with RaceID

Clustering of CEL-seq data (using unique transcript count tables from which Spike-in and bulk reads were removed) was performed in R using RaceID2 (ref. ¹⁰). For mouse CEL-seq datasets, all cells with unique transcript counts below 700 were filtered out. For mouse SORT-seq datasets, cells with unique transcript counts below 3,000 were filtered out. Downsampling was applied to all datasets. For all datasets, the RaceID outlier detection option was turned off and genes detected with less than 3 transcripts in at least one cell were filtered out. After filtering, RaceID calculates distances between transcriptomes of cells as $1 - \text{Pearson correlation}$ and clusters cells based on their transcriptome similarities using k-medoids clustering¹⁰. For mouse CEL-seq data, 2 clusters (178 and 57 cells respectively) were detected by RaceID, and for mouse SORT-seq dissociation time course data, 5 clusters could be identified. In this manuscript, distance and clustering results are presented as heat maps (Fig. 1a and Supplementary Fig. 4e) where each line represents a cell, colouring indicates $1 - \text{Pearson correlation}$ between cells and clustering is indicated by colours and numbers along the axes. The data is also visualized in 2 dimensions using t-distributed stochastic neighbor embedding (t-SNE) maps^{10,24}. In these maps, each dot represents a cell and cells that are more similar are plotted closer together. In t-SNE maps, cells can be coloured according to the cluster they are assigned to (Supplementary Fig. 1f and Supplementary Fig. 4f), mouse of origin (Supplementary Fig. 1g), duration of collagenase treatment that was applied to the cell (Supplementary Fig. 4g) or number of unique transcripts detected of specific genes in that cell (Supplementary Fig. 2 and Supplementary Fig. 5). The zebrafish dataset (Supplementary Fig. 9) was analysed using this same method, the only difference being that the zebrafish data was downsampled to 500.

For Supplementary Fig. 4h, we calculated for all SORT-seq clusters the percentage of 1-hour and 2-hour collagenase-treated cells in that cluster. The percentages were corrected for a difference in total number of 1-hour and 2-hour collagenase treated cells (after filtering, 272 1-hour and 223 2-hour collagenase treated cells remained). Corrected cluster compositions were calculated as follows:

$$\begin{aligned} 1 \text{ h cluster composition of } C_i &= 1 \text{ h\% in } C_i / (1 \text{ h\% in } C_i + 2 \text{ h\% in } C_i) * 100 \\ 2 \text{ h cluster composition of } C_i &= 2 \text{ h\% in } C_i / (1 \text{ h\% in } C_i + 2 \text{ h\% in } C_i) * 100 \end{aligned}$$

Where 1 h% in C_i is the percentage of all 1-hour-dissociated cells that fall in cluster i and 2 h% in C_i is the percentage of all 2-hour dissociated cells that fall in cluster i .

95%-confidence intervals in Supplementary Fig. 4h were calculated by bootstrapping. For this, we randomly drew cells from all 1-hour and 2-hour dissociated cells with replacement. Sample size was 495, which is the same as the total number of cells in the actual dataset. For each bootstrap result the calculations explained above were repeated. After performing 1,000 bootstraps, the interval that contained 95% of all observed percentages were reported and included in Supplementary Fig. 4h as error bars.

Differential gene expression analysis using DESeq

Differential gene expression between SC and zebrafish fin cell clusters (Fig. 1a, Supplementary Fig. 4i, Supplementary Fig. 9a and Supplementary Tables 1,3,7) or between 1-hour and 2-hour collagenase-treated SCs (Fig. 1c and Supplementary Table 4) were calculated using a RaceID-adapted version of the previously described DESeq method²⁵. Using DESeq, P values corrected for multiple testing using the Benjamini-Hochberg method were calculated for all genes as described before²⁵. Only genes with a corrected P value below 0.001 are shown in Supplementary Tables 1,3,4-7. A full list of all genes that are defined as differentially expressed between CEL-seq clusters 1 and 2 according to this method, including their fold change and P value, can be found in Supplementary Table 1. A list of genes specific for SORT-seq clusters 1-5, and a list of genes that are significantly upregulated in cluster 1 versus cluster 4 and in cluster 4 versus cluster 1 can be found in Supplementary Table 3. A complete list of all genes that are significantly upregulated in 1-hour versus 2-hour and a list of genes that are significantly upregulated in 2-hour versus 1-hour collagenase-treated cells can be found in Supplementary Table 4.

Comparison of differential gene expression list with existing microarray datasets

To compare our list of genes that are significantly differentially expressed between CEL-seq clusters 1 and 2 with previous bulk RNA microarray studies^{3,4,6}, Affymetrix expression data was downloaded. Probes that mapped to multiple genes and probes that had no expression over 100 in any sample were removed. Next, the functions *lmFit* and *eBayes* from the R package *limm*²⁶ and linear models and empirical Bayes methods were used to assess differential expression in microarray experiments. Finally, a two-tailed Fisher's exact test was applied to compare the overlap between genes found upregulated in the literature (Benjamini-Hochberg corrected *P* value cutoff of 0.01 and at least a 2-fold upregulation) and cluster 2 upregulated genes in our dataset (Benjamini-Hochberg corrected *P* value cutoff of 0.001). For comparison between young and old mice, gene expression data from SCs isolated from > 1-year-old mice was compared to expression data from SCs isolated from 3-months old mice³. For comparison between quiescent and activated SCs, gene expression data from quiescent SCs was compared to that from activated (cultured) SCs⁴. For comparison between injured and uninjured muscles, gene expression data from 6 hours after freeze-injured and 6 hours after contraction-injured muscles were compared to that in uninjured muscles⁶.

Fixation, smFISH and mounting of samples for microscopy analysis

For validation experiments (Fig. 1b, left panels and Supplementary Fig. 3a-b), fixation, cryosectioning and smFISH were performed as described before²⁷ on intact Pax7nGFP TA muscles (muscles fixed after step 1 from Supplementary Fig. 1a). Muscles were fixed for 3 hours (step 15 in smFISH-protocol from Lyubimova. et al., 2013 (ref. ²⁷) and optional step 16 (overnight incubation in cryoprotection solution) was performed. Cryosections of 7 μ m thickness were made, and smFISH was always performed immediately after cryosectioning (i.e. incubation in 70% (vol/vol) ethanol in step 26 was only performed for 1 hour) to make sure that the GFP signal was preserved. The optional proteinase K digestion steps in the smFISH protocol were not performed. Probes for *Pax7*, *Fos* and *Socs3* were designed as previously described²⁷; oligonucleotide sequences are provided in Supplementary Table 2. Probe oligonucleotide libraries were conjugated to Cy5 succinimidyl ester (Cy5, GE Healthcare, PA25001) and to Alexa Fluor 594 carboxylic acid succinimidyl ester (Alexa Fluor 594, Molecular probes/Invitrogen, A37572) as described before²⁷. After HPLC purification, pellets were reconstituted in 30 μ l of TE buffer. During smFISH, *Fos*, *Socs3* and *Pax7* probes were applied respectively in 1:1,000, 1:500 and 1:1,200x dilutions from this stock solution. During the washes that were performed after overnight incubation with probes, DAPI was added (1:200 from 10 μ g/ml stock, Sigma-Aldrich, D9542-10MG) to stain the nuclei, and mounting was performed as described in the smFISH protocol²⁷.

For experiments where smFISH was performed on dissociated (Fig. 1b (right panels), Supplementary Fig. 3c-d and Supplementary Fig. 3g) and sorted (Supplementary Fig. 3e) SCs, one muscle of all animals used was fixed intact (after step 1 of Supplementary Fig. 1a). This muscle was then cryosectioned and stained as described above. The other muscle was dissociated and prepared for FACS as described above. Before FACS, the dissociated muscle was filtered as described in the FACS part of this methods section, and the dissociated muscle pieces that did not pass the filter were scraped off from the filter, after which they were fixed, sectioned and stained as described above for the uninjured muscle, the only modifications being that fixation was shortened to 30 minutes because of the small size of the muscle pieces, and step 16 of smFISH protocol (cryoprotection solution incubation) was skipped. These dissociated muscle pieces contained dissociated SCs that could be identified during microscopy based on their expression of GFP. The cells that did pass the FACS filter were sorted as described above. In contrast to CEL-seq experiments, SCs were now not sorted in plates but in a 1.5 ml protein LoBind tube (VWR, 525-0133) that was pre-filled with 500 μ l of PBS/FBS. After sorting, these cells were fixed and stained using an adapted version of the smFISH protocol²⁷. First, the cells were fixed 5 minutes in 4% paraformaldehyde (PFA) by adding 500 μ l of 8% PFA to the tube. Next, cells were washed twice in 50 μ l 70% (vol/vol) ethanol and incubated in 70% ethanol for 5 hours at 4 $^{\circ}$ C. Subsequently, the ethanol was removed and the cells were incubated with 100 μ l wash buffer (see smFISH protocol in Lyubimova, et al., 2013 (ref. ²⁷) for details) for 5 minutes. Then, after removing wash buffer, cells were incubated overnight with 50 μ l hybridization buffer containing *Pax7* and *Fos* smFISH probe libraries. Next, cells were incubated in 100 μ l wash buffer 2x; DAPI was added to the wash buffer during the second incubation, after which cells were incubated in GLOX buffer (see smFISH protocol for details). All wash steps were performed by spinning the tube in a swing-out centrifuge (400 rcf, 4 $^{\circ}$ C, 10 min), after which liquid was carefully removed. As the number of cells was so small that we could not see a pellet, some (~50 μ l) liquid was left behind after all washes to minimize cell loss. After the last centrifugation step, almost all GLOX buffer was removed, 5 μ l smFISH imaging buffer (see ref. ²⁷) was added and the liquid was mounted on a slide using small round coverslips.

In all smFISH experiments, sections of wildtype mouse small intestines (leftover material) were stained for *Fos* or *Socs3* as positive controls. These positive controls were included to make sure that our smFISH experiments worked that specific day and were especially useful on experimental days where we could not detect *Fos* or *Socs3* in SCs (for example, on days where intact muscles were imaged).

Microscopy and processing of microscopy data

Imaging of all experiments were samples were stained for *Fos* was performed using a Perking-Elmer Spinning Disc confocal microscope with a 100x oil-immersion objective (numerical aperture 1.4) equipped with Perking Elmer Velocity software. *Socs3*-stained samples were imaged using an inverted epifluorescence microscope (Eclipse TI, Nikon) equipped with a 100x oil-immersion objective, a high-quantum-efficiency cooled CCD camera and a metal halide lamp (Prior Lumen 220). Epifluorescence images were acquired using Metamorph software (Molecular Devices)²⁷. In all microscopy experiments, SCs were identified based on their expression of Pax7nGFP (data not shown). SCs are relatively rare, and therefore, we screened cryosections for SCs by searching for GFP while looking through the eyepieces. When a SC was found, stacks of ~6-8 μm thickness spaced 0.3 μm apart in z-direction were acquired. All sections were co-stained with a smFISH probe directed against *Pax7* RNA (magenta), which was used to confirm SC identity and also served as a positive control for our smFISH staining.

Microscopy data analysis was performed in ImageJ (version 1.49). With ImageJ, z-projections based on maximum intensity were created for all channels. SCs were then identified based on their expression of GFP, and for each SC imaged, we determined whether *Pax7* mRNA smFISH dots could be detected and whether no, 1-10 or more than 10 molecules of *Fos* or *Socs3* were detected. In the first intact muscle that was stained for both *Fos* and *Socs3*, we did not even detect a single molecule of *Fos* ($n = 80$ SCs imaged, $P = 2.2 \times 10^{-10}$) or *Socs3* ($n = 100$ SCs imaged, $P = 8.6 \times 10^{-13}$). These P values were based on a comparison with our CEL-seq data as follows: based on our CEL-seq-data, 24% of all SCs falls in cluster 2; therefore, the probability that out of 80 cells screened no *Fos*-expressing cells were found assuming that 24% should express *Fos* is $(1-0.24)^{80}$. Likewise, the P value for *Socs3* was calculated as $(1-0.24)^{100}$. In the dissociation smFISH experiments (two independent replicates) that were performed next, we could detect expression of *Fos* (Fig. 1b (right panel), Supplementary Fig. 3c-e and Supplementary Fig. 3g). In some dissociated and sorted cells, we found *Fos* transcription sites (arrow in Supplementary Fig. 3e). Transcription sites are sites in the genome where many mRNA molecules are synthesized simultaneously. Due to the proximity of mRNA molecules in such a site, the number of *Fos* mRNA molecules in cells with such a site could not be determined. We therefore counted all encountered transcription sites as 1 molecule of *Fos*. In most SCs, we also detected 2 background dots, that were assigned as background because they were present in both the Cy5 and the Alexa Fluor 594 channel. These dots were excluded from the analysis.

After all SCs imaged during the two replicates of the dissociation experiment had been analysed, we made bar graphs to show the percentages of *Fos*-expressing SCs in intact (control) muscles and in dissociated and sorted SCs (Supplementary Fig. 3f). For this bar graph, the numbers originating from the two independent replicates were pooled and only SCs in which we could also detect *Pax7* smFISH signal were included. In our experiments, the *Pax7* probe represents an internal control that was used to make sure that our smFISH protocol was working in this particular SC. To test whether the number of cells with ≥ 1 molecule of *Fos* was significantly higher after dissociation and after dissociation and FACS than the number of cells with ≥ 1 molecule of *Fos* in the negative control (non-dissociated muscles) we performed a two-tailed fisher's exact test (P value in both cases < 0.0001). For the generation of the microscopy fig. panels, z-projections based on maximum intensity were created in ImageJ, after which the image type was changed to RGB colour and images were saved as Tiffs and opened in Adobe Photoshop CC (version 2015.1.2). In Photoshop, levels were adjusted linearly for all channels using the levels tool. Images were then recoloured, merged and cropped in Photoshop, after which they were copied to Adobe Illustrator CC (version 2015.1.2). The resolution of all microscopy panels is 150 dpi, which is lower than required. The reason for this lower resolution is the small size of SCs; while we imaged with maximum resolution, we had to zoom in and crop away large part of the image to make the small SCs visible. For imaging and processing of the *Fos* channel, all settings were kept constant across all experimental conditions, the only exception being Supplementary Fig. 3g; here, *Fos* expression was so high that the image was overexposed. For this reason, this section was re-imaged with decreased laser power and exposure time.

In silico purification

We developed a computational method that can be used to identify and remove dissociation-affected cells from single-cell datasets. In the case of our CEL-seq dataset, the result of this in silico purification method would be similar to what would be accomplished when cluster 2-cells would be removed, and in the case of our SORT-seq dataset, the results of this in silico purification method would be similar to what would be accomplished when all cluster 1 and 4-cells would be removed. We however wanted our in silico purification method to be independent of RaceID clustering parameters, so that it can also be applied to new SC (and potentially also to non-SC) single-cell datasets. In order to do so, we set out to find general properties of the cells that are assigned to dissociation-affected clusters. Here, we used our SORT-seq dataset to find a measure for the cells in our dataset that could be used to discriminate dissociation-affected cells (cells in clusters 1 and 4) from non-dissociation-affected cells (cells in clusters 2, 3 and 5) independent of the RaceID cluster numbers. The method was subsequently validated using our CEL-seq dataset.

Using our SORT-seq dataset, we found that cells that are assigned to dissociation-affected clusters (clusters 1 and 4) and cells that are assigned to non-dissociation affected clusters (clusters 2, 3 and 5) can be separated based on what percentage of their transcriptome is occupied by dissociation-affected reads. To calculate this percentage, we first made a list of dissociation-affected genes. To make this list, we assumed that all genes that are specifically expressed in cluster 1 and cluster 4-cells are genes of which the expression levels are increased during the dissociation protocol, and the list of dissociation-affected genes thus contained all genes that are specifically upregulated in cluster 1 (versus clusters 2, 3 and 5, using DESeq²⁵ with a *P* value of 0.001) and genes that are specifically upregulated in cluster 4 (versus clusters 2, 3 and 5) (Supplementary Table 5). We then used the `sc@ndata` output of RaceID (dataset from which cells with < 3,000 reads are removed and that is downsampled to 3,000), subtracted the pseudocounts and calculated for each cell what percentage of the reads in that cell came from genes that are in our list of dissociation-affected genes. With this method, each cell thus gets assigned a value that represents a measure of how dissociation-affected that particular cell is. The distribution of this measure was then plotted as a histogram for both the dissociation-affected and for the non-dissociation affected cells (Supplementary Fig. 6a). Next, a threshold value can be chosen, and all cells that have a value equal to or above this threshold value are then classified as being dissociation-affected. The threshold can be optimized by calculating for each possible threshold-value the percentage of cluster 1 and 4-cells that are correctly classified as dissociation-affected, the percentage of cluster 2, 3 and 5-cells that are correctly classified as non-dissociation affected and the overall percentage of correctly classified cells (Supplementary Fig. 6b). After a threshold cutoff has been chosen, dissociation-affected cells can be marked in a t-SNE map (Supplementary Fig. 6c-d and Supplementary Fig. 6g).

Our *in silico* purification method was validated with our CEL-seq dataset, which was generated on different experimental days and with a different CEL-seq protocol than our SORT-seq dataset. First, we calculated for each cell in our CEL-seq dataset what percentage of its transcriptome was occupied by dissociation-affected genes as described above, using the same list of dissociation-affected genes as for the SORT-seq dataset. The distribution of this measure was then plotted in a histogram for all cells (Supplementary Fig. 6e). We then choose a threshold without looking at differences in the distribution of cluster 1 and cluster 2-cells; the threshold of 7.5% was chosen such that the cells in the tail of the distribution were classified as dissociation-affected cells (red line in Supplementary Fig. 6e). With this threshold, 33.2% of the cells are classified as dissociation-affected cells. With this threshold that was chosen without taking clustering into account, 100% of the cluster 2 (dissociation-affected cluster) cells and 11.8% of the cluster 1 (non-dissociation-affected cluster) cells are classified as being dissociation-affected (Supplementary Fig. 6f). Next, the cells that were classified as being dissociation-affected were marked in the t-SNE map (Supplementary Fig. 6g). The cluster 1-cells that were marked as dissociation-affected using our *in silico* purification method were all close to the cluster 2-cells in t-SNE space (Supplementary Fig. 6g), suggesting that these cells might also be partly stressed. Taken together, our validation shows that our *in silico* purification method that is independent on RaceID-clustering can be used to identify and remove dissociation-affected cells from SC datasets.

Our *in silico* purification method can be applied to other datasets using the following R-code, which is an extension to a previously published single-cell data-analysis script named RaceID2 (ref. ¹⁰):

```
#After running RaceID2, make new dataframe containing normalized data
output of RaceID 2 (sc@ndata) and remove pseudocounts:
Data <- (sc@ndata - 0.1)
#From this dataframe, make a selection that only contains genes of which
the expression levels change during the dissociation protocol (this list
contains all genes that are upregulated in the dissociation-affected
satellite cell clusters - Supplementary Table 5).
#Note: genes used here are mouse genes; in case other model organisms are
used this list needs adjustment.

Selection <- Data[c(
  "Actg1_chr11", "Ankrd1_chr19", "Arid5a_chr1", "Atf3_chr1", "Atf4_
chr15", "Bag3_chr7", "Bhlhe40_chr6", "Brd2_chr17", "Btg1_chr10", "Btg2_
chr1", "Ccn11_chr3", "Ccrn41_chr3", "Cebp_b__chr2", "Cebp_d_
chr16", "Cebpg_chr7", "Csrnp1_chr9", "Cxcl1_chr5", "Cyr61_chr3", "Dcn_
chr10", "Ddx3x_chrX", "Ddx5_chr11", "Des_chr1", "Dnaj1_chr4", "Dnajb1_
chr8", "Dnajb4_chr3", "Dusp1_chr17", "Dusp8_chr7", "Egr1_chr18", "Egr2_
chr10", "Eif1_chr11", "Eif5_chr12", "Erf_chr7", "Errf1_chr4", "Fam132b_
chr1", "Fos_chr12", "Fosb_chr7", "Fosl2_chr5", "Gadd45a_chr6", "Gcc1_
chr6", "Gem__chr4", "H3f3b__chr11", "Hipk3__chr2", "Hsp90aa1__
```

```

chr12", "Hsp90ab1__chr17", "Hspala__chr17", "Hspalb__chr17", "Hspa5__
chr2", "Hspa8__chr9", "Hspb1__chr5", "Hsph1__chr5", "Id3__chr4", "Idi1__
chr13", "Ier2__chr8", "Ier3__chr17", "Ifrd1__chr12", "Il6__chr5", "Irf1__
chr11", "Irf8__chr8", "Itpkc__chr7", "Jun__chr4", "Junb__chr8", "Jund__
chr8", "Klf2__chr8", "Klf4__chr4", "Klf6__chr13", "Klf9__chr19", "Litaf__
chr16", "Lmna__chr3", "Maff__chr15", "Mafk__chr5", "Mcl1__chr3", "Midn__
chr10", "Mir22hg__chr11", "Mt1__chr8", "Mt2__chr8", "Myadm__chr7", "Myc__
chr15", "Myd88__chr9", "Nkap51__chr15", "Ncoa7__chr10", "Nfkbia__
chr12", "Nfkbiz__chr16", "Nop58__chr1", "Nppc__chr1", "Nr4a1__
chr15", "Odc1__chr12", "Osgin1__chr8", "Oxnad1__chr14", "Pcf11__
chr7", "Pde4b__chr4", "Per1__chr11", "Phlda1__chr10", "Pnp__chr14", "Pnrcl__
chr4", "Ppp1cc__chr5", "Ppp1r15a__chr7", "Pxdcl1__chr13", "Rap1b__
chr10", "Rassf1__chr9", "Rhob__chr12", "Rhoj__chr5", "Ripk1__chr13", "Sat1__
chrX", "Sbno2__chr10", "Sdc4__chr2", "Serpine1__chr5", "Skil__
chr3", "Slc10a6__chr5", "Slc38a2__chr15", "Slc41a1__chr1", "Socs3__
chr11", "Sqstm1__chr11", "Srf__chr17", "Srsf5__chr12", "Srsf7__
chr17", "Stat3__chr11", "Tagln2__chr1", "Tiparp__chr3", "Tnfaip3__
chr10", "Tnfaip6__chr2", "Tpm3__chr3", "Tppp3__chr8", "Tra2a__
chr6", "Tra2b__chr16", "Trib1__chr15", "Tubb4b__chr2", "Tubb6__
chr18", "Ubc__chr5", "Usp2__chr9", "Wac__chr18", "Zc3h12a__chr4", "Zfand5__
chr19", "Zfp36__chr7", "Zfp3611__chr12", "Zfp3612__chr17", "Zyx__
chr6", "Gadd45g__chr13", "Hspe1__chr1", "Ier5__chr1", "Kcne4__chr1"
),]
Selection[is.na(Selection)] <- 0

#Generate a new dataframe (DataPercentages) containing for each cell:
t-SNE dimensions ("V1" and "V2"), sum of reads from all dissociation-
affected genes ("Sums") and percentage of transcriptome of that cell that
maps to dissociation affected reads ("Percentage"; this equals "Sums"-
column divided by total read count of that cell):
tsNECoordinates <- sc@tsne
row.names(tsNECoordinates) <- colnames(sc@ndata)
Sums <- colSums(Selection)
DataPercentages <- merge(tsNECoordinates, Sums, by="row.names", all=T)
row.names(DataPercentages) <- DataPercentages$Row.names
DataPercentages <- DataPercentages[, -1]
colnames(DataPercentages)[3] <- "Sums"
DataPercentages$Percentage <- DataPercentages$Sums*100/mintotal

#Make a histogram showing the distribution of the metric "Percentage of
dissociation-affected reads per cell":
hist(DataPercentages$Percentage, breaks = 100, col = "lightgrey", main =
"Expression level dissociation-affected genes", xlab = "Sum expression
level of dissociation-affected genes", ylab = "Number of cells")

#Based on this histogram, choose an appropriate cutoff value. All cells
with a percentage equal to or above this value are affected by the
dissociation procedure, will be labelled as "Dissociation-affected" in the
"DataPercentages" dataframe:
SetCutoff <- 7.5
DataPercentages$Dissociation_affected <- ifelse(DataPercentages$Percentage
>= SetCutoff, 1, 0)

#Calculate what percentage of the cells will be annotated as dissociation-
affected cells with this cutoff value:
PercentageDissociationAffected <-
round((nrow(DataPercentages[DataPercentages$Percentage >= SetCutoff, ])/
(nrow(DataPercentages))*100, digits = 2)
print(c("Percentage of cells annotated as dissociation-affected cells is",

```

```

PercentageDissociationAffected) )
#Next, all cells that are dissociation affected (cells with a value of "1"
in "Dissociation-affected" column of "DissociationAffectedCells") can be
removed from the data.

#In addition, these cells can be marked in the t-SNE map:
plottsne(sc,final=TRUE)
DissociationAffectedCells <- DataPercentages[DataPercentages$Percentage >
SetCutoff, ]
points(DissociationAffectedCells$V1, DissociationAffectedCells$V2, pch =
"0", add = T)

```

Index-file analysis for MitoTracker FACS gating strategy experiments

To experimentally exclude dissociation-affected cells, we designed a NOT-gate on a pilot experiment of index-sorted MitoTracker stained Pax7nGFP⁺ cells (Supplementary Fig. 7). During indexed cell sorting, all FACS information of a cell that is sorted into a specific well is stored in an index-file. After SORT-seq, which identified 14 dissociation-affected cells, we analysed the FACS index information to investigate whether dissociation-affected cells stain higher for MitoTracker, and we found that dissociation-affected cells indeed have a high mitochondrial activity (Supplementary Fig. 7d). We then systematically analysed all other properties recorded by the FACS-machine. We found that dissociation-affected cells have a confined range in both side- and forward-scatter that is only partially overlapping with that of non-stressed cells (Supplementary Fig. 7e). We then confirmed that this property is conserved in index data of older sorts without MitoTracker staining (data not shown). Finally, by analysing all combinations together with the MitoTracker channel, we manually determined that Forward Scatter Pulse Height (FSC-H) in combination with MitoTracker levels yields the best separation between dissociation affected and non-affected cells (Supplementary Fig. 7f). In our second MitoTracker experiment, most (74 out of the 80) dissociation-affected cells fall in the recorded NOT-gate (Fig. 1d), showing that the NOT-gate can be used to remove most of the dissociation-affected cells. Purity in Fig. 1d was calculated as the percentage of dissociation-affected (red) cells in population outside of the NOT-gate. Yield in Fig. 1d was calculated as the percentage of non-affected cells that is preserved with this gating strategy.

Calculation of downregulation of genes in bulk for MitoTracker FACS gating strategy experiments

To calculate the average expression of IEG and HSP genes (Fig. 1e and Supplementary Fig. 8d) in bulk, we used the raw unique transcript counts tables and not the tables in which read counts of all single cells were downsampled to 3,000. The reason for this is that we wanted to calculate the expression levels that we would have detected if this experiment would have been a bulk experiment, and in bulk experiments the read counts in all cells are added up without correcting for differences in expression levels between individual cells. Box-and-whisker plots were based on a distribution that was generated using bootstrapping. For bootstrapping, we sampled 1,000 times n cells with replacement from the n total cells, as well as 1000 times k cells with replacement from the k cells outside the NOT-gate. Average reads counts per cell were then calculated as: $\text{sum}(\text{gate}) / k$ and: $\text{sum}(\text{total})/n$. Summary statistics (box-and-whisker plots) were calculated on these distributions.

Analysis of downloaded mouse acinar cell data

The mouse acinar single-cell gene expression matrix⁸ was downloaded from GEO (GEO:GSE80032). The two outlier cells (proliferative acinar cells, cells #31 and #40) were removed, leaving 106 cells, and all genes that are not in our reference transcriptome were removed to allow an accurate comparison with our dataset. Next, we ran RaceID2 and performed differential gene expression analysis as described above, using the same P value as for the SC datasets.

Statistics and reproducibility

No sample sizes were predetermined in this study. Replicates of all mice and zebrafish CEL-seq and SORT-seq experiments are described in the section "Mice and Zebrafish". P values for differential gene expression analysis studies were calculated as described in the section "Differential gene expression analysis using DESeq". P values for literature comparison (Supplementary Fig. 1h) were calculated as described in the section "Comparison of differential gene expression list with existing microarray datasets". Calculations of P values in analysis of microscopy data are described in the section "Microscopy and processing of microscopy data". Error bars for Supplementary Fig. 4h were calculated as described in the section "Clustering with RaceID". Box-and whisker plots in Fig. 1e and Supplementary Fig. 8d were generated as described in the section "Calculation of downregulation of genes in bulk for MitoTracker FACS gating strategy experiments".

Supplementary Tables

Supplementary Tables 1-7 are provided online at <https://bit.ly/3eyS6ZY>.

Supplementary table 1 | List of all genes that are upregulated in cluster 2-cells compared to cluster 1-cells (CEL-seq data). Differential gene expression analysis was performed with DESeq as described in the methods section. Only the 32 genes with a *P* value below 0.001 are shown in this table.

Supplementary table 2 | List of smFISH probes used in this study.

Supplementary table 3 | List of genes differentially expressed between the 5 SORT-seq clusters.

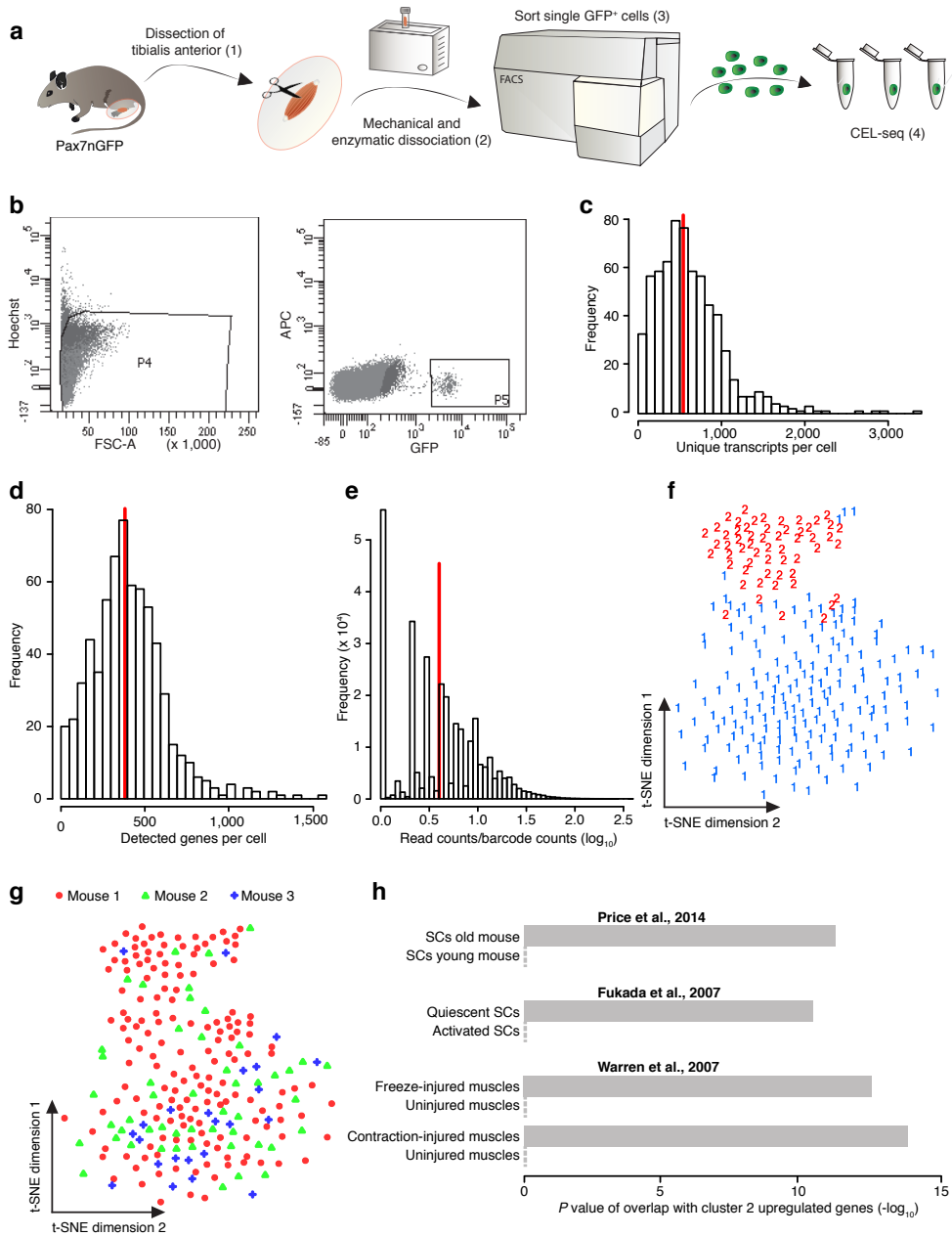
Supplementary table 4 | List of genes upregulated in 1h versus 2h and in 2h versus 1h collagenase-treated cells in SORT-seq data.

Supplementary table 5 | List of genes of which expression levels were assumed to be affected by the dissociation procedure. This list contains all genes that are significantly upregulated in the dissociation-affected clusters (cluster 1 (versus clusters 2, 3 and 5) and cluster 4 (versus clusters 2, 3 and 5) in our SORT-seq dataset). This list is used for our *in silico* purification method.

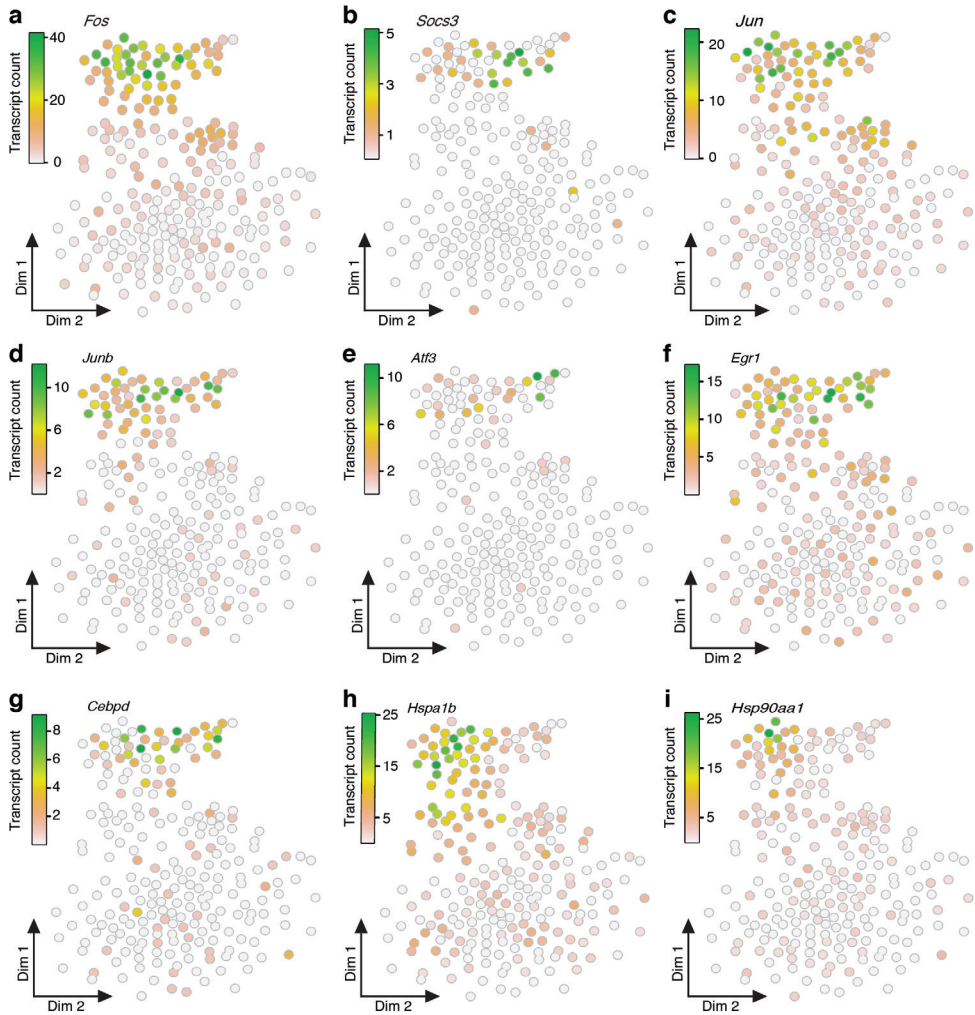
Supplementary table 6 | List of genes differentially expressed between *Fos*-expressing and non *Fos*-expressing cluster of mouse acinar cells (data from Wollny et al., 2016 (ref.⁸) - GEO: GSE80032).

Supplementary table 7 | List of genes differentially expressed between *fosab*-expressing (cluster 8) and non *fosab*-expressing (cluster 2) osteoblasts in zebrafish fin dataset. The mouse orthologue of *fosab* is *Fos*. Genes that are labelled in bold and green are genes that are overlapping with Supplementary Table 5 (list of genes that are significantly upregulated in the *Fos*-expressing mouse satellite cell populations). Genes that are labelled in grey do not have an orthologue in mouse and can therefore not be compared with the mouse satellite cell dataset.

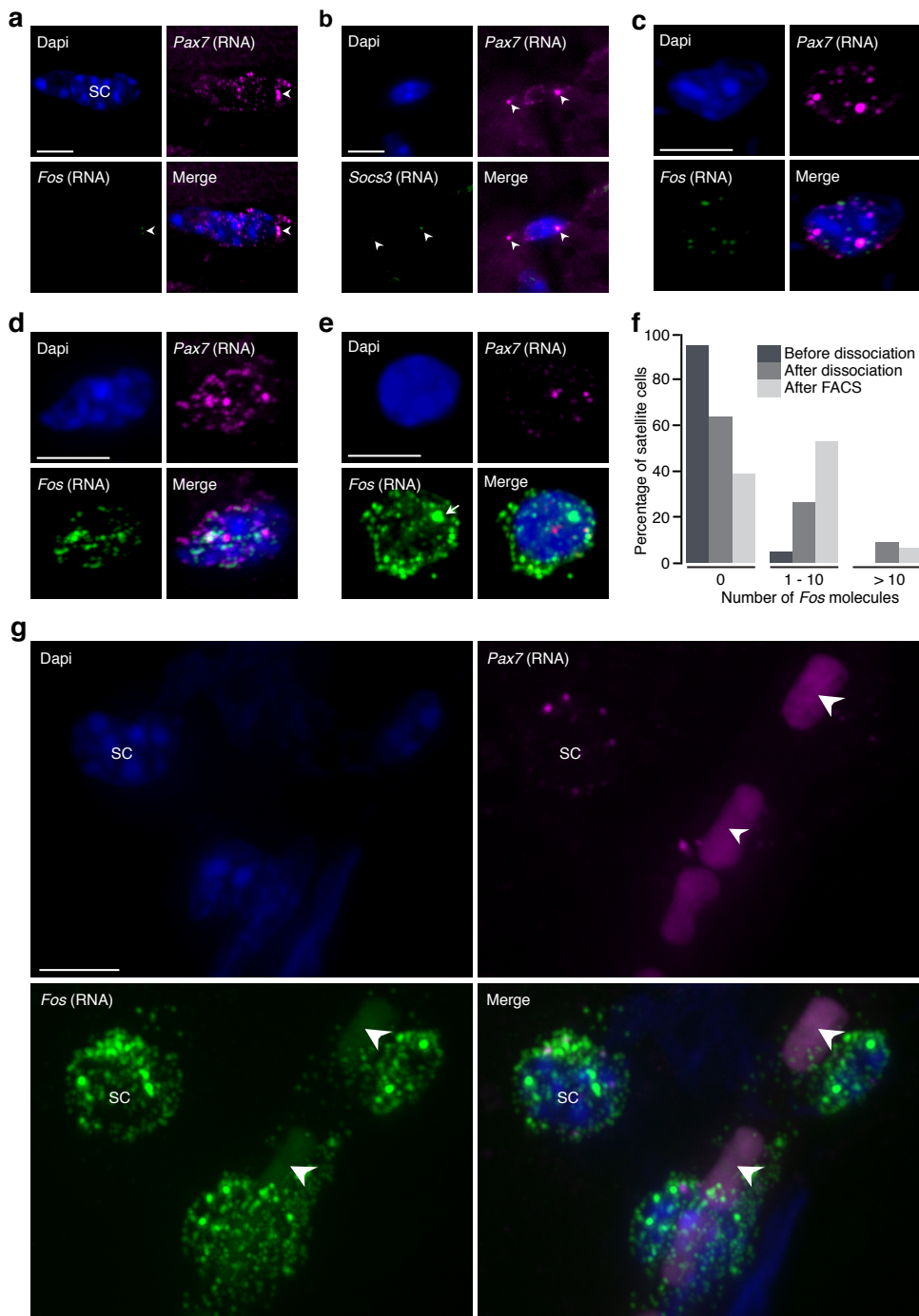
Supplementary Figure 1 | CEL-seq unravels two subpopulations of SCs. **a**, Schematic explanation of SC isolation protocol; *Pax7* is a marker for SCs. **b**, SCs were sorted from a single cell suspension of 6 TA muscles isolated from 3 mice via FACS. Left panel: live cells were selected based on Hoechst staining and Forward Scatter Area (FSC-A). Right panel: SCs were selected based on GFP; percentage of GFP+ cells (from viable population) varied between 0.1 and 1.7%. Gates are shown as black boxes. **c**, Histogram of number of unique transcripts per cell. Median number of transcripts detected was 556 (red line). Five cells with more than 10,000 unique transcripts detected were omitted for viewing purposes. In total, CEL-seq was applied to 665 cells, of which the 235 cells with ≥ 700 transcripts were used for RaceID-analysis. **d**, Histogram of the number of genes detected per cell. Median number of genes detected per cell was 381 (red line). Five cells with more than 3,000 genes detected were omitted from the plot. **e**, Histogram of oversequencing per molecule. Median level of oversequencing is 4 (red line). **f**, t-SNE map representation of transcriptome similarities between individual cells; every dot is a cell. Red and blue numbers refer to clustering; see also Fig. 1a. **g**, t-SNE map displaying repartition over clusters between experimental replicates. This plot shows that both clusters were identified in all three independent experiments, excluding the possibility that clustering could be due to physiological differences between mice. **h**, Comparison to existing literature. Shown is the *P* value of overlap between our list of cluster 2 upregulated genes and fold change lists generated based on downloaded microarray data (Supplementary Methods). Our list has significant overlap with genes that are upregulated in SCs isolated from old mice compared to young mice³, with genes upregulated in quiescent versus activated SCs⁴ and with genes upregulated in injured versus uninjured muscles⁶. Dotted lines indicate *P* value of 1 (no overlap).



Supplementary Fig. 1 | See previous page for caption.



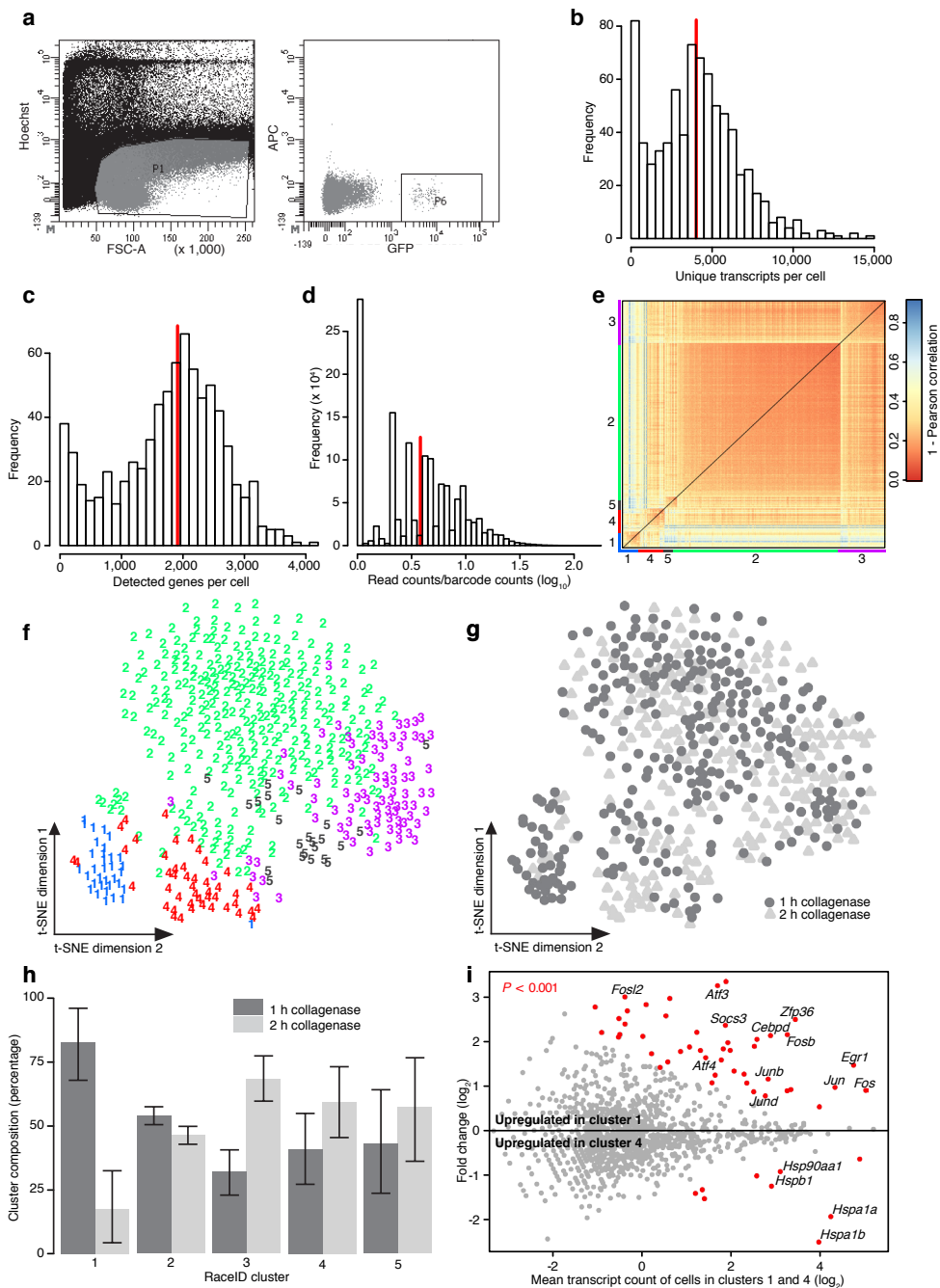
Supplementary Figure 2 | Expression of selection of genes characterizing SCs belonging to cluster 2. a-i, Expression of selection of genes that are significantly higher expressed in cluster 2 cells than in cluster 1 cells, plotted over t-SNE map. Color-coding shows number of unique transcripts (after downsampling to 700 transcripts). Dim, t-SNE dimension. For clustering of cells in these t-SNE maps, see Supplementary Fig 1f.



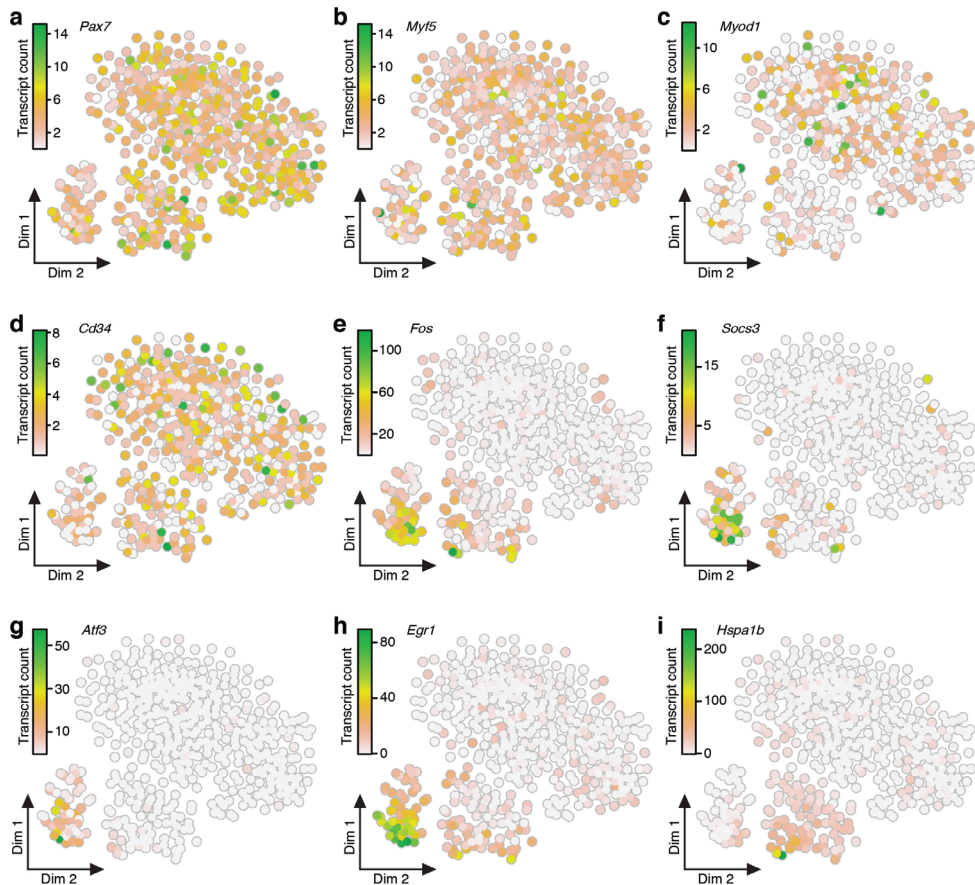
Supplementary Fig. 3 | See next page for caption.

Supplementary Figure 3 | Single molecule FISH analysis shows that *Fos* expression is induced during the SC isolation procedure. a, Additional example of a SC in an intact Pax7nGFP muscle (GFP channel not shown) that was stained for *Fos* (probe library coupled to Cy5; shown in green) and *Pax7* (coupled to Alexa594, shown in magenta) RNA. *Fos* was not detected in any of the 80 cells that were screened for *Fos* expression. b, smFISH on cryosection of intact muscle showing that *Socs3* (coupled to Alexa Fluor 594; shown in green) expression could also not be detected in SCs in intact muscles. *Socs3* was not detected in any of the 100 cells that were screened for *Socs3* expression. c-d, Two more examples of SCs in dissociated muscles that express *Fos* (coupled to Cy5; shown in green). e, smFISH on SC that was fixed after FACS. *Fos* was detected in 17 out of the 28 sorted SCs imaged. f, Quantification of smFISH data. Number of *Fos*-expressing cells is significantly higher in dissociated SCs and in sorted SCs than in SCs in intact muscles that were obtained from the same animals ($P > 0.0001$). Dissociation smFISH-experiment was repeated 2 times; results from 2 replicates were pooled. g, Cryosection in which expression of *Fos* was detected in both a SC and in two non-SCs, showing that the response to dissociation is not specific to SCs. The SC cell shown here is the same as the one shown in Fig. 1b (right panels; after dissociation), however, this supplementary image was acquired using a wider z-range and using lower gain and laser power for the *Fos* channel. Nuclei were stained with DAPI (blue). SC, satellite cell (identified by expression of GFP (not shown) and *Pax7* RNA (magenta)); arrowheads point at background signal; arrow points at *Fos* transcription site; scale bar, 5 μ m. All images shown were taken using confocal microscopy, except for panel b; this image was acquired using epifluorescence microscopy. In all images, GFP (not shown) was used to identify SCs, and all sections were co-stained with a smFISH probe directed against *Pax7* mRNA as a positive control for our smFISH staining.

Supplementary Figure 4 | Dissociation time experiment confirms that the dissociation procedure influences the transcriptome of SCs. SCs were sorted from a single cell suspension of 8 TA muscles from 4 mice via FACS. Half of this material was treated with collagenase for 1 hour; the other half of the cells treated with collagenase for 2 hours. a, Left panel: live cells were selected based on Hoechst staining and Forward Scatter Area (FSC-A). Right panel: SCs were selected based on GFP; percentage of GFP+ cells (from viable population) varied between 0.1 and 1.7%. Gates are shown as black boxes. b, Histogram of number of unique transcripts per cell. Median number of transcripts detected was 4,022 (red line). In total, SORT-seq was applied to 752 cells, of which only the 495 cells with $\geq 3,000$ transcripts were used for RaceID2-analysis. c, Histogram of the number of genes detected per cell. Median number of genes detected per cell was 1,912 (red line). d, Histogram of oversequencing per molecule. Median level of oversequencing is 3.8 (red line). e, Heat map showing transcriptome correlations between individual SCs. RaceID2 identified 5 clusters, as indicated by colouring on the axes. f, t-SNE representation of 272 1-hour and 223 2-hour collagenase treated SCs that were isolated from 8 TA muscles of 4 mice. Numbers represent clustering. g, t-SNE map where cells are coloured according to the duration of their enzymatic dissociation. Together, panels f and g reveal that cluster 1 mostly consists of 1-hour collagenase-treated cells (see also Supplementary Fig. 4h). h, Percentages of 1-hour and 2-hour collagenase-treated cells in all five clusters show that cluster 1 mostly consists of 1-hour collagenase-treated cells. Percentages are corrected for total number of cells per collagenase-treatment as described in the Supplementary Methods. Error bars are 95% confidence intervals generated by bootstrapping. i, Differential gene expression analysis identified 55 genes that are differentially expressed between clusters 1 (34 cells) and 4 (46 cells). For list of all significant genes, see Supplementary Table 3.



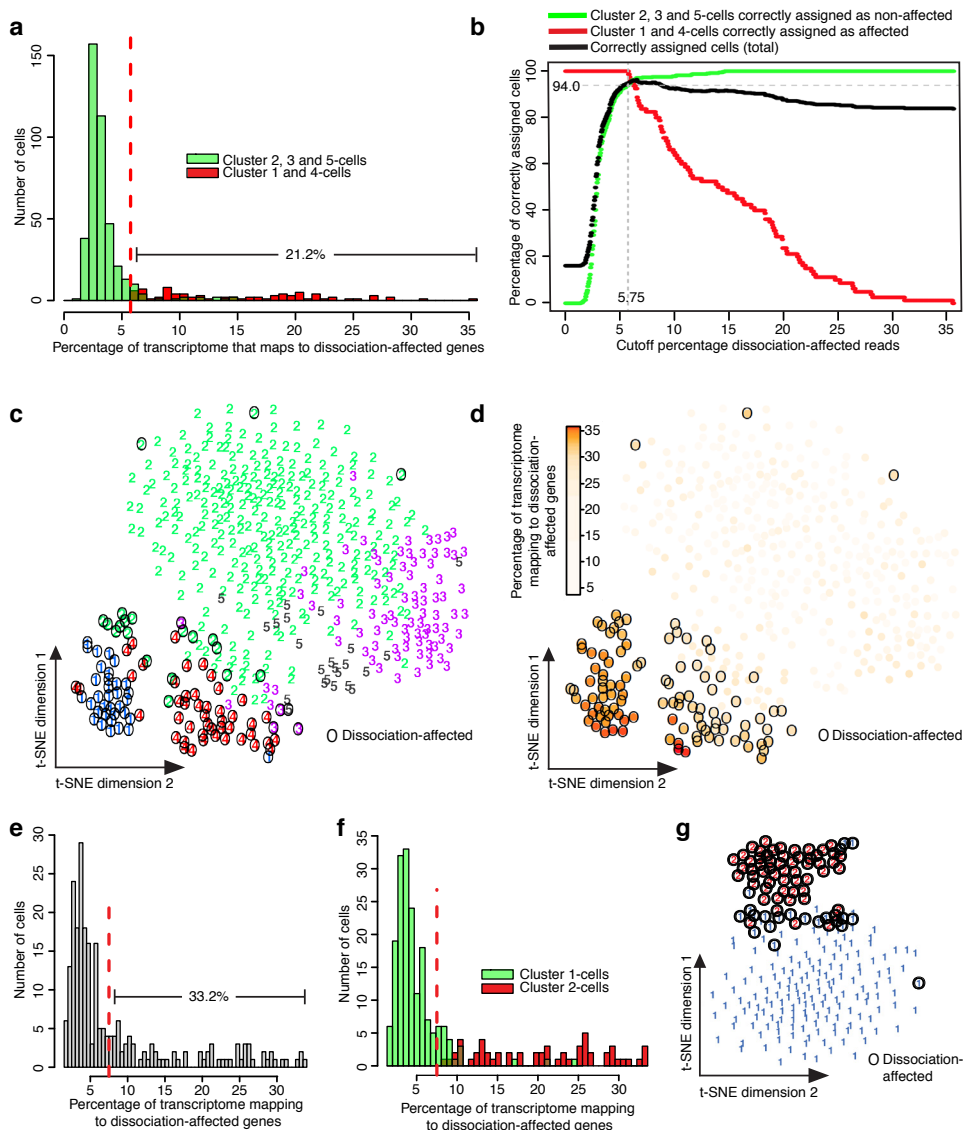
Supplementary Fig. 4 | See previous page for caption.



Supplementary Figure 5 | Expression of selection of SC genes and of genes characterizing SCs in clusters 1 and 4 in SORT-seq dataset. a-d, Expression levels of SC markers plotted over t-SNE map. All markers were detected in all clusters, showing that cells that fall in clusters 1 and 4 are indeed SCs. e-h, Selection of genes that are significantly upregulated in cluster 1 cells (versus cells in clusters 2, 3 and 5). These genes are also higher expressed in 1-hour collagenase treated cells than in 2-hour collagenase treated cells (Fig. 1c). i, Expression of *Hspa1b* plotted over t-SNE map. *Hspa1b* is higher expressed in cluster 4 cells than in cluster 1 cells (Supplementary Fig. 4i). *Hspa1b* is also higher expressed in 2-hour collagenase-treated than in 1-hour collagenase treated cells (Fig. 1c). Color-coding shows number of unique transcripts (after downsampling to 3,000) detected in these cells. Dim, t-SNE dimension.

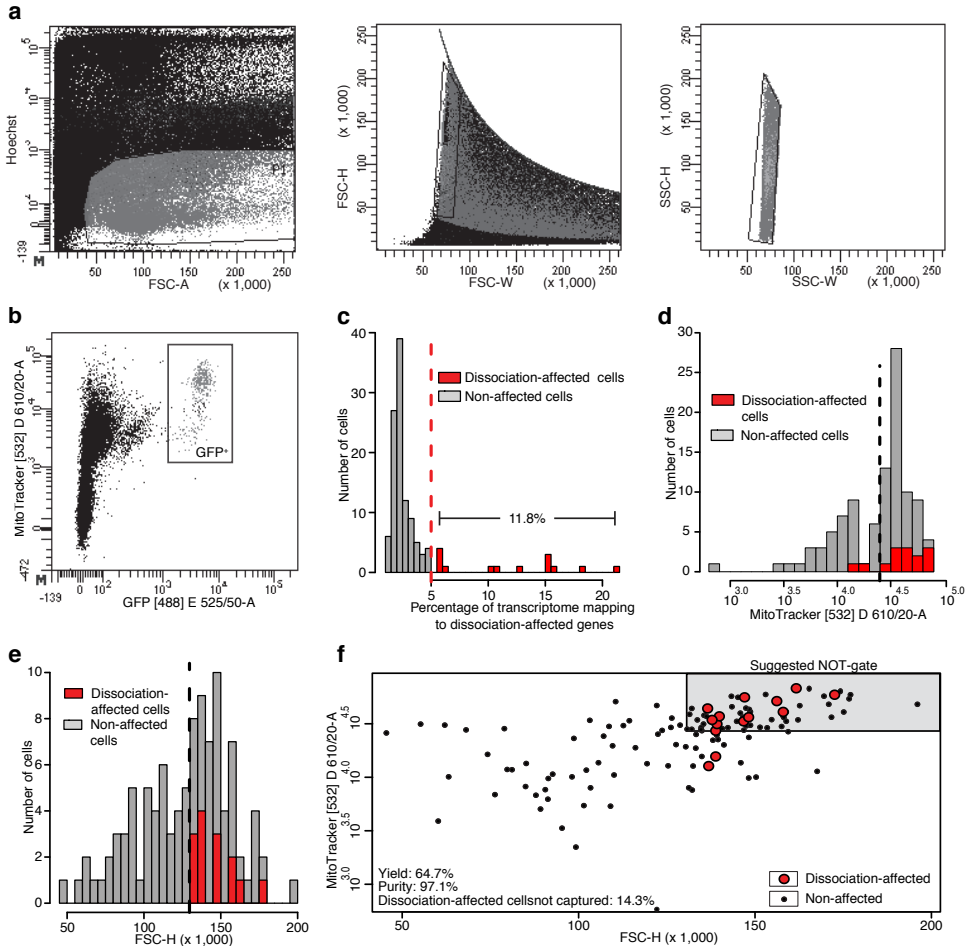
Supplementary Fig. 6 (figure on next page) | In silico purification can be used to identify and remove dissociation-affected cells from single-cell datasets. a, Histograms showing the distribution of the percentage of transcriptome that maps to dissociation-affected reads in dissociation-affected (red) and non-dissociation affected (green) cells in our SORT-seq dataset (see Supplementary Methods for details). Filtering out cells of which \geq than 5.75% (red dotted line; see Supplementary Fig. 6b for threshold optimization) of the transcriptome consists of dissociation-affected reads allows the removal of all dissociation-affected cells while removing only 6% of the non-dissociation affected cells. With a threshold of 5.75%, 21.2% of the cells in this dataset are classified as being dissociation-affected. b, Threshold optimization. For all possible threshold values, the percentage of cluster 1 and 4-cells that is correctly assigned as being dissociation-affected (red), the percentage of cluster 2, 3 and 5-cells that is correctly assigned as non-dissociation affected (green) and the overall percentage of cells that are assigned correctly (black) is plotted. The overall percentage of correctly assigned cells would be optimal (96.2%) if the threshold cutoff value would be set to 6.25%, and with a threshold value of 6.25%, 95% of the dissociation-affected cells are correctly characterized as being dissociation-affected.

(Legend continues on next page.)

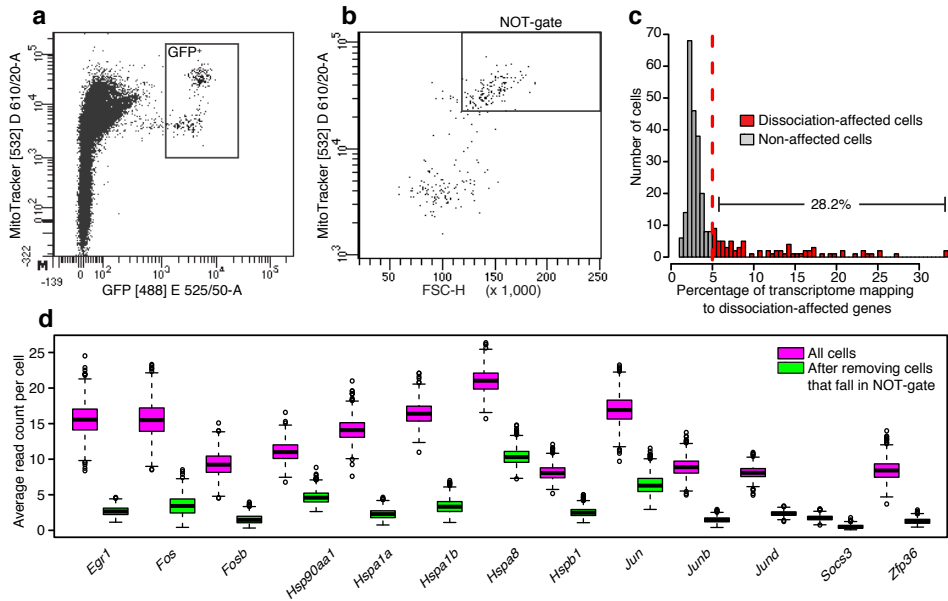


(Supplementary Figure 6 | First part of legend on previous page)

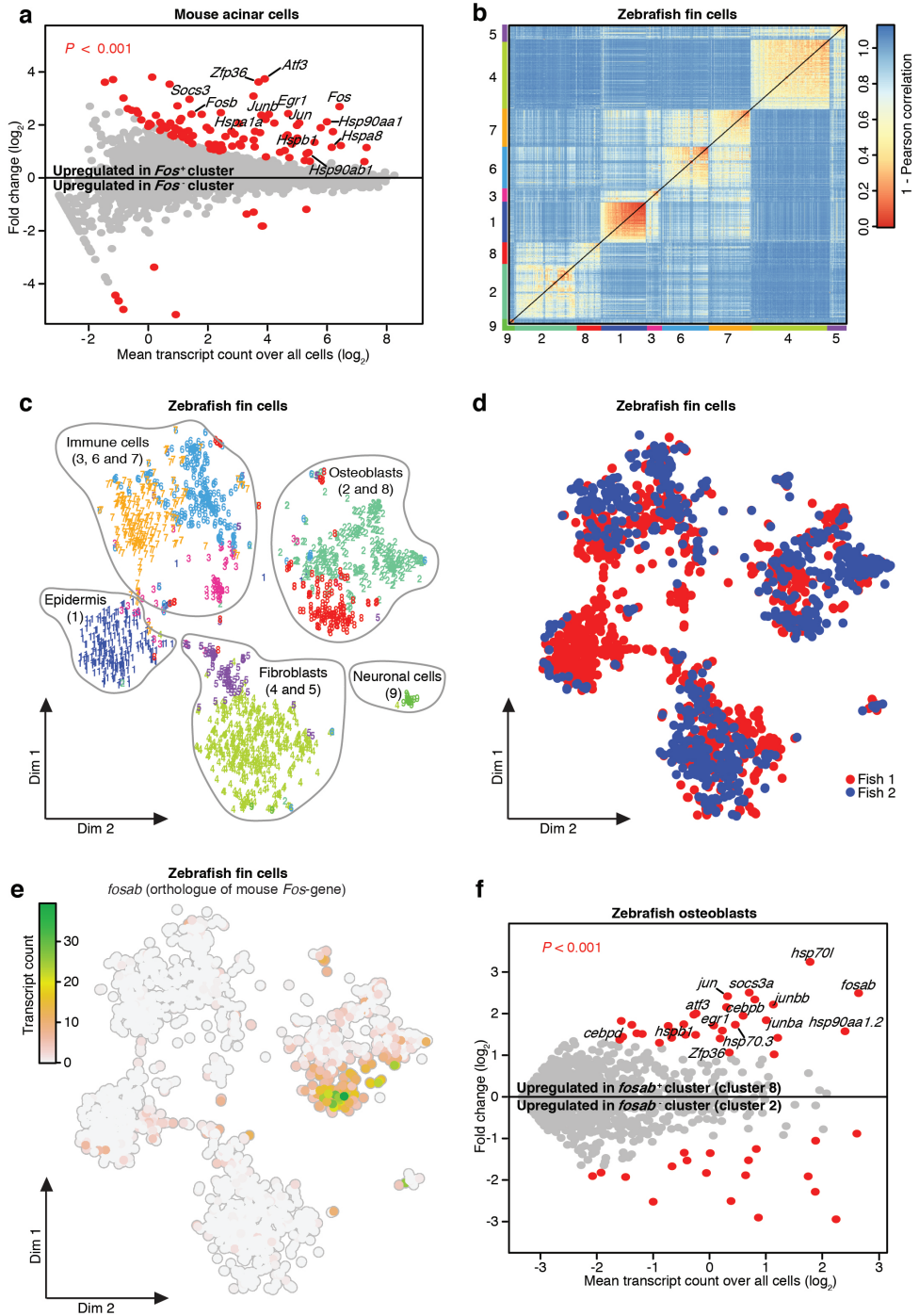
We choose however to instead set the threshold at 5.75% (vertical grey dotted line), because with this threshold, 100% of the cluster 1 and 4-cells are correctly classified as dissociation-affected (vertical grey dotted line). c, Cells that are identified as dissociation-affected by our *in silico* purification method can be marked as dissociation-affected in a t-SNE map and can, if desired, be removed from the dataset. d, Percentage of transcriptome that maps to dissociation-affected genes plotted over t-SNE map. Circles mark cells in which $\geq 5.75\%$ of the transcriptome maps to dissociation-affected genes. e, *In silico* purification method is verified by blindly applying it to CEL-seq SC dataset (from Supplementary Fig. 1-2). Shown is a histogram of the percentage of transcriptome occupied by dissociation-affected genes for all cells in our CEL-seq dataset. The threshold (red dotted line) is, without taking the RaceID cluster numbers into account, set to 7.5%. With this threshold, 33.2% of our CEL-seq SCs are classified as being dissociation-affected. f, The blindly set threshold of 7.5% then appeared to remove all dissociation affected (cluster 2) and 11.8% of the non-dissociation-affected (cluster 1) cells. g, Cells of which $\geq 7.5\%$ of the transcriptome maps to dissociation-affected reads are encircled in the t-SNE map.



Supplementary Figure 7 | Indexed FACS in combination with SORT-seq can be used to identify dissociation-affected cells after MitoTracker staining. Indexed FACS and SORT-seq of 119 SCs extracted from 2 TA muscles of one 4.7 months old female Pax7nGFP mouse was used to identify FACS-properties of dissociation-affected cells. **a**, Gating strategy to select viable cells in first experiment on MitoTracker-stained SCs. **b**, MitoTracker Red and GFP repartition of viable cells (Supplementary Fig. 7a) showing that some GFP-positive cells stain higher for MitoTracker than others. All GFP positive cells were sorted and their index-information was stored. **c**, The percentage of transcriptome occupied by dissociation-affected reads for all cells that were sorted during the MitoTracker experiment was determined via SORT-seq (using our *in silico* purification method described in Supplementary Note 2). Out of the 119 cells sequenced, 14 cells had more than 5% dissociation-affected reads and were identified as dissociation-affected cells. **d**, Histogram of MitoTracker levels of dissociation-affected (red) and non-dissociation affected (grey) cells showing that it is possible to remove most of the dissociation-affected cells by selecting against MitoTracker-high cells during FACS. **e**, Histogram of FSC-H levels of dissociation-affected (red) and non-dissociation affected (grey) cells shows that it is possible to remove dissociation-affected cells by discarding cells with high FSC-H values during FACS. Dotted lines in panels **d** and **e** refer to borders of the NOT-gate suggested in Supplementary Fig. 7f. **f**, Scatterplot showing MitoTracker and FSC-H levels of the 119 sequenced cells. MitoTracker and FSC-H levels of all cells were retrieved from the FACS index file. Red cells represent cells that were shown to be dissociation-affected by SORT-seq (Supplementary Fig. 7c). Shaded area represents NOT-gate that was designed on this dataset and that could be used to filter out 12 out of the 14 dissociation-affected cells during FACS.



Supplementary Figure 8 | Gate designed by indexed FACS in combination with SORT-seq on SCs stained for mitochondrial activity can be used to experimentally remove dissociation-affected cells during FACS. The NOT-gate that was designed based on a pilot experiment (Supplementary Fig. 7) was tested on a larger number of cells (6 muscles from 3 female 6-months old Pax7nGFP mice). **a**, MitoTracker and GFP repartition of all viable cells in second MitoTracker experiment showing that some SCs have a higher metabolic activity than others. **b**, MitoTracker and FSC-H repartition of Pax7nGFP SCs during second MitoTracker experiment. Drawn is the NOT-gate that was drawn during FACS and that was designed based on a pilot experiment in which dissociation-affected cells were found to stain higher for MitoTracker and to have higher FSC-H values (Supplementary Fig. 7). All Pax7nGFP⁺ cells, also the cells that fell in the NOT-gate, were sequenced, however, during FACS we recorded for all cells whether they fell in or out of the NOT-gate. **c**, Dissociation-affected cells were identified by SORT-seq (using our *in silico* purification method described in Supplementary Note 2). Out of the 284 successfully sequenced cells, 80 cells were identified as dissociation-affected cells because $\geq 5\%$ of their transcriptome mapped to dissociation-affected genes. **d**, The gating strategy successfully reduces the detected expression levels of HSP and IEG genes in bulk. Shown are the average expression levels of several HSP and IEG genes in the non-gated (all Pax7nGFP cells; shown in magenta) and the gated (Pax7nGFP cells out of the NOT-gate; shown in green) population. Some of these genes (*Fos*, *Jun* and *Hspa1b*) are also shown in Fig. 1e.



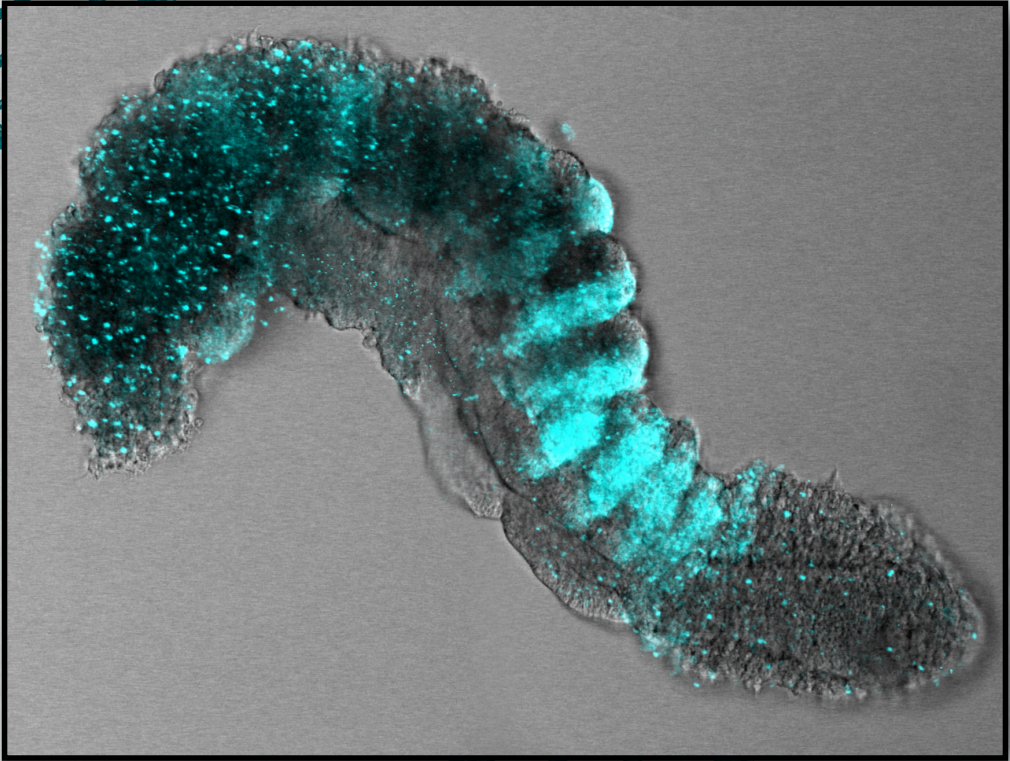
Supplementary Fig. 9 | See next page for caption.

Supplementary Figure 9 | Similar *Fos/Jun* expressing subpopulations can also be found in other single-cell datasets.

a, A *Fos/Jun* population described in a published mouse acinar single-cell study has an expression profile that is similar to that of dissociation-affected satellite cells. The authors of this study performed a dissociation procedure to extract acinar cells from the mouse pancreas and found two subpopulations of acinar cells, of which one expresses high levels of *Fos* and *Jun* (Fig. 6e in Wollny et al., 2016 (ref.⁸)). We analysed their data to generate a list of all genes that are differentially expressed between these two subpopulations (Supplementary methods; cells #31 and #40, the proliferative acinar cells, were excluded from the analysis). The resulting differential gene expression analysis plot is shown in this panel and reveals that the expression profile of the *Fos*-expressing acinar cell population is strikingly similar to that of the dissociation-affected subpopulation of satellite cells (compare this panel with Fig. 1a). The overlap with our satellite cell data suggests that this subpopulation of acinar cells might also be induced by the dissociation protocol. The authors do however not validate the in vivo existence of this *Fos/Jun* expressing subpopulation of acinar cells. For a full list of differentially expressed genes and overlap with our satellite cell dataset, see Supplementary Table 6. b, We detected a similar subpopulation of *Fos/Jun* expressing cells in a single-cell zebrafish fin dataset that was generated in our lab, suggesting that the dissociation protocol might also induce a stress response in other animals. To generate this dataset, we dissociated the fin of two fish to extract all fin cells (Supplementary methods), after which we performed SORT-seq. We then analysed the zebrafish fin data with RaceID2 and detected 9 clusters in the 1683 cells that survived our filtering criteria, as shown in this heat map. c, t-SNE representation of the clusters in the zebrafish fin dataset with cell-type annotation. d, All clusters were detected in all animals that were used for this experiment. e, A subpopulation of osteoblast cells (bone cells, which are harder to liberate from the tissue) expresses high levels of *fosab*, the zebrafish orthologue of *Fos*. f, Differential gene expression analysis comparing the expression profile of *fosab*-positive (cluster 8; 124 cells) and *fosab*-negative (cluster 2; 305 cells) osteoblasts shows that the expression profile of the *fosab*-positive cells is very similar to that of the dissociation-affected subpopulation of satellite cells (compare this panel with Fig. 1a). For a full list of differentially expressed genes and overlap with our satellite cell dataset, see Supplementary Table 7. Dim, t-SNE dimension.

References

1. Tierney, M. T. & Sacco, A. Satellite cell heterogeneity in skeletal muscle homeostasis. *Trends Cell Biol.* **26**, 434–444 (2016).
2. Rocheteau, P., Gayraud-Morel, B., Siegl-Cachedenier, I., Blasco, M. A. & Tajbakhsh, S. A subpopulation of adult skeletal muscle stem cells retains all template DNA strands after cell division. *Cell* **148**, 112–125 (2012).
3. Price, F. D. et al. Inhibition of JAK-STAT signaling stimulates adult satellite cell function. *Nat. Med.* **20**, 1174–1181 (2014).
4. Fukada, S. et al. Molecular signature of quiescent satellite cells in adult skeletal muscle. *Stem Cells* **25**, 2448–2459 (2007).
5. Hashimshony, T., Wagner, F., Sher, N. & Yanai, I. CEL-seq: single-cell RNA-seq by multiplexed linear amplification. *Cell Rep.* **2**, 666–673 (2012).
6. Warren, G. L. et al. Mechanisms of skeletal muscle injury and repair revealed by gene expression studies in mouse models. *J. Physiol.* **582**, 825–841 (2007).
7. Muraro, M. J. et al. A single-cell transcriptome atlas of the human pancreas. *Cell Syst.* **3**, 385–394.e3 (2016).
8. Wollny, D. et al. Single-cell analysis uncovers clonal acinar cell heterogeneity in the adult pancreas. *Dev. Cell* **39**, 289–301 (2016).
9. Hashimshony, T. et al. CEL-seq2: sensitive highly-multiplexed single-cell RNA-Seq. *Genome Biol.* **17**, 77 (2016).
10. Grün, D. et al. De novo prediction of stem cell identity using single-cell transcriptome data. *Cell Stem Cell* **19**, 266–277 (2016).
11. Singh, A., Puri, D., Kumar, B. & Singh, S.K. Heat shock proteins: knowledge so far and its future prospects. *Asian J. Pharm. Clin. Res.* **9**, 1–8 (2016).
12. Bahrami, S. & Drabløs, F. Gene regulation in the immediate-early response process. *Adv. Biol. Regul.* **62**, 37–49 (2016).
13. Kami, K., Noguchi, K. & Senba, E. Localization of myogenin, c-fos, c-jun, and muscle-specific gene mRNAs in regenerating rat skeletal muscle. *Cell Tissue Res.* **280**, 11–19 (1995).
14. Rodgers, J. T. et al. mTORC1 controls the adaptive transition of quiescent stem cells from G0 to GAlert. *Nature* **510**, 393–396 (2014).
15. Wood, L. K. et al. Intrinsic stiffness of extracellular matrix increases with age in skeletal muscles of mice. *Journal of Applied Physiology* **117**, 363–369 (2014).
16. Sambasivan, R. et al. Distinct regulatory cascades govern extraocular and pharyngeal arch muscle progenitor cell fates. *Dev. Cell* **16**, 810–821 (2009).
17. Sacco, A., Doyonnas, R., Kraft, P., Vitorovic, S. & Blau, H. M. Self-renewal and expansion of single transplanted muscle stem cells. *Nature* **456**, 502–506 (2008).
18. Motohashi, N., Asakura, Y. & Asakura, A. Isolation, culture, and transplantation of muscle satellite cells. *J. Vis. Exp.* (2014) doi:10.3791/50846.
19. Poss, K. D. et al. Roles for Fgf Signaling during Zebrafish Fin Regeneration. *Dev. Biol.* **222**, 347–358 (2000).
20. Jiang, L. et al. Synthetic spike-in standards for RNA-seq experiments. *Genome Res.* **21**, 1543–1551 (2011).
21. Grün, D., Kester, L. & van Oudenaarden, A. Validation of noise models for single-cell transcriptomics. *Nat. Methods* **11**, 637–640 (2014).
22. Hug, H. & Schuler, R. Measurement of the number of molecules of a single mRNA species in a complex mRNA preparation. *J. Theor. Biol.* **221**, 615–624 (2003).
23. Grün, D. et al. Single-cell messenger RNA sequencing reveals rare intestinal cell types. *Nature* **525**, 251–255 (2015).
24. van der Maaten L. & Hinton, G. Visualizing data using t-SNE. *J. Mach. Learn. Res.* **9**, 2579–2605 (2008).
25. Anders, S. & Huber, W. Differential expression analysis for sequence count data. *Genome Biol.* **11**, R106 (2010).
26. Smyth, G. K. Linear models and empirical bayes methods for assessing differential expression in microarray experiments. *Stat. Appl. Genet. Mol. Biol.* **3**, 1–25 (2004).
27. Lyubimova, A. et al. Single-molecule mRNA detection and counting in mammalian tissue. *Nat. Protoc.* **8**, 1743–1758 (2013).



"What I cannot create, I do not understand."
(R. Feynman)

*"Well... Even that what I can create,
I often still don't understand..."*
(S.C. van den Brink)

3

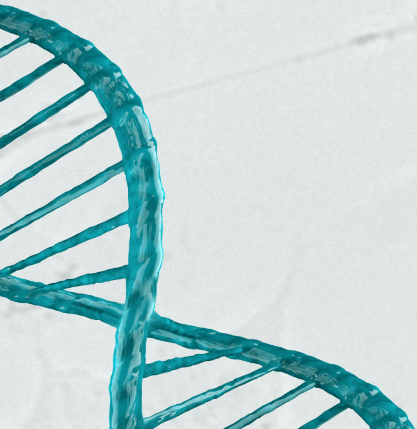
Single-cell and spatial transcriptomics reveal somitogenesis in gastruloids

Susanne C. van den Brink^{*,§}, Anna Alemany^{*}, Vincent van Batenburg^{*}, Naomi Moris, Marloes Blotenburg, Judith Vivié, Peter Baillie-Johnson, Jennifer Nichols, Katharina F. Sonnen, Alfonso Martinez Arias & Alexander van Oudenaarden[§]

* Equal contribution

§ Corresponding authors

Nature (2020)



Gastruloids are three-dimensional aggregates of embryonic stem cells that display key features of mammalian development after implantation, including germ-layer specification and axial organization¹⁻³. To date, the expression pattern of only a small number of genes in gastruloids has been explored with microscopy, and the extent to which genome-wide expression patterns in gastruloids mimic those in embryos is unclear. Here we compare mouse gastruloids with mouse embryos using single-cell RNA sequencing and spatial transcriptomics. We identify various embryonic cell types that were not previously known to be present in gastruloids, and show that key regulators of somitogenesis are expressed similarly between embryos and gastruloids. Using live imaging, we show that the somitogenesis clock is active in gastruloids and has dynamics that resemble those in vivo. Because gastruloids can be grown in large quantities, we performed a small screen that revealed how reduced FGF signalling induces a short-tail phenotype in embryos. Finally, we demonstrate that embedding in Matrigel induces gastruloids to generate somites with the correct rostral–caudal patterning, which appear sequentially in an anterior-to-posterior direction over time. This study thus shows the power of gastruloids as a model system for exploring development and somitogenesis in vitro in a high-throughput manner.

It has previously been shown that transcriptomes of entire gastruloids at 120 h after aggregation resemble that of mouse embryos at embryonic day (E)8.5 (ref.³). To extend this characterization to the single-cell level, we applied single-cell RNA sequencing (scRNA-seq) to 25,202 cells obtained from 100 gastruloids at 120 h after aggregation that were generated using the mouse embryonic stem (ES) cell lines E14-IB10 or LfngT2AVenus (Extended Data Fig. 1a, b, Methods), and clustered cells on the basis of highly variable genes (Fig. 1a, Extended Data Fig. 1c–f, Supplementary Tables 1, 2). To annotate the 13 resulting clusters, we compared their transcriptomes to a scRNA-seq dataset from E8.5 mouse embryos⁴ (Extended Data Fig. 1g, h, Methods, Supplementary Table 3). We confirmed previous reports^{1,3} of the absence of anterior neuronal cell types and the presence of ectodermal cells that resemble embryonic spinal cord (cluster 8) (Extended Data Figs. 1g–i, 2). Additionally, we identified endothelial and haemato-endothelial cells (cluster 10), and found a cluster of cells with signatures of primordial germ cells and extra-embryonic ectoderm (cluster 12) (Extended Data Fig. 1i). Cluster 13 correlates with the visceral endoderm; however, we suggest that this cluster represents definitive endoderm, because previous studies have shown that visceral endoderm has been incorporated into definitive endoderm in mouse embryos by E8.5 (refs.^{5,6}). We find the olfactory-receptor genes *Olfr959* and *Olfr129* upregulated in cluster 9, which suggests the presence of sensory neuron precursors. This cluster also expresses markers linked to head mesenchyme, pharyngeal pouches, branchial arches and neural crest, and correlates with mesenchyme in embryos. Cluster 11 might represent allantoic cells, as it expresses *Tbx4* (which in E8.5 embryos is found exclusively in the allantois^{4,7}). A comparison between both ES cell lines revealed that some cell types are more prevalent in one of the two lines (Extended Data Fig. 1e, Supplementary Tables 1, 4), which indicates that genetic background can skew the cell-type composition of gastruloids.

While exploring cells in clusters 1–8, we observed that these cells are ordered along neural and mesodermal differentiation trajectories. To further explore this, we plotted the expression of genes linked to neural and mesodermal differentiation processes along clusters 1–8 (Extended Data Fig. 2b, d, Methods). First, we observed a neuromesodermal progenitor-to-neural differentiation trajectory from cluster 7 to cluster 8 that starts with the expression of the tail-bud genes *T* (also known as *Brachyury*), *Nkx1-2* and *Cyp26a1*, and is followed by the expression of neural differentiation markers such as *Sox2*, *Hes3*, *Sox1* and *Pax6* (ref. ⁸). Second, we observed a mesodermal differentiation trajectory from cluster 6 to cluster 2. Consistent with what happens in embryos, the expression levels of tail-bud and FGF/WNT signalling genes (*Fgf8*, *Fgf17* and *Wnt3a*) decline in cells that differentiate towards a presomitic fate (characterized by the expression of *Tbx6* and *Hes7* (ref. ⁹), with expression levels being lower in the somite differentiation front (which expresses *Ripply2*). Upon somitic differentiation, cells first express *Uncx4.1* (also known as *Uncx*) and *Tbx18*, and later express markers of more-differentiated somites such as *Meox2* and *Pax3* (ref. ⁹) (Extended Data Fig. 2d). Finally, cluster 1 expresses heart markers (*Gata6* and *Hand2* (ref. ¹⁰)).

3 In embryos, neural and mesodermal differentiation trajectories have a strong spatial component: neuromesodermal progenitors are located within the tail bud, and differentiated tissues are located more anteriorly⁸. To determine whether this is also the case in gastruloids, we applied RNA tomography (tomo-seq¹¹), a spatial transcriptomics technology, to 120-h E14-IB10 and LfngT2AVenus gastruloids (Extended Data Figs. 3–5, Methods). In these experiments, gastruloids were cryosectioned along their anterior-posterior axis, after which the mRNA content of the sequential sections was sequenced (Methods). For each cell line, we selected reproducible genes between replicates, and clustered these according to their anterior–posterior expression pattern (Methods, Supplementary Tables 5, 6; tomo-seq clusters are referred to with Roman numerals). The overall gene-expression patterns between gastruloids generated from the two ES cell lines are similar to one another (Fig. 1b, Extended Data Figs. 5, 6, Supplementary Tables 6–8). To annotate the various expression domains, we projected the mean expression of the genes in each tomo-seq cluster onto the uniform manifold approximation and projection (UMAP) plot (Fig. 1c). This revealed that neuromesodermal progenitors (cluster 7 in Fig. 1a; cluster II in Fig. 1b) are located in the most-posterior part of the gastruloids. More-differentiated neural cells are found slightly more anteriorly (Extended Data Fig. 3e). Furthermore, mesodermal clusters in the UMAP plot are sequentially ordered along the anterior–posterior axis of gastruloids: cluster 6 (which roughly corresponds to cluster IV in tomo-seq) is the most posterior, and cluster 2 (which roughly corresponds to cluster VIII in tomo-seq) the most anterior (Fig. 1b, c, Extended Data Fig. 3e). This revealed that the neural and mesodermal differentiation trajectories in gastruloids are linked to their anterior–posterior axis, which is consistent with what occurs in embryos^{8,9}. Additionally, we found that the anterior domain in gastruloids (clusters VI, VII and VIII) contains cardiac, endothelial and head mesenchymal cells (Fig. 1b, c, Extended Data Fig. 3e). This is consistent with the locations of these tissues in embryos.

To further investigate the extent to which anterior–posterior gene expression patterns in gastruloids recapitulate those in embryos, we applied tomo-seq to E8.5 mouse embryos (Fig. 1d, Extended Data Figs. 3–6, Methods, Supplementary Tables 5–8). This revealed that mesoderm genes, including genes that regulate somitogenesis, are expressed very similarly between embryos and gastruloids. We detected cardiac and brain domains in embryos (clusters VII and I, respectively, in Extended Data Fig. 5b) that are not clearly defined and absent, respectively, in gastruloids. Additional differences and similarities between embryos

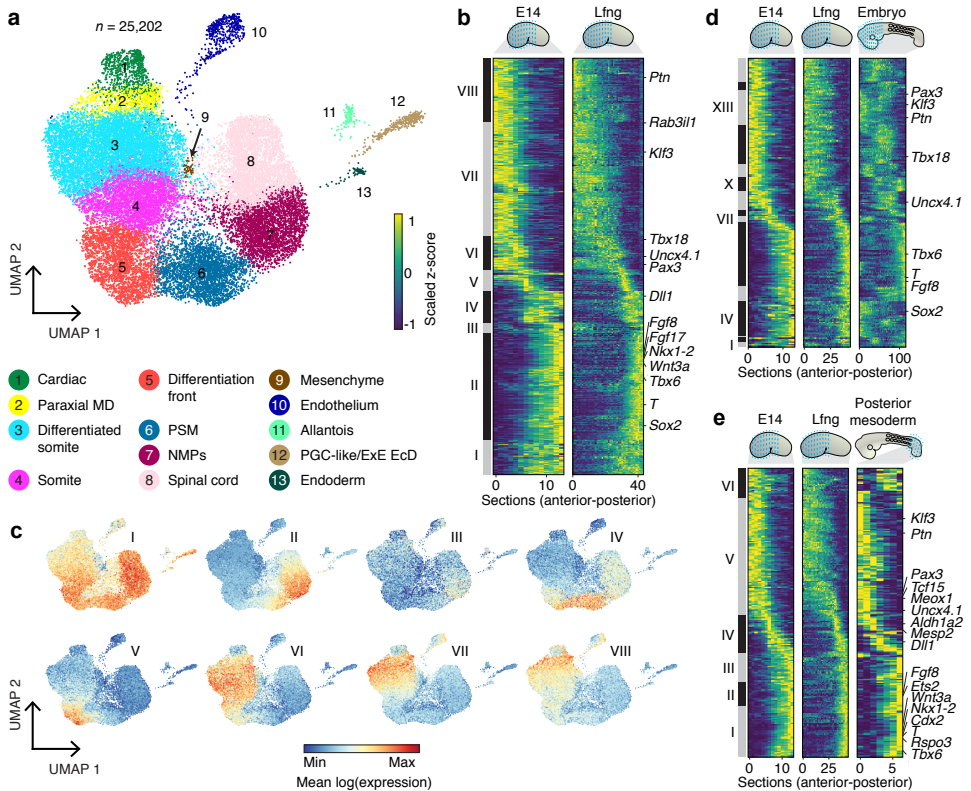


Fig. 1 | scRNA-seq and tomo-seq on mouse gastruloids and comparison to embryos. **a**, UMAP plot showing $n = 25,202$ cells isolated from 120-h gastruloids ($n = 26$ and 74 biologically independent gastruloids grown using E14-IB10 and LfngT2AVenus (ref. ¹⁵) ES cell lines, respectively; $n = 6$ independent experiments) cultured in standard^{1,20} conditions. Cells are coloured and numbered by their cluster annotation. **b**, Heat map showing the average anterior–posterior expression pattern of 514 genes detected by tomo-seq¹¹ in 120-h gastruloids generated from E14-IB10 and LfngT2AVenus¹⁵ mouse ES cells using standard^{1,20} culture protocols. Only genes reproducible between all E14-IB10 ($n = 5$ biological replicates) and LfngT2AVenus ($n = 3$ biological replicates) gastruloids are shown (Methods). Genes are clustered (clusters I–VIII) based on their anterior–posterior expression pattern (Supplementary Tables 5, 6, Methods). **c**, Mean log expression of genes present in each tomo-seq cluster from **b** plotted on the UMAP plot ($n = 3$, 132, 13, 39, 26, 42, 141 and 78 genes for clusters I, II, III, IV, V, VI, VII and VIII, respectively). **d**, **e**, As in **b**, but showing 222 (**d**) or 239 genes (**e**) found to be reproducible (Methods) between $n = 5$ biological replicates of E14-IB10 and $n = 3$ biological replicates of LfngT2AVenus gastruloids, and E8.5 mouse embryos (**d**) or posterior mesoderm of E9.5 mouse embryos¹² ($n = 3$ biological replicates) (**e**). E14, E14-IB10; ExE, extra-embryonic; EcD, ectoderm; Lfng, LfngT2AVenus; MD, mesoderm; NMPs, neuromesodermal progenitors; PGC, primordial germ cells; PSM, presomitic mesoderm. Blue dashed lines refer to anterior–posterior sectioning of gastruloids or embryos during the tomo-seq procedure.

and gastruloids are presented in Extended Data Fig. 5, Supplementary Tables 7, 8, and visualization is provided at <https://avolab.hubrecht.eu/MouseGastruloids2020>. We also compared our gastruloid tomo-seq dataset to a previously published microarray dataset in which the posterior mesoderm (from the tail bud to the newly formed somite) of E9.5 mouse embryos was dissected into 7 anterior–posterior regions to recover gene-expression patterns¹² (Fig. 1e, Extended Data Figs. 4, 5, Supplementary Tables 5–8). This comparison revealed a notable similarity between gastruloids and the mesoderm of embryos.

In embryos, the organization of the mesoderm is established by dynamic gene regulatory networks that are tightly linked to the process of somitogenesis⁹. During somitogenesis, retinoic acid and opposing FGF/WNT signalling gradients along the anterior–posterior axis determine the position of the differentiation front, which induces the differentiation of the mesoderm into epithelial blocks known as somites (Fig. 2a). These somites have defined rostral and caudal halves, and appear sequentially in an anterior-posterior direction. During this process, the tail bud of the embryo grows and -consequently- the signalling gradients and differentiation front move posteriorly over time. A second component of somitogenesis entails oscillations of WNT, Notch and FGF signalling, in which signalling waves travel from the tail bud towards the differentiation front about every two hours in mice^{9,13}. This cyclic component of somitogenesis is known as the segmentation clock and is thought to regulate the timing of somite formation^{9,14}. To investigate whether the segmentation clock is active in gastruloids, we monitored Notch signalling activity by performing fluorescence time-lapse imaging on gastruloids generated from *Lfng*T2AVenus mouse ES cells¹⁵ (Methods). Similar to what has previously been seen in embryos¹⁵, we observed a dynamic differentiation front that expresses high levels of *Lfng* and regresses posteriorly as the gastruloids extend (Fig. 2b, Extended Data Fig. 7, Supplementary Video 1). Additionally, we observed oscillating waves with low expression of *Lfng* and a period of about 2 h that travel from the tip of the tail bud towards the differentiation front, where they stall (Fig. 2c–e, Extended Data Fig. 8). The expression of *Lfng* disappears in the presence of the Notch inhibitor DAPT (Extended Data Fig. 7e, Supplementary Video 2), which confirms that the reporter expression is dependent on Notch signalling in gastruloids—as it is in embryos¹⁶. These experiments indicate that the segmentation clock is active in gastruloids with dynamics that are very similar to the *in vivo* situation.

Gastruloids can easily be generated in large numbers, opening the possibility of performing screens. To exemplify this, we performed a small compound screen on *Lfng*T2AVenus gastruloids and investigated the effect of inhibitors and agonists of FGF, WNT and BMP signalling pathways on the speed of the differentiation front (Extended Data Figs. 7, 8e, f, Supplementary Video 3). This revealed that application of the MEK inhibitor PD03—which inhibits FGF signalling—speeds up the differentiation front in a dose-dependent manner, without altering the speed at which gastruloids grow posteriorly (Fig. 2f, Extended Data Fig. 9a, Supplementary Video 4). This imbalance between the speed of the differentiation front and gastruloid growth results in both a progressive decrease in the length of the presomitic

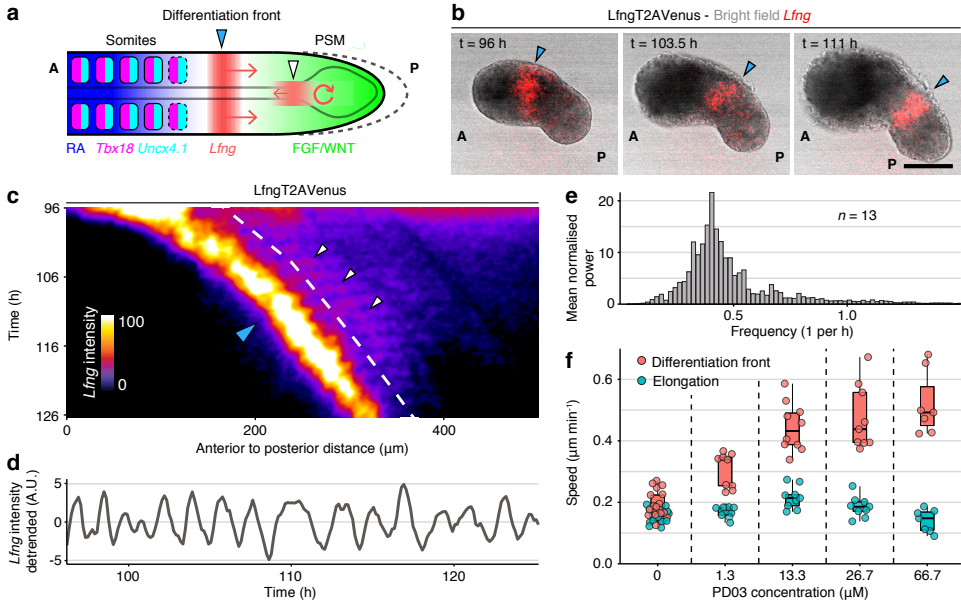


Fig. 2 | Time-lapse imaging and perturbation of the segmentation clock in mouse gastruloids. **a**, Illustration of somitogenesis in mouse embryos. Dark blue, retinoic acid (RA) gradient; red area and arrows, dynamic expression of *Lfng*; green, FGF/WNT signalling gradient in presomitic mesoderm; magenta and cyan blocks, somites; blocks with dotted lines, newly forming somites; posterior dotted line, posterior elongation of the presomitic mesoderm. **b**, Representative example of imaging of a *LfngT2AVenus*¹⁵ gastruloid embedded in 100% Matrigel at 96 h and subsequently imaged for 17 h (Supplementary Video 1). Blue arrowheads show the anterior–posterior displacement of the differentiation front (red, *Lfng*-expressing). Similar results were obtained in *n* = 9 independent experiments. **c**, Representative example of kymograph along the anterior–posterior axis of a *LfngT2AVenus* gastruloid embedded in 100% Matrigel at 96 h and subsequently imaged for 30 h. Similar results were obtained in *n* = 5 independent experiments. Highest-intensity signal reflects the posteriorly moving differentiation front (blue arrowhead in **b**); white arrowheads indicate periodic oscillations in the presomitic mesoderm. **d**, Detrended *LfngT2AVenus* intensity along the dashed white line in **c**. AU, arbitrary units. **e**, Periodogram of the *Lfng* oscillations detected in *n* = 13 biologically independent replicates of *LfngT2AVenus* gastruloids, as determined by Lomb–Scargle decomposition (Methods). **f**, Speed of elongation and differentiation front in *LfngT2AVenus* gastruloids treated with PD03 (*n* = 14, 9, 10, 9 and 7 biological replicates for PD03 concentrations 0, 1.3, 13.3, 26.7 and 66.7 μM, respectively). In the box plots, centre line indicates median; box limits the 1st and 3rd quartiles; and whiskers the range. Each point is one replicate. A, anterior; P, posterior. Scale bar, 200 μm.

mesoderm and in gastruloids that stop growing prematurely (Extended Data Fig. 9b). Similar results were obtained with the FGF-receptor inhibitors PD17 and BGJ398 (Extended Data Figs. 7, 8f, Supplementary Video 5). Our observations provide an explanation for the short-tail phenotype observed in FGF-mutant mouse embryos¹⁷ and for the posteriorly shifted differentiation fronts that have previously been observed after FGF inhibition^{18,19}.

Even though our experiments reveal that key regulators of somitogenesis are expressed in the correct location and that the segmentation clock is active in gastruloids, gastruloids that are generated with previously published protocols do not form somites^{1,3,20}. During our imaging experiments, we occasionally observed small ‘indentations’ that appeared anteriorly to the differentiation front (Supplementary Video 4). These indentations were

visible only in gastruloids mounted in Matrigel at 96 h, which was done before the imaging experiments to stabilize them (Methods). We then performed in situ hybridization stainings for *Uncx4.1* (a marker for the caudal halves of somites⁹) (Fig. 2a) and found that *Uncx4.1* was expressed in a stripy pattern in 4% (4 out of 100) of the 120-h gastruloids that were embedded in 100% Matrigel at 96 h (Extended Data Fig. 9c). This pattern was never detected in 120-h gastruloids cultured without Matrigel. To explore the effect of the concentration of Matrigel, we performed a titration experiment. We found that embedding 96-h gastruloids in 10–25% Matrigel results in the formation of clear segments, of which the posterior half is marked by *Uncx4.1* expression in up to 50% of the gastruloids (in situ hybridization and hybridization chain reaction (HCR)²¹); Fig. 3a, Extended Data Fig. 9c,d). Time-lapse imaging videos of these gastruloids revealed that these segments appear sequentially in an anterior–posterior direction, anteriorly to the *Lfng* expression domain (Fig. 3b, Extended Data Fig. 9e, Supplementary Video 6). Lastly, double stainings for *Uncx4.1* and *Ripply2* (which marks newly forming somites), and for *Uncx4.1* and *Tbx18* (a marker of rostral somites⁹), revealed that *Uncx4.1* and *Tbx18* are expressed in an alternating pattern (Fig. 3c), and that it is indeed the caudal half of the segments that expresses *Uncx4.1* (Extended Data Fig. 10). At 120 h of culture (after 24 h in 10% Matrigel), gastruloids have about 10 or 11 somites (Fig. 3c, Extended Data Fig. 10), the size of which decreases in the anterior–posterior direction from (on average) 183 μm to 43.4 μm (Extended Data Fig. 10c–e). In embryos, the size of these somites decreases from 120 μm to 80 μm (Methods). Our experiments thus reveal that embedding gastruloids in low-percentage Matrigel induces the formation of somite-like structures, which have the correct rostral–caudal patterning and appear sequentially along

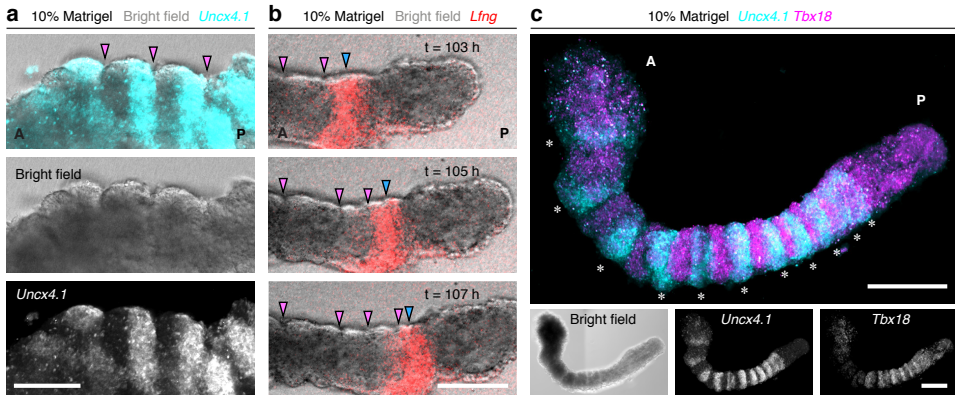


Fig. 3 | Stainings and time-lapse imaging of somite formation in gastruloids embedded in low percentages of Matrigel. **a**, Somites in a representative LfngT2AVenus gastruloid (zoomed in) (Extended Data Fig. 9d) embedded in 10% Matrigel at 96 h and stained for *Uncx4.1* using HCR (ref. ²¹) at 120 h. Magenta arrowheads, segment boundaries. Similar results were obtained in $n = 5$ independent experiments. **b**, Imaging (Supplementary Video 6) of a representative LfngT2AVenus gastruloid embedded in 10% Matrigel at 96 h. Blue arrowheads, differentiation front (red, *Lfng*-expressing); magenta arrowheads, appearing segment boundaries. Similar results were obtained in $n = 2$ independent experiments. **c**, HCR (ref. ²¹) double staining for *Uncx4.1* (cyan) and *Tbx18* (magenta), on a 120-h LfngT2AVenus gastruloid embedded in 10% Matrigel at 96 h and to which 1.3 μM of PD03 was added at 96.5 h. White asterisks, *Uncx4.1* expression stripes. Similar results were obtained in $n = 4$ independent experiments. Scale bars, 100 μm (a, b), 200 μm (c).

the anterior–posterior direction over time. So far, we have not observed gastruloids with two neighbouring rows of somites.

Using single-cell and spatial transcriptomics, we demonstrate that gene expression in mouse gastruloids is very similar to embryos. Gastruloids can therefore be used as a model system for embryology, and have some key advantages over embryos: they can be grown in large quantities (allowing screens), are easier to genetically modify as they can be grown directly from ES cells and can be used to study the effect of external signals on morphogenesis. We used several of these advantages to study somitogenesis *in vitro*. Recent studies have explored *ex vivo* and *in vitro* models for somitogenesis, such as monolayer pre-somitic mesoderm cultures^{16,22} and cultures of embryoid-body-like aggregates of mouse ES cells that display travelling somitogenesis waves *in vitro*²³. However, such cultures do not form proper somites, lack a correctly defined anterior–posterior axis and do not elongate in the posterior direction. Here we have shown that gastruloids overcome these limitations, and thus provide a powerful tool for studying somitogenesis *in vitro*. In general, *in vitro* mimics of development—such as gastruloids—are promising systems with which we are starting to obtain insights that could not readily be obtained with embryos. We therefore anticipate many applications of this system, which will help to unravel the complex processes that regulate embryogenesis.

Methods

Mouse gastruloid culture, with and without Matrigel

E14-IB10 (a subclone of 129/Ola-derived E14 ES cells, from The Netherlands Cancer Institute), LfngT2AVenus¹⁵ (Notch signalling reporter, which contains a single copy of Venus that was inserted in the endogenous Lfng locus¹⁵; the selection cassette was removed), Brachyury-GFP (ref. ²⁴), WNT/ β -catenin transcriptional reporter TCF/LEF-mCherry (refs. ^{25,26}) and Nodal-YFP (ref. ²⁷) mouse ES cells were maintained in standard conditions in ESLIF medium (GMEM supplemented with sodium pyruvate, non-essential amino acids, GlutaMAX, penicillin-streptomycin, β -mercaptoethanol, 10% FBS and LIF) on gelatinized 6-well plates and in a humidified incubator (5% CO₂, 37 °C) as previously described^{20,25,28–31} (Supplementary Methods 1, 2). E14-IB10 mouse ES cells were obtained from E. R. Maandag (Netherlands Cancer Institute). LfngT2AVenus mouse ES cells from which the selection cassette has been removed were obtained from the Aulehla laboratory. Brachyury-GFP mouse ES cells were obtained from the Keller laboratory. TCF/LEF-mCherry mouse ES cells were obtained from the Hadjantonakis laboratory, and Nodal-YFP mouse ES cells were obtained from the Collignon laboratory. These cell lines were validated as follows: for the Brachyury-GFP and TCF/LEF-mCherry lines, stimulation with Chiron resulted in reporter expression in a region that overlapped with the expression of Brachyury or Wnt3a, respectively, in our tomo-seq data (Extended Data Fig. 3d); for the Nodal-YFP line, we tested whether the reporter expression was blocked by the Nodal inhibitor SB43 and switched on by Nodal and activin A; for the LfngT2AVenus line, we showed dynamics very similar to the dynamics reported in embryos *in vivo*, and tested whether the reporter signal disappeared upon application of the Notch inhibitor DAPT. Our RNA sequencing experiments confirmed that all these cell lines were derived from mice. All cell lines were routinely tested and confirmed to be free of mycoplasma.

Gastruloids for scRNA-seq and tomo-seq experiments were generated as previously described^{1,20}, with the following minor modifications: after neutralization of trypsin with ESLIF, cells were washed with PBS (containing Ca²⁺ and Mg²⁺) twice. Next, cells were resuspended in N2B27 medium (NDiff 227 medium, Takara, Y40002), and the cell concentration was determined only after resuspension in N2B27 medium. Cells were then diluted in N2B27 to a concentration of 7.5 cells per microlitre, and 40 μ l (with about 300 cells) of this suspension was transferred to each well of a U-bottomed 96-well plate (Greiner Bio-One, 650185). N2B27 aliquots were stored at –20 °C and thawed by rocking them at 4 °C for several hours, after which aliquots were transferred to a cell-culture flask in a CO₂-controlled 37-°C incubator for pH equilibration 1 day before gastruloid formation. A step-by-step protocol is provided in the Supplementary Methods. Aggregates that did not elongate and that did not form gastruloids were excluded from this study, and curved gastruloids were excluded from tomo-seq experiments. For the scRNA-seq and tomo-seq experiments, 120-h gastruloids generated with the original gastruloids protocol^{1,20} were used, as these gastruloids were—in our experiments—more reproducible (showing considerably less variation in morphology between wells) than more recent versions of the protocol that allow culture up to 168 h (ref. ³). For *in situ* hybridization, HCR staining and imaging experiments, gastruloids were cultured as described, but then embedded in Matrigel at 96 h. To embed gastruloids in 50–100% Matrigel (Corning, 356231, lot number 6137007, protein concentration 9.8 mg/ml), Matrigel was thawed on ice, mixed with the required amount of cold N2B27 medium and 60 μ l was added to each well of a multiwell imaging chamber (Sigma, EP0030741021 or M9312) on ice. Ninety-six-hour gastruloids were then transferred to the Matrigel using a 20- μ l pipette and allowed to settle for approximately 5 min before the chamber was incubated at 37 °C for 10 min, allowing the Matrigel to solidify. After this, 500 μ l N2B27 medium was added to each well. Embedding gastruloids in diluted 10–25% Matrigel was done by first pooling the gastruloids in a 5-ml DNA LoBind Eppendorf tube on ice, replacing the N2B27 medium with fresh cold medium and then adding the correct volume of Matrigel. The gastruloids were then transferred to a 24-well plate (Sigma, EP0030741021 or M9312) using a P1000 pipette with the tip cut off, at a concentration of about 8 gastruloids per ml, 500 μ l per well; plates were gently agitated to prevent gastruloids from clumping together in the centre of the wells before the plates were placed in the incubator. In our experiments, somite formation was more efficient when gastruloids were generated from cells with a low passage number. In all experiments, gastruloids were allocated to the various conditions randomly. No statistical methods were used to predetermine sample size, and blinding was not relevant to the study. A step-by-step protocol describing how gastruloids were cultured, embedded in Matrigel and fixed is provided in the Supplementary Methods. This protocol has also been deposited in the Protocol Exchange repository³².

Dissociation and fluorescence-activated cell sorting of gastruloids before scRNA-seq

To dissociate gastruloids for scRNA-seq, gastruloids were washed with PBS twice, incubated in trypsin–EDTA at 37 °C for 5 min and titrated with a P200 pipette, after which ESLIF was added to neutralize the trypsin. After centrifugation (200g, 3 min), cells were resuspended in PBS with 10% serum and filtered through a 35- μ m filter (Falcon, 352235). Prior to fluorescence-activated cell sorting (FACS), DAPI (Thermo Fisher) was added to assess cell viability. For SORT-seq, individual live cells were sorted into the wells of a 384-well plate as previously described³³ using a BD FACSJazz

Cell Sorter (BD Biosciences) that was equipped with BD FACS software (version 1.2.0.124). For 10x Genomics scRNA-seq, washes were done using PBSO (PBS without calcium and magnesium), and 100,000 live cells were sorted into 1.5-ml DNA LoBind tubes (Eppendorf, 022431021) that were pre-filled with 50 μ l PBSO, after which cells were centrifuged for 3 min at 200g, resuspended in 80 μ l PBSO containing 5–10% serum, and filtered through a 35- μ m filter (Falcon, 352235). After resuspension and filtering, the cell concentration was determined using a counting chamber (Bürker-Türk, Marienfeld).

SORT-seq and 10x Genomics scRNA-seq

For scRNA-seq, cells extracted from 120-h gastruloids (generated with a previously published, non-Matrigel-based protocol^{1,20}) were processed using either SORT-seq (CEL-seq2-based scRNA-seq on cells that were sorted into 384-well plates³³) or using the 10x Genomics Chromium Single Cell 3' (v.3 Chemistry) gene-expression kit, according to manufacturer's instructions.

Mouse experimentation

Mouse embryos ($n = 3$) used for tomo-seq were derived from crosses between CD-1 females and CD-1 stud males. Experiments were performed in accordance with European Union (EU) guidelines, under the authority of appropriate UK governmental legislation. All mouse experiments for this project were approved by the Animal Welfare and Ethical Review Body for the University of Cambridge. Relevant Home Office licences are in place.

Tomo-seq

Tomo-seq was performed using a robotized (SORT-seq³³-based) version of a previously published tomo-seq protocol¹¹. In brief, 120-h gastruloids ($n = 3$ E14-IB10 gastruloids sectioned along their anterior–posterior axis using 20- μ m sections; $n = 2$ E14-IB10 gastruloids sectioned along their anterior–posterior axis using 8- μ m sections; and $n = 3$ LfngT2AVenus gastruloids sectioned along their anterior–posterior axis using 20- μ m sections, generated with previously published, non-Matrigel-based gastruloid protocols^{1,20}) or E8.5 mouse embryos ($n = 3$ sectioned along their anterior–posterior axis using 20- μ m sections) were embedded in cryosolution (Leica, 14020108926), snap-frozen on dry ice, stored at -80 °C and sectioned using a cryotome. Sections were collected in the wells of a hard-shell PCR low-profile, semi-skirted 96-well plate (Biorad, HSL9601) that was pre-filled with mineral oil (Sigma, M8410-1L) and CEL-seq2 primers. For each well, a unique, barcoded CEL-seq2 primer was used, which allowed us to pool the content of the wells after second-strand synthesis. To sequence the mRNA content of the wells, SORT-seq (robotized CEL-seq2-based scRNA-seq³³) was performed using a Nanodrop II liquid handling platform (GC biotech).

Sequencing

Sequencing was performed on the Illumina next-seq sequencing platform. For SORT-seq and tomo-seq, paired-end (75-bp) sequencing was performed; and for 10x Genomics, sequencing was performed according to 10x Genomics manufacturer's instructions (read 1, 28 cycles; index i7, 8 cycles; and read 2, 91 cycles).

Mapping sequencing data

For SORT-seq and tomo-seq, the first six bases of read 1 contain the unique molecular identifier and the next seven bases contain the cell or section barcode. For 10x Genomics, the first 16 bases of read 1 contain the cell barcode, and the next 12 contain the unique molecular identifier. For all sequencing experiments, read 2 contains the biological information. Reads 2 with a valid cell or section barcode were selected, trimmed using TrimGalore (v.0.4.3) with default parameters, and mapped using STAR (v.2.5.3a) with default parameters to the mouse mm10 genome (Ensembl 93). Only reads mapping to gene bodies (exons or introns) were used for downstream analysis. Reads mapping simultaneously to an exon and to an intron were assigned to the exon. For each cell or section, the number of transcripts was obtained as previously described³⁴. We refer to transcripts as unique molecules based on unique molecular identifier correction. Mappabilities for both scRNA-seq and tomo-seq experiments range from 35% to 60%. Spike-ins, ribosomal and mitochondrial genes were removed from downstream analysis, together with Kcnq1ot1, Lars2 and Malat1, because these genes seem to be linked to mapping errors and have previously been shown to be erroneous³⁴.

Processing single-cell data

scRNA-seq analysis was performed using the Scanpy package³⁵ (v.1.4.3). In each experiment, cell barcodes with more than 1,000 transcripts and fewer than 6,000 genes were selected. Genes detected in fewer than three cells were excluded. Expression levels for each cell were size-normalized to 10,000 transcripts. Highly variable genes were defined as those with a mean expression value between 0.0125 and 5, and with a minimum dispersion, and used to generate the UMAP plots shown in Fig. 1, Extended Data Figs. 1, 2, 4, 5. Next, cells from the three independent experiments were analysed together. Here, we kept cells with more than 700 and fewer than 8,000 genes, and more than 1,000 and fewer than 40,000 transcripts. Selection of highly variable genes and cell normalization were then

performed. To remove batch effects, we used the combat function from Scanpy (a Python implementation (<https://github.com/brentp/combat.py>) of the R-package Bioconductor^{36,37}). Cells were clustered using a combination of k-medoids and Leiden algorithms³⁸ (Supplementary Table 1). Differentially expressed genes in each cluster were determined using the t-test (Supplementary Table 2).

Comparison between gastruloid cell types and mouse embryonic-cell types

Common genes between marker genes detected in the gastruloid cell clusters (Supplementary Table 1) (P value < 0.01 and \log_2 -transformed fold change > 1.01) and markers genes found for the different embryonic-cell types defined in a previously published mouse embryo scRNA-seq dataset⁴ were found. P value for significance was assigned using a binomial test, in which the probability of sharing a number of common marker genes between a gastruloid cell type and an embryonic-cell type was determined by randomizing the list of marker genes for the embryonic-cell type from the full list of marker genes in the embryonic-cell types ($n = 200$). Extended Data Fig. 1h shows only the comparison to embryonic-cell types found at E8.5. Extended Data Fig. 1i shows the comparison to all embryonic-cell types detected from E7.0 until E8.5. Only embryonic cell types with at least one cluster comparison with a P value below 0.2 are shown. Using different P value thresholds to define upregulated genes does not have a considerable effect on the results of the comparison between gastruloid cell populations and embryonic cell types.

Linearization of the UMAP plot

Cells in clusters 1–8 were projected on the symmetry axis along the clusters 1–8 in the UMAP plot (Extended Data Fig. 1d). The position of each cell along this symmetry axis defines the x-position in Extended Data Fig. 2d. To plot gene expression along the linearized UMAP plot, 1,000 evenly spaced bins were defined along the x-axis for which the expression average of all cells per respective bin was scaled and plotted. For visualization, a LOESS smoother was used with span set to 0.2.

Processing tomo-seq data

Twenty-micrometre sectioned slices with fewer than 3,200 genes and 8- μm sectioned slices with fewer than 6,000 genes were filtered out (Extended Data Fig. 3). In each tomo-seq sample, data were normalized to the median number of unique transcripts per slide. Sequencing libraries contain a maximum of 96 slices. In samples with more than 96 sections, several libraries were generated. For these samples, we corrected batch effects between sequenced libraries by imposing the continuity of expression profiles along the anterior–posterior axis for each gene separately.

Gene reproducibility analysis between replicates

The Pearson correlation coefficient between the anterior–posterior expression pattern (in z-score units) of two different samples is computed for all possible pairs of replicates. Linearly interpolated gene-expression profiles are used when the number of sections is different between replicates. To assess for significant correlations, we randomly generate 10,000 expression profiles with the same number of sections as in the pair of replicates and determine a threshold for the correlation value at which less than n random profiles have larger correlation values ($n = 100$ for P value < 0.01 , $n = 500$ for P value < 0.05 and so on) (Supplementary Table 5). Adjusted P values are obtained with the Benjamini–Hochberg correction. Only genes that are significantly correlated (P value < 0.01) in at least five possible pairs of replicates are considered as reproducible between replicates (Supplementary Tables 6, 9). Custom-made code was used for this analysis.

Clustering genes on the basis of anterior–posterior expression patterns

Genes were first clustered on the basis of z-score anterior–posterior expression pattern using self-organizing maps with an initial number of clusters set to about $5\sqrt{n}$, in which n is the total number of genes. Average z-score expression patterns for each cluster were then hierarchically clustered using Euclidean distances and the Ward.D method.

Comparison between tomo-seq data of mouse embryos, mouse gastruloids and mouse presomitic mesoderm dataset

Gene reproducibility analyses between the individual replicates of the systems that are being compared were performed independently, as described in ‘Gene reproducibility analysis between replicates’ (Supplementary Tables 5–9). For heat maps in Fig. 1b, d, e, only genes present in the two separate lists of significantly correlated genes were used for downstream analysis (Supplementary Tables 7,9). For heat maps in Extended Data Fig. 5, genes that were present in only one of the two separate lists were included as well (Supplementary Tables 8, 9). Genes were clustered on the basis of their anterior–posterior expression pattern in the systems that were being compared simultaneously, as described in ‘Clustering genes on the basis of anterior-posterior expression patterns’. The Pearson correlation coefficient for each gene was calculated between the anterior–posterior expression pattern of two different samples (in z-score units). To assess for significantly correlated genes, we randomly generated 10,000 expression profiles with the same number of sections as in the pair of replicates and determined the correlation value at which less than 500

random profiles have larger correlation values (P value < 0.05). Adjusted P values were obtained with the Benjamini–Hochberg correction. For the presomitic mesoderm comparison, we used a previously published microarray dataset in which the posterior mesoderm (from the tail bud to the newly formed somite) of E9.5 mouse embryos was investigated¹² (accession number GSE39615).

Comparison between genes in tomo-seq clusters and mouse embryonic-cell types

This was performed as described in ‘Comparison between gastruloid cell types and mouse embryonic-cell types’, but then calculating the number of overlapping genes and the P value of this overlap by comparing the genes in each tomo-seq cluster with the list of genes upregulated in the cell types of a previously published E8.5 mouse embryo scRNA-seq dataset⁴ (Supplementary Tables 5–9).

Wide-field microscopy

Wide-field images of gastruloids made from Brachyury-GFP (ref. ²⁴), Nodal-YFP (ref. ²⁷) and TCF/LEF-mCherry (TLC2) (refs. ^{25,26}) mouse ES cells were acquired at 120 h using a Zeiss AxioObserver Z1 in a humidified CO₂ incubator (5% CO₂, 37 °C) and a 20× LD Plan-Neofluar 0.4 NA Ph2 objective with the correction collar set to image through plastic, as previously described². Illumination was provided by an LED white-light system (Laser2000) in combination with filter cubes GFP-1828A-ZHE (Semrock), YFP-2427B-ZHE (Semrock) and Filter Set 45 (Carl Zeiss Microscopy) used for GFP, YFP and RFP, respectively. Emitted light was recorded using a back-illuminated iXon888 Ultra EMCCD (Andor) and images were processed using Fiji (v.2.0.0)³⁹.

Multiphoton time-lapse imaging of gastruloids

Gastruloids were embedded in 10–100% Matrigel in 24-well plates (Sigma, EP0030741021 or M9312) at 96 h as described in ‘Mouse gastruloid culture, with and without Matrigel’ (Supplementary Methods 3), and imaged immediately following embedding at 37 °C, 5% CO₂ with humidified air influx on a Leica SP8 multiphoton microscope system using an HC PL APO 20×/0.75 air CS2 objective, a Coherent Chameleon Vision-S multiphoton laser tuned to 960 nm and the pinhole maximally opened. The bright field channel was recorded using a 488-nm laser set at low intensity in combination with a transmission PMT. A z-stack of around 4 images with a z-interval of 15 μm was taken every 15 min (10 images per stack and at 12 min interval) (Fig. 3b) for each individual gastruloid (frame accumulation 2 times, pixel dwell time 2.425 μs). Photons with a wavelength between 505–555 nm, and 555–680 nm were collected with two separate hybrid detectors and assigned to a 16-bit pixel range. Alternatively, in Extended Data Fig. 7d, a 514-nm solid state laser was used, during which photons were collected with a wavelength between 524–575 nm and 600–700 nm with two separate hybrid detectors and assigned to a 16-bit pixel range. In this case, the bright field channel was recorded simultaneously with the other channels using a transmission photomultiplier tube.

Treatment of Matrigel-embedded gastruloids with inhibitors

Gastruloids were embedded in 10–100% Matrigel at 96 h as described in ‘Mouse gastruloid culture, with and without Matrigel’, and time-lapse imaging was started immediately after embedding. After recording at least 2 time points (and at most 4 time points) for each replicate (about 30–60 min in total), the microscope was paused and inhibitors were added without removing the culturing plate from the stage. The inhibitors used were DAPT (Sigma, D5942; stock 10 mM in DMSO; used at 27 μM); PD0325901 (Sigma, PZ0162; stock 10 mM in DMSO); BGJ398 (Selleckchem, S2183; stock 1 mM in DMSO; used at 0.2 μM); PD173074 (Peprotech, 2191178; stock 10 mM in DMSO; used at 0.5 μM); FGF1 (Peprotech, 100-17A; stock 10 μg/ml in H₂O; used at 0.02 μg/ml); FGF10 (Peprotech, 100-26; stock 100 μg/ml in H₂O; used at 0.2 μg/ml); Chiron (CHI99021; Sigma, SML1046; stock 10 mM in DMSO; used at 10 μM); IWP-2 (Sigma, I0536; stock 2 mM in DMSO; used at 2 μM); IWR-1 (Sigma, I0161; stock 10 mM in DMSO; used at 10 μM); and LDN193189 (Sigma, SML0559; stock 0.1 mM in H₂O; used at 0.2 μM).

Analysis of multiphoton time-lapse imaging data

Image analysis was done similarly to previously described image-analysis methods^{15,22}. Time-lapse imaging data were analysed using the ImageJ data processing package Fiji (v.2.0.0)³⁹. To filter out auto-fluorescence, the first channel (555–680 nm) was multiplied by 0.3 and subtracted from the second channel (505–555 nm). Then, a sum projection of all z-slices was generated for all time points. The resulting image was convolved using a Gaussian filter with a sigma value of 1 μm. Kymographs were generated using the plug-in KymoResliceWide (v.0.5, <https://github.com/ekatrakha/KymoResliceWide>) by tracing the path of the differentiation front as it moves along the anterior–posterior axis with a segmented line (60 pixels wide) and then blurred using a Gaussian filter with a sigma value of 1 pixel. The intensity profile of the oscillations was measured at a constant distance from the differentiation front (dashed white line in Fig. 2c) on the kymograph. The intensity profile of the oscillations was decomposed into a trend and a cycle component using Hodrick–Prescott filtering with an l of 800. Trend and cycle components for all replicates are shown in Extended Data Fig. 8. To make an estimation of the period of the Lfng oscillations, Lomb–Scargle analysis

was performed with the maximum scanned frequency at half the temporal resolution and over-sampling set to 3 (ref. ⁴⁰). The speed of the differentiation front and the elongation speed of the gastruloid were measured by first drawing a line along the differentiation front or posterior tip of the gastruloid on the kymograph, respectively, and then measuring the angle, as explained in Extended Data Fig. 9a.

Sample fixation for staining

For gastruloids grown in 100–50% Matrigel, the medium was removed and the samples were washed twice for 5 min in PBS before fixation in 4% PFA in PBS overnight at 4 °C. For gastruloids grown in 25–10% Matrigel, the Matrigel was not removed in the first washing step with PBS (Supplementary Methods 4). After fixation, all samples were washed 3 times for 5 min in PBS-Tween (0.1% Tween-20 (v/v)), transferred to DNA LoBind tubes using a P1000 pipette with the tip cut off, and washed 3 times for 3 min in TBS-Tween (0.1% Tween-20 (v/v)) before digesting for 4 min with 25 µg/ml proteinase K in TBS-Tween. The samples were then rinsed briefly 3 times with 2 mg/ml glycine in TBS-Tween, washed with TBS-Tween once, refixed for 30 min in 4% PFA and 0.05% GA in PBS at room temperature and washed 3 times in TBS-Tween.

In situ hybridization

In situ hybridization was performed as previously described^{3,15}. In brief, samples were incubated for 4–5 h in hybridization mix (5 mg/ml torula RNA (Sigma, R6625), 50% deionized formamide (Sigma, AM9342) (v/v), 1.33x SSC, 0.1% BSA (w/v), 125 µg/ml heparin (Sigma, H3393), 10 mM EDTA 0.5 pH = 8.0, 0.1% Tween 20 (v/v)) at 68 °C followed by incubation overnight in 150 ng/ml DIG-labelled probe in hybridization mix at 68 °C. Carryover Matrigel that was still present degraded during this incubation step in most instances. The hybridization mix with the probe was preincubated for 10 min at 80 °C. Samples were then washed twice for 30 min in preheated hybridization mix at 68 °C, 4 times for 20 min in preheated 2x SSC-Tween (0.1% Tween-20 (v/v)) at 68 °C, allowed to cool down and washed twice for 5 min in MAB-Tween (0.1% Tween-20 (v/v)) at room temperature. The samples were blocked for 1.5 h in blocking buffer (10% heat-inactivated sheep serum (Sigma, S3772) (v/v) and 1% BSA (w/v) in MAB-Tween) at room temperature, incubated for 4–5 h in blocking buffer containing 1:2,000 anti-DIG-AP antibody (Sigma, 11093274910) at room temperature and washed 5 times for 10 min followed by washing overnight in MAB-Tween. Finally, the samples were washed 3 times in TBS-Tween, washed 3 times for 10 min in AP-buffer (100 mM Tris-HCl pH 8.0, 100 mM NaCl, 50 mM MgCl₂, 0.1% Tween-20), stained for several hours in 1 ml BM purple (Sigma, 11442074001), washed 3 times for 5 min in TBS-Tween and refixed in 4% PFA/PBS for 20 min at room temperature.

Imaging of gastruloids stained with in situ hybridization

In situ samples were imaged on a Leica M165FC stereo microscope with DMC5400 digital camera (Extended Data Fig. 9c, right) or using a Nikon SMZ800N microscope (Extended Data Fig. 9c, left panels) in TBS-Tween.

HCR of 10% Matrigel-embedded gastruloids

In situ whole mount HCR V3 was performed as previously described²¹ using reagents from Molecular Instruments. In brief, each condition (up to 100 gastruloids) was incubated in 200–500 µl of probe hybridization buffer for 5 min at room temperature and 30 min at 37 °C before incubation with 4 pM of each probe stock in 200–500 µl probe hybridization buffer for 12–16 h at 37 °C. Next, samples were washed 4x with 500 µl probe wash buffer for 15 min at 37 °C, 2x with 1 ml 5x SSC-Tween for 10 min at room temperature and 1x with 200–500 µl amplification buffer for 5 min at room temperature. The hairpin mixture was prepared by separately heating both h1 and h2 of each hairpin to 95 °C for 90 s and incubating these at room temperature for 30 min in the dark. All the hairpin mixtures were then added to 200–500 µl amplification buffer at a concentration of 48 pM, which was then added to the samples and incubated for 12–16 h at room temperature in the dark. Samples were then washed at least 2x with 1 ml SSC-Tween for 30 min before imaging. HCR probe design was as follows: *Uncx4.1* (Accession NM_013702.3, hairpin B1); *Tbx18* (Accession NM_023814.4, hairpin B3); *Ripply2* (Accession NM_001037907, hairpin B2); hairpin B1 was labelled with Alexa 594 and B2 and B3 with Alexa 488.

Multiphoton microscopy of HCR-stained gastruloids

HCR-stained samples were imaged in TBS-T on a Leica SP8 multiphoton microscope system using an HC PL APO 20x/0.75 air CS2 objective, a Coherent Chameleon Vision-S multiphoton laser tuned to 810 nm for the Alexa-594 dye, a 488-nm OPS-laser for the Alexa-488 dye and the pinhole maximally opened. A z-stack of around 30 images with a z-interval of 5 µm was taken with frame accumulation set to 4. Photons with a wavelength between 505–555 nm and 555–680 nm were collected with two separate hybrid detectors and assigned to a 16-bit pixel range for the Alexa-594 channel; photons with a wavelength between 498 and 550 nm were collected with a hybrid detector and assigned to a 16-bit pixel range for the Alexa-488 channel. The bright field channel was recorded simultaneously with the Alexa-488 channel using a transmission photomultiplier tube detector.

HCR data analysis

HCR imaging data were analysed using the ImageJ data processing package Fiji (v.2.0.0)³⁹. First, all the images in a single stack were aligned using the ImageJ plug-in Correlescence (v.0.0.3, <https://github.com/ekatruxha/Correlescence>), after which a maximum projection was generated for the fluorescence channels. The posterior region of gastruloids was identified visually (the anterior end of gastruloids is darker than the posterior end), and confirmed with *Ripply2* staining. To plot the intensity profile along the anterior–posterior axis, a segmented line with a width of 100 pixels was drawn, and the intensity was measured along this line. To measure the peak-to-peak distances in the *Uncx4.1* intensity profiles, a LOWESS smoother (0.002 span) was applied, after which the maximal values corresponding to the peaks were selected in R (v.3.6.1).

Somite-size measurements in embryos

Somite sizes were measured in 10 somite-stage paraffin-embedded mouse embryos that were sectioned with 6- μ m sections, stained using a standard haematoxylin and eosin staining and imaged with a Leica DM 4000 B LED microscope with Leica DFC450 camera that was size-calibrated using a microscope calibration slide (Pyser-SGI). Somite sizes were next measured using Fiji (v.2.0.0). Measurements were validated by comparing results to somite sizes in the EMAP eMouse Atlas Project (<http://www.emouseatlas.org/>)⁴¹.

Acknowledgements

This work was supported by an European Research Council Advanced grant (ERC-AdG 742225-IntScOmics), a Nederlandse Organisatie voor Wetenschappelijk Onderzoek (NWO) TOP award (NWO-CW 714.016.001) and the Foundation for Fundamental Research on Matter, financially supported by NWO (FOM-14NOISE01) to S.C.v.d.B., A.A., V.v.B., M.B., J.V. and A.v.O., a Biotechnology and Biological Sciences Research Council (no. BB/P003184/1), Newton Trust (INT16.24b) and Medical Research Council (MR/R017190/1) grant to A.M.A., a Newnham College Cambridge Junior Research Fellowship to N.M. and a studentship from the Engineering and Physical Sciences Research Council to P.B.-J. The Cambridge Stem Cell Institute is supported by core funding from the Wellcome Trust and Medical Research Council; J.N. was funded by the University of Cambridge and K.F.S. by core funding from the Hubrecht Institute. This work is part of the Oncode Institute, which is partly financed by the Dutch Cancer Society. We thank A. Ebbing and M. Betist for the robotized tomo-seq protocol; G. Keller for the *Brachyury-GFP* cell line; J. Collignon for the *Nodal-YFP* line; K. Hadjantonakis for the TCF/LEF-*mCherry* line; S. van den Brink and E. R. Maandag for the E14-IB10 cells; J. Kress and A. Aulehla for the LfngT2AVenus mouse ES cell line; I. Misteli Guerreiro, J. Peterson-Maduro and J. Hoeksma for suggestions for in situ hybridization experiments; W. Thomas, Y. el Azhar, J. Juksar and J. Beumer for reagents and inhibitors; A. de Graaff and A. Stokermans for help with multiphoton microscopy and analysis of the microscopy data; D. A. Turner for microscopy panels that were used for tomo-seq validation; J. Korving for help with the somite-size measurements in embryos; the Hubrecht FACS facility and R. van der Linden for FACS experiments; Single Cell Discoveries for 10x Genomics scRNA-seq; the Utrecht Sequencing facility for sequencing; and P. Zeller, H. Viñas Gaza, M. Vaninsberghe, V. Bhardwaj and all members of the van Oudenaarden, Sonnen and Martinez Arias laboratories for discussions.

Author contributions

S.C.v.d.B. and A.v.O. conceived and designed the project. S.C.v.d.B. and V.v.B. generated gastruloids, and S.C.v.d.B., M.B. and J.V. performed scRNA-seq experiments. Embedding of mouse gastruloids for tomo-seq was done by S.C.v.d.B. N.M. and P.B.-J. embedded mouse embryos for tomo-seq, with help from J.N. S.C.v.d.B. cryosectioned gastruloids and embryos, and performed tomo-seq experiments. J.V. developed the robotized tomo-seq protocol. A.A. performed the mapping and analysis, including comparisons with embryonic datasets, of the scRNA-seq and tomo-seq data. A.v.O. performed the linearized UMAP analysis. S.C.v.d.B., M.B., A.A., N.M. and A.M.A. interpreted the sequencing datasets. P.B.-J. performed the first Matrigel-embedding pilot experiments. V.v.B. performed time-lapse imaging experiments, in situ hybridization and HCR stainings, with help from S.C.v.d.B. and K.F.S. V.v.B. analysed the microscopy data, with support from K.F.S. V.v.B., S.C.v.d.B., A.v.O. and K.F.S. interpreted the imaging results. S.C.v.d.B., A.A., V.v.B. and A.v.O. wrote the manuscript with support from K.F.S. and A.M.A., and A.M.A. and A.v.O. guided the project.

Data availability

All RNA sequencing datasets produced in this study are deposited in the Gene Expression Omnibus (GEO) under accession code GSE123187. All scRNA-seq and tomo-seq data can be explored at <https://avolab.hubrecht.eu/MouseGastruloids2020>. Source Data for Figs. 1, 2 and Extended Data Fig. 1–6, 8, 10 are provided online at <https://bit.ly/3eyS6ZY>. Any other relevant data are available from the corresponding authors upon reasonable request.

Code availability

All code is available at https://github.com/anna-alemany/mouseGastruloids_scRNAseq_tomoseq and <https://github.com/vincentvbatenburg/MouseGastruloids>.

Supplementary Information for Chapter 3

Corresponding protocol publication

Generating gastruloids with somite-like structures from mouse embryonic stem cells. Vincent van Batenburg, Susanne C. van den Brink, Marloes Blotenburg, Anna Alemany, Naomi Moris, Peter Baillie-Johnson, Yasmine el Azhar, Katharina F. Sonnen, Alfonso Martinez Arias & Alexander van Oudenaarden. *Protocol Exchange*, doi: 10.21203/rs.2.18203/v1 (2020).

Supplementary Methods

Supplementary Methods 1-4 are available online at <https://bit.ly/3eyS6ZY>.

Supplementary Videos

Supplementary Videos 1-6 are available online at <https://bit.ly/3eyS6ZY>.

Supplementary Video 1 | Time-lapse imaging of LfngT2AVenus mouse gastruloids that are embedded in 100% Matrigel at 96 h. Gastruloids were mounted in 100% Matrigel at 96 h to stabilize them during imaging (Methods). Multi-photon imaging was started directly after embedding, and a z-stack was taken every 15 minutes for 17 hours. In red we show the summed projection of the fluorescence intensity (Methods). All images were rotated such that their AP axis is approximately oriented from left to right. Similar results obtained in $n = 9$ independent experiments. Scale bar, 200 μm .

Supplementary Video 2 | Time-lapse imaging of LfngT2AVenus mouse gastruloids treated with DMSO or DAPT. Gastruloids were mounted in 100% Matrigel at 96 h to stabilize them during imaging (Methods). Top row, DMSO treated control gastruloids; bottom row, gastruloids treated with the Notch-inhibitor DAPT (27 μM). DMSO/inhibitor was added at 97 h (Methods). Multi-photon imaging was started directly after embedding, and a z-stack was taken every 15 minutes for 16 hours. Red, summed projection of the fluorescence intensity (Methods). All images were rotated such that their AP axis is approximately oriented from left to right. Similar results obtained in $n = 5$ independent experiments. Scale bar, 200 μm .

Supplementary Video 3 | Time-lapse imaging of LfngT2AVenus mouse gastruloids treated with agonists or inhibitors of FGF, WNT and BMP signalling pathways. Gastruloids were mounted in 100% Matrigel at 96 h (Methods). DMSO (control), Chiron (CHI99021; WNT-agonist; 10 μM), FGF1 (0.02 $\mu\text{g}/\text{ml}$), FGF10 (0.2 $\mu\text{g}/\text{ml}$), IWP (IWP-2; WNT-antagonist; 2 μM), IWR (IWR-1; WNT-antagonist; 10 μM), LDN (LDN193189; BMP-inhibitor; 0.2 μM), or PD03 (PD0325901; MEK/ERK inhibitor; 13.3 μM) was added at 97 h (Methods). Imaging was started directly after embedding, and z-stacks were taken every 15 minutes for 17 hours. Red, summed intensity projection (Methods). All gastruloids were oriented with their AP axis approximately from left to right. Similar results obtained in $n = 2$ independent experiments.

Supplementary Video 4 | Time-lapse imaging of LfngT2AVenus mouse gastruloids treated with 1.3-66.7 μM PD03. Gastruloids were mounted in 100% Matrigel at 96 h to stabilize them during imaging (Methods). DMSO (control; top row) or PD03 (PD0325901; MEK/ERK (downstream of FGF signalling) inhibitor; concentrations between 1.3-66.7 μM as indicated in the video) was added at 97 h (Methods). Imaging was started directly after embedding, and a z-stack was taken every 15 minutes for 17 hours. Red, summed projection of the fluorescence intensity (Methods). All images were rotated such that their AP axis is approximately oriented from left to right. Similar results obtained in $n = 4$ independent experiments. Scale bar, 200 μm .

Supplementary Video 5 | Time-lapse imaging of LfngT2AVenus mouse gastruloids treated with DMSO, BGJ398 or PD17. Gastruloids were mounted in 100% Matrigel at 96 h to stabilize them during imaging (Methods). DMSO (control; top row), BGJ396 (FGF receptor inhibitor; 0.2 μM ; middle row) or PD17 (PD 173074; FGF receptor inhibitor; 0.5 μM ; bottom row) was added at 97 h (Methods). Imaging was started directly after embedding, and a z-stack was taken every 15 minutes for 17 hours. Red, summed projection of the fluorescence intensity (Methods). All images were rotated such that their AP axis is approximately oriented from left to right. Similar results obtained in $n = 2$ independent experiments. Scale bar, 200 μm .

Supplementary Video 6 | Time-lapse imaging of LfngT2AVenus mouse gastruloids that are embedded in 10% Matrigel at 96 h. Gastruloids were embedded in 10% Matrigel at 96 h (Methods). Multi-photon imaging was started

directly after embedding, and a z-stack was taken every 15 minutes for 20 hours. In red we show the summed projection of the fluorescence intensity (Methods). All images were rotated such that their AP axis is approximately oriented from left to right. Similar results obtained in $n = 2$ independent experiments. Scale bar, 200 μm .

Supplementary Tables

Supplementary tables 1-9 are available online at <https://bit.ly/3eyS6ZY>.

Supplementary Table 1 | Metadata for all the cells from the 120 h mouse gastruloid scRNA-seq dataset that passed our quality-control checks. Table provides UMAP coordinates obtained for the $n = 25,202$ cells isolated from 120 h gastruloids ($n = 26$ and 74 biologically independent gastruloids grown using E14-IB10 and LfngT2AVenus ESC lines, respectively, from $n = 6$ independent experiments). CellID, cell id; u1, UMAP coordinate 1; u2, UMAP coordinate 2; n_counts, number of unique reads detected in this cell; n_genes, number of genes detected in this cell. E14_sort corresponds to SORT-seq experiments performed on the E14-IB10 cell line; Lfng_sort corresponds to SORT-seq experiments performed on the LfngT2AVenus cell line; 10x correspond to 10x Genomics scRNA-seq experiments performed on the LfngT2AVenus cell line.

Supplementary Table 2 | Differentially expressed genes detected for each cluster of cells in scRNA-seq dataset of 120 h mouse gastruloids, determined using the two-side t-test and adjusted for multiple testing with Benjamini-Hochberg correction.

Supplementary Table 3 | The number of overlapping genes between significantly upregulated genes ($n = 79, 87, 84, 22, 84, 66, 82, 78, 100, 97, 100, 96, 90$ genes for clusters 1-13 in the gastruloid dataset, determined using the two-side t-test, followed by selection of genes with fold change above 1.01 and P value below 0.01; $n = 7, 20, 21, 35, 200, 39, 23, 200, 200, 95, 54, 21, 58, 57, 200, 81, 135, 28, 200, 200$ genes for the embryonic cell types reported in the x axis, determined in reference ⁴ and selecting genes with P value below 0.01) for each gastruloid cluster ($n = 25,202$ cells extracted from 100 biologically independent samples) and each E8.5 mouse embryonic cell type⁴. P value was determined by binomial testing, one-sided, no adjustments for multiple corrections were made. PS, Pijuan-Sala dataset⁴.

Supplementary Table 4 | Number of cells detected for each cluster in each experimental 120 h mouse gastruloid scRNA-seq batch. E14_sort corresponds to SORT-seq experiments performed on the E14-IB10 cell line; Lfng_sort corresponds to SORT-seq experiments performed on the LfngT2AVenus cell line; Lfng_10x correspond to 10x Genomics scRNA-seq experiments performed on the LfngT2AVenus cell line.

Supplementary Table 5 | For each gene, the Pearson correlation value of the expression profiles detected in each pair-wise comparison of the different replicates is provided for all the tomo-seq experiments performed with E14-IB10 and LfngT2AVenus gastruloids ($n = 5$ and $n = 3$ biological replicates, respectively) and with E8.5 mouse embryos ($n = 3$ biological replicates). Additionally, the same analysis is performed on the posterior mesoderm ($n = 3$ biological replicates, tail bud to newly formed somite; previously published microarray data¹²). Corr(x,x) refers to the correlation value between expression patterns of a gene in the two replicates that are being compared in each case. P values and adjusted P values have been obtained as described in the Methods.

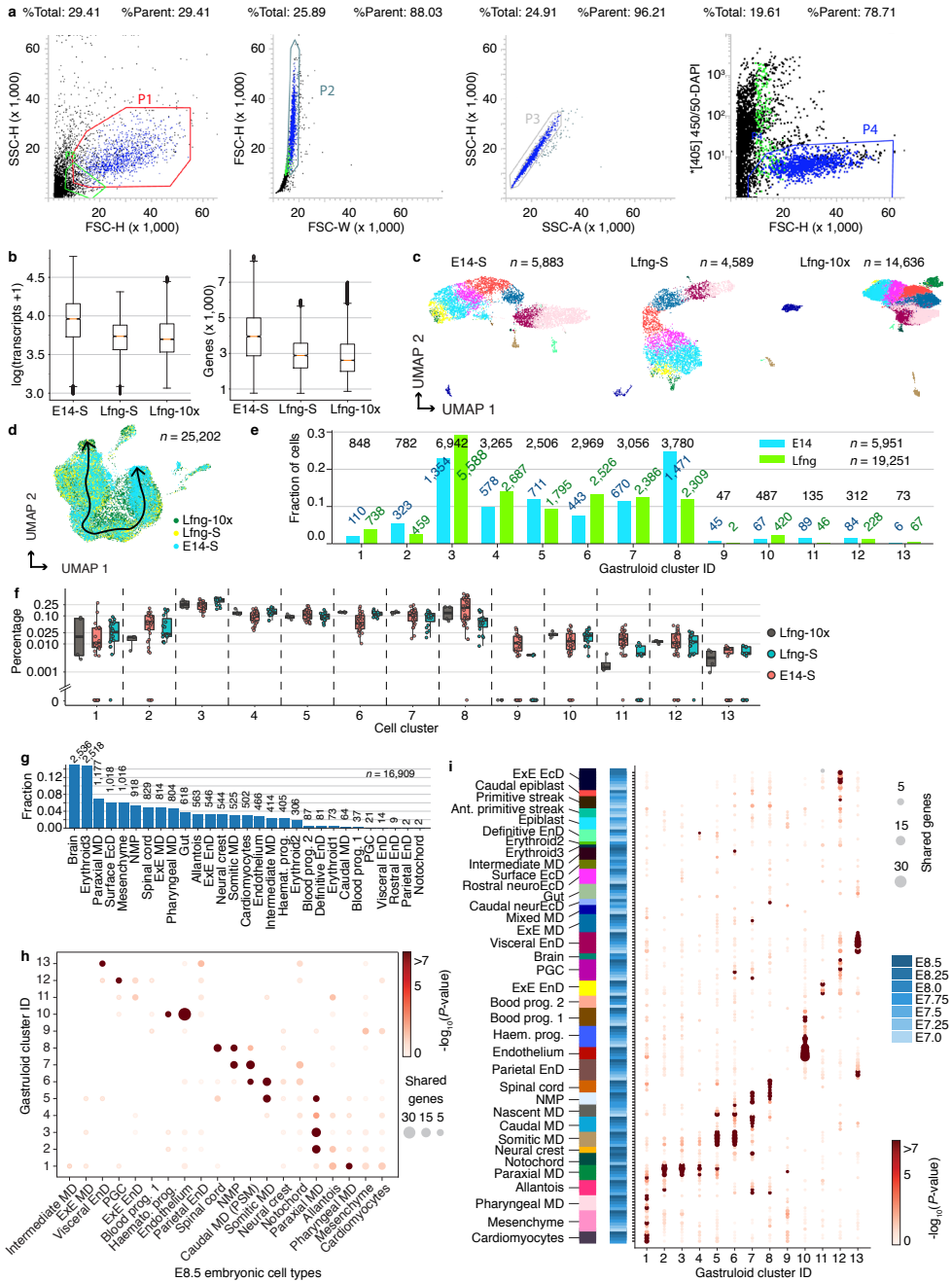
Supplementary Table 6 | Clusters found for reproducible genes identified in E14-IB10 and LfngT2AVenus gastruloid tomo-seq data, E8.5 mouse embryos tomo-seq data, and posterior mesoderm of E9.5 mouse embryo (tail bud to newly formed somite; previously published microarray data¹²) (Methods, Extended Data Fig. 4).

Supplementary Table 7 | Clusters found for the comparison between gene expression patterns of the E14-IB10 ($n = 5$ biological replicates) and LfngT2AVenus gastruloids ($n = 3$ biological replicates), the E14-IB10 and LfngT2AVenus gastruloids and the E8.5 mouse embryos ($n = 3$ biological replicates), and the E14-IB10 and LfngT2AVenus gastruloids and the posterior mesoderm of E9.5 embryos ($n = 3$ biological replicates; tail bud to newly formed somite; previously published microarray data¹²) (Methods). Gene selection here took the genes that are reproducible in both of the systems that are being compared. This table is associated with Fig. 1b, d, and e.

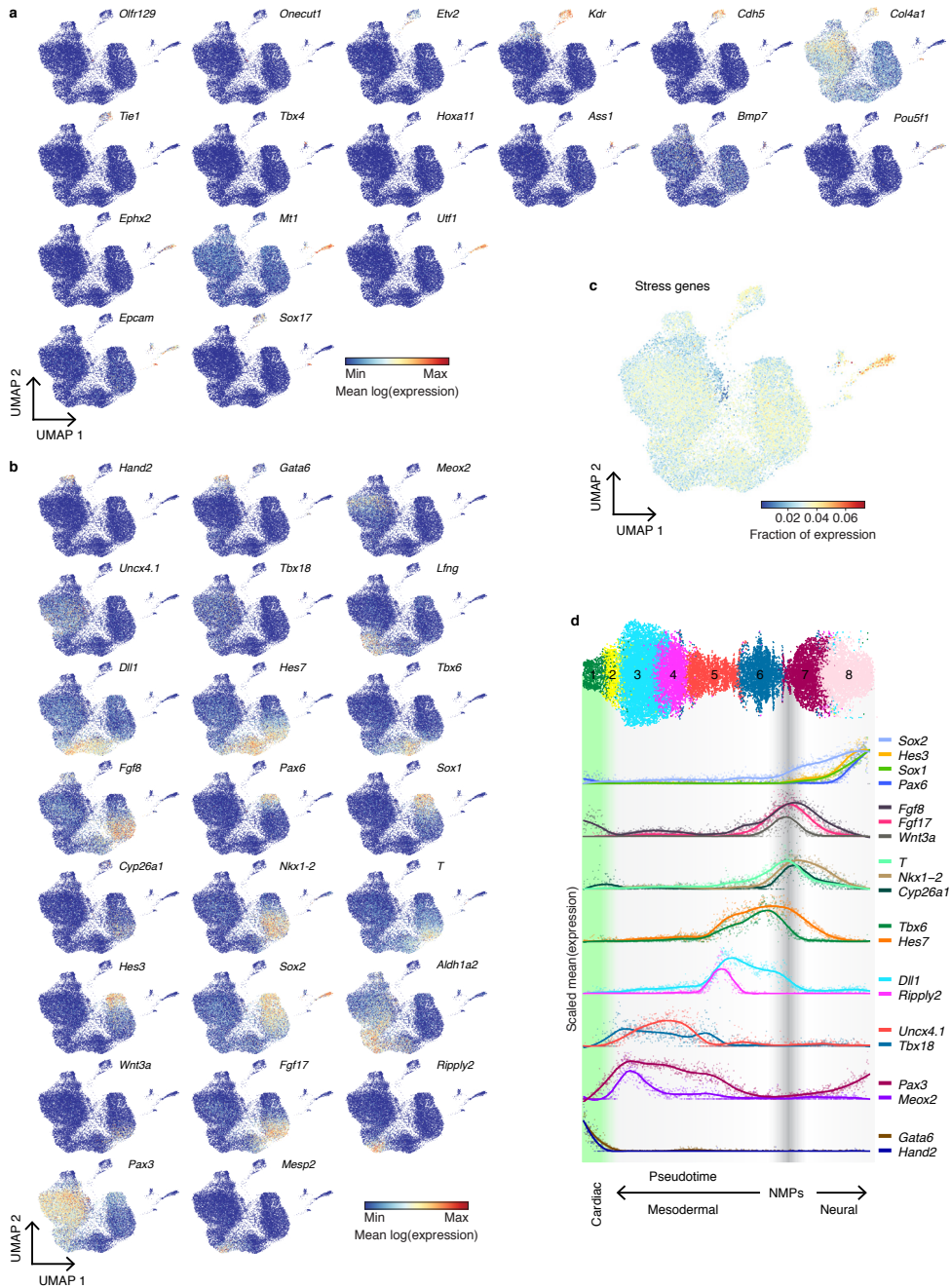
Supplementary Table 8 | Clusters found for the comparison between gene expression patterns of the E14-IB10 ($n = 5$ biological replicates) and LfngT2AVenus gastruloids ($n = 3$ biological replicates), the E14-IB10 and LfngT2AVenus gastruloids and the E8.5 mouse embryos ($n = 3$ biological replicates), and the E14-IB10 and LfngT2AVenus gastruloids and the posterior mesoderm of a E9.5 embryo ($n = 3$ biological replicates; tail bud to newly formed somite; previously published microarray data¹²; Methods, Extended Data Fig. 5). Gene selection here took the union of genes that are reproducible in at least one of the systems that are being compared. This table is associated with Extended Data Fig. 5.

Supplementary Table 9 | Number of replicates, number of genes detected and number of reproducible genes found in the different tomo-seq experiments ($n = 5$ biological replicates of E14-IB10 gastruloids, $n = 3$ biological replicates of LfngT2AVenus gastruloids and $n = 3$ biological replicates of E8.5 mouse embryos) and in the posterior mesoderm of E9.5 mouse embryo ($n = 3$ biological replicates; tail bud to newly formed somite; previously published microarray data¹²); number of genes being simultaneously reproducible in different tomo-seq experiments (labelled as intersection), and number of genes that are reproducible in at least one of the tomo-seq experiments being compared (labelled as union) between E14-IB10 and LfngT2AVenus gastruloids, between E14-IB10 gastruloids, LfngT2AVenus gastruloids and E8.5 mouse embryos, and between E14-IB10 gastruloids, LfngT2AVenus gastruloids and the posterior mesoderm of E9.5 mouse embryo¹². This table explains how gene selection was performed in Supplementary Tables 6-8, Fig. 1b, d, and e, and Extended Data Figs. 4-5.

Supplementary Fig. 1 | scRNA-seq on 120-h mouse gastruloids and comparison to embryos. **a**, FACS gating strategy before scRNA-seq. Live cells were selected on the basis of DAPI staining. Four sequential gates (P1–P4) were used; cells from gate P4 were used for scRNA-seq. SSC, side scatter; FSC, forward scatter; H, height; W, width; A, area. **b**, Box plot showing the median number of transcripts (left) and genes (right) detected per cell for SORT-seq experiments on E14-IB10 (E14-S, $n = 5,951$ cells from 26 biologically independent samples) and LfngT2AVenus gastruloids (Lfng-S, $n = 4,592$ cells from 74 biologically independent samples), and for 10x Genomics experiments on LfngT2AVenus gastruloids (Lfng-10x, $n = 14,659$ cells from 74 biologically independent samples). SORT-seq and 10x Genomics analyses were performed in parallel on the same 74 biologically independent LfngT2AVenus gastruloids; all cells extracted from these gastruloids were pooled and split into two tubes, of which one was used for SORT-seq and the other for 10x Genomics. The box extends from the lower to the upper quartile; whiskers are 1.5x the interquartile range; flier points are those past the end of the whiskers. **c**, UMAP plot for each experiment separately ($n = 5,883$, 4,589 and 14,636 cells for E14-S, Lfng-S and Lfng-10x, respectively; Methods). The E14-S cells ($n = 5,883$) were extracted from $n = 26$ biologically independent samples; the Lfng-S and Lfng-10x cells ($n = 4,589$ and 14,636, respectively) were extracted from $n = 74$ biologically independent samples that were pooled and then split into one tube for SORT-seq and one tube for 10x Genomics. The colour of each cell is the same as the colour of that particular cell in Fig. 1a. **d**, UMAP plot obtained by analysing all the cells from the different experiments together ($n = 25,202$ cells from 100 biologically independent samples), in which cells are coloured according to their batch (Methods, Supplementary Table 1). The black line indicates the symmetry line in clusters 1–8 used to generate the linearized UMAP plot in Supplementary Fig. 2d (Methods). **e**, Fraction of E14-IB10 ($n = 26$ biologically independent samples) and LfngT2AVenus ($n = 74$ biologically independent samples) cells in each scRNA-seq cluster from Fig. 1a. Blue, green and black numbers, number of E14-IB10, LfngT2AVenus and total cells in each cluster, respectively (Supplementary Tables 1, 4). **f**, Fraction of cells for each cell type in each plate in SORT-seq experiments (Lfng-S, $n = 19$ plates containing cells from $n = 74$ biologically independent gastruloids; E14-S, $n = 30$ plates containing cells from $n = 26$ biologically independent gastruloids), and in each experimental batch in 10x Genomics experiments (Lfng-10x, $n = 2$ independent batches containing cells extracted from $n = 44$ and 30 biologically independent gastruloids, respectively, with 2 technical replicates each). In the box plots, centre line is median; box limits are the 1st and 3rd quartiles; and whiskers denote the range. **g**, Fraction of cells detected in the E8.5 mouse embryo scRNA-seq dataset⁴ with which we compared our gastruloid scRNA-seq data. Exact numbers in each cluster are indicated. **h**, Dot plot showing the number of overlapping genes between significantly upregulated genes ($n = 79, 87, 84, 22, 84, 66, 82, 78, 100, 97, 100, 96$ and 90 genes for clusters 1, 2, 3, 4, 5, 6, 7, 8, 9, 10, 11, 12 and 13 (respectively) in the gastruloid dataset, determined using the two-side *t*-test, followed by selection of genes with fold change above 1.01 and *P* value below 0.01; $n = 7, 20, 21, 35, 200, 39, 23, 200, 200, 95, 54, 21, 58, 57, 200, 81, 135, 28, 200$ and 200 genes for the embryonic-cell types reported in the *x* axis, determined in ref. ⁴ and selecting genes with *P* value below 0.01) for each gastruloid cluster ($n = 25,202$ cells extracted from 100 biologically independent samples) and each E8.5 mouse embryonic-cell type⁴. Dot colour indicates the probability of finding such a number of overlapping genes between the two sets by random chance (*P* value determined by binomial testing, one-sided, no adjustments for multiple corrections were made). Dot size represents the number of overlapping genes. **i**, Dot plot showing overlapping genes between significantly upregulated genes for each gastruloid scRNA-seq cluster ($n = 79, 87, 84, 22, 84, 66, 82, 78, 100, 97, 100, 96$ and 90 genes for clusters 1, 2, 3, 4, 5, 6, 7, 8, 9, 10, 11, 12 and 13, respectively (Supplementary Table 2); scRNA-seq dataset obtained for 25,202 cells that were extracted from $n = 100$ biologically independent gastruloids), and upregulated genes for each E7.0–E8.5 mouse embryonic-cell type⁴. Dot colour indicates the probability of finding such a number of overlapping genes between the two sets by random chance (*P* value determined by binomial testing, one-sided, no adjustments for multiple corrections were made), and dot size represents the number of overlapping genes. Blue, embryonic stage. 10x, 10x Genomics; Ant, anterior; EnD, endoderm; haemato, haemato-endothelial; prog, progenitors; S, SORT-seq³³.

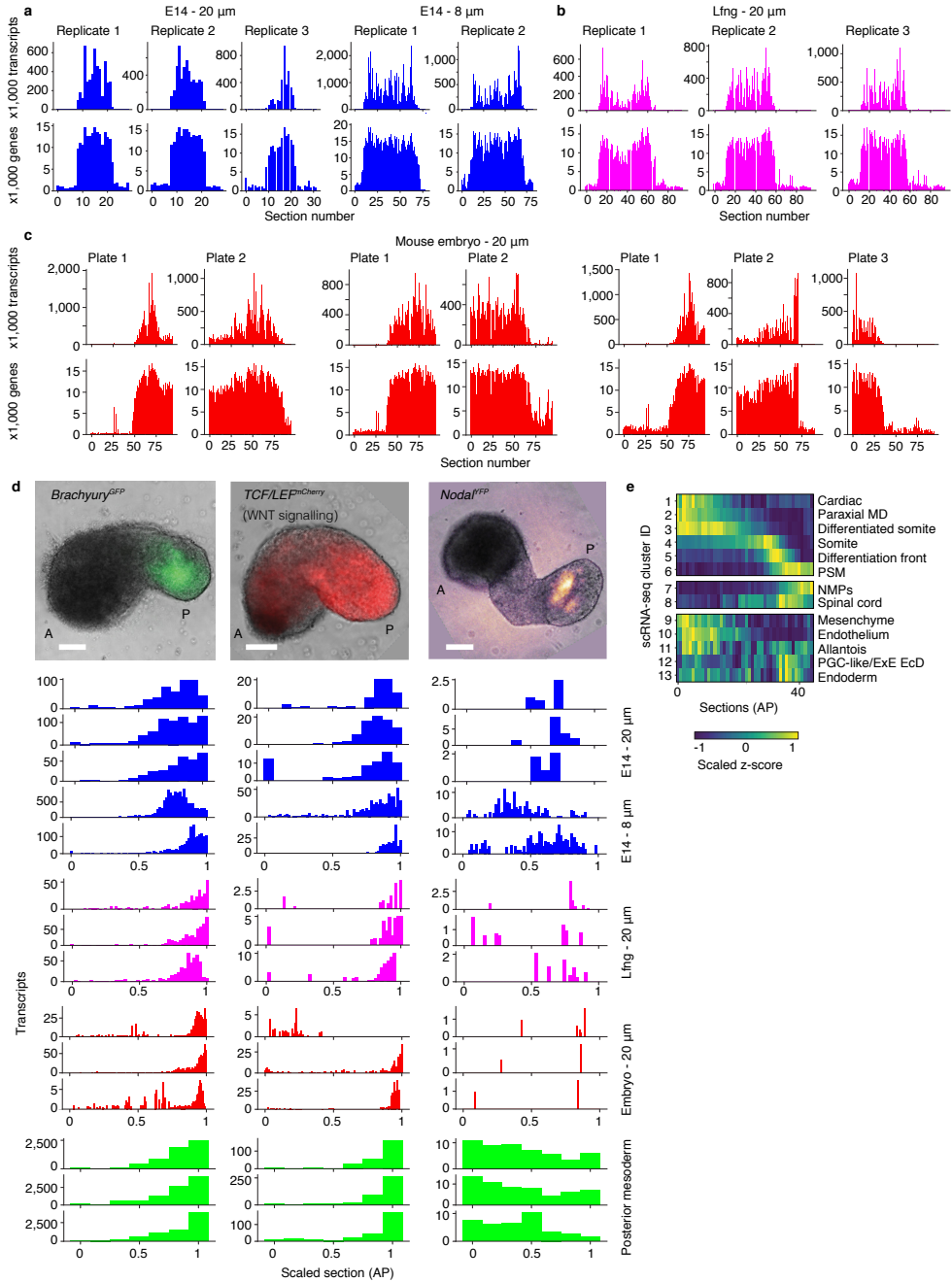


Supplementary Fig. 1 | See previous page for caption.



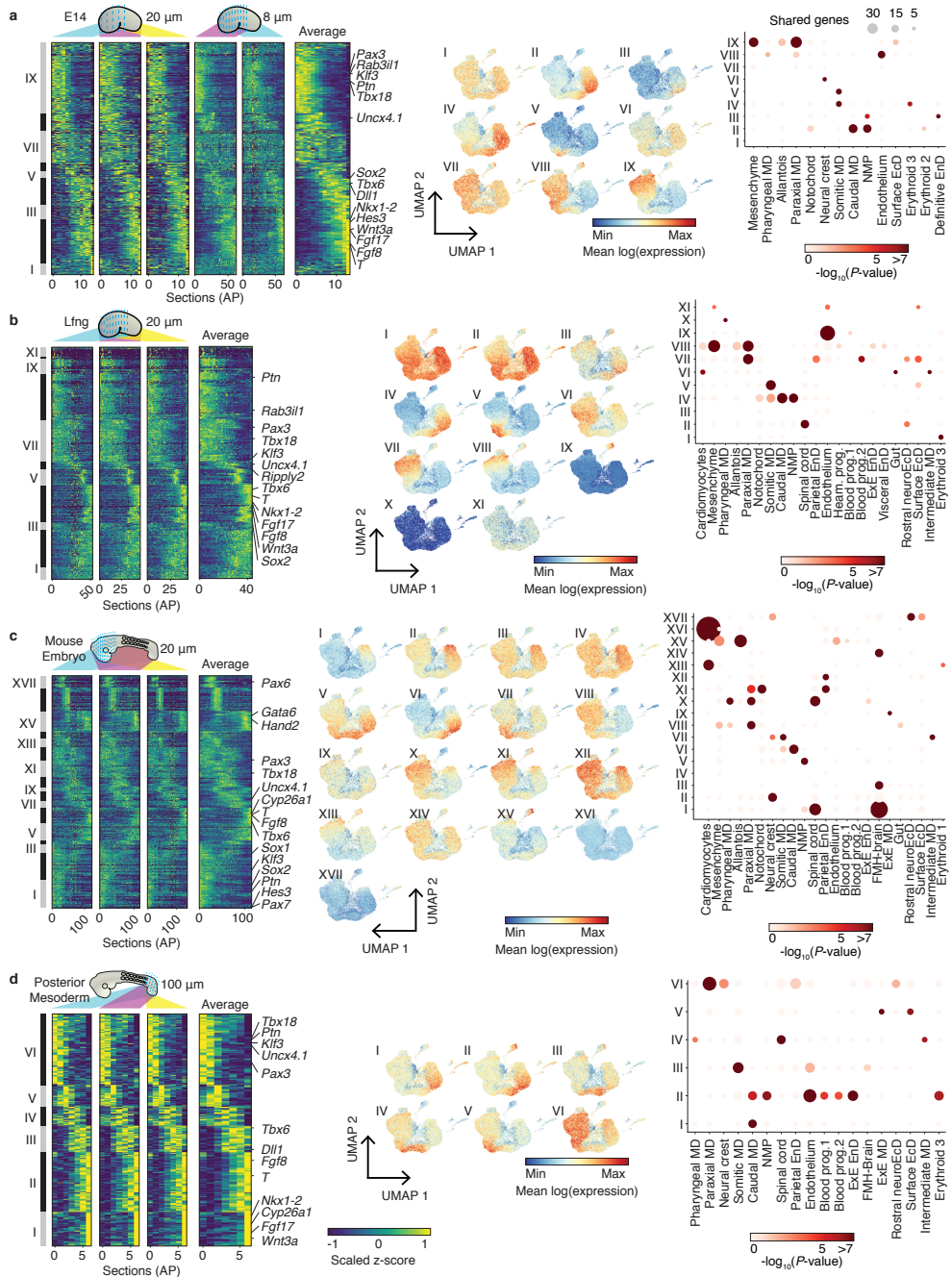
Supplementary Fig. 2 | See next page for caption.

Supplementary Fig. 2 | Expression of relevant markers in the gastruloid scRNA-seq dataset. **a**, Mean log expression of relevant markers of outlier populations (clusters 9–13) plotted on the UMAP plot from Fig. 1a. *Olfm129* and *Onecut1*, head mesenchyme (cluster 9); *Etv2*, haemato-endothelial progenitors (bottom part of cluster 10); *Kdr*, haemato-endothelial progenitors and endothelium (cluster 10); *Cdh5* and *Tie1*, endothelium (top part of cluster 10); *Tbx4*, *Hoxa11*, *Ass1* and *Bmp7*, allantois (cluster 11); *Ephx2*, *Mt1*, *Utf1* and *Pou5f1*, primordial-germ-cell-like or extra-embryonic ectoderm (cluster 12); *Col4a1*, *Epcam* and *Sox17*, endoderm (cluster 13). **b**, Mean log normalized expression of relevant markers of clusters 1–8 plotted on the UMAP plot from Fig. 1a. *Hand2* and *Gata6*, heart (cluster 1); *Meox2* and *Pax3*, differentiated somite (cluster 3); *Aldh1a2* and *Uncx4.1*, somite (cluster 4); *Lfng*, *Mesp2*, *Ripply2* and *Dll1*, differentiation front (cluster 5); *Hes7* and *Tbx6*, presomitic mesoderm (cluster 6); *Wnt3a*, *Fgf17*, *Fgf8*, *Cyp26a1*, *Nkx1-2* and *T*, tail bud containing neuromesodermal progenitors (cluster 7); *Pax6*, *Sox1*, *Hes3* and *Sox2*, differentiated neural cells (spinal cord; cluster 8). Expression was first count-normalized to 10,000 for each cell (Methods), and then log-transformed. Additional markers of all clusters are provided in Supplementary Table 2. **c**, Percentage of total unique transcripts per cell corresponding to stress genes⁴² plotted on the UMAP plot from Fig. 1a. **d**, Linearized UMAP plot of clusters 1–8 (top, $n = 24,148$ cells, isolated from 100 biologically independent gastruloids during $n = 6$ independent experiments) and expression profiles of genes related to neural and mesodermal differentiation^{8,9} (bottom). Green and grey shades indicate location of cardiac cells and neuromesodermal progenitors, respectively. The position of each cell along the x-axis relates to its differentiated state towards a neural or mesodermal fate.



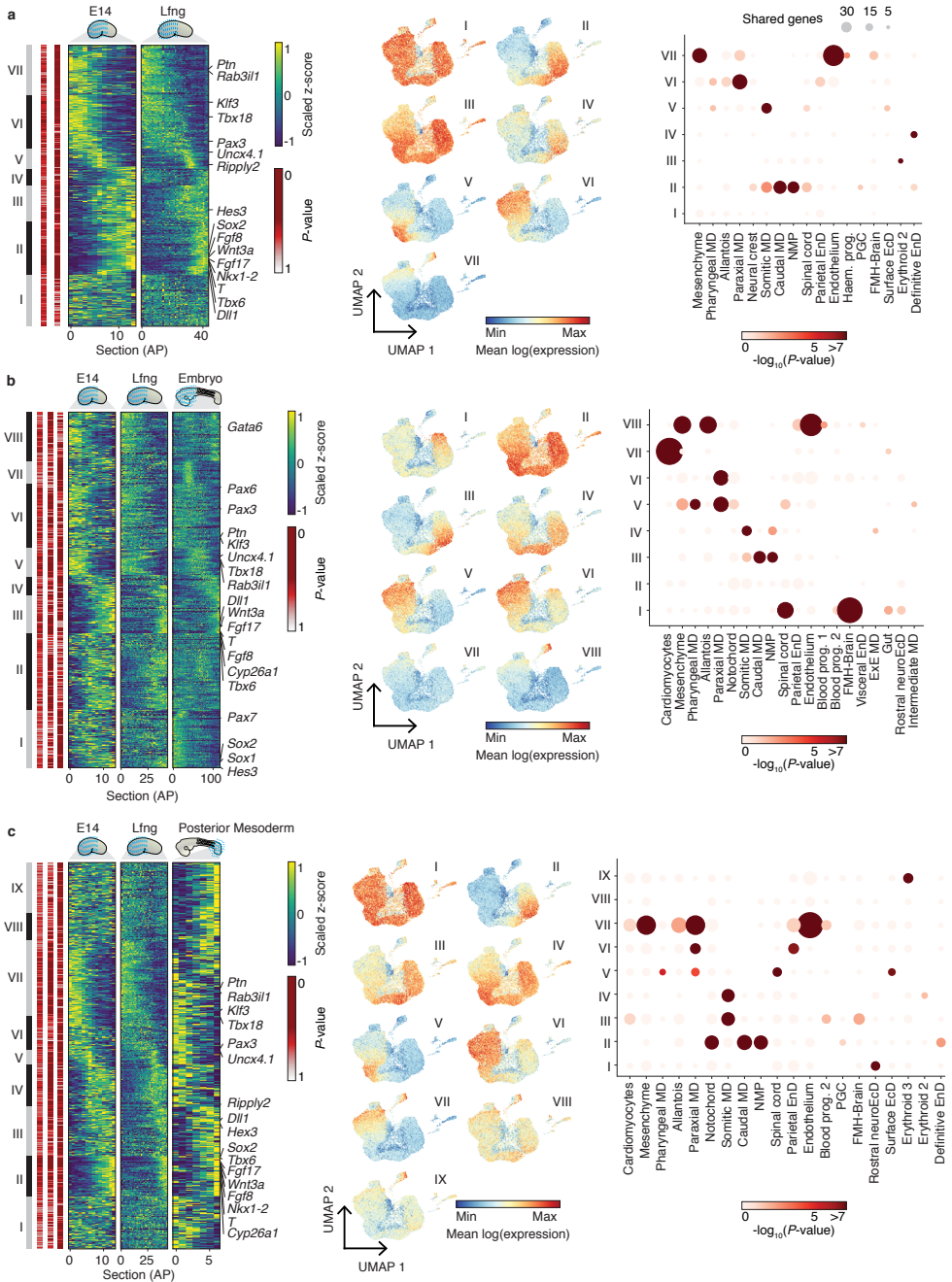
Supplementary Fig. 3 | See next page for caption.

Supplementary Fig. 3 | The number of genes and reads in gastruloid and embryo tomo-seq datasets, and comparison to microscopy data. a–c, Number of unique transcripts and genes detected in 3 E14-IB10 120-h mouse gastruloids that were sectioned using 20- μm sections and 2 E14-IB10 120-h mouse gastruloids that were sectioned using 8- μm sections (a); in 3 LfngT2AVenus 120-h mouse gastruloids that were sectioned using 20- μm sections (b); and in 3 E8.5 mouse embryos that were sectioned using 20- μm sections (c). Owing to their lengths, embryo sections were collected in 2 or 3 sequential 96-well plates. d, Validation of tomo-seq data with microscopy. Top panels, *Brachyury-GFP*, WNT signalling activity (as reported using a TCF/LEF-*mCherry* mouse ES cell line) and *Nodal-YFP* expression in 120-h mouse gastruloids as measured by microscopy (Methods). With each reporter line, we obtained similar results in $n = 5$ independent experiments. Bar plots show the normalized expression levels of *Brachyury*, *Wnt3a* and *Nodal* in 120-h E14-IB10 gastruloids, 120-h LfngT2AVenus gastruloids and E8.5 mouse embryos as determined by tomo-seq (Methods), and in the posterior mesoderm of E9.5 mouse embryos as determined by microarray¹². e, Scaled average z-score of significantly upregulated genes (P value < 0.01 and \log_2 -transformed fold change > 1.01) detected in each single-cell cluster from Fig. 1a (Supplementary Table 2) as measured in the averaged LfngT2AVenus tomo-seq gastruloid. Scale bar, 100 μm .



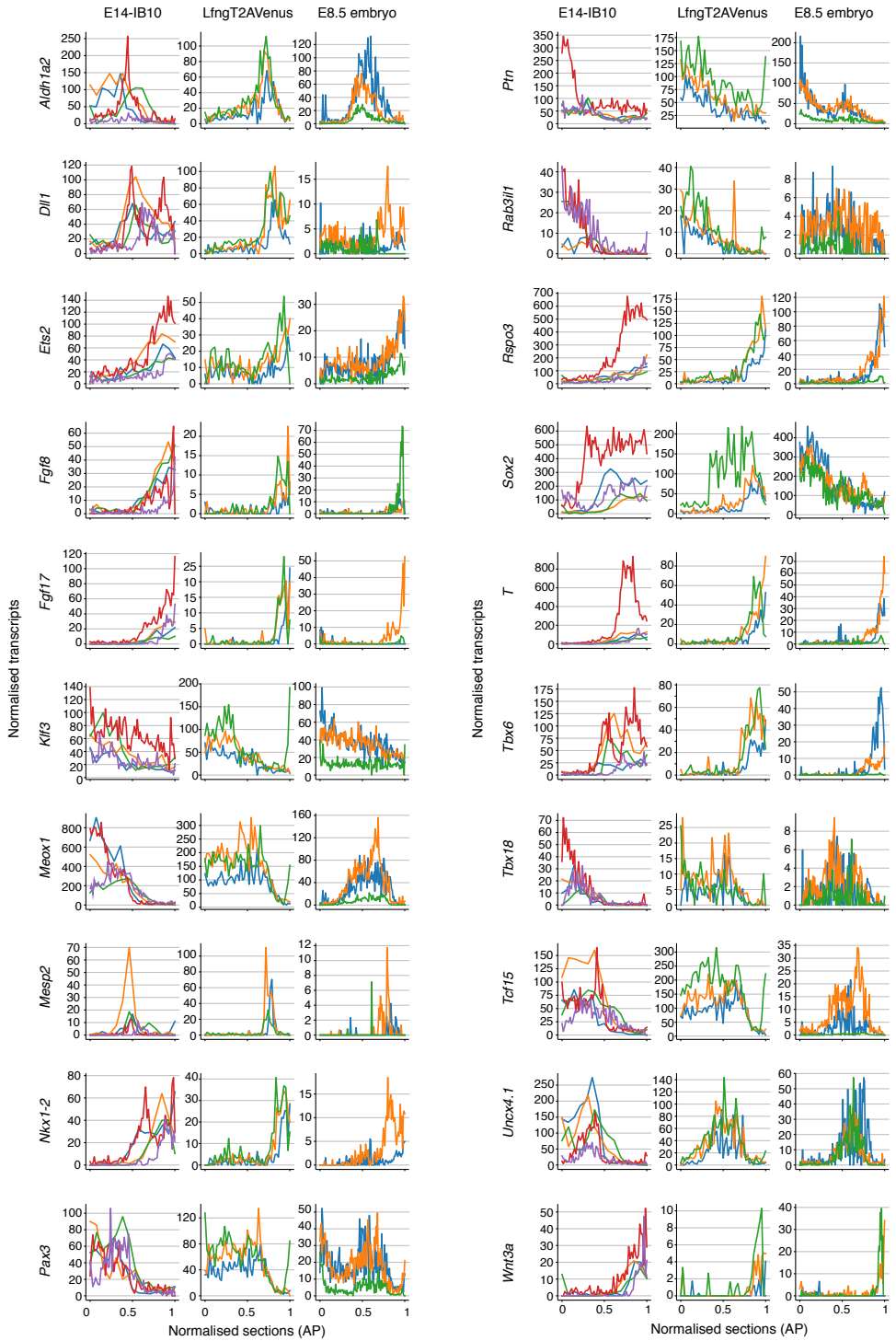
Supplementary Fig. 4 | See next page for caption.

Supplementary Fig. 4 | Individual replicates of gastruloids, E8.5 embryo tomo-seq and E9.5 posterior mesoderm datasets, and comparison to gastruloid and E8.5 embryonic scRNA-seq datasets. **a**, Heat maps showing the anterior–posterior expression patterns of 1,199 genes as detected by tomo-seq¹¹ in individual replicates of 120-h E14-IB10 gastruloids ($n = 3$ gastruloids, 20- μm sections and $n = 2$ gastruloids, 8- μm sections) that were cultured in standard^{1,20} (non-Matrigel-based) conditions; average heat map of the five replicates; average expression of genes found in each tomo-seq domain in the E14-IB10 tomo-seq dataset, projected in the UMAP plot from Fig. 1a; dot plot showing overlapping genes between genes detected in each tomo-seq domain in the E14-IB10 tomo-seq dataset, and upregulated genes for each E8.5 mouse embryonic-cell type⁴. Dot colour represents the probability of finding such a number of overlapping genes between the two sets by random chance (Methods), and dot size represents the number of overlapping genes. Only genes that were reproducible between replicates are shown (Methods). Genes are clustered on the basis of their anterior–posterior expression pattern (Methods); bars marked with Roman numerals represent tomo-seq clusters. Clusters I, II, III, IV, V, VI, VII, VIII and IX contain $n = 58, 231, 72, 138, 38, 43, 165, 90$ and 364 genes, respectively. **b**, Similar to **a**, but for 1,456 genes in 120-h LfngT2AVenus¹⁵ ($n = 3$ gastruloids, 20- μm sections) gastruloids that were cultured in standard^{1,20} (non-Matrigel-based) conditions. Clusters I, II, III, IV, V, VI, VII, VIII, IX, X and XI contain $n = 74, 235, 47, 235, 99, 47, 264, 287, 99, 14$ and 55 genes, respectively. **c**, Similar to **a**, but for 1,553 genes in E8.5 embryos ($n = 3$ embryos, 20- μm sections). Clusters I, II, III, IV, V, VI, VII, VIII, IX, X, XI, XII, XIII, XIV, XV, XVI, XVII, XVIII and XIX contain $n = 186, 179, 63, 25, 114, 103, 48, 65, 28, 65, 111, 89, 61, 44, 134, 155, 79, 2$ and 2 genes, respectively. **d**, Similar to **a**, but for 1,989 genes in an E9.5 mouse embryo posterior-mesoderm dataset (tail bud to newly formed somite) ($n = 3$ embryos; previously published microarray data; approximately 100- μm sections¹²). Clusters I, II, III, IV, V and VI contain $n = 294, 512, 226, 165, 181$ and 611 genes, respectively. All genes are shown in Supplementary Table 6. AP, anterior–posterior; FMH, fore-, mid- and hind-.



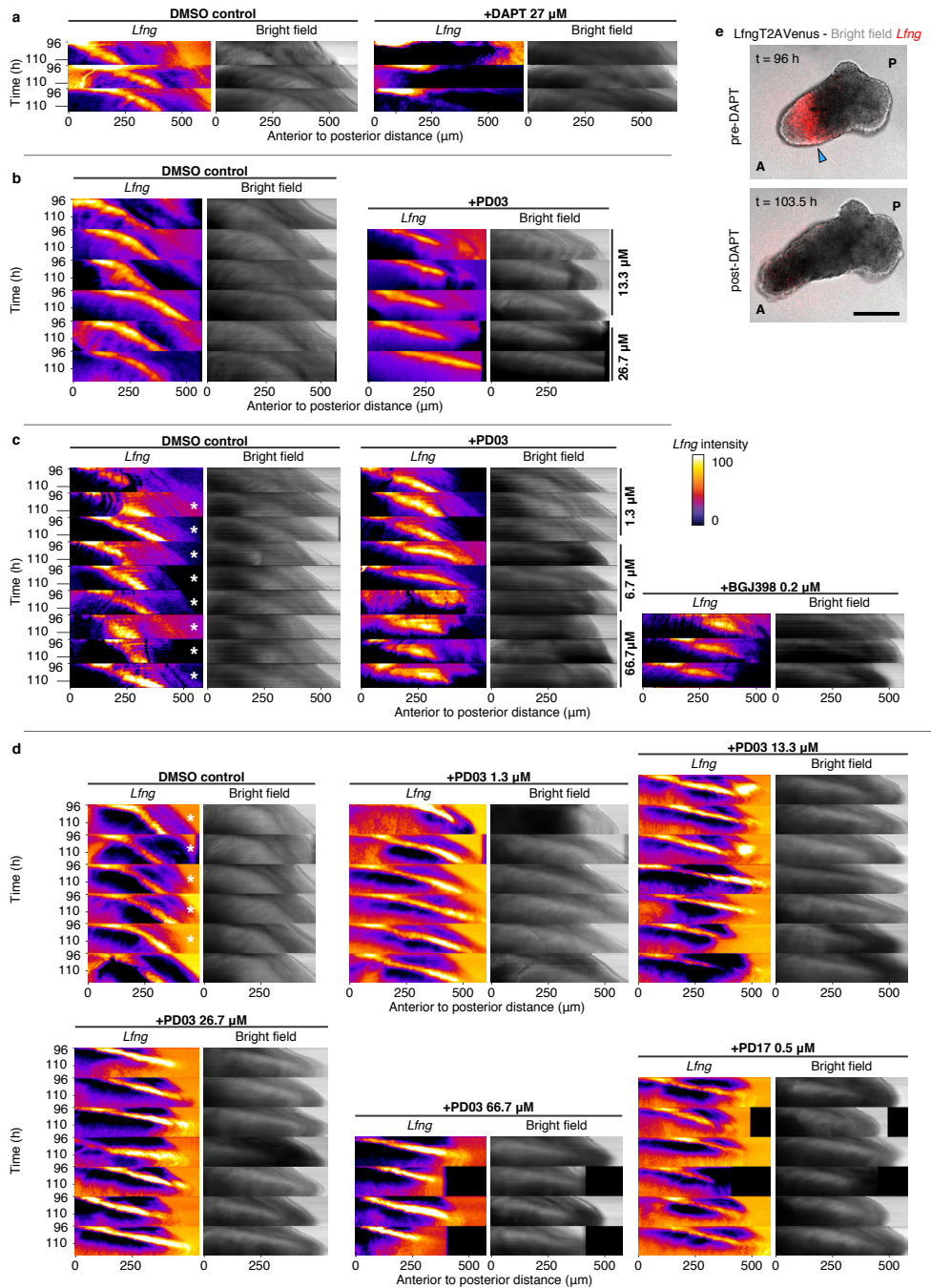
Supplementary Fig. 5 | See next page for caption.

Supplementary Fig. 5 | Comparisons between mouse gastruloid and mouse embryo datasets, including genes that are reproducible in at least one system. **a**, Heat map showing the average anterior–posterior expression pattern of 2,065 genes as detected by tomo-seq¹¹ in 120-h mouse gastruloids that were generated from E14-IB10 and LfngT2AVenus¹⁵ mouse ES cells and that were cultured in standard^{1,20} (non-Matrigel-based) conditions; average expression of genes found in each tomo-seq domain in the E14-IB10– LfngT2AVenus comparison heat map, projected in the UMAP plot from Fig. 1a; dot plot showing overlapping genes between genes detected in each tomo-seq domain in **a**, and upregulated genes for E8.5 mouse embryonic-cell types⁴. Dot colour represents the probability of finding such a number of overlapping genes by random chance (Methods), and dot size represents the number of overlapping genes. In contrast to the heat maps in Fig. 1, this heat map contains genes that were reproducible in either E14-IB10 ($n = 3$ biologically independent gastruloids, 20- μm sections and $n = 2$ biologically independent gastruloids, 8- μm sections) or LfngT2AVenus ($n = 3$ biologically independent gastruloids, 20- μm sections) gastruloids (Supplementary Fig. 4, Methods, Supplementary Tables 5, 6). This means that genes that are reproducible in E14-IB10 replicates but not in LfngT2AVenus replicates—and vice versa—are included. Genes are clustered on the basis of their anterior–posterior expression pattern (Methods); bars marked by Roman numerals represent tomo-seq clusters, which are also indicated with the grey–black bar plot. The red-to-white bar plots indicate the P value of reproducibility of each gene in each heat map. The order of these bar plots corresponds to the order of the heat maps. Clusters I, II, III, IV, V, VI and VII contain $n = 377, 398, 259, 124, 145, 395$ and 367 genes, respectively. **b**, Similar to **a**, but for 2,894 genes that were reproducible in E14-IB10 ($n = 3$ gastruloids, 20- μm sections and $n = 2$ gastruloids, 8- μm sections) or LfngT2AVenus ($n = 3$ gastruloids, 20- μm sections) or E8.5 mouse embryos ($n = 3$ embryos, 20- μm sections). Clusters I, II, III, IV, V, VI, VII and VIII contain $n = 477, 618, 302, 161, 230, 527, 179$ and 400 genes, respectively. **c**, Similar to **a**, but for 3,086 genes that were reproducible in E14-IB10 ($n = 3$ gastruloids, 20- μm sections and $n = 2$ gastruloids, 8- μm sections) or LfngT2AVenus ($n = 3$ gastruloids, 20- μm sections) or the E9.5 mouse embryo posterior-mesoderm dataset (tail bud to newly formed somite) ($n = 3$ embryos; previously published microarray data; approximately 100- μm sections¹²). Clusters I, II, III, IV, V, VI, VII, VIII and IX contain 419, 325, 392, 337, 114, 279, 602, 220 and 398 genes, respectively. Gene lists are provided in Supplementary Table 8.



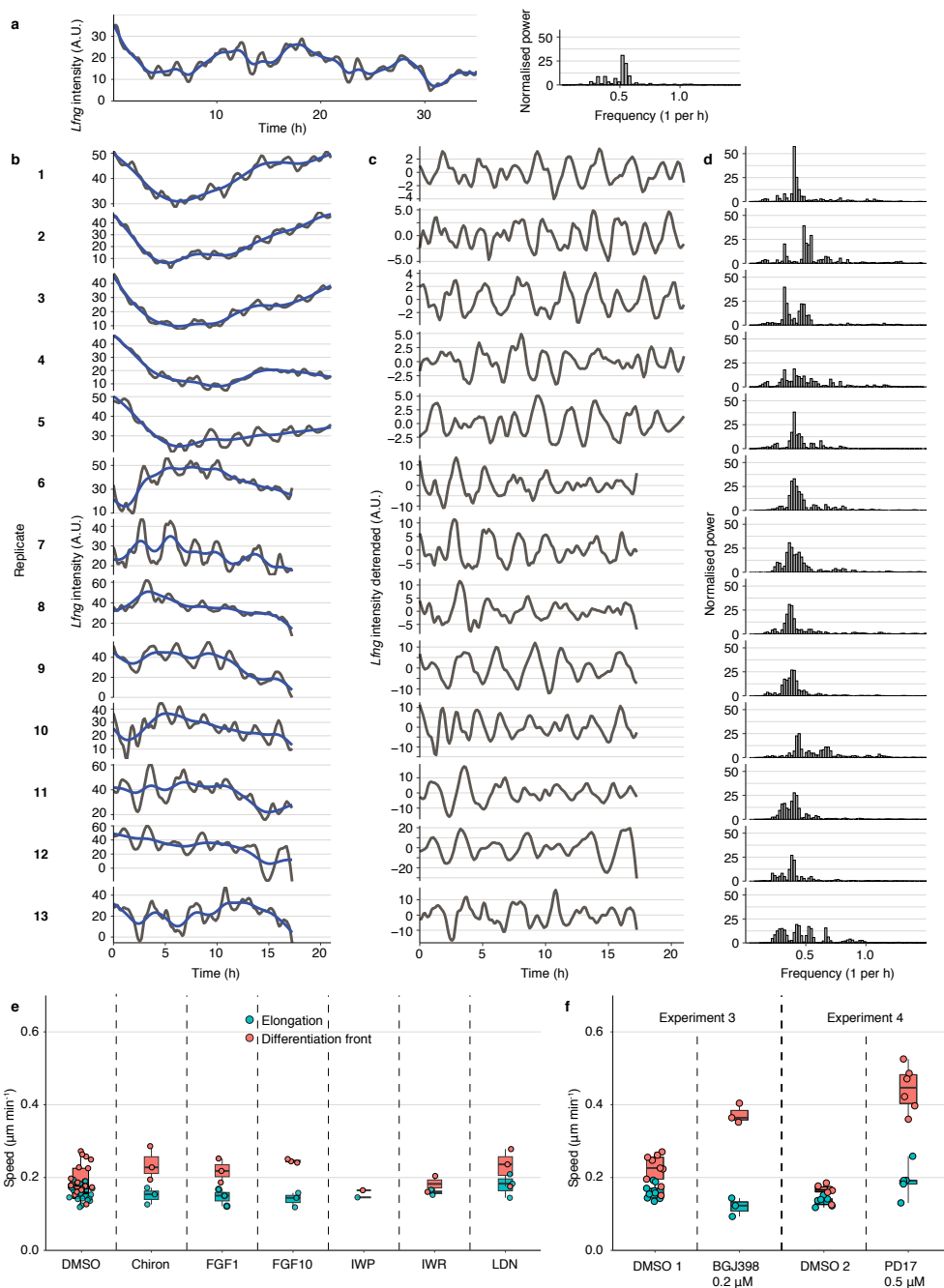
Supplementary Fig. 6 | See next page for caption.

Supplementary Fig. 6 | Gene-expression profiles in gastruloid and embryo tomo-seq datasets. Line plots for the normalized anterior–posterior expression of genes emphasized in Fig. 1b, d, e for the E14-IB10 and LfngT2AVenus gastruloids, and for the E8.5 mouse embryo, as measured by tomo-seq¹¹. Each colour denotes a different replicate.



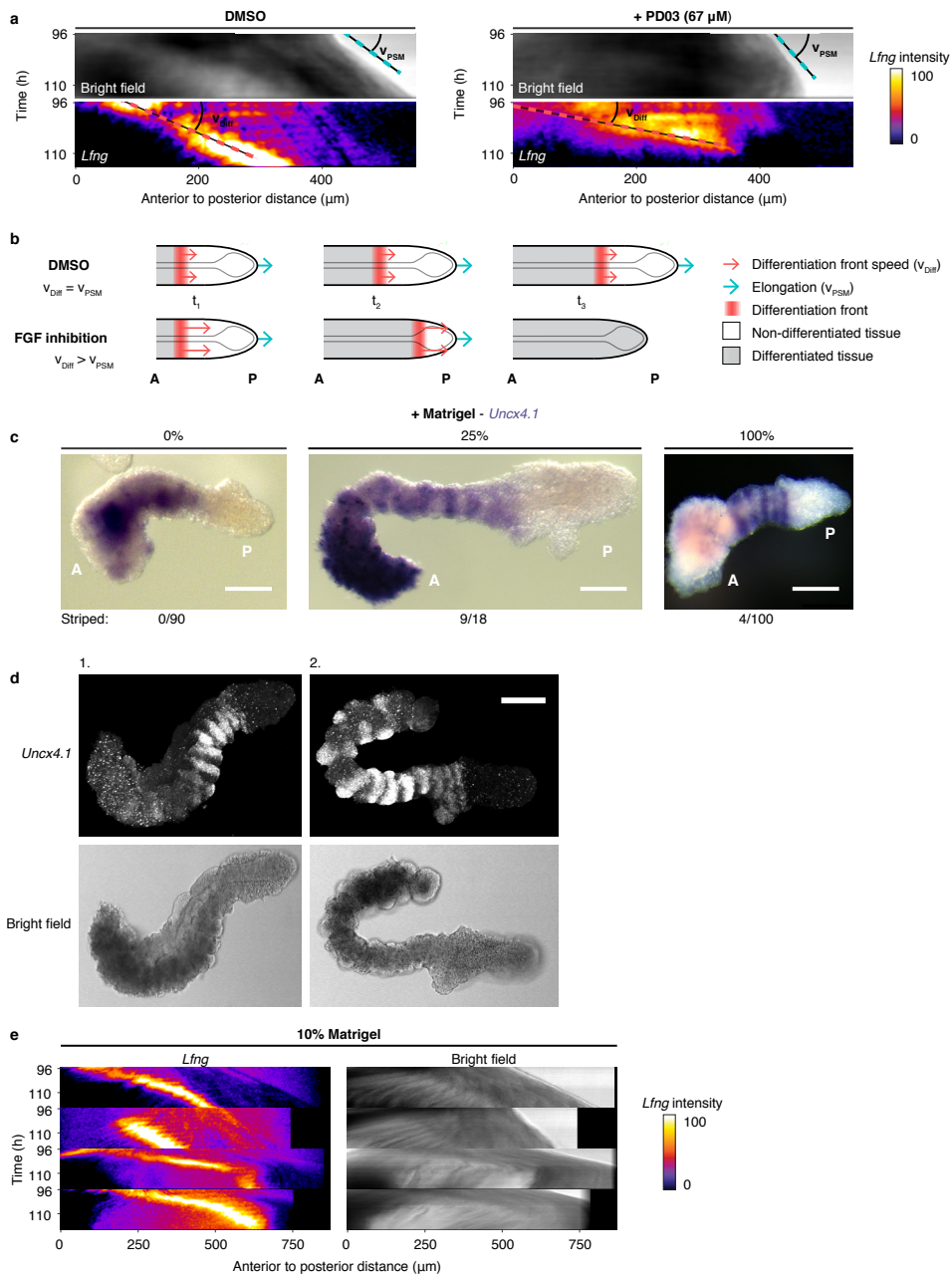
Supplementary Fig. 7 | See next page for caption.

Supplementary Fig. 7 | Kymographs of time-lapse experiments performed on *LfngT2AVenus* gastruloids that were embedded in 100% Matrigel at 96 h. a–d, Kymographs (space–time plots) of bright field channel and *LfngT2AVenus* signal along the anterior–posterior axis of all replicates from all time-lapse experiments (experiments 1–4) that are presented in Fig. 2e, Supplementary Fig. 8e, f. These gastruloids were embedded in 100% Matrigel (Methods) to stabilize them during imaging, and subsequently imaged for at least 17 h (Supplementary Videos 1, 2, 4, 5). Inhibitors were added at the start of the time lapse (Methods) and are indicated above the kymographs, together with their concentration. Asterisks refer to gastruloids used to generate Fig. 2e, Supplementary Fig. 8b–d. Similar results were obtained in $n = 5$ and 4 independent experiments for a and b–d, respectively. e, Imaging of a *LfngT2AVenus* gastruloid that was embedded in 100% Matrigel at 96 h, and to which the Notch inhibitor DAPT was added at 96.5 h (Supplementary Video 2); the *Lfng* signal disappears about 6 h after addition of DAPT. Corresponding kymographs in a. Similar results were obtained in $n = 5$ independent experiments. Scale bar, 200 μm .



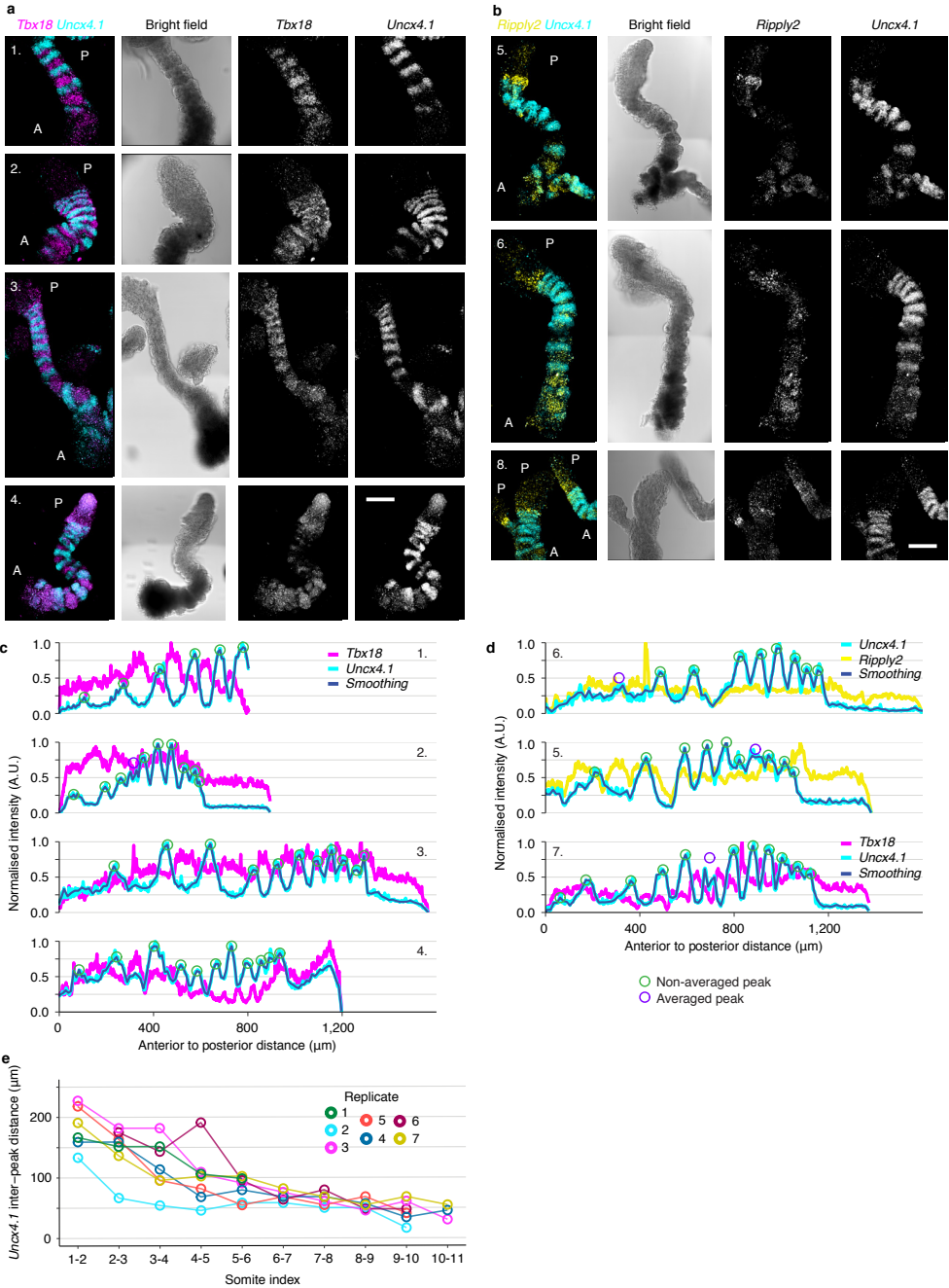
Supplementary Fig. 8 | See next page for caption.

Supplementary Fig. 8 | Detrending procedure and Lomb–Scargle analysis of replicates, as well as measurements of elongation and differentiation front speed in small panel screening, and upon BGJ389 and PD17 treatment. Replicates subjected to detrending and Lomb–Scargle analysis are from Fig. 2. **a**, Black line, measured intensity of the *Lfng* signal along the white dashed line in Fig. 2c; blue line, trend (Methods) of this signal and periodogram of the *Lfng* oscillations in Fig. 2d, as determined by Lomb–Scargle decomposition. **b**, As in **a**, but then for the 13 DMSO-control *Lfng*T2AVenus gastruloid replicates shown in Supplementary Fig. 7c, d. **c**, Cyclical component of the scaled intensity of the *Lfng*T2AVenus oscillations relative to the trend line shown in **b**. A.U., arbitrary units. **d**, Periodogram of the *Lfng* oscillations in **c**, as determined by Lomb–Scargle decomposition (Methods). Gastruloids used for this experiment were embedded in 100% Matrigel at 96 h, and subsequently imaged for at least 17 h. **e**, **f**, Speed of posterior gastruloid elongation (V_{PSM}) and speed of posteriorly moving differentiation front (V_{Diff}) (see explanation in Supplementary Fig. 9a) in *Lfng*T2AVenus gastruloids treated with DMSO (control) or with various inhibitors (Supplementary Videos 3, 5). Points refer to replicates; $n = 14, 3, 3, 3, 1, 2$ and 3 (from left to right) and $9, 3, 6$ and 6 (from left to right) replicates for **e** and **f**, respectively. Kymographs of replicates are shown in Supplementary Fig. 7. In the box plots, centre line is median; box limits are the 1st and 3rd quartiles; and whiskers denote the range.



Supplementary Fig. 9 | See next page for caption.

Supplementary Fig. 9 | Explanation for how elongation and differentiation-front speed were measured, and HCR stainings and kymographs of gastruloids embedded in 10% Matrigel. **a**, Kymographs (space–time plots) of bright field channel and LfngT2AVenus signal along the anterior–posterior axis of a DMSO-treated (control) and a PD03 (MEK inhibitor)-treated LfngT2AVenus gastruloid. Gastruloids were embedded in 100% Matrigel at 96 h; DMSO or PD03 (66.7 μ M) was added at 96.5 h. Kymographs were used to measure the elongation speed of the gastruloid (angle of blue dashed line; V_{PSM}) (Methods) and the speed of the differentiation front (angle of red dashed line; V_{Diff}). Similar results were obtained in $n = 4$ independent experiments. **b**, Illustration explaining the effect of FGF inhibition, which increases the speed of the differentiation front (red arrows, V_{Diff}) without altering the elongation rate (blue arrows, V_{PSM}) of gastruloids. Three time points (t_1 , t_2 and t_3) are depicted. White tissue, nondifferentiated tissue (presomitic mesoderm); grey tissue, differentiated tissue. **c**, In situ hybridization staining for *Uncx4.1* on 120-h LfngT2AVenus gastruloids that were not embedded in Matrigel (0%) (standard, previously published protocol^{1,20}) or that were embedded in 25% or 100% Matrigel at 96 h. Numbers below the panels indicate the number of gastruloids in which stripy *Uncx4.1* expression patterns were observed. Similar results were obtained in $n = 3$ independent experiments. **d**, LfngT2AVenus gastruloids that were embedded in 10% Matrigel (Methods) at 96 h and stained for *Uncx4.1* using HCR²¹ at 120 h. A magnified view of the left gastruloid is shown in Fig. 3a. Similar results were obtained in $n = 5$ independent experiments. **e**, Kymographs of LfngT2AVenus signal and bright field channel along the anterior–posterior axis of gastruloids that were embedded in 10% Matrigel at 96 h, and subsequently imaged for 20 h (Supplementary Video 6). Top kymograph belongs to the gastruloid that is shown in Fig. 3b. Similar results were obtained in $n = 2$ independent experiments. Scale bars, 200 μ m.



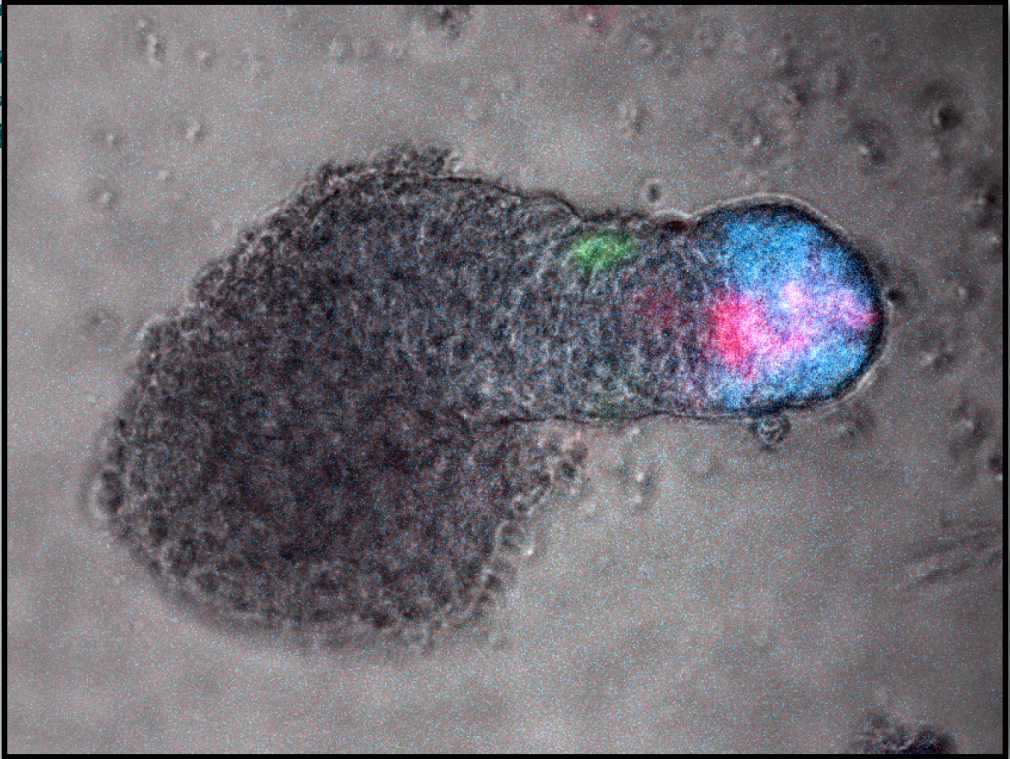
Supplementary Fig. 10 | See next page for caption.

Supplementary Fig. 10 | *Uncx4.1*, *Tbx18* and *Ripply2* stainings and somite-size measurements. **a**, HCR²¹ double staining for *Uncx4.1* (cyan) and *Tbx18* (magenta) on 120-h LfngT2AVenus gastruloids embedded in 10% Matrigel at 96 h. For replicate 4, 1.3 μ M of PD03 was added at 96.5 h. Similar results were obtained in $n = 4$ independent experiments. **b**, Similar to **a**, but for *Uncx4.1* (cyan) and *Ripply2* (yellow). Similar results were obtained in $n = 2$ independent experiments. **c**, Intensity of *Uncx4.1* and *Tbx18* signal along the anterior–posterior axis of the gastruloids in **a**. Peaks (circles) are called on the smoothed *Uncx4.1* profile (dark blue) (Methods). **d**, Similar to **c**, but for the *Uncx4.1*- and *Ripply2*-stained gastruloids from **b**. **e**, Distance between *Uncx4.1* peaks in the 120-h LfngT2AVenus gastruloids ($n = 7$) from replicates 1–6 in **a–d** and in replicate 7 (which is shown in Fig. 3c). Replicate 8 was excluded from quantification and both replicate 4 and replicate 7 were incubated in 1.3 μ M PD03 from 96–120 h. Scale bars, 200 μ m.

References

1. van den Brink, S. C. et al. Symmetry breaking, germ layer specification and axial organisation in aggregates of mouse embryonic stem cells. *Development* **141**, 4231–4242 (2014).
2. Turner, D. A. et al. Anteroposterior polarity and elongation in the absence of extra-embryonic tissues and of spatially localised signalling in gastruloids: mammalian embryonic organoids. *Development* **144**, 3894–3906 (2017).
3. Beccari, L. et al. Multi-axial self-organization properties of mouse embryonic stem cells into gastruloids. *Nature* **562**, 272–276 (2018).
4. Pijuan-Sala, B. et al. A single-cell molecular map of mouse gastrulation and early organogenesis. *Nature* **566**, 490–495 (2019).
5. Nowotschin, S. et al. The emergent landscape of the mouse gut endoderm at single-cell resolution. *Nature* **569**, 361–367 (2019).
6. Kwon, G. S., Viotti, M. & Hadjantonakis, A. K. The endoderm of the mouse embryo arises by dynamic widespread intercalation of embryonic and extraembryonic lineages. *Dev. Cell* **15**, 509–520 (2008).
7. Scotti, M. & Kmita, M. Recruitment of 5' Hoxa genes in the allantois is essential for proper extra-embryonic function in placental mammals. *Development* **139**, 731–739 (2012).
8. Koch, F. et al. Antagonistic activities of Sox2 and Brachyury control the fate choice of neuro-mesodermal progenitors. *Dev. Cell* **42**, 514–526 (2017).
9. Chal, J. & Pourquié, O. Making muscle: skeletal myogenesis in vivo and in vitro. *Development* **144**, 2104–2122 (2017).
10. Laurent, F. et al. HAND2 target gene regulatory networks control atrioventricular canal and cardiac valve development. *Cell Rep.* **19**, 1602–1613 (2017).
11. Junker, J. P. et al. Genome-wide RNA tomography in the zebrafish embryo. *Cell* **159**, 662–675 (2014).
12. Chal, J. et al. Differentiation of pluripotent stem cells to muscle fiber to model Duchenne muscular dystrophy. *Nat. Biotechnol.* **33**, 962–969 (2015).
13. Dequéant, M. L. et al. A complex oscillating network of signaling genes underlies the mouse segmentation clock. *Science* **314**, 1595–1598 (2006).
14. Oates, A. C., Morelli, L. G. & Ares, S. Patterning embryos with oscillations: structure, function and dynamics of the vertebrate segmentation clock. *Development* **139**, 625–639 (2012).
15. Sonnen, K. F. et al. Modulation of phase shift between Wnt and Notch signaling oscillations controls mesoderm segmentation. *Cell* **172**, 1079–1090.e12 (2018).
16. Hubaud, A., Regev, I., Mahadevan, L. & Pourquié, O. Excitable dynamics and Yap-dependent mechanical cues drive the segmentation clock. *Cell* **171**, 668–682.e11 (2017).
17. Naiche, L. A., Holder, N. & Lewandoski, M. FGF4 and FGF8 comprise the wavefront activity that controls somitogenesis. *Proc. Natl Acad. Sci. USA* **108**, 4018–4023 (2011).
18. Dubrulle, J., McGrew, M. J. & Pourquié, O. FGF signaling controls somite boundary position and regulates segmentation clock control of spatiotemporal Hox gene activation. *Cell* **106**, 219–232 (2001).
19. Sawada, A. et al. Fgf/MAPK signalling is a crucial positional cue in somite boundary formation. *Development* **128**, 4873–4880 (2001).
20. Baillie-Johnson, P., van den Brink, S. C., Balayo, T., Turner, D. A. & Martinez Arias, A. Generation of aggregates of mouse embryonic stem cells that show symmetry breaking, polarization and emergent collective behaviour in vitro. *J. Vis. Exp.* **105**, e53252 (2015).
21. Choi, H. M. T. et al. Third-generation in situ hybridization chain reaction: multiplexed, quantitative, sensitive, versatile, robust. *Development* **145**, dev165753 (2018).
22. Lauschke, V. M., Tsiairis, C. D., François, P. & Aulehla, A. Scaling of embryonic patterning based on phase-gradient encoding. *Nature* **493**, 101–105 (2013).
23. Matsumiya, M., Tomita, T., Yoshioka-Kobayashi, K., Isomura, A. & Kageyama, R. ES cell-derived presomitic mesoderm-like tissues for analysis of synchronized oscillations in the segmentation clock. *Development* **145**, dev156836 (2018).
24. Fehling, H. J. et al. Tracking mesoderm induction and its specification to the hemangioblast during embryonic stem cell differentiation. *Development* **130**, 4217–4227 (2003).
25. Faunes, F. et al. A membrane-associated β -catenin/Oct4 complex correlates with ground-state pluripotency in mouse embryonic stem cells. *Development* **140**, 1171–1183 (2013).
26. Ferrer-Vaquer, A. et al. A sensitive and bright single-cell resolution live imaging reporter of Wnt/ β -catenin signaling in the mouse. *BMC Dev. Biol.* **10**, 121 (2010).
27. Papanayotou, C. et al. A novel Nodal enhancer dependent on pluripotency factors and Smad2/3 signaling conditions a regulatory switch during epiblast maturation. *PLoS Biol.* **12**, e1001890 (2014).
28. Kalmar, T. et al. Regulated fluctuations in Nanog expression mediate cell fate decisions in embryonic stem

- cells. *PLoS Biol.* **7**, e1000149 (2009).
29. Turner, D. A. et al. Wnt/ β -catenin and FGF signalling direct the specification and maintenance of a neuromesodermal axial progenitor in ensembles of mouse embryonic stem cells. *Development* **141**, 4243–4253 (2014).
 30. Turner, D. A., Rué, P., Mackenzie, J. P., Davies, E. & Martinez Arias, A. Brachyury cooperates with Wnt/ β -catenin signalling to elicit primitive-streak-like behaviour in differentiating mouse embryonic stem cells. *BMC Biol.* **12**, 63 (2014).
 31. Turner, D. A., Trott, J., Hayward, P., Rué, P. & Martinez Arias, A. An interplay between extracellular signalling and the dynamics of the exit from pluripotency drives cell fate decisions in mouse ES cells. *Biol. Open* **3**, 614–626 (2014).
 32. van Batenburg, V. et al. Generating gastruloids with somite-like structures from mouse embryonic stem cells. *Protoc. Exch.* <https://doi.org/10.21203/rs.2.18203/v1> (2020).
 33. Muraro, M. J. et al. A single-cell transcriptome atlas of the human pancreas. *Cell Syst.* **3**, 385–394.e3 (2016).
 34. Grün, D. et al. Single-cell messenger RNA sequencing reveals rare intestinal cell types. *Nature* **525**, 251–255 (2015).
 35. Wolf, F. A., Angerer, P. & Theis, F. J. SCANPY: large-scale single-cell gene expression data analysis. *Genome Biol.* **19**, 15 (2018).
 36. Johnson, W. E., Li, C. & Rabinovic, A. Adjusting batch effects in microarray expression data using empirical Bayes methods. *Biostatistics* **8**, 118–127 (2007).
 37. Chakraborty, S., Datta, S. & Datta, S. Surrogate variable analysis using partial least squares (SVA-PLS) in gene expression studies. *Bioinformatics* **28**, 799–806 (2012).
 38. Traag, V. A., Waltman, L. & van Eck, N. J. From Louvain to Leiden: guaranteeing well-connected communities. *Sci. Rep.* **9**, 5233 (2019).
 39. Schindelin, J. et al. Fiji: an open-source platform for biological-image analysis. *Nat. Methods* **9**, 676–682 (2012).
 40. Glynn, E. F., Chen, J. & Mushegian, A. R. Detecting periodic patterns in unevenly spaced gene expression time series using Lomb–Scargle periodograms. *Bioinformatics* **22**, 310–316 (2006).
 41. Richardson, L. et al. EMAGE mouse embryo spatial gene expression database: 2014 update. *Nucleic Acids Res.* **42**, D835–D844 (2014).
 42. van den Brink, S. C. et al. Single-cell sequencing reveals dissociation-induced gene expression in tissue subpopulations. *Nat. Methods* **14**, 935–936 (2017).



"It always seems impossible until it's done."
(N. Mandela)

4

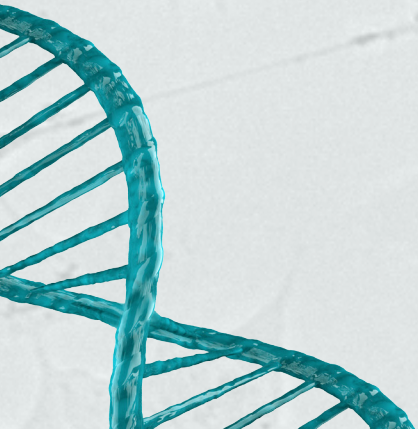
An in vitro model for early anteroposterior organisation during human development

Naomi Moris^{*,§}, Kerim Anlas^{*}, Susanne C. van den Brink^{*}, Anna Alemany^{*}, Julia Schröder, Sabitri Ghimire, Tina Balayo, Alexander van Oudenaarden[§] & Alfonso Martinez Arias[§]

* Equal contribution

§ Corresponding authors

Nature (2020)



4

The body plan of the mammalian embryo is shaped through the process of gastrulation, an early developmental event that transforms an isotropic group of cells into an ensemble of tissues ordered with reference to three orthogonal axes¹. While model organisms have provided much insight into this process, we know very little about gastrulation in humans due to the difficulty of obtaining embryos at such early stages of development, as well as to the ethical and technical restrictions that limit the feasibility of observing gastrulation ex vivo². Here we show that human embryonic stem cells can be used to generate gastruloids: three dimensional multicellular aggregates that differentiate to derivatives of the three germ layers organised spatiotemporally, without additional extra-embryonic tissues. Human gastruloids undergo elongation along an anteroposterior axis and, using spatial transcriptomics, we show that they exhibit patterned gene expression. This includes a somitogenesis signature that suggests that 72 hour human gastruloids exhibit features of Carnegie Stage 9 embryos³. Our study represents a new, experimentally tractable model system to reveal and probe human-specific regulatory processes occurring during axial organisation in early development.

The body plan of mammalian embryos emerges through interactions of sequential cell fate decisions and morphogenetic events, which have hitherto been difficult to observe in humans. Human Embryonic Stem Cells (hESCs)⁴ have opened up opportunities for studying early fate decisions, and have hinted at the existence of regulatory mechanisms specific to humans^{5,6}. But, in contrast to the embryo, where proportionate populations interact with one another to generate tissues and organs, differentiation in adherent culture is heterogeneous and favours a limited number of cell types⁷. Seeding hESCs on micropatterned surfaces yields coordinated patterns of gene expression, but without the axial organization characteristic of embryos⁸. However, when mouse ESCs are aggregated in suspension under defined conditions, they generate 'gastruloids': a three-dimensional, in vitro model of mammalian development, which exhibits an embryo-like spatiotemporal organization of gene expression^{9,10}. We hypothesised that similar human gastruloids could be derived from hESCs.

Generation of human gastruloids

When hESCs in 2D culture were treated with Chiron, a WNT agonist, for one day before seeding defined numbers in low-adherence plates in the presence of Chiron, they formed compact, spherical aggregates within a few hours (Fig. 1a, Supplementary Fig. 1a-c). These aggregates progressively broke symmetry and formed elongated structures, with maximal elongation at 72-96h (Fig. 1a-d). On average, ~66% of aggregates from each experiment displayed an elongated morphology at 72h (Fig. 1e-f and Supplementary Fig. 1d; see Methods for details of classification). Although some of the structures remained elongated until 96h, the majority tended to curl or retract after 72h. Different cell lines required different concentrations of Chiron stimulation (Supplementary Fig. 1e).

Before aggregation, pre-treated hESCs were found to express pluripotency markers but with increased expression of mesendodermal marker genes including BRA, MIXL1, EOMES

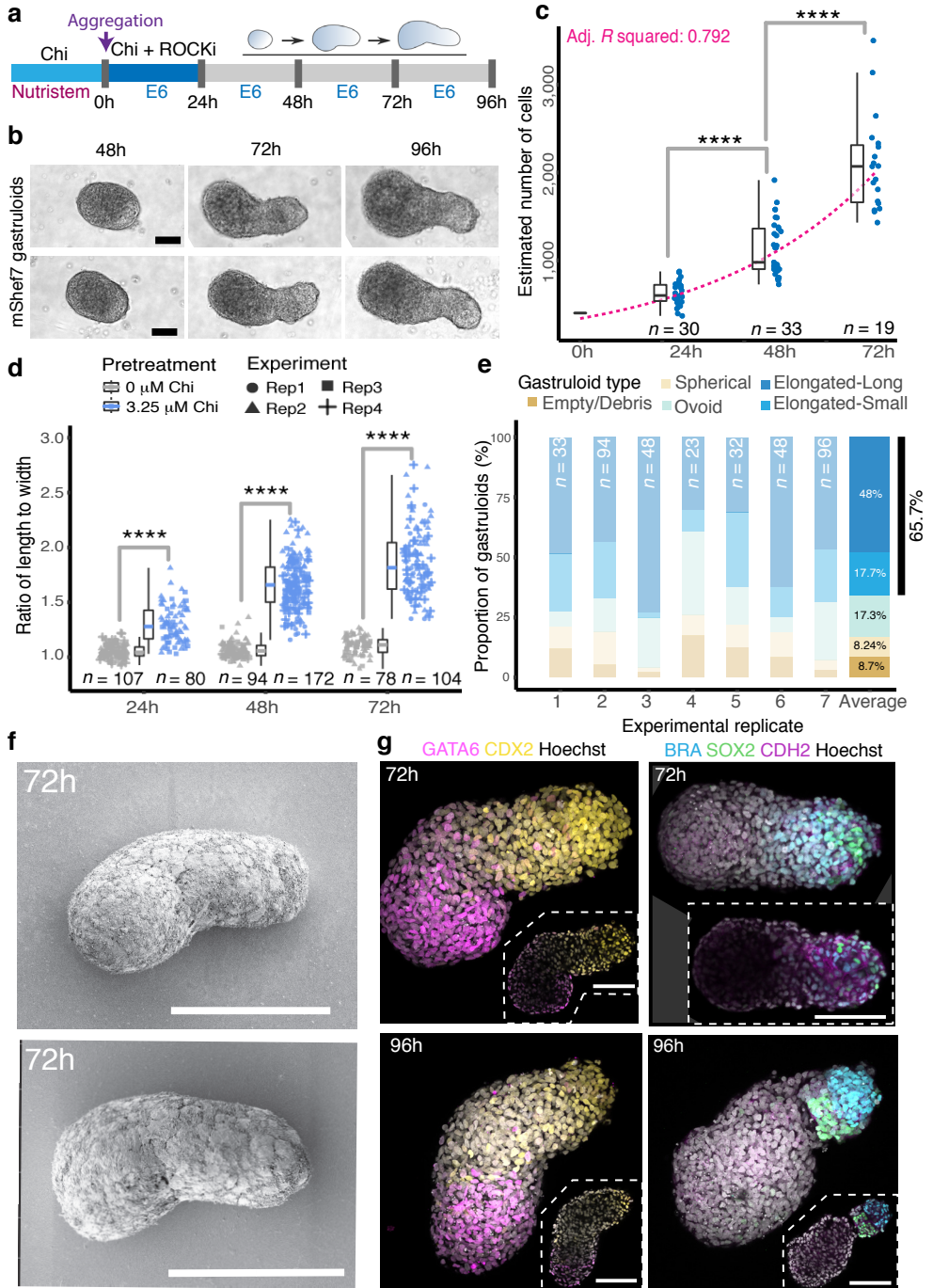


Fig. 1 | See next page for caption.

Fig. 1 | Structure and morphology of human gastruloids. **a**, Schematic of human gastruloid protocol. Chi, CHIR99021; ROCKi, ROCK inhibitor; E6, Essential 6 medium. **b**, Temporal morphology. Shown are two representative examples from MasterShef7 (mShef7) cell line. ($n = 3$ experiments). Scale bar, 200 μm . **c**, Estimated number of cells in human gastruloids. Data from 2-4 independent biological replicates (Welch two-sided, two-sample t-test; Source Data). **d**, Elongation of RUES2-GLR gastruloids (center line, median; whiskers, interquartile range). Shown are data from $n = 2-4$ independent biological replicates (Rep) (Welch two-sided, two-sample t-test; ****, $P < 2.2e^{-16}$; see Source Data and Methods). **e**, Proportion of elongated RUES2-GLR gastruloids at 72h, as quantified using an automated measure of morphological elongation (see Methods for details). Shown are $n = 7$ independent biological replicates (left), and the average proportions (right). Representative images of each elongation category can be seen in Supplementary Fig. 1d. **f**, Scanning Electron Micrograph (SEM) of RUES2-GLR human gastruloids at 72h. Shown are two representative examples, $n = 28$ gastruloids. Scale bars; 200 μm . **g**, Projections of immunofluorescence-labelled RUES2-GLR human gastruloids at 72h (top) and 96h (bottom). Insets, individual sections (bounded by dashed lines). Scale bars; 100 μm . c-e, n , number of gastruloids.

(Supplementary Fig. 2a; Supplementary Table 1) and membrane localised CDH2 (N-Cadherin) (Supplementary Fig. 2b-d). These results suggest that following Chiron pre-treatment, hESCs become partially primed towards a primitive streak-like state, in agreement with observations that WNT signalling induces mesodermal differentiation of hESCs^{7,11}.

Axial organisation of gene expression

Polarised expression of BRA protein was detectable as early as 24h (Supplementary Fig. 3a) overlapping a SOX2 expressing domain which, by 96h, had resolved into distinct BRA+ and SOX2+ expressing regions (Fig. 1g). All cells exhibited CDH2 expression with higher levels in the posterior BRA+ and SOX2+ domain (Fig. 1g; Supplementary Fig. 3b). A group of GATA6 expressing cells were localized at one end, opposite to cells expressing CDX2 (Fig. 1g) and this pattern was refined as the aggregates underwent elongation (Supplementary Fig. 3c-f; see Methods for details of classification). The polarisation of GATA6 was confirmed using live-imaging of a S4-GATA6 reporter line¹² and occurred as early as 24h (Supplementary Video 1 and Supplementary Fig. 3g). The CDX2 expressing region also contained BRA expressing cells (Fig. 1g), suggesting a correspondence to posterior embryonic identity, since co-expression of these genes is restricted to the tailbud of mammalian embryos.

To ascertain whether human gastruloids were capable of generating derivatives of the three germ layers, we made use of a reporter line (RUES2-GLR¹³) to identify progenitors for the mesoderm (BRA), endoderm (SOX17) and neuroectoderm (SOX2) (Fig. 2a). Time lapse video of RUES2-GLR during aggregation (Supplementary Video 2) and elongation (Supplementary Video 3) allowed us to follow the process of symmetry-breaking and segregation of germ layer progenitors. Initially, all cells express SOX2 (Fig. 2b) before individual SOX17+ cells emerge throughout the aggregate and SOX2 expression becomes confined to one end of the aggregates (Fig. 2c). Between 24-48h, BRA expression, initially low and ubiquitous, increases and becomes localised to the SOX2 expressing region of the aggregate. By 72h, aggregates expressed BRA at the distal end, with neighbouring SOX17 and SOX2 expressing domains (Fig. 2d). The profiles of these fluorescent reporter genes were comparable among individual gastruloids when aligned along their AP axis (Fig. 2e).

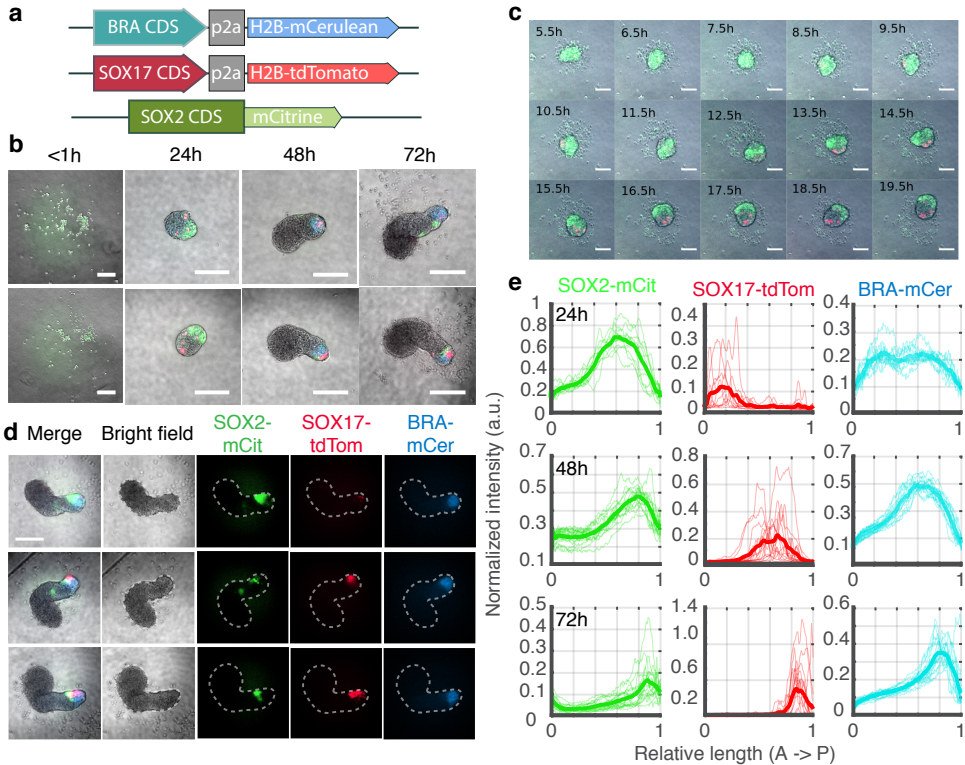


Fig. 2 | Dynamic polarization of cell types associated with three germ layers in human gastruloids. a, Schematic of the RUES2-GLR cell line. CDS, Coding Sequence; mCit, mCitrine; tdTom, tdTomato; mCer, mCerulean. b, The temporal dynamics of RUES2-GLR human gastruloid development. Shown are two representative examples. Colours indicate reporter fluorescence as in panel (a). Scale bar; 200 μm . Representative example, from $n > 5$ independent experiments. c, Stills from live-imaging of RUES2-GLR human gastruloids. Colours as in panel b. Scale bar; 100 μm . Representative example, from 3 independent experiments. d, Localization of the three germ layer reporters at 72h. Shown are 3 examples. Representative example, from $n > 5$ independent experiments. Scale bar, 100 μm . e, Quantification of the dynamics of reporters along the anteroposterior axis of elongating gastruloids. Thin line, individual gastruloids; thicker line, average of each timepoint. A = Anterior, P = Posterior.

The Chiron pre-treatment was absolutely necessary for elongation and patterned gene expression (Fig. 1d and Supplementary Fig. 1a-b). However, in our experiments, Wnt3a pre-treatment was unable to substitute for Chiron, as evidenced by a lack of elongation and absence of BRA expression (Supplementary Fig. 4a), suggesting differential effects between Chiron and Wnt3a in hESCs¹⁴. We also found that BMP4, which is used to trigger patterned gene expression in micropatterns⁸, was unable to substitute for Chiron and led to small, spherical aggregates with no discernible patterning (Supplementary Fig. 4b). These observations highlight differences in the cellular response to signals, perhaps associated with the dimensionality of the system. They also suggest that the formation of human gastruloids is highly dependent on the signalling exposure of the initial cell population.

To investigate further the dependence of human gastruloid formation on signalling, we

applied small molecule inhibitors of BMP, WNT and Nodal signalling during pre-treatment. When RUES2-GLR cells were exposed to routine levels of Chiron in the presence of BMP (LDN193189) or WNT (XAV-939) inhibition, hESCs were not able to form patterned aggregates or to elongate (Supplementary Fig. 4c). Likewise, inhibition of Nodal signalling (SB431542; “SB43”) led to ovoid aggregates that co-express both SOX2 and BRA (Supplementary Fig. 4d), though increasing the concentration of Chiron during aggregation elevated BRA expression and led to robust elongations, with co-expression of BRA and SOX2 at the posterior pole (Supplementary Fig. 4d). These results suggest that a balance between the levels of Nodal and WNT/ β -catenin signalling plays a role in establishing fate decisions and promoting elongation in human gastruloids.

Having observed this signal-dependence during human gastruloid formation, we examined the effect of sustained gastruloid culture with Retinoic Acid (RA), known to disrupt axial patterning and cause congenital malformations¹⁵. RA treated gastruloids were typically rounded and exhibited high SOX2 expression, with a strong reduction in BRA expression, although they had separate domains of CDX2 and GATA6 (Supplementary Fig. 4e-f). This suggests that certain elements of axial patterning and organisation, particularly elongation, were adversely affected by RA application in the human gastruloids.

These results support the notion that the signalling environment, before and during gastruloid development, is a critical factor in establishing both the morphology and patterning of human gastruloids.

A transcriptional body plan in human gastruloids

To explore the transcriptional complexity of human gastruloids, we applied tomo-sequencing (tomo-seq)¹⁶ to 72h Chiron pre-treated RUES2-GLR gastruloids (Methods). Two replicates were embedded and sectioned along their AP axis, before RNA-seq processing each of the sections (Fig. 3a-b and Supplementary Fig. 5a; Methods).

We found 1,023 genes that were reproducible between the two replicates (Methods), organised into 22 main classes of expression patterns with representatives of all three germ layers (Fig. 3c-e and Supplementary Fig. 5b-c, Supplementary Data 1-2). Most notably, six clusters, localised to the posterior-most region of the gastruloid (Clusters 0-5), contained genes whose homologues are localized in the tailbud of mouse embryos, including BRA, CDX2, and CYP26A1. At the opposing end, we observed 9 clusters (Clusters 6-14), containing genes associated with cardiac and anterior endoderm development in the mouse embryo, including KDR, MEIS1/2, PBX1, TWIST1, ISL1, IRX1/2/3 and PRDM1 (Supplementary Data 3; Fig. 3c, d). Cluster 21 was strongly enriched for genes involved in somitogenesis and the Notch signalling pathway.

We did not find evidence for the expression of genes associated with the development of anterior neural structures (Supplementary Fig. 6a) but observed expression of many

paralogues from the 4 HOX clusters (Supplementary Fig. 6b). In mouse embryos, *Hox* genes are known to be sequentially expressed along the anteroposterior axis. In human gastruloids, HOX genes exhibit variable expression domains along the length of the gastruloid AP axis, but display a somewhat broader domain of paralogues 1-5, and more posterior-biased

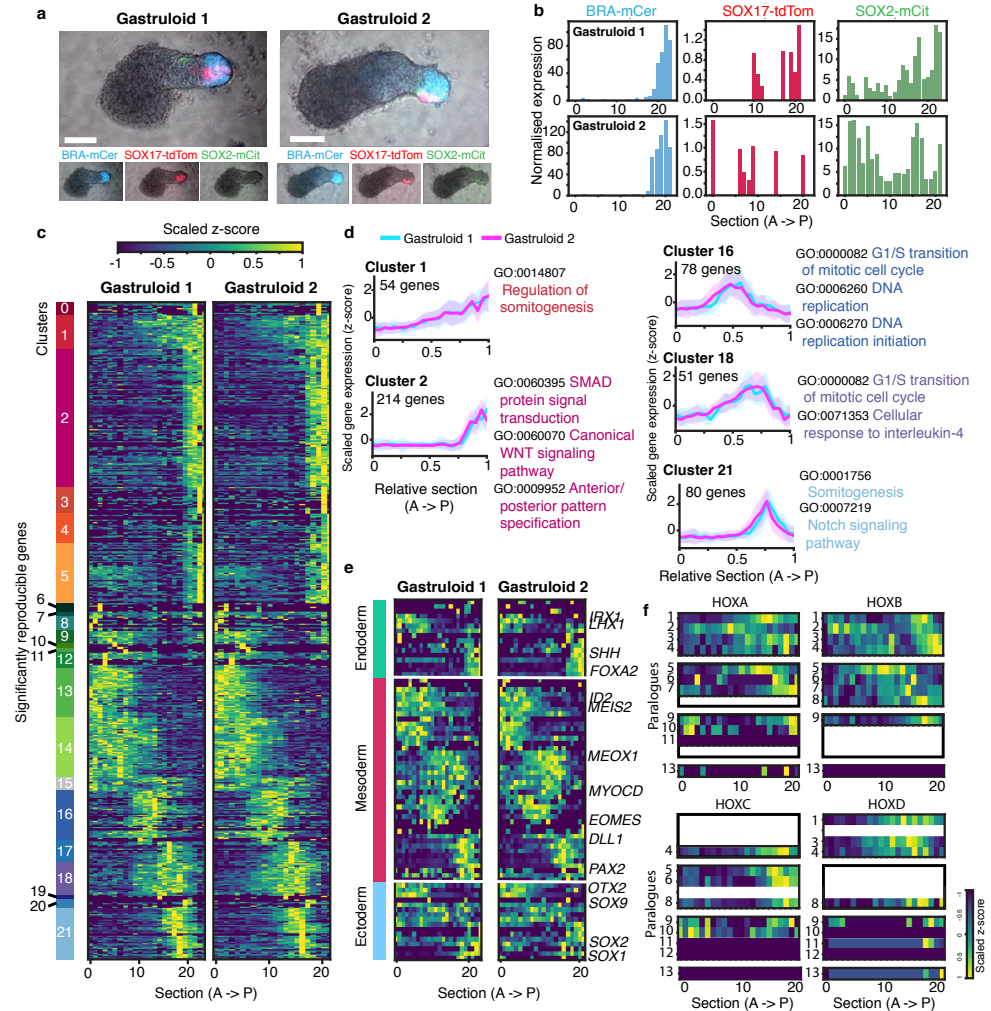


Fig. 3 | Transcriptomic anteroposterior organization of human gastruloids. **a**, Widefield imaging of 72h RUES2-GLR derived human gastruloids used for tomo-sequencing. Scale bars; 100 μ m. mCer, mCerulean; tdTom, tdTomato; mCit, mCitrine. $n = 2$ gastruloids. **b**, mRNA of the fluorescent reporter transgenes along the anteroposterior (AP) axis. **c**, Transcriptomic analysis of 1,023 significantly reproducible genes along the AP axis of two 72h RUES2-GLR derived Chiron pre-treated human gastruloids. Coloured panels (left) show clusters of genes with similar expression patterns (see Methods, Supplementary Data 1). Two replicates are shown. **d**, Average AP expression for genes in selected clusters, and corresponding enriched Gene Ontology (GO) terms. Shaded ribbon corresponds to the standard deviation of the cluster, line to the mean average (Supplementary Data 3). **e**, Expression of characteristic markers of all three germ layers. Selected genes are highlighted (Supplementary Data 2). Colour-scale equivalent to that of panel (c). **f**, Localisation of HOX gene expression along the AP axis. White bars indicate lack of paralogue. **a-f**, $n = 2$ gastruloids. See Source Data and Methods.

distribution of groups 6-8. Paralogues 9-13 were variably or lowly/not expressed (Fig. 3f and Supplementary Fig. 6b). Some posterior genes also exhibited expression in the anterior part of the gastruloid (e.g. HOXA9-10 and HOXC9-10; Fig. 3f). Currently, in the absence of an embryonic reference it is not possible to discern whether this localization reflects an early phase in the regulation of HOX gene expression, a species difference or a feature of this model system.

These global patterns of gene expression raised the question of whether this organization reflects elements of a body plan, the blueprint for the organism. This possibility is supported by the organization of a posterior domain of gene expression in the human gastruloids (Fig. 4a-b), where we observed a node-like transcriptional domain (Fig. 4c-d, Supplementary Fig. 6c)¹⁷. At the anterior end, we observed the polarisation of genes associated with cardiac mesoderm development (Fig. 4e-f)^{18,19}.

Signalling and pattern organisation

One of the mechanisms by which gastruloids might establish or maintain patterning along their AP axis includes the organization of signalling components along their length. Assessing this in the tomo-seq data, we observed a number of WNT ligands preferentially expressed at the posterior-end (WNT5A, WNT3A, WNT5B, LEF1 and WNT3) and some BMP ligands anteriorly (BMP2, BMP4 and BMP5; Supplementary Fig. 6d). Using a BMP/SMAD1 reporter line²⁰, we observed increased nuclear SMAD1-RFP at the anterior end (Supplementary Fig. 6e-f). Anterior BMP signalling localisation is consistent with its function in cardiac development of the mammalian embryo. At the posterior end we observed expression of WNT3a and LEF1, indicating WNT signalling within the posterior region (Supplementary Fig. 6g-h). Additionally, we observed a peak of Nodal signalling components and targets, including NODAL, LEFTY1/2 and CER1, within the posterior region of human gastruloids (Supplementary Fig. 6i). This is consistent with a known role of WNT and Nodal signalling in the mammalian tailbud, and together suggests that human gastruloids might utilise signalling gradients along their AP axis to establish patterning.

In mouse embryos, Nodal signalling plays an early role in establishing different fates along the AP axis, before becoming localized to the posterior pole and the node^{21,22}. Having observed that suppression of Nodal signalling during pre-treatment could still lead to robust elongation of human gastruloids (Supplementary Fig. 7a-b and Supplementary Fig. 4d), we wanted to examine the organization of gene expression in these gastruloids closely. Gastruloids pre-treated with Chiron and SB43 displayed a larger, well-defined SOX2 domain at their posterior end, diffuse expression of BRA that approximated an anteroposterior gradient, and an absence of detectable SOX17 expression (Supplementary Fig. 7b-d; Supplementary Table 2). Comparative analysis between 120h Chiron and SB43 pre-treated gastruloids and those without Nodal-signalling inhibition (Supplementary Fig. 7d-g and Supplementary Fig. 8a-c, Supplementary Data 4-5 and Methods) showed that although 301 genes were reproducibly localised in both conditions, SB43 treatment led to the acquisition of 944 genes with novel

spatial localisation, and the loss of reproducible localisation of 509 genes (Supplementary Fig. 7e; Supplementary Data 5). Additionally, 564 genes (33%) were differentially expressed between the two treatments (Supplementary Fig. 7f and Supplementary Data 6). One cluster of genes lost on SB43 pre-treatment (Cluster 4; Supplementary Fig. 7g) included genes known to be involved in Nodal signalling and many associated with the node in mammalian embryos (Supplementary Data 5), consistent with a loss of Nodal activity. We also noticed a decrease in expression of genes associated with definitive endoderm (SHH, LHX1, CER1, FOXA3, SORCS2, FOXA2) consistent with a role of Nodal in the specification of this germ layer in mouse embryos²¹, and a loss of genes associated with cardiac development (TBX5, GATA6, LBX1, NKX2.5) likely to be a consequence of the loss of induction from the endoderm²³ (Supplementary Fig. 8d, e and Supplementary Data 7).

Together, these observations indicate that the spatial organization of signalling molecules, and their activity in human gastruloids, mirror those of mammalian embryos.

Comparative spatial transcriptomics

The high degree of organization in gene expression that we observed in human gastruloids prompted us to explore the correspondence of these patterns with other developmental models. To do this, we focused on mouse gastruloids as an equivalent model system^{9,10}. The comparison of tomo-seq datasets showed a high degree of conservation in axial patterning (Fig. 4g and Supplementary Data 8). In particular we observed a conserved pattern of mesodermal differentiation in the axial region of the gastruloids²⁴. There was a posterior-to-anterior signature for somitogenesis with expression of tailbud genes (BRA, CDX2 and LFNG) posteriorly, a short domain of MESP1 and MESP2, followed by a more anterior, broader domain of MEOX1 and TCF15 expression (Fig. 4h). The overall pattern of gene expression therefore mirrors the organisation of paraxial mesoderm specification and differentiation in a mammalian embryo²⁵, as well as temporal sequences of somitogenesis in hESCs^{7,26}. In contrast to these conserved patterns, we also noticed genes that were expressed in different regions (Clusters 0, 2-3 and 13 for example, Supplementary Data 8) or uniquely expressed (Supplementary Fig. 9a-e and Supplementary Data 9) in each of the two systems, supporting the notion that species-specific regulation of patterning might be occurring in the gastruloid models.

Perspectives

The human gastruloid system that we have introduced represents a first step towards the *in vitro* modelling of the emergence of the human body plan in a 3D context. In this regard, the axial organization of the somitogenesis program of gene expression that we observed, suggests an approximate staging. Examination of images of extant collections of human embryos³ reveals a major transition between Carnegie Stages (CS) 8 and 9 (corresponding to days 17-19 and days 19-21, respectively), associated with the onset of somitogenesis (Fig. 4i); images of CS9 embryos reveal the presence of 1 to 3 somite pairs that are absent in

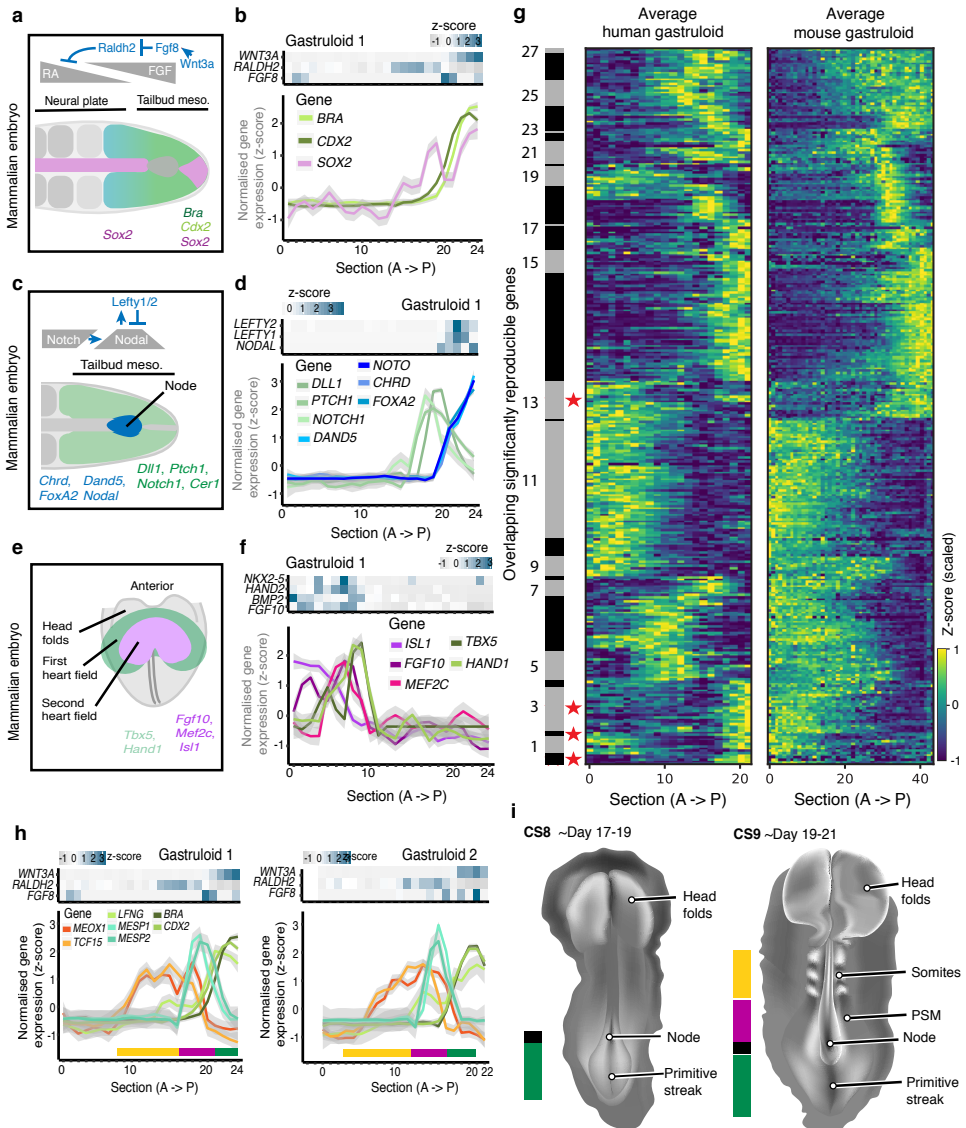


Fig. 4 | Comparative elements of early embryogenesis. a, Schematic of the mammalian embryo tailbud. b, Heatmaps (upper), and line graphs (lower), showing expression localisation of tailbud-associated genes in human gastruloids. Line graphs are displayed as smoothed gene expression patterns; grey ribbon, 50% Confidence Interval. One replicate shown, $n = 2$ gastruloids; Supplementary Fig. 5c. c, Schematic of the mammalian embryo node region. d, AP organization of node-associated genes in human gastruloids. Panel organized as in panel b. e, Schematic of the mammalian embryo cardiac mesoderm region. f, AP organization of cardiac mesoderm region-associated genes in human gastruloids. Panel organized as in panel b. g, Heatmap showing AP expression of 253 orthologous, reproducible genes in mouse and human gastruloids (left, average human gastruloid; right, average mouse gastruloid), 20 μ m tomo-seq data. Greyscale numbered bars, clustering based on expression patterns; red stars, deviation of expression pattern. $n = 2$ human gastruloids, 5 mouse gastruloids. h, Patterned organization of somitogenesis-related genes in human gastruloids, including signaling gradients (upper heatmaps) and genes related to the tailbud and somitic tissue (lower linegraphs) for $n = 2$ gastruloids. i, Illustration of Carnegie Stage (CS) 8 and 9, showing gross anatomical features, including somite boundaries. Adapted from ref. ³². Yellow bars, somites; magenta bars, developing somites and presomitic mesoderm; green bars, primitive streak and tailbud mesoderm; black bars, node. See Source Data and Methods.

CS8. In the human gastruloids, the pattern of gene expression, with a central somitic domain and posterior presomitic domain of a similar length, leads us to suggest that 72h human gastruloids might serve as a model for some of the features of late CS8 or early CS9 human development. Since, with the current protocol, the majority of human gastruloids curl or retract after 72h, this likely represents a technical limitation, and extension beyond this point will be subject of future studies.

The lack of anterior neural and extraembryonic lineages, characteristic of gastruloids, raises important questions about the self-organisation of the mammalian body plan, but also removes several of the ethical considerations associated with prolonged human embryo culture. The tractable nature of human gastruloids should allow the detailed exploration of a variety of questions associated with early human development and represents an experimental model that could prove fruitful in the study of the mechanisms associated with early human development and disease.

Methods

Ethical statement

The human gastruloid model introduced in this study does not show any evidence of cell types associated with anterior neural fates, which would be required to form brain tissue, nor do they form extraembryonic tissues, which would be required for implantation or show evidence of multiorgan differentiation which would be necessary for integrated organ system development. Significantly, they lack the morphology of an early human embryo, and therefore do not manifest human organisational form. As such, they are non-intact, non-autonomous, and non-equivalent to in vivo human embryos, and do not have human organisational potential. Our research was subject to review and approval from the Human Biology Research Ethics Committee of the University of Cambridge, in compliance with the ISSCR 2016 guidelines.

Human cell lines

The cell lines used in this study include the hESC lines: MasterShef7²⁷, S4-GATA6-GFP¹², RUES2-GLR¹³ and RUES2:SMAD1-RFP;H2B-mCitrine²⁰. All cells were cultured in humidified incubators at 37 °C and 5% CO₂. Human ESCs were cultured routinely in Nutristem hPSC XF medium (Biological Industries, 05-100-1A) on 0.5 µg/cm² Vitronectin-coated plates (Gibco, A14700). Cells were passaged using 0.5 mM EDTA in PBS^{-/-} (Invitrogen, 15575-038).

Culturing human gastruloids

A critical part of the process is the starting state of the cells, which must be in optimal condition before beginning. When cells were ~40-60% confluent, adherent cultures were pre-treated in Nutristem supplemented with CHIR99021 ('Chiron'; Tocris Biosciences, 4423). We found that cells did not form elongated gastruloids when cultured in alternative pluripotency medium, including mTeSR or Essential8. The optimal concentration of Chiron in this pre-treatment was cell line dependent and was determined empirically by titration for each new line. Concentrations for the lines used in this study are described in the following section. After pre-treatment for 24 hours, cells were dissociated using 0.5 mM EDTA in PBS^{-/-} (Invitrogen, 15575-038), washed in PBS^{-/-} and reaggregated in basal differentiation medium, Essential 6 ('E6'; ThermoFisher, A15165-01), supplemented with 1:2000 Y-27632 ('ROCK inhibitor'; Sigma Aldrich, Y0503) and a cell-line dependent concentration of Chiron. Cell numbers were determined using an automated cell counter (Moxi Z Mini, ORFLO Technologies, MXZ002) and 400-600 cells per 40 µl were added to each well of an ultra-low adherence 96-well plate (CellStar, 650970). For all images shown here, 400 cells per well of a 96-well plate were used to generate human gastruloids, unless otherwise stated. The cell suspension was centrifuged using a benchtop plate centrifuge at 700 rpm for 2 minutes. The following day, 150 µl fresh E6 medium was added to each well. Medium was exchanged for fresh E6 medium daily following this timepoint. Detailed instructions for generating human gastruloids can be found in Protocol Exchange²⁸.

Cell line-dependent Chiron pulse

We found that different human ESC lines required different concentrations of Chiron both before aggregation and for the first day of aggregation, in order to generate elongating gastruloids (Supplementary Fig. 1d). Cell-line dependent Chiron doses used in this study were as follows: RUES2-GLR, 3.25 µM Chiron pre-treatment, 0.5 µM Chiron aggregation; MasterShef7, 5 µM Chiron pre-treatment, 3 µM Chiron aggregation; GATA6-GFP, 3.25 µM Chiron pre-treatment, 0.5 µM Chiron aggregation; RUES2-SMAD1-RFP;H2B-mCitrine, 5 µM Chiron pre-treatment, 3 µM Chiron aggregation.

Signal modulation experiments

RUES2-GLR cells were pre-treated for 1 day in Nutristem supplemented with 100 ng/ml recombinant human Wnt3a (5036-WN-010) or 50 ng/ml BMP4 (314-BP), and aggregated in E6 and ROCK inhibitor with additional supplementation as shown. Subsequent media changes were performed daily with E6 alone. To test the effect of signal modulation on gastruloid formation, RUES2-GLR cells were pre-treated in Nutristem supplemented with 3.25 µM Chiron and one of 1 µM LDN193189 (04-0074), 1 µM XAV-939 (04-0046), or 10 µM SB431542 (1614) before aggregation in E6 with 0.5 µM Chiron and ROCK inhibitor, unless otherwise stated. Subsequent media changes were performed daily with E6 alone. For Retinoic Acid (RA) experiments, RUES2-GLR cells were pre-treated as usual in 3.25 µM Chiron for 1 day, before aggregation in E6 supplemented with 0.5 µM Chiron, ROCK inhibitor and 0.5 µM RA (R2625). Subsequent media changes were performed daily with E6 and 0.5 µM RA.

The SB43 pre-treated gastruloids for tomo-sequencing were made with RUES2-GLR cells pre-treated in Nutristem with 3.25 µM Chiron and 10 µM SB431542 (1614). They were then aggregated in E6 with 3 µM Chiron and ROCK inhibitor. Subsequent media changes were performed daily with E6 alone.

Scanning electron microscopy

Human gastruloids, made from the RUES2-GLR line at 72h after aggregation, were washed twice with HEPES buffer and fixed overnight in 3% Glutaraldehyde, 0.05 M sodium cacodylate buffer pH 7.4 at 4 °C. Samples were washed several times in de-ionised water (DIW) at room temperature (RT) to remove fixative. Melinex coverslips at 12 mm diameter were covered with a large drop of poly-L-lysine solution (Sigma P4707) and incubated for 15 minutes at RT. Excess solution was drained off and the coverslips were allowed to air-dry at 37 °C. The gastruloids were transferred to the poly-L-lysine coated coverslips in a drop of DIW and allowed to adhere for about 30 min at RT whilst ensuring that the gastruloids remained covered with DIW. Excess DIW was carefully drained off using a tissue paper and the samples were immediately plunge-frozen in liquid nitrogen-cooled ethane. After freeze-drying overnight in a liquid nitrogen-cooled turbo freeze drier (Quorum Emitech K775X), samples were mounted on aluminium SEM stubs using sticky carbon pads and sputter coated with 35 nm Au followed by 15 nm iridium. Samples were viewed in a FEI Verios 460 scanning electron microscope using an Everhart-Thornley detector in secondary electron mode at 2 keV accelerating voltage and 25 pA probe current.

Immunostaining

Human gastruloids were fixed and immunostained according to the existing methods for gastruloid staining²⁹ unless otherwise stated. The antibodies used were: 1:200 Rabbit anti-CDX2 (ThermoScientific, EPR2764Y); 1:200 Goat anti-GATA6 (R&D Systems, AF1700); 1:200 Rabbit anti-BRACHYURY (AbCam, ab209665); 1:200 Goat anti-SOX2 (R&D Systems, AF2018); 1:200 Mouse anti-CDH2 (BD Biosciences, BD10920); 1:200 Rat anti-CDH1 (Takara, M108), 1:100 Rabbit anti-Wnt3a (ab219412), 1:200 Rabbit anti-LEF1 (ab137872), 1:200 Rabbit anti-FOXA2 (ab108422). All secondary antibodies were all diluted 1:500, and included Alexa-Fluor-488, -568 and -647 conjugated antibodies (Invitrogen).

Adherent cell staining was done using 1:200 Mouse anti-CDH2 (BD Biosciences, BD10920), 1:200 Rat anti-CDH1 (Takara, M108) and 1:200 Rabbit anti-BRACHYURY (AbCam, ab209665) primary antibodies. Quantification was performed using Fiji software on the whole image (histograms) or using a line ROI through the colony (line graph).

In situ hybridisation

Human gastruloids were collected at 72h or 96h post aggregation. After rinsing them briefly in PBS, they were fixed in 4% PFA either overnight or 2h at 4 °C and stored in 100% methanol at -20 °C until further used. In situ hybridization was performed on whole mount gastruloids as described⁹ with minor modifications. Gastruloids were rehydrated by incubating them for 3-5min in series of decreasing concentration of methanol (75%, 50%, 25% and 0% respectively) in TBST (20mM Tris 137mM NaCl, 2.7mM KCl, 0.1% Tween, pH = 7,4). After washing gastruloids in TBST, they were incubated in proteinase K (2.5µg/ml) for 2 mins to make them permeable to probes and post-fixed in 4% PFA for 20min at room temperature, before washing again in TBST. To block non-specific interactions, they were prehybridized at 68 °C for 4-5 h. Hybridization was performed by incubating them in 200ng/ml of specific digoxigenin (DIG)-labelled RNA probes at 68 °C overnight. The probe sequences used can be found in Supplementary Table 2. The following day, after washing the gastruloids at 68 °C, they were incubated in blocking solution for 1.5h at solution at room temperature. Gastruloids were then incubated overnight in anti-DIG antibody coupled to alkaline phosphatase (Sigma) at 1:3,000 dilution in blocking buffer at 4 °C. The next day, they were washed in MABT (100 mM maleic acid, 150 mM NaCl, 0.1% Tween, pH 7.5) overnight at 4 °C. Gastruloids were then washed 3 times with TBST and 3 times in alkaline phosphatase buffer (0.1 M Tris pH 9.5, 100 mM NaCl, 0.1% Tween) and incubated in BM purple solution (Sigma) either at 4 °C or RT until the signal was fully developed. Gastruloids were washed in TBST and post fixed in 4% PFA for 20min at RT. For imaging gastruloids were suspended in CUBIC-R1A tissue clearing reagent^{30,31}.

RT-qPCR

Gene expression was analysed from adherent cells using TRIzol (Ambion Life Technologies) according to manufacturer's instructions. Total RNA was quantified using a NanoDrop 2000C (ThermoScientific) and 5 µg was added to a reverse transcription reaction with Superscript III (Invitrogen) according to manufacturer's instructions. Resultant cDNA was quantified by qPCR with SYBRGreen (Merck) using a liquid handling robot (Qiagility, Qiagen) and analysed on a RotorGeneQ thermocycler (Qiagen). Primer sequences can be found in Supplementary Table 1. Concentration of cDNA was estimated using an in-house MAK2 analysis method, as described in³².

Imaging

Confocal imaging was performed using a LSM700 (Zeiss) on a Zeiss Axiovert 200 M using a 40 EC Plan-NeoFluar 1.3 NA DIC oil-immersion objective. Image capture was performed using Zen2010 v6 (Carl Zeiss Microscopy Ltd, Cambridge UK). All samples were fixed and immunostained prior to imaging. For gastruloids made from the RUES2-GLR reporter line, we never observed fluorescent signal of reporter proteins following our fixation protocol, and therefore used the same antibody design and microscope settings as described.

Wide-field imaging was performed using a 37 °C incubated chamber supplied with 5% CO₂, attached to a Zeiss AxioObserver.Z1 (Carl Zeiss, UK) as described in³³. All images were analysed using Fiji software³⁴, and any adjustments are always consistent within a panel. Presented images have been rotated to align their AP axis horizontally where necessary, as indicated by a dark grey background.

Image analysis: germ layer patterning

Human gastruloids made using the RUES2-GLR reporter line were specifically analysed for dynamic reporter expression. An in-house MATLAB script was developed to assess the dynamic fluorescent marker expression along the AP axis of human gastruloids. Widefield images of gastruloids were taken at 24h, 48h and 72h and aligned along their anteroposterior axis with reference to fluorescent reporter expression. For each sample, a binary image was generated in the bright field channel and used as a mask for all fluorescent channels and the major (length) axis was identified. Consequently, for every pixel along the length axis, the sum of intensity values of the respective channel along the width of the aggregate was divided by the width of the gastruloid at that specific point, yielding the normalized fluorescence intensity along the length of the sample. This process was then repeated for every acquired fluorescent channel. Gastruloids used for this analysis were a full set from one experimental batch, and images were only excluded from the analysis when anteroposterior alignment or binarization were unsuccessful.

Image analysis: elongation quantification

In order to quantify the degree of elongation of human gastruloids, bright field channel widefield images were imported into Fiji³⁴. The length of the longest axis was measured using the line tool, followed by the length of the perpendicular axis at the mid-point of the longest axis line. The ratio of these two values was calculated and plotted by time-point and condition, using R. Significance was assessed using the Welch Two-Sample t-test. This method was used to assess the difference in elongation with and without Chiron pre-treatment, as shown in Fig. 1d.

Image analysis: morphological quantification

The estimate of the proportions of gastruloid shapes (spherical, ovoid, elongated-short and elongated-long) was estimated for multiple independent biological replicates. This was performed using an in-house method derived from that previously described (Turner 2017, doi: 10.1242/dev.150391). Briefly, images were converted into single-channel, 8-bit TIFF files using FIJI³⁴. These were then processed using Python 3.6 (Python Software Foundation, <https://www.python.org/>) and the Open-CV package³⁵ to apply a Gaussian blur before performing Otsu's thresholding and floodfilling with erosion to assign a mask around the shape of each gastruloid. The length and width values were calculated using a rotated bounding box (minAreaRect), which identifies and measures the orthogonally widest and longest parts of the gastruloid. Various additional quantitative features were then extracted from the contours, which were further processed using R. The categories of each shape descriptor were defined as follows: Spherical, Circularity less than or equal to 1.1 or Max Width : Max Length (WL) greater than or equal to 0.95; Ovoid, Circularity less than or equal to 1.2 or WL greater than or equal to 0.9; Elongated – Short, Circularity greater than 1.2 and less than or equal to 1.4 and WL less than 0.9; Elongated – Long, Circularity less than 1.4 and WL less than 0.9. Images were quality controlled for empty wells or those with debris that compromised shape descriptors, using quantification of area or circularity outliers and confirmed manually by examination of images. This method was used to assess the reproducibility of human gastruloid experiments, as shown in Fig. 1e and Supplementary Fig. 1d.

Image Analysis: estimates of cell number

The number of cells per aggregate was estimated using Imaris software (Bitplane) on confocal images stained with Hoechst. Spots were drawn using the internal algorithm, using an estimated xy size of 6 µm, a quality threshold of 2.5 and background subtraction. Because the light penetration only allowed us to image part of the gastruloid we assumed this was on average half of the gastruloid, and so doubled the resultant nuclei estimate. It is likely that this process slightly underestimates the number of nuclei. The quantitative data were subsequently analysed in R. The fitting of an exponential curve was done using the `lm()` function of log transformed data.

Image analysis: subcellular localisation of SMAD1-RFP

To quantify the level of active SMAD1 in each cell of the gastruloid, we sought to determine the nuclear to cytoplasmic ratio of SMAD1-RFP. To do this, we used Imaris software to identify nuclear positions by creating a surface using the Hoechst channel. We then used these surfaces to create two masks: one where everything inside the nuclear mask was set to zero, and one where everything outside the nuclear mask was set to zero. This allowed us to distinguish the nuclear and cytoplasmic components of the SMAD1-RFP signal. To assign the cytoplasmic component to each individual cell, we used Imaris to create Spots using the Hoechst channel (estimated xy diameter: 5.25 µm). These were then processed using 'Spots to Spots Nearest Neighbour Distance' to create maximal cell areas relative to their neighbours. We then used these distance-spots to assess the internal nuclear and cytoplasmic component of SMAD1-RFP in each cell along the AP axis.

The data was subsequently analysed in R, by normalising the mean intensity of the nuclear SMAD1-RFP component to the mean intensity of the H2B-mCitrine value, in order to account for depth bias. This normalised SMAD1-RFP intensity was then divided by the mean intensity of the cytoplasmic SMAD1-RFP, to get the normalised nuclear : cytoplasmic SMAD1-RFP values.

Image analysis: axial patterning quantification

RUES2-GLR gastruloids were fixed at 24, 48 and 72h timepoints, stained for GATA6 and CDX2, and imaged on a confocal. Maximal projection images were generated using Imaris software, and nuclei were identified with Imaris using Hoechst staining (estimated xy size of 6 μm , and quality threshold of 2.5). For each nuclear spot, the mean intensity of GATA6 and CDX2 fluorescence was acquired and plotted using R. Axial patterning was determined in Fiji using the segmented line tool with width 80 and the plotprofile tool. For each gastruloid, the AP axis was normalised between 0 and 1, and the fluorescent intensities were also scaled between 0 and 1 for the minimum and maximum values, in order to aid comparison between gastruloids. The Aspect Ratio of these gastruloids was calculated manually in Fiji using the line tool, where the length of the perpendicular axis at the mid-point of the longest axis line was defined as the width. Three categories, with cut-offs of < 2.0, > 2.0 and < 2.4, and > 2.4, corresponded to the observed longest elongation at 24, 48 and 72 hours, respectively. This method was used for quantifying elongation in confocal images, as shown in Supplementary Fig. 3e-f.

Tomo-sequencing and mapping

Tomo-sequencing was performed using an updated version of published methods^{16,36} and analysed with methods described in van den Brink et al (ref. ³⁹). Briefly, gastruloids were sectioned along their AP axis, and the mRNA-content of each section was extracted using SORT-seq³⁷. Paired end (75 bp) sequencing was performed on the resulting RNA-seq libraries using the Illumina Next-seq sequencing platform. Read 1 contains the section barcode and the unique molecular identifier (UMI). Read 2 contains the biological information. Reads 2 with a valid cell/section barcode were selected and mapped using STAR-2.5.3a with default parameters to the human GRCh38 genome (ENSEMBL version 93), and only reads mapping to gene bodies (exons or introns) were used for downstream analysis. Reads mapping simultaneously to an exon and to an intron were assigned to the exon. Mappabilities for the different samples range between 44% and 47%. For each section, the number of transcripts was obtained as previously described³⁸. We refer to transcripts as unique molecules based on UMI correction.

After mapping, spike-ins, ribosomal, and mitochondrial genes were removed from downstream analysis, together with KCNQ1OT1, LARS2, and MALAT1, because these genes seem to be linked to mapping errors and have been shown to be erroneous in earlier studies. In each gastruloid, data was then normalized to the median number of unique transcripts per slice, and the z-score of each gene was extracted along sections.

Gene expression data analysis

The reproducibility of AP expression pattern between different gastruloid replicates was scored for each gene using a random background model to calculate the Pearson correlation coefficient *P* value (see ref ³⁹ for further details). The *P* value threshold to select reproducible genes was set at 0.001. These significantly reproducible genes were then clustered using a Self-Organising Map (SOM) method, followed by Hierarchical Clustering to determine general patterns of gene expression along the AP axis.

Average gastruloid profiles were generated using the mean of z-scores along the AP axis. When the number of sections between replicates was different, values were quadratically interpolated to fill spaces using the `interp1d` function from the package `scipy.interpolate` (Python 3.6).

Differential gene expression was performed by normalizing the transcripts in each section to 100,000 for all gastruloids; then pooling all sections of each gastruloid together; and finally assessing significant differentially expressed genes based on total expression using the Binomial test.

For smoothed line-graphs of gene expression, the distribution of gene expression along the sections was plotted using R, and smoothed using the `geom_smooth()` function (method = `loess`, span = 0.3, level = 0.5) to minimise background variability. For each gene expression distribution, the confidence interval is therefore shown (at 0.5 Confidence Interval) as a grey ribbon.

Gene Ontology (GO) term analysis for each hierarchical cluster of the Chiron pre-treated human gastruloids was performed using ENSEMBL IDs run with the DAVID Annotation tool⁴⁰ with the human genome as a background model, focussing on Biological Process terms. Statistical correction for multiple comparisons was achieved using Benjamini adjustment.

Gene Ontology for each hierarchical cluster of the human-to-mouse gastruloid comparison was performed using the python package `goatools`⁴¹, which uses Fishers exact test, setting the *P* value at 0.05. Both the list of reproducible genes in each corresponding condition, or the full human transcriptome was set as a background model, focussing on Biological Process terms. Statistical correction for multiple comparisons was achieved using Bonferroni adjustment.

Mouse gastruloid comparison

We compared 72h human gastruloids, which we believe correspond approximately to the ~CS9 human embryo, with 120h mouse gastruloids which are thought to represent an ~E8.0-E8.5 stage embryo and approximately equivalent developmental stages of both species³⁹. These mouse gastruloids were generated from the LfngT2AVenus line⁴². Full details of this dataset can be found in ref³⁹.

Gene reproducibility analysis between the replicates of mouse gastruloids (*P* value < 0.01) and the 2 replicates of human gastruloids (*P* value < 0.001) was performed, independently (as described above). Only genes present in the two separate lists that had human-mouse orthologs were used for downstream analysis. The list of human-mouse orthologs was obtained from Biomart, Ensembl 93. Genes were clustered based on their AP expression pattern in both the mouse and the human average gastruloid simultaneously, as described above. The Pearson correlation coefficient for each gene was calculated between the AP expression pattern of two different samples (in *z*-score units). To assess for significantly correlated genes, we randomly generated 10,000 expression profiles with the same number of sections as in the pair of replicates and determine the correlation value at which less than 100 random profiles have larger correlation values (*P* value < 0.01).

Acknowledgements

We thank V. Trivedi for his help writing the dynamic fluorescent reporter analysis code, D. Turner and A. Baranowski for their help developing the image analysis code, K. Muller from the Cambridge Advance Imaging Centre (CAIC) for help with Scanning Electron Microscopy, the Utrecht Sequencing facility for sequencing and A. Ebbing, J. Vivie and M. Betist for the robotized tomo-seq protocol. We also wish to thank members of the Martinez Arias and van Oudenaarden laboratories, as well as B. Steventon, P. Rugg-Gunn, M. Lütolf, M. Johnson and N. Hopwood for discussions over the course of this work. This work was supported by funds from the Newton Trust (INT16.24b), Leverhulme Trust (RPG-2018-356) and MRC (MR/R017190/1) to A.M.A., and a European Research Council Advanced grant (ERC-AdG 742225-IntScOmics), a Nederlandse Organisatie voor Wetenschappelijk Onderzoek (NWO) TOP award (NWO-CW 714.016.001), and the Foundation for Fundamental Research on Matter, financially supported by NWO (FOM-14NOISE01) to S.C.v.d.B., A.A. and A.v.O. This work is part of the OncoCode Institute which is partly financed by the Dutch Cancer Society. It was also supported by a Constance Work Junior Research Fellowship from Newnham College, Cambridge to N.M. and an Erasmus+ grant to K.A.

Author contributions

N.M. and K.A. designed, optimised and performed the human gastruloid experiments, with help from T.B. and A.M.A. and the A.v.O. lab replicated the entire process, independently. N.M. and S.C.v.d.B. embedded the human gastruloids, and S.v.d.B. performed sectioning and tomo-sequencing preparation. A.A. analysed transcriptomic datasets, with analysis input from N.M., S.C.v.d.B., A.v.O. and A.M.A. N.M. created embryonic illustrations. J.S. designed and made in situ probes, and J.S. and S.G. performed in situ hybridisations. A.M.A. and A.v.O. supervised research. N.M. and A.M.A. wrote the manuscript with considerable input from all authors. All authors reviewed the manuscript.

Data availability

All RNA-seq datasets produced in this study are deposited in the Gene Expression Omnibus (GEO) under accession code GSE123187. Source data for Figs. 1-4 and Supplementary Figs. 1-9 are provided online at <https://bit.ly/3eyS6ZY>.

Code availability

Code is available at https://github.com/vikas-trivedi/HumanGastruloids_Fluorescence, https://github.com/anna-alemany/humanGastruloids_tomoseq and https://github.com/naomi-moris/humanGastruloids_shapeDescriptors.

Supplementary Information for Chapter 4

Corresponding protocol publication

Generating human gastruloids from human embryonic stem cells. Naomi Moris, Kerim Anlas, Sabitri Ghimire, Tina Balayo, Susanne C. van den Brink, Anna Alemany, Alexander van Oudenaarden & Alfonso Martinez Arias. *Protocol Exchange*, doi: 10.21203/rs.2.18203/v1 (2020).

Supplementary Videos

Supplementary Videos 1-3 are available online at <https://bit.ly/3eyS6ZY>.

Supplementary Video 1 | Time-lapse imaging of the S4-GATA6 human ESC line, showing GATA6-GFP expression, from 24 – 35 hours. Representative example of $n = 25$ gastruloids, from 2 independent experiments.

Supplementary Video 2 | Time-lapse imaging of the RUES2-GLR human ESC line, showing BRA-mCerulean, SOX17-tdTomato and SOX2-mCitrine expression, from 0 – 24 hours. Three representative gastruloids are shown. $n = 2$ independent experiments.

Supplementary Video 3 | Time-lapse imaging of the RUES2-GLR human ESC line, showing BRA-mCerulean, SOX17-tdTomato and SOX2-mCitrine expression, from 4 – 61 hours. Multiple individual live-imaging movies of the same gastruloid have been stitched together to give a longer time-course. Note that the objective used changes from 10x (4-12h) to 20x (22-49h) and 10x (52-61h). $n = 3$ independent experiments.

Supplementary Tables

Supplementary Tables 1 & 2 are available online at <https://bit.ly/3eyS6ZY>.

Supplementary Table 1 | Primer sequences for RT-qPCR experiments.

Supplementary Table 2 | Primer sequences for in situ hybridisation experiments.

Supplementary Data

Supplementary Data 1-9 are available online at <https://bit.ly/3eyS6ZY>.

Supplementary Data 1 | Clusters of reproducible gene expression from tomo-sequencing of Chiron pre-treated human gastruloids. ID column includes ENSEMBL ID, Gene name and Chromosome position. For each gene, the assignment to a cluster using Hierarchical Clustering methods is given. Relates to Fig. 3c-d and Supplementary Fig. 5b.

Supplementary Data 2 | Germ layer representation in Chiron pre-treated human gastruloids. Selection of genes from all three germ layers which are represented along the anterioposterior (AP) axis of the human gastruloids. Localisation of each gene along the axis is shown in Fig. 3e. Relates to Fig. 3e.

Supplementary Data 3 | Gene ontology enrichment per tomo-sequencing cluster of Chiron pre-treated human gastruloids. Each sheet of the file corresponds to a different Hierarchical Cluster (cl) and contains the list of enriched Biological Process Gene Ontology (GO) terms for that cluster. GO enrichment was performed using DAVID Functional Annotation tool using the human genome as a background. Adjustment for multiple comparisons was performed, and is reported as Bonferroni, Benjamini and FDR values. Relates to Fig. 3c-d.

Supplementary Data 4 | Clusters of reproducible gene expression from tomo-sequencing of Chiron + SB43 pre-treated human gastruloids. ID column includes ENSEMBL ID, Gene name and Chromosome position. For each gene, the assignment to a cluster using Hierarchical Clustering methods is given. Relates to Supplementary Fig. 8b-c.

Supplementary Data 5 | Clusters of gene expression from tomo-sequencing of Chiron + SB43 pre-treated human gastruloids compared to Chiron pre-treated human gastruloids. ID column includes ENSEMBL ID, Gene name and Chromosome position. For each gene, the assignment to a cluster using Hierarchical Clustering methods is given.

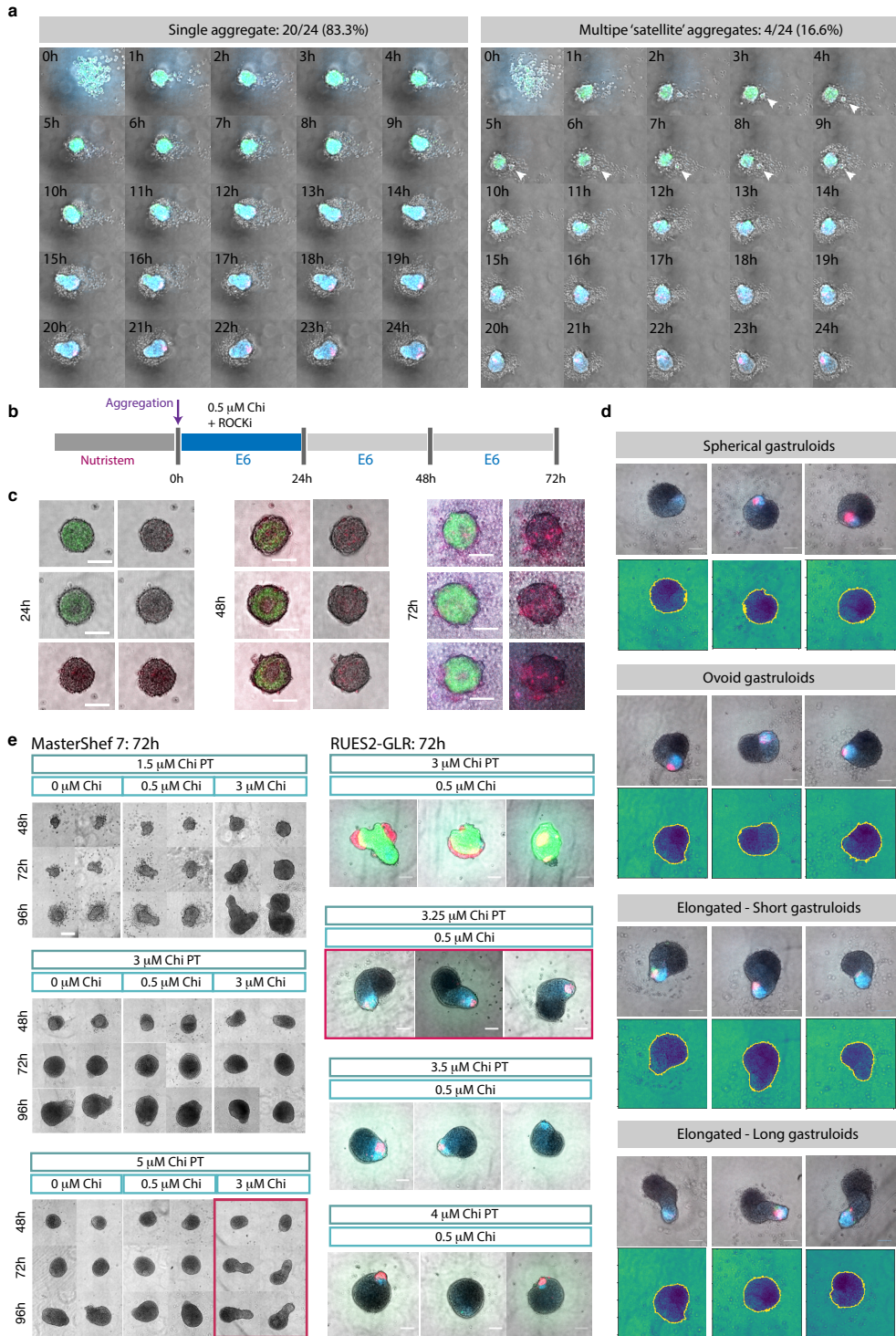
Relates to Supplementary Fig. 7g.

Supplementary Data 6 | Differential gene expression from tomo-sequencing between Chiron and Chiron + SB43 pre-treated human gastruloids. ID column includes ENSEMBL ID, Gene name and Chromosome position. For each gene, the total expression level as the sum of each section is shown for both conditions (total-Chi and total-SB) as well as the mean level of expression in both systems (total-mean). The \log_2 fold change in expression (\log_2FC) and μ ($\log_2\mu$) are calculated alongside the probabilities (prob-Chi and prob-SB) total number (N-Chi and N-SB). The resultant P values are calculated using a Binomial test with the alternative condition used as a background (PvalChi and PvalSB). $n = 2$ Chiron pre-treated gastruloids and 2 Chiron + SB43 pre-treated gastruloids. Relates to Supplementary Fig. 7f.

Supplementary Data 7 | Germ layer representation in Chiron and Chiron + SB43 pre-treated human gastruloids. ID column includes ENSEMBL ID, Gene name and Chromosome position. For each gene, the level of expression across all sections of the average gastruloid are shown. The two sheets correspond to the Chiron pre-treated human gastruloids and the Chiron and SB43 pre-treated human gastruloids, respectively. Relates to Supplementary Fig. 8d.

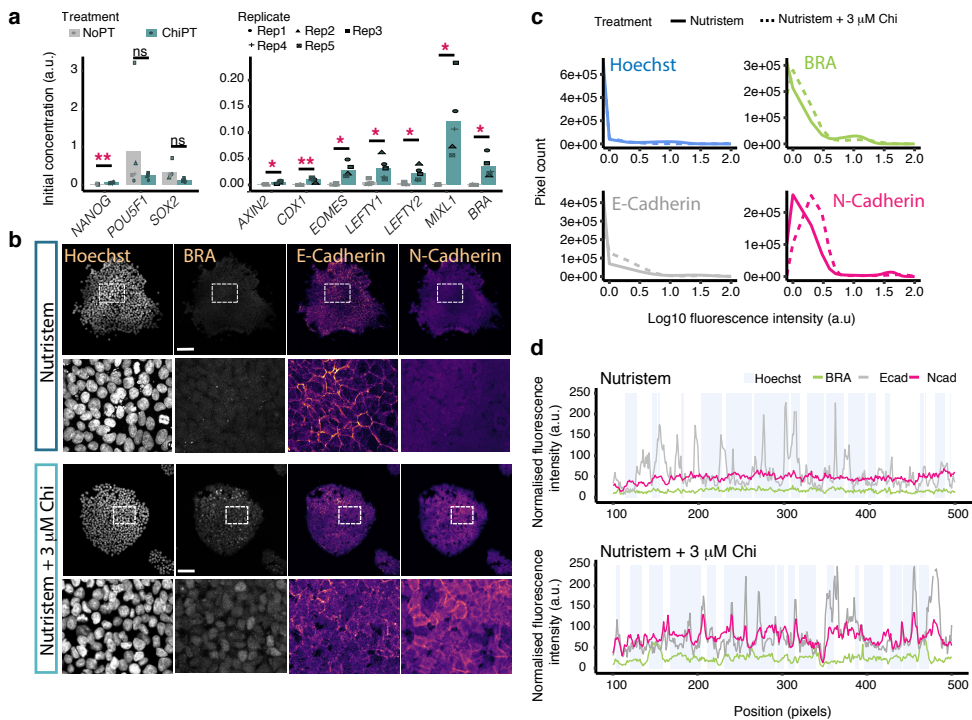
Supplementary Data 8 | Clusters of gene expression from tomo-sequencing of Chiron pre-treated human gastruloids and mouse gastruloids, including GO term enrichment. ID column includes ENSEMBL ID, Gene name and Chromosome position. For each gene, the assignment to a cluster using Hierarchical Clustering methods is given. Each subsequent sheet shows the results of Gene Ontology (GO) term enrichment analysis, per cluster. Relates to Fig. 4g.

Supplementary Data 9 | Clusters of unique and specific gene expression from tomo-sequencing of Chiron pre-treated human gastruloids and mouse gastruloids. ID column includes ENSEMBL ID, Gene name and Chromosome position. For each gene, the assignment to a cluster using Hierarchical Clustering methods is given. Relates to Supplementary Fig. 9.

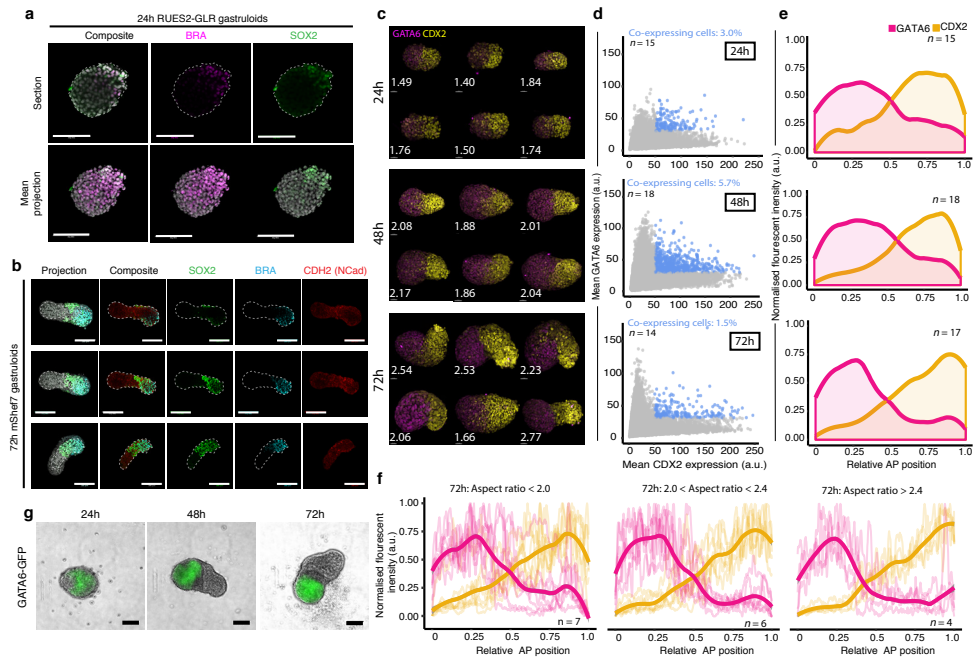


Supplementary Fig. 1 | See next page for caption.

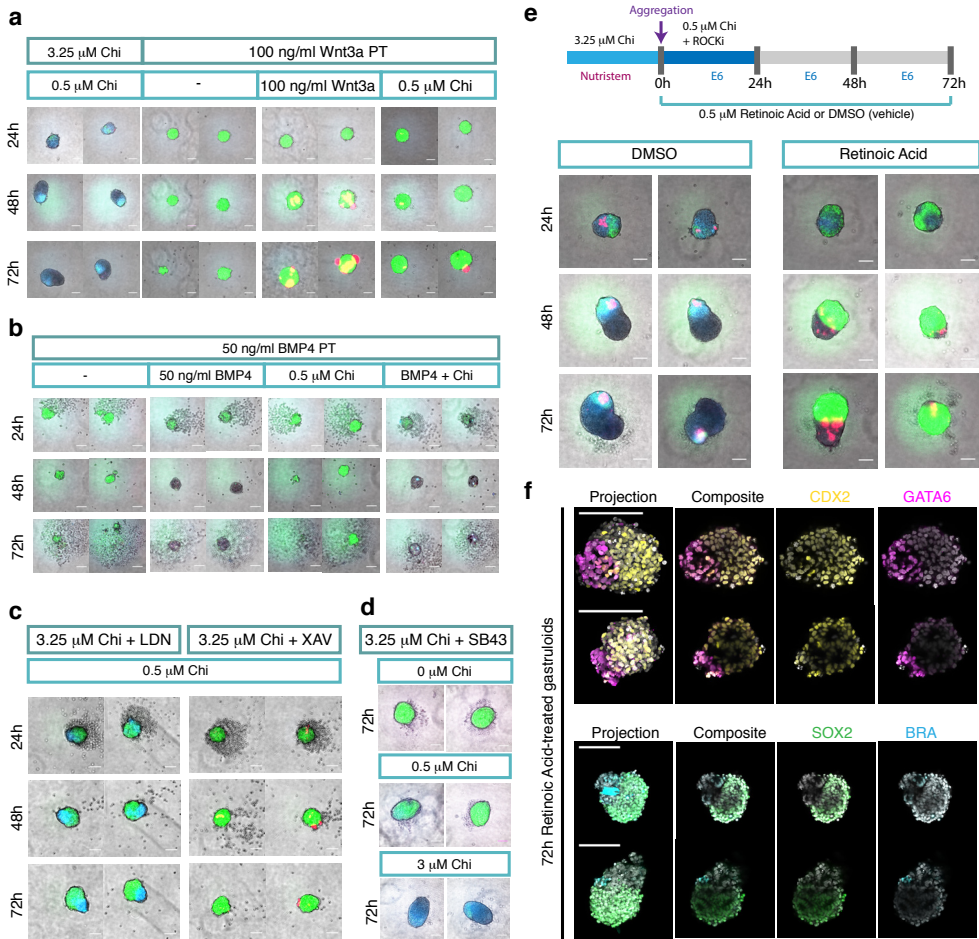
Supplementary Fig. 1 | Chiron pre-treatment optimisation and morphological variability. **a**, Aggregation of single RUES2-GLR cells following Chiron pre-treatment, showing either a single aggregate (left) or presence of transient ‘satellite’ aggregates (right). These typically merge within 10 hours ($n = 38$ gastruloids from $n = 2$ experiments). **b**, Schematic of protocol without Chiron pre-treatment, but with aggregation in Chiron (Chi) and ROCK inhibitor (ROCKi) medium. **c**, Gastruloids made from the RUES2-GLR line without Chiron pre-treatment at 24, 48 and 72h after aggregation. Shown are 3 representative examples for each timepoint ($n = 415$ gastruloids), with all three fluorescent reporters (SOX2-mCitrine, SOX17-tdTomato and BRA-mCerulean; left) and without SOX2-mCitrine (right). Scale bar; 100 μ m. Representative example, from $n = 5$ independent experiments. **d**, Examples of reporter patterning in differential morphology classes, as assessed by automated segmentation providing gastruloid outline boundaries (yellow line indicates boundary used for quantifications). Three representative gastruloids per category are shown ($n = 374$ gastruloids). See methods for details of classification method. Scale bar, 100 μ m. Representative examples, from $n = 7$ independent experiments. **e**, Cell line-dependent optimisation of Chiron conditions. Shown are MasterShef7 cell-derived human gastruloids (left; two examples shown) or RUES2-GLR cell-derived human gastruloids (right; three examples are shown). Scale bars; 100 μ m. Red bounding boxes indicate concentrations at which gastruloids were deemed to be optimally elongated, and resultant conditions for subsequent gastruloid derivation. Representative examples, from $n = 3$ independent experiments.

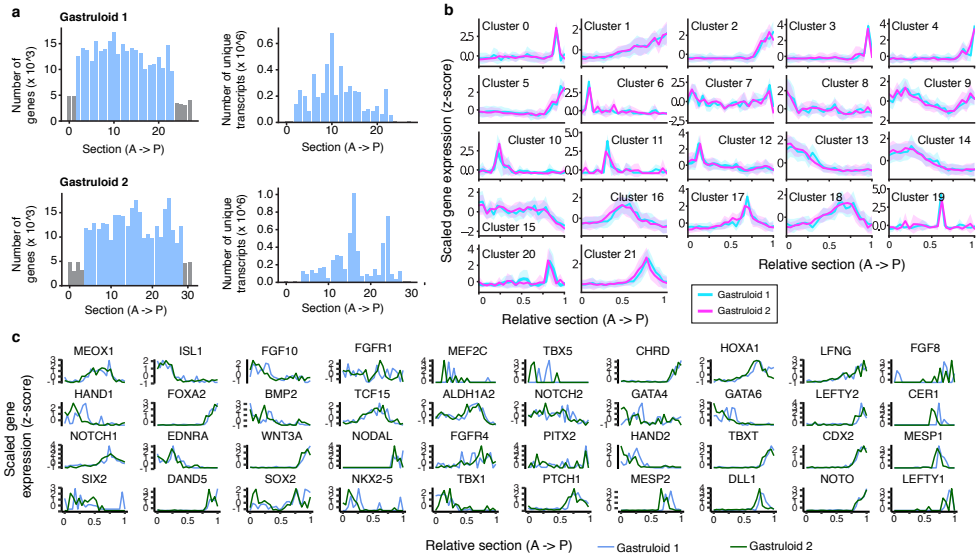


Supplementary Fig. 2 | Effect of Chiron pre-treatment on human embryonic stem cells. **a**, Gene expression following 24 hours of Chiron pre-treatment (Chi PT) in adherent RUES2-GLR cells compared to non-pretreated cells (No PT) in Nutristem alone, as assessed by RT-qPCR. Shown are averages from 5 biological replicates; bars, mean average; points, technical averages for each experimental replicate. Significance (ns, $P > 0.05$, *, $P < 0.05$; **, $P < 0.01$; ***, $P < 0.001$; Welch two-sided, two-sample t-test; Source Data and Methods). **b**, Immunostaining of adherent colonies of RUES2-GLR cells for BRACHYURY, E-CADHERIN and N-CADHERIN (CDH1 and CDH2 respectively) with non-pretreated cells (top) or following 24h Chiron (Chi) pre-treatment (bottom). Dotted region on colony (top panels) shows position of enlarged region (bottom panels). Representative example, from $n = 2$ independent experiments. **c**, Quantified expression from immunostaining of RUES2-GLR cells, as shown in panel b. The whole image was used to generate this data. **d**, Profiles of membrane localisation of E- and N-cadherin from immunostaining of RUES2-GLR cell colonies, as shown in panel b.



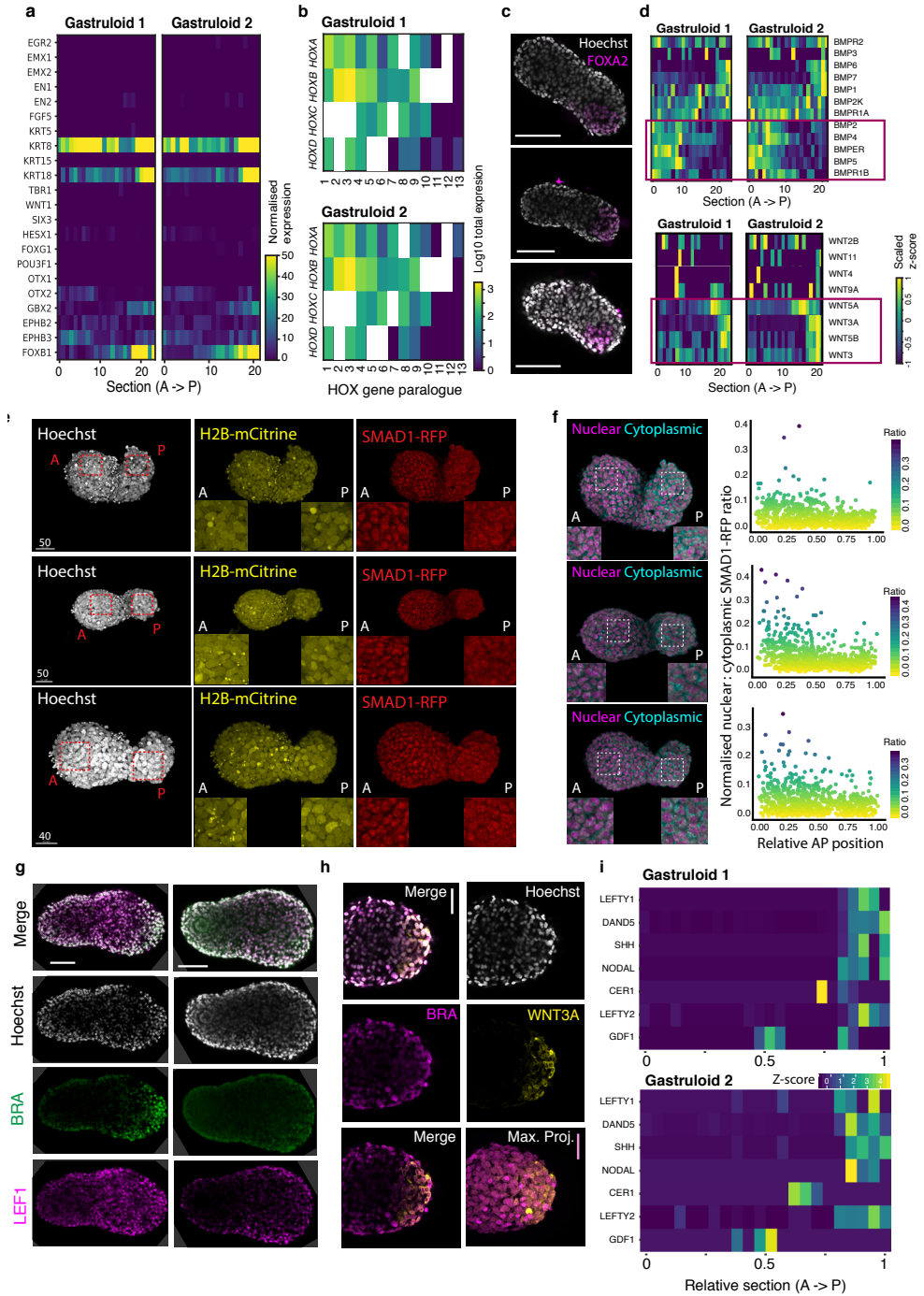
Supplementary Fig. 3 | Establishing axial patterning in human gastruloids. **a**, Immunofluorescence imaging of a RUES2-GLR human gastruloid at 24h. Shown are confocal sections (top) and mean projection (bottom) of the gastruloid. Scale bar; 100 μ m. Representative example from $n = 12$ gastruloids, from $n = 2$ experiments. **b**, Human gastruloids made from MasterShef7 cell line at 72 hours after aggregation, showing BRA, SOX2 and N-Cadherin (CDH2) localisation. Shown are 3 representative examples. Scale bar; 100 μ m. Representative example from $n = 13$ gastruloids, from $n = 3$ experiments. **c**, Projection of immunofluorescently labelled RUES2-GLR derived human gastruloids at 24, 48 and 72h with GATA6 (magenta) and CDX2 (yellow) staining. Shown are 6 representative gastruloids at each timepoint. Scale bar, 30 μ m; small text, Aspect Ratio. Representative examples from $n = 63$ gastruloids from $n = 2$ independent experiments. **d**, Scatterplot of co-expression of GATA6 and CDX2 per cell, across the three timepoints. Blue points, co-expression over threshold; Grey points, expression below threshold; Small text, number of gastruloids in each plot (n). **e**, Relative axial expression of GATA6 (magenta) and CDX2 (yellow) along the AP axis. Small text, number of gastruloids in each plot (n). **f**, Relative axial expression of GATA6 (magenta) and CDX2 (yellow) along the AP axis, as stratified by aspect ratio (as determined using a manual axial patterning quantification, see Methods for details). Small text, number of gastruloids in each plot (n). Thick lines, mean average; Thin lines, individual gastruloids. Representative images of such gastruloid elongation classifications can be seen in panel **c**. **g**, Progressive polarisation and restriction of GATA6-GFP fluorescence to the anterior pole of human gastruloids made from the S4-GATA6-GFP cell line. Scale bar; 100 μ m. Representative example from $n = 17$ gastruloids.



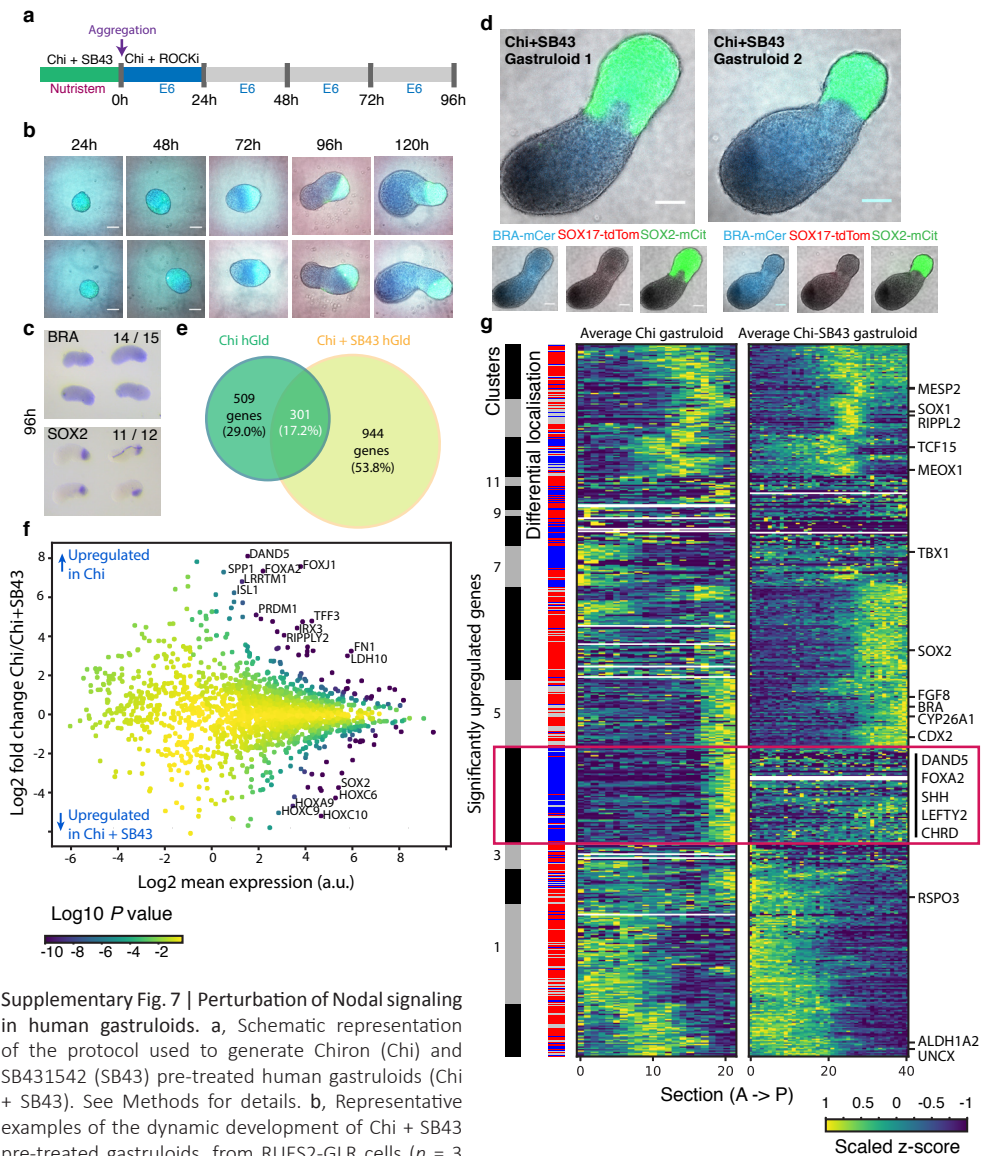


Supplementary Fig. 5 | Spatial transcriptomics by tomo-seq identifies clusters of gene expression. a, Quantification of number of genes (left) and number of unique transcripts (right) detectable in each section along the anterior-posterior (AP) axis of 72h Chiron pre-treated human gastruloids made from RUES2-GLR cells. Blue bars, sections above the threshold used for downstream tomo-seq analysis; Grey bars, sections below the threshold (see Methods for details). Two replicates are shown. b, Average expression patterns along the AP axis of all genes detected in each cluster. Clusters correspond to those in Fig. 3b and Supplementary Data 1. Ribbon indicates standard deviation for the set of genes within each cluster, line to the mean average. $n = 2$ gastruloids. c, Selection of gene traces along the AP axis for both gastruloids. Blue and green lines, expression values for replicate 1 and 2 respectively.

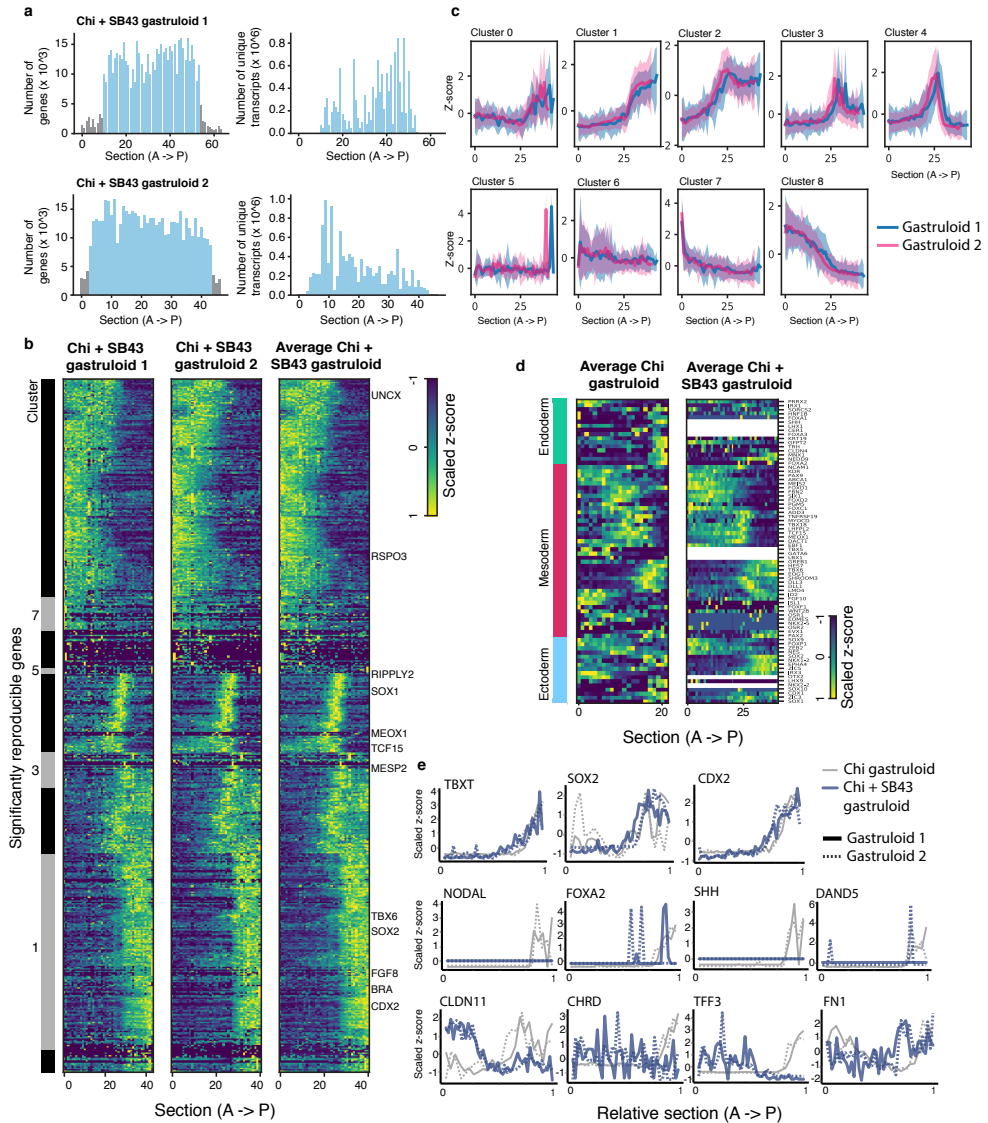
Supplementary Fig. 6 | Transcriptional profiles and antero-posterior (AP) localisation in human gastruloids. a, Normalised expression of anterior neural genes in human gastruloids. b, Total expression (\log_{10} transformed) of each HOX gene across all sections of Gastruloid 1 (upper) and Gastruloid 2 (lower), for all 4 clusters (HOXA, HOXB, HOXC and HOXD). White boxes indicate that a gene is not present in the human genome. a-b, $n = 2$ gastruloids. c, Expression of FOXA2 in the posterior end of 72h Chiron pre-treated RUES2-GLR gastruloids. Three representative examples are shown ($n = 8$ gastruloids). d, Expression of ligands of the BMP (top) and WNT (bottom) signalling pathways. Red box indicates genes with particularly strong AP localisation bias, $n = 2$ gastruloids. e, Maximum projection confocal images of human gastruloids at 72h made from the SMAD1-RFP;H2B-mCitrine cell line. Three representative examples are shown. Inset, close-up of region shown in red dashed-line bounded boxes. Scale bar; 40-50 μm (indicated on image). Representative examples of $n = 19$ gastruloids, from $n = 2$ independent experiments. f, Processing to separate nuclear and cytoplasmic component of SMAD1-RFP signal (left; see Methods for details) and resultant quantification of normalised nuclear : cytoplasmic ratio of SMAD1-RFP along the AP axis (right; each point represents a cell). Three representative examples are shown. Representative examples from $n = 2$ independent experiments. Scale bar as in panel e. g, Immunostaining of LEF1 and BRA expression in 96h RUES2-GLR human gastruloids. LEF1 is localised in a gradient primarily in the posterior portion of the gastruloids. Scale bar; 100 μm . Shown are two representative examples, of $n = 10$ gastruloids, from $n = 3$ independent experiments. h, Immunostaining of WNT3A and BRA expression in 72h RUES2-GLR human gastruloids, showing close-up of posterior end. Scale bar; 50 μm . Max Proj; Maximum Projection. Shown is one representative example from $n = 8$ gastruloids, $n = 2$ independent experiments. i, Localised expression of Nodal signalling-related genes towards the posterior of Chiron pre-treated human gastruloids by tomo-sequencing, $n = 2$ gastruloids.



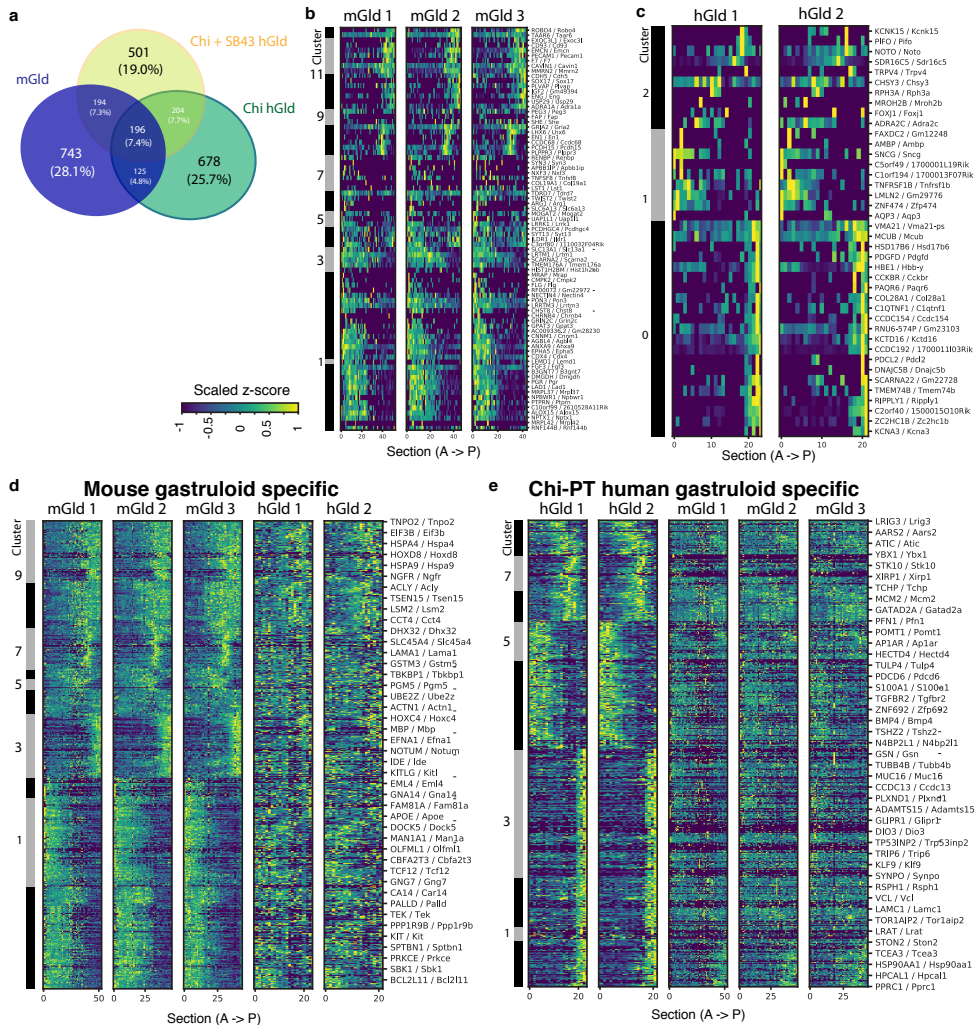
Supplementary Fig. 6 | See previous page for caption.



Supplementary Fig. 7 | Perturbation of Nodal signaling in human gastruloids. **a**, Schematic representation of the protocol used to generate Chiron (Chi) and SB431542 (SB43) pre-treated human gastruloids (Chi + SB43). See Methods for details. **b**, Representative examples of the dynamic development of Chi + SB43 pre-treated gastruloids, from RUES2-GLR cells ($n = 3$ experiments). Colours indicate reporter fluorescence as indicated in Fig. 2a. Scale bar, 100 μm . **c**, In situ hybridisation against BRA and SOX2 mRNA in 96h Chi + SB43 gastruloids. Four representative examples are shown for each gene. **d**, Widefield imaging of the two 120h RUES2-GLR derived Chi + SB43 pre-treated human gastruloids used for tomography. Scale bars, 100 μm . mCer, mCerulean; tdTom, tdTomato; mCit, mCitrine. **e**, Venn diagram showing number of reproducibly-localised genes in the Chiron pre-treated human gastruloids (Chi hGld; green) and in the Chiron and SB43 pre-treated human gastruloids (Chi + SB43 hGld; yellow). Numbers indicate counts of genes and percentage values in brackets indicate proportion of the full figure. See Source Data. **f**, Differentially expressed genes between Chi and Chi + SB43 pre-treated gastruloids (total expression). See Source Data and Supplementary Data 6 and Methods. **g**, Gene expression patterns detected in an averaged Chi pre-treated and averaged Chi + SB43 pre-treated gastruloid. Grey/Black panels show the hierarchical clustering of gene expression; Blue/Red bands indicate selective reproducibility between replicates from one or other pre-treatment conditions (Red, Chi + SB43 only; Blue, Chi only; Grey, both); Dark red box, cluster for which expression is lost following SB43 pre-treatment (Cluster 4); White rows, lack of expression detected. See Methods for details. See Source Data and Supplementary Data 4. **a-g**, $n = 2$ Chi and 2 Chi + SB43 gastruloids.



Supplementary Fig. 8 | Transcriptional profiles of gastruloids exposed to Nodal inhibition before aggregation. **a**, Quantification of number of genes (left) and number of unique transcripts (right) detectable in each section along the anterior-posterior (AP) axis of Chiron + SB43 pre-treated human gastruloids made from 120 h RUES2-GLR gastruloids. Blue bars, sections above the threshold used for downstream tomo-seq analysis; Grey bars, sections below the threshold (see Methods for details). Two replicates are shown. **b**, Significantly reproducible gene expression patterns of individual replicates of Chiron + SB43 pre-treated human gastruloids (left), and resultant average gastruloid (right) along the AP axis. See Source Data and Supplementary Data 4. **c**, Average expression pattern of genes from each cluster shown in panel (b). Ribbon indicates standard deviation for the set of genes within each cluster, line to the mean average. **d**, Expression detected for markers of all three germ layers. White rows indicate lack of expression detected for that gene. See Source Data and Supplementary Data 7. **e**, Gene expression traces along the AP axis of the four human gastruloids (gray lines, Chiron pre-treatment; blue lines, Chi + SB43 pre-treatment; solid lines, Replicate 1; dashed lines, Replicate 2). **a-e**, $n = 2$ gastruloids.



Supplementary Fig. 9 | Unique transcriptional profiles of mouse and human gastruloids. **a**, Venn diagram showing number of common reproducibly localised genes in the Chiron pre-treated human gastruloids (Chi hGld; green), the Chiron and SB43 pre-treated human gastruloids (Chi + SB43 hGld; yellow) and the mouse gastruloids (mGld; blue). Numbers indicate counts of genes and percentage values in brackets indicate proportion of the full figure. **b**, Unique reproducibly-localised gene expression in mouse gastruloids, not detected in Chiron pre-treated human gastruloids. **c**, Unique reproducibly localised gene expression in Chiron pre-treated human gastruloids, not detected in mouse gastruloids. **d**, Genes reproducibly localised in mouse gastruloids and expressed, but not reproducibly localized, in Chiron pre-treated human gastruloids. **e**, Genes reproducibly-localised in Chiron pre-treated human gastruloids and expressed, but not reproducibly localized, in mouse gastruloids. See Source Data and Supplementary Data 9. **a-e**, $n = 2$ human gastruloids, 3 mouse gastruloids.

References

1. Solnica-Krezel, L. & Sepich, D. S. Gastrulation: making and shaping germ layers. *Annu. Rev. Cell Dev. Biol.* **28**, 687-717 (2012).
2. Hyun, I., Wilkerson, A. & Johnston, J. Embryology policy: revisit the 14-day rule. *Nature* **533**, 169-171 (2016).
3. O'Rahilly, R., Bossy, J. & Muller, F. Introduction to the study of embryonic stages in man. *Bull. Assoc. Anat. (Nancy)* **65**, 141-236 (1981).
4. Thomson, J. A. et al. Embryonic stem cell lines derived from human blastocysts. *Science* **282**, 1145-1147 (1998).
5. Zhang, X. et al. *Pax6* is a human neuroectoderm cell fate determinant. *Cell Stem Cell* **7**, 90-100 (2010).
6. Barry, C. et al. Species-specific developmental timing is maintained by pluripotent stem cells ex utero. *Dev. Biol.* **423**, 101-110 (2017).
7. Loh, K. M. et al. Mapping the pairwise choices leading from pluripotency to human bone, heart, and other mesoderm cell types. *Cell* **166**, 451-467 (2016).
8. Warmflash, A., Sorre, B., Etoc, F., Siggia, E. D. & Brivanlou, A. H. A method to recapitulate early embryonic spatial patterning in human embryonic stem cells. *Nat. Methods* **11**, 847-854 (2014).
9. Beccari, L. et al. Multi-axial self-organization properties of mouse embryonic stem cells into gastruloids. *Nature* **562**, 272-276 (2018).
10. van den Brink, S. C. et al. Symmetry breaking, germ layer specification and axial organisation in aggregates of mouse embryonic stem cells. *Development* **141**, 4231-4242 (2014).
11. Davidson, K. C. et al. Wnt/beta-catenin signaling promotes differentiation, not self-renewal, of human embryonic stem cells and is repressed by Oct4. *Proc. Natl. Acad. Sci. USA* **109**, 4485-4490 (2012).
12. Allison, T. F. et al. Identification and single-cell functional characterization of an endodermally biased pluripotent substate in human embryonic stem cells. *Stem cell reports* **10**, 1895-1907 (2018).
13. Martyn, I., Kanno, T. Y., Ruzo, A., Siggia, E. D. & Brivanlou, A. H. Self-organization of a human organizer by combined Wnt and Nodal signalling. *Nature* **558**, 132-135 (2018).
14. Massey, J. et al. Synergy with TGFbeta ligands switches WNT pathway dynamics from transient to sustained during human pluripotent cell differentiation. *Proc. Natl. Acad. Sci. USA* **116**, 4989-4998 (2019).
15. Piersma, A. H., Hessel, E. V. & Staal, Y. C. Retinoic acid in developmental toxicology: teratogen, morphogen and biomarker. *Reprod. Toxicol.* **72**, 53-61 (2017).
16. Junker, J. P. et al. Genome-wide RNA tomography in the zebrafish embryo. *Cell* **159**, 662-675 (2014).
17. Wymeersch, F. J. et al. Transcriptionally dynamic progenitor populations organised around a stable niche drive axial patterning. *Development* **146**, dev168161 (2019).
18. Vega-Hernandez, M., Kovacs, A., De Langhe, S. & Ornitz, D. M. FGF10/FGFR2b signaling is essential for cardiac fibroblast development and growth of the myocardium. *Development* **138**, 3331-3340 (2011).
19. Watanabe, Y. et al. Fibroblast growth factor 10 gene regulation in the second heart field by *Tbx1*, *Nkx2-5*, and *Islet1* reveals a genetic switch for down-regulation in the myocardium. *Proc. Natl. Acad. Sci. USA* **109**, 18273-18280 (2012).
20. Yoney, A. et al. WNT signaling memory is required for ACTIVIN to function as a morphogen in human gastruloids. *Elife* **7**, e38279 (2018).
21. Dunn, N. R., Vincent, S. D., Oxburgh, L., Robertson, E. J. & Bikoff, E. K. Combinatorial activities of *Smad2* and *Smad3* regulate mesoderm formation and patterning in the mouse embryo. *Development* **131**, 1717-1728 (2004).
22. Juan, H. & Hamada, H. Roles of nodal-lefty regulatory loops in embryonic patterning of vertebrates. *Genes Cells* **6**, 923-930 (2001).
23. Kelly, R. G., Buckingham, M. E. & Moorman, A. F. Heart fields and cardiac morphogenesis. *Cold Spring Harb. Perspect. Med.* **4**, a015750 (2014).
24. Wilson, V., Olivera-Martinez, I. & Storey, K. G. Stem cells, signals and vertebrate body axis extension. *Development* **136**, 1591-1604 (2009).
25. Koch, F. et al. Antagonistic activities of *Sox2* and *Brachyury* control the fate choice of neuro-mesodermal progenitors. *Dev. Cell* **42**, 514-526 (2017).
26. Diaz-Cuadros, M. et al. In vitro characterization of the human segmentation clock. *Nature*, doi:10.1038/s41586-019-1885-9 (2020).
27. Canham, M. A. et al. The molecular karyotype of 25 clinical-grade human embryonic stem cell lines. *Sci. Rep.* **5**, 17258 (2015).
28. Moris, N. et al. Generating human gastruloids from human embryonic stem cells. *Prot. Exch.* <https://doi.org/10.21203/rs.2.21540/v1> (2020).
29. BaillieJohnson, P., van den Brink, S., Balayo, T., Turner, D. A. & Martinez Arias, A. Generation of aggregates of mouse ES cells that show symmetry breaking, polarisation and emergent collective behaviour in vitro. *J. Vis.*

- Exp.* **105**, e53252 (2015).
30. Susaki, E. A. et al. Whole-brain imaging with single-cell resolution using chemical cocktails and computational analysis. *Cell* **157**, 726-739 (2014).
 31. Susaki, E. A. et al. Advanced CUBIC protocols for whole-brain and whole-body clearing and imaging. *Nat. Protoc.* **10**, 1709-1727 (2015).
 32. Turner, D. A. et al. Wnt/beta-catenin and FGF signalling direct the specification and maintenance of a neuromesodermal axial progenitor in ensembles of mouse embryonic stem cells. *Development* **141**, 4243-4253 (2014).
 33. Turner, D. A. et al. Anteroposterior polarity and elongation in the absence of extra-embryonic tissues and of spatially localised signalling in gastruloids: mammalian embryonic organoids. *Development* **144**, 3894-3906 (2017).
 34. Schindelin, J. et al. Fiji: an open-source platform for biological-image analysis. *Nat. Methods* **9**, 676-682 (2012).
 35. Bradski, G. The OpenCV library. *Jour. Softw Tools Dr. Dobb* **39**, 184404318 (2000).
 36. Kruse, F., Junker, J. P., van Oudenaarden, A. & Bakkers, J. Tomo-seq: a method to obtain genome-wide expression data with spatial resolution. *Methods Cell. Biol.* **135**, 299-307 (2016).
 37. Muraro, M. J. et al. A single-cell transcriptome atlas of the human pancreas. *Cell Syst.* **3**, 385-394.e3 (2016).
 38. Grün, D., Kester, L. & van Oudenaarden, A. Validation of noise models for single-cell transcriptomics. *Nat. Methods* **11**, 637-640 (2014).
 39. van den Brink, S. et al. Single-cell and spatial transcriptomics reveal somitogenesis in gastruloids. *Nature* (2020) <https://doi.org/10.1038/s41586-020-2024-3>.
 40. Huang da, W., Sherman, B. T. & Lempicki, R. A. Systematic and integrative analysis of large gene lists using DAVID bioinformatics resources. *Nat. Protoc.* **4**, 44-57 (2009).
 41. Klopfenstein, D. V. et al. GOATOOLS: A Python library for gene ontology analyses. *Sci. Rep.* **8**, 10872 (2018).
 42. Theiler, K. The house mouse: atlas of embryonic development. *Springer Verslag*, 2nd edition (1989).



*"A scientist in his laboratory is not a mere technician:
he is also a child confronting natural phenomena that
impress him as though they were fairy tales."*

(M. Curie)

5

Discussion

Some parts of this chapter are based on sections from the following publications:

Generating gastruloids with somite-like structures from mouse embryonic stem cells.

Vincent van Batenburg, Susanne C. van den Brink[§], Marloes Blotenburg, Anna Alemany, Naomi Moris, Peter Baillie-Johnson, Yasmine el Azhar, Katharina F. Sonnen, Alfonso Martinez Arias & Alexander van Oudenaarden[§].

Protocol Exchange (2020)

Debate ethics of embryo models from stem cells.

Nicolas Rivron^{*§}, Martin Pera^{*§}, Janet Rossant, Alfonso Martinez Arias, Magdalena Zernicka-Goetz, Jianping Fu, Susanne C. van den Brink, Annelien Bredenoord, Wybo Dondorp, Guido de Wert, Insoo Hyun, Megan Munsie & Rosario Isasi.

Nature (2018)

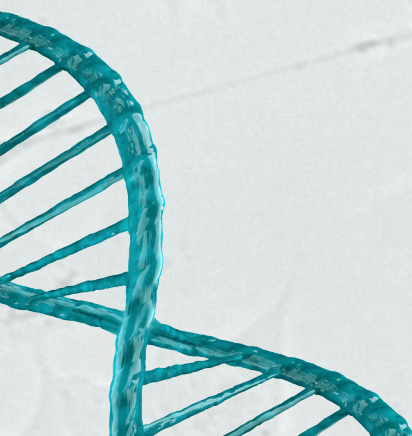
Modelling human embryogenesis: embryo-like structures spark ethical and policy debate.

Ana Pereira Daoud^{*}, Mina Popovic^{*}, Wybo Dondorp, Marc Trani Bustos, Annelien Bredenoord, Susana M. Chuva de Sousa Lopes, Susanne C. van den Brink, Bernard A.J. Roelen, Guido de Wert & Björn Heindryckx[§].

Human Reproduction Update (2020)

* Equal contribution

§ Corresponding author(s)



The first aim of this thesis was to characterize the heterogeneity of quiescent satellite cells in more detail. The second aim of this thesis was to characterize mouse gastruloids in more detail and to develop an improved version of the mouse gastruloids protocol. The third aim of this thesis was to develop and characterize a first human gastruloids culture protocol. The results from the experiments that were performed to address these aims are presented in Chapters 2-4 of this thesis, and are discussed in more detail and put in a broader context in this chapter.

Dissociation protocols can perturb bulk and scRNA-seq gene expression studies

In Chapter 2, we applied scRNA-seq to satellite cells extracted from uninjured muscles. This quiescent satellite cell population had previously been shown to consist of at least two subpopulations^{1,2} (for details, see Introduction in Chapter 1). The full heterogeneity of this population was however not yet known, and had not yet been explored in detail with the at the time still very new scRNA-seq technology. In agreement with previous studies², we indeed observed two subpopulations of satellite cells in our scRNA-seq dataset. One of these populations expressed very high levels of immediate-early genes (IEGs, such as *Fos* and *Jun*) and heat shock protein (HSP) genes (Fig. 1a in Chapter 2). As these genes are well-known stress-response genes³ that are induced in muscles within 3 hours after injury^{4,5}, we hypothesized that their expression could have been induced during the relatively long (~3.5 hours) and harsh dissociation procedure that we employed prior to scRNA-seq in order to extract these cells from their *in vivo* environment.

To explore whether the IEG and HSP transcripts that we detected in our scRNA-seq dataset were induced by the dissociation procedure, we performed single-molecule fluorescent *in situ* hybridization (smFISH⁶) stainings on dissociated and non-dissociated muscles. In addition, we investigated how the duration of the dissociation procedure affected the detected expression levels of these genes. These experiments revealed that the transcriptome of satellite cells is strongly affected by the widely-used dissociation and FACS procedures that we employed prior to scRNA-seq. One major implication of these findings is that various other satellite cell studies in which similar dissociation and FACS procedures have been used may need to be reinterpreted (for examples and extensive discussion, see Supplementary Note 4 in Chapter 2).

Importantly, our stainings revealed that the dissociation procedure used in our study did not only affect satellite cells, but also induced the expression of *Fos* in other cell types present within muscles (Supplementary Fig. 3 in Chapter 2). This observation suggested that the dissociation-induced stress response that we had identified in satellite cells could be more broadly relevant. Consistent with this hypothesis, we found similar stress gene expressing populations in a published pancreas scRNA-seq dataset⁷ and in a zebrafish fin scRNA-seq dataset from our lab. We did in our study however not prove that the expression of stress genes that we observed in these other datasets was indeed induced by the dissociation procedure, as we did not perform stainings on non-dissociated pancreatic and zebrafish

fin tissues. Therefore, we cannot exclude that such stressed populations are not already present *in vivo* in these tissues. Later follow-up studies from other groups however confirmed that similar experimental artifacts indeed also affect various other tissues. By now, similar dissociation-induced stress responses have for example been identified in patient-derived tumour samples⁸, macrophages extracted from mouse brains⁹ and kidney cells extracted from postnatal day 1 mice¹⁰.

The dissociation-induced stress response that we identified in Chapter 2 hampers many gene expression studies. This explains the currently still ongoing efforts into the development of approaches that reduce this artifact. In Chapter 2, we describe two approaches that can be used to remove stressed cells. The first approach entails the *in silico* removal of stressed cells from scRNA-seq datasets, and in the second approach cells are removed experimentally during FACS. While these two approaches work well for satellite cells extracted from uninjured muscles, they have important limitations and cannot easily be applied to other tissues. Both approaches rely on the removal of stressed cells, and can therefore not be applied to cell populations that *in vivo* express stress genes, such as activated satellite cells in injured muscles. Additionally, subpopulations that upregulate stress genes upon dissociation could represent important, functionally distinct subpopulations that respond more strongly to stress. In various recent studies that followed up on our findings, more generally applicable solutions for such gene expression artifacts have been developed. One elegant example of such a solution entails the use of cold-active proteases derived from bacterial species that live in cold environments^{8,10}. Such cold-active proteases allow dissociation at 6 °C instead of at 37 °C, which drastically reduces the dissociation-induced up-regulation of stress genes as the mammalian transcriptional machinery is largely inactive at such low temperatures. Similar reductions in stress gene levels can be achieved by the application of transcriptional inhibitors, such as Actinomycin D, during tissue dissociation procedures^{9,11}. Various other examples of methods that have recently been developed to reduce the effect of such *ex vivo* gene expression changes are discussed in detail elsewhere¹².

5 Interestingly, while dissociation procedures can have a strong effect in some cell and tissue types, not all cell types are equally sensitive to such experimental procedures. Some subpopulations of brain macrophages for example respond more strongly to tissue dissociation than others⁹. Similarly, while adult satellite cells respond strongly to dissociation, we did never detect significant levels of stress gene expression in satellite cells extracted from embryonic muscles (data not shown) or in cells extracted from gastruloids (Supplementary Fig. 2 in Chapter 3). These observations can perhaps be explained by the relatively small size and soft tissue structure of embryos and gastruloids, which consequently can be dissociated with mild and short (~10 minute) dissociation protocols that do- in contrast to the dissociation of adult muscles- not require chopping or tituration through a thin needle. Cells extracted from embryos or gastruloids may therefore experience only minimal levels of cellular stress during dissociation procedures.

scRNA-seq and tomo-seq: useful tools for the characterization of gastruloids

In Chapter 3, we applied scRNA-seq to 120h after aggregation mouse gastruloids and compared the resulting dataset to a previously published mouse embryo scRNA-seq dataset¹³. This allowed us not only to explore what embryonic cell types are present or absent in gastruloids, but also allowed us to investigate to what extent gene expression in specific cell types in gastruloids compares to the *in vivo* population. This comparison revealed various previously unknown features of gastruloids. For instance, we found that neural-crest like cells are present in gastruloids, suggesting that gastruloids could be used to study how and when such cells are formed, and how their migratory behaviour is regulated. In addition, we detected a group of endothelial cells which could be further subdivided into an haemato-endothelial progenitor-like and an endothelium-like subpopulation, suggesting that it might be possible to use gastruloids to model the development of blood vessels and the appearance of blood stem cell precursors within these vessels. We also identify a cell population that expresses many, but not all key markers of primordial germ cells (PGCs). This cluster displayed similarities with both PGCs and extra-embryonic ectodermal cells in embryos. It is therefore currently unclear what these cells are, and follow-up studies are needed to explore what cell type these cells represent.

One limitation of scRNA-seq based characterizations of new model systems is that tissues have to be dissociated into a single-cell suspension before their RNA content can be sequenced. Such dissociation procedures do not only induce the expression of stress genes in some tissues, as shown in Chapter 2, but also inherently result in a loss of spatial information. As spatial information is important for many embryonic processes, such as somitogenesis, we decided to measure spatial gene expression patterns in gastruloids with a robotized version¹⁴ of tomo-seq¹⁵ (Chapter 3 & Chapter 4). One limitation of tomo-seq is that the resulting dataset is one-dimensional. Also, particularly in the case of gastruloids, it is not straightforward to obtain information about gene expression along the dorsal-ventral or left-right axis with tomo-seq. For this reason, we only applied tomo-seq to gastruloids sectioned along their anterior-posterior axis. The resulting dataset is however still very informative, and revealed for instance that the endothelial cells detected by scRNA-seq are localized anteriorly in gastruloids, while the neuromesodermal progenitor (NMP; see Fig. 4 in Chapter 1)-like cells that we detected with scRNA-seq are located posteriorly. In Chapter 3, we also applied tomo-seq to mouse embryos and compared the resulting anterior-posterior gene expression patterns to the ones detected in mouse gastruloids. This comparison revealed many similarities, but also important differences between embryos and gastruloids. Many of the observed differences can be related back to the absence of anterior neural structures. However, we also identified various differences between these two systems that could not be attributed to the absence of the brain, and we did unfortunately not yet manage to draw any strong conclusions from these differences.

Matrigel induces the formation of somite-like structures in mouse gastruloids

The scRNA-seq and tomo-seq based characterization of mouse gastruloids that is presented in

the first part of Chapter 3 revealed that key markers of somitogenesis, such as those that are expressed in the somite differentiation front, are expressed in the correct anterior-posterior location in gastruloids. In embryos, the expression pattern of these genes is dynamic and changes over time, while the embryo grows in posterior direction and generates somites¹⁶. To explore to what extent the dynamic gene expression patterns that regulate somitogenesis in embryos are recapitulated in gastruloids, we followed up on our scRNA-seq and tomo-seq based findings with live imaging microscopy experiments. These movies resulting from these experiments revealed that the periodic Notch-signalling oscillations that are thought to regulate the timing of somite formation in embryos^{16,17} are present in gastruloids. Our findings regarding the expression patterns of key somitogenesis genes and Notch signalling dynamics in gastruloids thus revealed that important parts of the genetic mechanisms that regulate somite formation in vivo are present in gastruloids, which suggested to us that it should be possible to somehow induce somite formation in gastruloids. And indeed, after trial and error and with a bit of luck, we discovered that the formation of somite-like structures can be induced in gastruloids by embedding them in low percentages of Matrigel at 96h after aggregation (Chapter 3). These somite-like structures have defined rostral and caudal halves and appear sequentially in anterior-posterior direction along a clearly defined anterior-posterior axis. Under these conditions, about 50% of the gastruloids form such somite-like structures. This finding may represent a key step towards in vitro high-throughput models that allow the study of somitogenesis in the context of 3D axially organized structures, and shows the potential of gastruloids, which can apparently be optimized and used to study various aspects of embryology, such as somitogenesis, in vitro.

Gastruloids that are cultured without Matrigel display a clear disconnection between body plan formation and the formation of precise morphological structures, such as somites¹⁸ (Fig. 7 in Chapter 1). It had already been hypothesized previously that this disconnection could be linked to the lack of specific mechanical cues that are in embryos provided by the extra-embryonic tissues that are missing in gastruloids¹⁸ (for details, see Introduction and Fig. 1 in Chapter 1). In this thesis, we found that the addition of a small percentage of Matrigel can bridge this disconnection between body plan and detailed morphology, at least in terms of the formation of somite-like structures (Chapter 3). We do currently not know why the addition of Matrigel induces the formation of such somite-like structures. In addition, we do currently not know why the concentration of Matrigel influences the percentage of gastruloids that successfully form somite-like structures. It would be interesting to try to address such questions in follow-up studies, as such studies, which cannot readily be done in mouse embryos, could perhaps provide new insights into the developmental processes that direct somitogenesis.

Human gastruloids model ~19-20 days post fertilization human embryos

In Chapter 4, we describe the establishment of the first human version of the gastruloids system. These human gastruloids are subsequently characterized and compared to mouse gastruloids with microscopy and tomo-seq. Based on this comparison, we suggest that

human gastruloids resemble ~19-20 days post fertilization (dpf) human embryos after 3 days in culture in terms of their anterior-posterior gene expression patterns and body plan organization (Fig. 4 in Chapter 4). This human gastruloid system is the first system that models human embryos at such later stages of development, as other currently published human embryo-like model systems^{19,20} represent earlier developmental stages. In Chapter 4, we also show that such human gastruloids can be used to study how Nodal-inhibition and application of the known vitamin A derived teratogen Retinoic Acid²¹ results in human gastruloids with defects in their body plan organization. These experiments thus illustrate how human gastruloids can be used to study developmental abnormalities in a human context.

The human gastruloids system can be used to study various aspects of human embryology that cannot be studied with in vivo human embryos due to ethical and legal constraints. As it is not allowed to do experiments on > 14 dpf human embryos, the results obtained in such studies can however not easily be validated. We could for these reasons not compare our human gastruloid tomo-seq dataset to a tomo-seq dataset generated for human embryos that are in an equivalent stage of development, and had to rely on a comparison with mouse gastruloids (which have been shown to be comparable to mouse embryos in terms of their anterior-posterior gene expression patterns and cell type composition in Chapter 3) instead. This comparison revealed many similarities, but also some differences between mouse and human gastruloids. We did not manage to draw conclusions from the observed differences between the human and mouse gastruloids systems, partly because the expression patterns of these genes in in vivo human embryos are not known. For similar reasons, we do currently not know whether the differences that we observed between mouse and human gastruloids reflect species-specific differences or differences in the mouse and human gastruloid protocols.

The mouse-human gastruloid comparison presented in Chapter 4 revealed that the anterior-posterior organization of the mesoderm is similar between both systems, and that human gastruloids do also express key markers of somitogenesis in the correct position. Yet, the human gastruloids culture protocol presented in Chapter 4 does, similar to the first version of the mouse gastruloid protocol²², not result in gastruloids that generate somite-like structures. We briefly tested whether Matrigel-embedding could induce the formation of somite-like structures in human gastruloids, as is the case in mouse gastruloids (Chapter 3). However, in our hands, Matrigel had a detrimental effect on human gastruloids and did not induce the formation of somite-like structures (preliminary observations; data not shown). This observation highlights that it is not straightforward to extrapolate findings obtained with embryo-models that are based on mouse embryonic stem (ES) cells to their respective human versions.

Gastruloids: current challenges, potential applications and future perspectives

The results described in Chapters 3 & 4 of this thesis illustrate that it is becoming possible to generate increasingly complex embryo-like structures from mouse ES cells, and suggest

that work with human cells is likely to follow a similar path in the coming years. Although it is currently hard to predict how the gastruloid field will develop, it is not unthinkable that follow-up studies may lead to various medical applications, of which some are briefly discussed below. It is important though to not forget that the field first needs to address various important challenges, and that thorough consultation with ethicists is required before such avenues can be pursued with human ES cells.

The gastruloid system discussed in this thesis might be particularly useful to study developmental processes that cannot easily be studied with other *in vitro* model systems, such as organoids or embryoid bodies (EBs). Examples of such processes include those for which interactions between different embryonic tissue types are important, and those for which body axis formation or posterior elongation are important. Such processes include for example heart development²³ (for which both interaction with the endoderm²⁴ and left-right asymmetry are important), neural tube closure and somitogenesis. Some of the experiments described in Chapter 3 of this thesis, such as those probing into the regulation of the speed of the somitogenesis differentiation front, could not easily have been performed with standard EB cultures, which generally do not form a clear anterior-posterior axis and do not elongate in posterior direction.

In addition to the potential insights into normal development that gastruloids can provide, it might also be possible to use this system to study various developmental abnormalities. Such studies may benefit from the development of gastruloid culture protocols that are based on induced pluripotent stem cells (iPSCs). With such protocols, which do already exist for mouse iPSCs^{18,25} but not yet for human iPSCs, it should become possible to generate patient-specific gastruloid models that could, in particularly when combined with genetic screens, be used to identify mutations underlying developmental defects in a patient-specific manner. Ultimately, the knowledge obtained with such experiments could be used in preimplantation genetic diagnosis tests during IVF procedures. It should also be possible to use embryo models for toxicological studies that assess the effect of environmental components on (human) developmental abnormalities. The results of such studies could guide dietary instructions during pregnancy. Our work from Chapter 4, which revealed that the addition of the known teratogen Retinoic Acid, that is derived from vitamin A (of which intake should be balanced during pregnancy to avoid developmental defects²¹) to human gastruloids disrupts their development, suggests that it may indeed be possible to use gastruloids to pursue such directions.

Interestingly, the gastruloid system is, like other systems that model various stages and aspects of embryonic development^{19,20,26–29} providing a new, different perspective on embryology. With this new approach we are starting to obtain new insights into embryology that could not readily have been obtained with embryos. Traditionally, the study of embryogenesis is based on observing and manipulating human and animal embryos directly, attempting to define biology from the whole embryo to its parts (top-down approach). In contrast, the field

of synthetic embryology is focused on building embryo-like structures *in vitro* from different stem cell types in an effort to mimic and study specific aspects of embryonic development (bottom-up approach). Both approaches are important and complement each other, and having both perspectives can broaden one's view and can provide additional insights into the processes that direct embryonic development. The new perspective on embryology provided by gastruloids has for example challenged the long-standing theory that the extra-embryonic tissues are essential for the symmetry breaking process that results in the anterior-posterior axis of embryos^{22,30}. Our Matrigel results in Chapter 3 provide another example of such a new insight and suggests that just having the key genetic regulators of somitogenesis expressed correctly is not sufficient to create morphological somites, and that specific environmental cues are needed to complete somite formation successfully. Follow-up experiments on such observations, which would be hard to perform with embryos, could teach us something about the role of signals that are *in vivo* provided by extra-embryonic cell layers in such developmental processes.

Another important advantage of gastruloids is that they can easily be generated in high numbers, making them compatible with large-scale drug or genetic screens. Importantly, in contrast to embryos, gastruloids generated for such screens will all be genetically identical when generated from the same stem cell line, which will eliminate potential effects of genetic variability in such screening procedures. In this thesis, we performed a small proof-of-principle screen that revealed that the inhibition of FGF signalling affects the speed of the somite differentiation front in a dose-dependent manner (Chapter 3). In order to successfully perform such high-throughput screening procedures, it is important though to ensure that the reproducibility between the morphology of individual gastruloids within one experiment and across experiments is high. In the first published version of the gastruloid system²² the reproducibility between gastruloids was not yet optimal. However, in the years that followed this initial publication various improved protocols in which higher reproducibility was achieved have been published^{25,31}. In the Matrigel-based modified mouse gastruloid culture protocol that we describe in Chapter 3, reproducibility is however still a limiting factor, as we observed somite-like structures in only a maximum of 50% of the gastruloids. Furthermore, even gastruloids that do generate somite-like structures display considerable variation in their exact morphology (Supplementary Fig. 10 in Chapter 3). In our hands, the percentage of gastruloids that formed somite-like structures successfully also varied between experiments, and was lower with gastruloids that were generated from cells that had been cultured for more than ~2 passages post thawing (preliminary results; data not shown). As a result of this variability it will not be straightforward to measure the effect of small compound inhibitors on the size of the somite-like structures in gastruloids. Such variability can thus be problematic for some experiments, and it is for these reasons important, although probably not straightforward, to develop gastruloid culture protocols that result in gastruloids that generate such somite-like structures in a more reproducible manner.

Another important feature of gastruloids is that they are generated directly from stem

cells and do in contrast to mouse embryos not need to be obtained by scarifying pregnant mice. Gastruloids therefore represent an opportunity to reduce animal use in embryological studies. In contrast to the human gastruloids protocol that we developed in Chapter 4, which is completely animal-free, none of the currently available mouse gastruloids culture protocols are however completely animal-free. The culture medium of the 2D stem cell cultures that are used to generate gastruloids is supplemented with foetal bovine serum, and therefore not free of animal products. In addition, the protocol to generate gastruloids with somite-like structures that we describe in this thesis (Chapter 3) requires Matrigel, which is derived from mouse tumours and hence not animal-free. It is probably wise if the field were to invest time and effort into the development of animal-free versions of such ingredients, as this will not only help to further reduce the amount for animals needed for embryological studies, but will also reduce the batch-effect issues that are associated with the use of such animal-derived products.

Work with human embryo models raises new ethical questions

This thesis describes various scientifically interesting features of gastruloids, such as their ability to generate axially organized somite-like structures *in vitro* and their potential usefulness for high-throughput drug or genetic screening procedures. The same features that make such embryo models scientifically interesting however also raise new ethical questions^{32–34}. The human gastruloids described in Chapter 4 of this thesis do not generate anterior neural (brain) and extra-embryonic tissues, and these structures are therefore not viable and not capable of developing into a foetus. For these reasons, this work has been approved by an independent ethics committee, which was consulted before these experiments were started (see ethics statement in Chapter 4). It is however not unlikely that advanced versions of such (human) models will be developed soon, and examples of ethical questions that will surround work with such (improved) human model embryos include: How far should attempts to develop human embryo models proceed? When do human embryo models become so similar to actual *in vivo* embryos that their moral status becomes equivalent to that of the human embryo? To what extent do the benefits of these embryo models outweigh possible concerns? Which applications of such model systems are or are not acceptable^{32–34}?

The ethical and societal questions surrounding research on stem cell-based embryo models are becoming increasingly complex now that the scientific possibilities are growing. It is not unlikely that it will soon be possible to generate more creative versions of embryo models in which the boundaries between different species are blurred, and it will not be straightforward to tell what the moral status of such mixed embryo models should be. For example, if human gastruloids without a (human) brain-like structure are considered acceptable, then what about human gastruloids with a brain-like structure that is generated with mouse cells? And what is the moral status of an embryo-like structure that is generated with human ES cells but that in terms of its morphology looks more like a fish embryo than like a human embryo? It is certainly important that the scientists that are pursuing such scientific avenues are involved in the debates regarding the ethical aspects of their work. These scientists should

consult with ethicists, philosophers and policy-makers to explain their work, and the potential implications thereof, with as much clarity as possible, so that policy-makers can make well-informed decisions on the guidelines surrounding such work. Lastly, it is important that scientists that are using human stem cells for such experiments share their research plans with independent ethical review committees before performing any experiments, which will ensure that experimentation with human embryo-like models will remain within ethically acceptable boundaries.

Summarizing conclusion

Taken together, the work described in this thesis demonstrates that it is increasingly becoming possible to generate accurate embryo models from mouse ES cells, and that work with human ES cells is following a similar path. Even though it is currently hard to foresee whether there will indeed be medical applications of such models, the field is certainly promising. It will therefore be exciting to see what future avenues, of which some may perhaps not be foreseen and expected, this unfolding field will bring.

References

1. Tierney, M. T. & Sacco, A. Satellite cell heterogeneity in skeletal muscle homeostasis. *Trends Cell Biol.* **26**, 434–444 (2016).
2. Rocheteau, P., Gayraud-Morel, B., Siegl-Cachedenier, I., Blasco, M. A. & Tajbakhsh, S. A subpopulation of adult skeletal muscle stem cells retains all template DNA strands after cell division. *Cell* **148**, 112–125 (2012).
3. Bahrami, S. & Drabløs, F. Gene regulation in the immediate-early response process. *Adv. Biol. Regul.* **62**, 37–49 (2016).
4. Kami, K., Noguchi, K. & Senba, E. Localization of myogenin, c-fos, c-jun, and muscle-specific gene mRNAs in regenerating rat skeletal muscle. *Cell Tissue Res.* **280**, 11–19 (1995).
5. Warren, G. L. et al. Mechanisms of skeletal muscle injury and repair revealed by gene expression studies in mouse models. *J. Physiol.* **582**, 825–841 (2007).
6. Lyubimova, A. et al. Single-molecule mRNA detection and counting in mammalian tissue. *Nat. Protoc.* **8**, 1743–1758 (2013).
7. Wollny, D. et al. Single-cell analysis uncovers clonal acinar cell heterogeneity in the adult pancreas. *Dev. Cell* **39**, 289–301 (2016).
8. O’Flanagan, C. H. et al. Dissociation of solid tumor tissues with cold active protease for single-cell RNA-seq minimizes conserved collagenase-associated stress responses. *Genome Biol.* **20**, 210 (2019).
9. Van Hove, H. et al. A single-cell atlas of mouse brain macrophages reveals unique transcriptional identities shaped by ontogeny and tissue environment. *Nat. Neurosci.* **22**, 1021–1035 (2019).
10. Adam, M., Potter, A. S. & Potter, S. S. Psychrophilic proteases dramatically reduce single-cell RNA-seq artifacts: a molecular atlas of kidney development. *Development* **144**, 3625–3632 (2017).
11. Wu, Y. E., Pan, L., Zuo, Y., Li, X. & Hong, W. Detecting activated cell populations using single-cell RNA-seq. *Neuron* **96**, 313–329.e6 (2017).
12. Pavel, A., Sandra, L., Jaroslav, T., Mikael, K. & Radek, S. Preparation of single-cell suspension from mouse breast cancer focusing on preservation of original cell state information and cell type composition. *bioRxiv* (2019) doi:10.1101/824714.
13. Pijuan-Sala, B. et al. A single-cell molecular map of mouse gastrulation and early organogenesis. *Nature* **566**, 490–495 (2019).
14. van den Brink, S. C. et al. Single-cell and spatial transcriptomics reveal somitogenesis in gastruloids. *Nature* (2020) - in press.
15. Junker, J. P. et al. Genome-wide RNA tomography in the zebrafish embryo. *Cell* **159**, 662–675 (2014).
16. Chal, J. & Pourquié, O. Making muscle: skeletal myogenesis in vivo and in vitro. *Development* **144**, 2104–2122 (2017).
17. Oates, A. C., Morelli, L. G. & Ares, S. Patterning embryos with oscillations: structure, function and dynamics of the vertebrate segmentation clock. *Development* **139**, 625–639 (2012).
18. Beccari, L. et al. Multi-axial self-organization properties of mouse embryonic stem cells into gastruloids. *Nature* **562**, 272–276 (2018).
19. Zheng, Y. et al. Controlled modelling of human epiblast and amnion development using stem cells. *Nature* **573**, 421–425 (2019).
20. Simunovic, M. et al. A 3D model of a human epiblast reveals BMP4-driven symmetry breaking. *Nat. Cell Biol.* **21**, 900–910 (2019).
21. Piersma, A. H., Hessel, E. V. & Staal, Y. C. Retinoic acid in developmental toxicology: Teratogen, morphogen and biomarker. *Reprod. Toxicol.* **72**, 53–61 (2017).
22. van den Brink, S. C. et al. Symmetry breaking, germ layer specification and axial organisation in aggregates of mouse embryonic stem cells. *Development* **141**, 4231–4242 (2014).
23. Rossi, G. et al. Embryonic organoids recapitulate early heart organogenesis. *bioRxiv* (2019) doi:10.1101/802181.
24. Lough, J. & Sugi, Y. Endoderm and heart development. *Dev. Dyn.* **217**, 327–342 (2000).
25. Girgin, M. et al. Generating gastruloids from mouse embryonic stem cells. *Protoc. Exch.* (2018) doi:10.1038/protex.2018.094.
26. Rivron, N. C. et al. Blastocyst-like structures generated solely from stem cells. *Nature* **557**, 106–111 (2018).
27. Sozen, B. et al. Self-assembly of embryonic and two extra-embryonic stem cell types into gastrulating embryo-like structures. *Nat. Cell Biol.* **20**, 979–989 (2018).
28. Harrison, S. E., Sozen, B., Christodoulou, N., Kyprianou, C. & Zernicka-Goetz, M. Assembly of embryonic and extraembryonic stem cells to mimic embryogenesis in vitro. *Science* **356**, (2017).
29. Shao, Y. et al. A pluripotent stem cell-based model for post-implantation human amniotic sac development. *Nat. Commun.* **8**, 208 (2017).
30. Turner, D. A. et al. Gastruloids develop the three body axes in the absence of extraembryonic tissues and

- spatially localised signalling. *bioRxiv* (2017) doi:10.1101/104539.
31. Baillie-Johnson, P., van den Brink, S. C., Balayo, T., Turner, D. A. & Martinez Arias, A. Generation of aggregates of mouse embryonic stem cells that show symmetry breaking, polarization and emergent collective behaviour in vitro. *J. Vis. Exp.* **105**, e53252 (2015).
 32. Pera, M. F. et al. What if stem cells turn into embryos in a dish? *Nat. Methods* **12**, 917–919 (2015).
 33. Rivron, N. et al. Debate ethics of embryo models from stem cells. *Nature* **564**, 183–185 (2018).
 34. Pereira Daoud, A. et al. Modelling human embryogenesis: embryo-like structures spark ethical and policy debate. *Human Reproduction Update* – under revision.



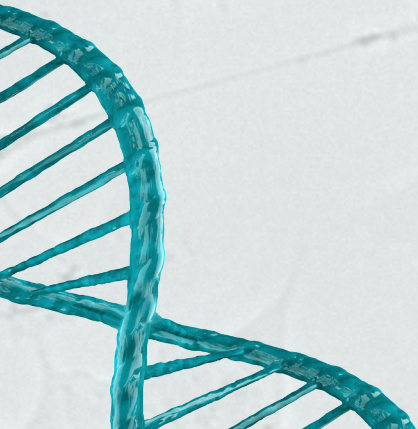
“Sometimes my courage fails me and I think I ought to stop working, live in the country and devote myself to gardening. But I am held by a thousand bonds, and I don’t know when I shall be able to arrange things otherwise. Nor do I know whether, even by writing scientific books, I could live without the laboratory.”

(M. Curie)

&

Addendum

Susanne C. van den Brink



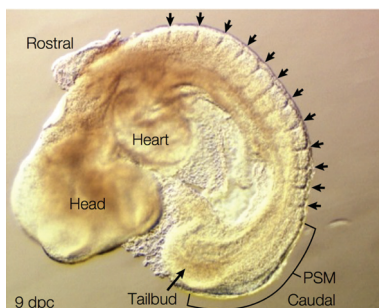
Samenvatting in het Nederlands

Tijdens de embryonale ontwikkeling groeit een bevruchte eicel uit tot een volledig organisme met miljoenen cellen en honderden verschillende celtypes. In de eerste dagen na de bevruchting deelt de eicel zich meerdere keren, wat resulteert in een vroeg embryo: een kleine, ronde structuur die uit slechts enkele honderden niet-gespecialiseerde cellen bestaat. Dit vroege embryo nestelt zich vervolgens in de wand van de baarmoeder. Vlak na de innesteling begint de 'gastrulatie': een proces waarin de embryonale cellen zich beginnen te specialiseren, waardoor steeds meer verschillende embryonale celtypes ontstaan. Tijdens de gastrulatie verandert het embryo ook van vorm: het balvormige klompje cellen groeit uit tot een langwerpige structuur met een duidelijke kop-staart as. Tijdens de gastrulatie worden de cel-specialisatie-processen gecoördineerd met de vormveranderingen van het embryo. Deze coördinatie is essentieel en zorgt ervoor dat de gespecialiseerde cellen op de juiste plek langs de kop-staart as van het embryo terecht komen. De gastrulatie zorgt er daarmee bijvoorbeeld voor dat de hersencellen in de kop van het organisme terecht komen en niet in de staart.

Vlak na de gastrulatie ontstaan langs de rugkant van het embryo somieten: blokjes weefsel die de 'embryonale ruggengraat' vormen. Deze embryonale ruggengraat is goed zichtbaar in Figuur 1. De cellen in deze blokjes weefsel groeien later uit tot de ruggenwervels en skeletspieren van het embryo. In een nog later stadium van de embryonale ontwikkeling specialiseren de skeletspiercellen zich nog weer verder: een deel van deze cellen vormt uiteindelijk de functionele spiercellen, terwijl een ander deel van deze cellen de spierstamcellen vormt.

Gastruloïden: embryonale ontwikkeling bestuderen met stamcellen

Er is nog veel onbekend over de processen die de embryonale ontwikkeling van zoogdieren sturen. Hoe wordt bijvoorbeeld bepaald hoeveel wervels er in onze ruggengraat moeten groeien, of aan welke kant van het lichaam het hart gevormd moet worden? En hoe komt het dat er in deze processen soms iets mis gaat, en kunnen we dat voorkomen? Welke stoffen en omgevingsfactoren zijn eigenlijk wel en juist niet goed voor de embryonale ontwikkeling? Hoe werkt gastrulatie precies, en waarom gaat de gastrulatie soms fout? Omdat het volgens de wet niet toegestaan is om experimenten te doen op menselijke embryo's die zich in het gastrulatie-stadium van de ontwikkeling bevinden, wordt onderzoek naar dit soort vragen



Figuur 1 | Een 9 dagen oud muizenembryo waarin de somieten, de blokjes weefsel die de 'embryonale ruggengraat' vormen, goed zichtbaar zijn. In deze foto zijn de overgangen tussen de blokjes aangegeven met zwarte pijltjes. Copyright informatie: "Reprinted by permission from Springer Nature Customer Service Centre GmbH: Springer Nature, *Nature Reviews Genetics*, "The making of the somite: molecular events in vertebrate segmentation", Saga and Takeda, Copyright © Macmillan Magazines Ltd (2001)."

vaak gedaan met muizenembryo's. Er zijn echter belangrijke verschillen tussen de embryonale ontwikkeling van muizen en mensen, waardoor de resultaten van dit soort experimenten niet altijd relevant zijn voor de embryonale ontwikkeling van mensen. Daarnaast is het lastig om muizenembryo's lang in leven te houden in een petrischaal en is het niet eenvoudig om deze embryo's in grote aantallen te verkrijgen.

Om deze redenen zijn wij in 2013 begonnen met het ontwikkelen van een alternatief onderzoeksmodel: gastruloïden, in het lab gekweekte embryo-achtige structuren gemaakt van stamcellen die in een petrischaal een gastrulatie-achtig proces ondergaan. Deze gastruloïden worden gemaakt door in het lab niet-gespecialiseerde stamcellen te laten samenklonteren. De klompjes cellen die zo gemaakt worden zijn rond en bevatten nog geen gespecialiseerde celtypes. Ze lijken daarmee op embryo's die net ingenesteld zijn in de baarmoederwand, maar die nog niet met de gastrulatie zijn begonnen. Echter, wanneer deze bolletjes vervolgens in de juiste kweekcondities geplaatst worden, 'denken' de cellen dat ze in een echt embryo zitten. Als gevolg hiervan start er in de bolletjes een gastrulatie-achtig proces. Tijdens dit proces groeien de ronde bolletjes uit tot langwerpige structuren met een duidelijk kop-staart as waarin verschillende gespecialiseerde embryonale celtypes op de juiste plek aanwezig zijn. Gastruloïden kunnen daarom gebruikt worden om de gastrulatie, inclusief de daarbij horende cel-specialisatie-processen en embryonale vormveranderingen, in een petrischaal te bestuderen.

De door ons in 2013 ontwikkelde versie van deze gastruloïden zijn gemaakt van muizenstamcellen en bootsen dus de embryonale ontwikkeling van muizen na. Een groot voordeel van dit modelsysteem ten opzichte van muizenembryo's is dat we gemakkelijk grote aantallen gastruloïden kunnen maken. Daardoor kunnen deze gastruloïden bijvoorbeeld gebruikt worden om op grote schaal medicijnen tegen defecten in de embryonale ontwikkeling te testen, of om te onderzoeken welke stoffen toxisch zijn voor ontwikkelende embryo's. Daarnaast kunnen gastruloïden makkelijker genetisch gemodificeerd worden dan echte embryo's, wat het makkelijker maakt om de effecten van DNA-veranderingen op de embryonale ontwikkeling te bestuderen.

Toen ik in 2014 met dit promotietraject begon was echter nog niet duidelijk hoe nauwkeurig de embryonale ontwikkeling van muizen precies wordt nagebootst in muizengastruloïden. Zo wisten we in 2014 nog niet of de gastruloïden alle of slechts een deel van de in embryo's aanwezige celtypes bevatten. Wel was in 2014 al duidelijk dat deze eerste versie van dit modelsysteem wel een aantal, maar niet alle aspecten van de embryonale ontwikkeling na kon bootsen. Zo bleken de gastruloïden bijvoorbeeld niet in staat om somieten, de 'embryonale ruggengraat' te vormen. Daarnaast was het in 2014 nog niet mogelijk om gastruloïden te maken van humane cellen, waardoor we de embryonale ontwikkeling van mensen nog niet met gastruloïden konden bestuderen.

Tijdens mijn promotietraject heb ik, in samenwerking met collega's in het Hubrecht Institute



en collega's aan de Universiteit van Cambridge, verschillende aspecten van dit modelsysteem verder uitgewerkt. Hierbij hebben we ons voornamelijk bezig gehouden met de volgende onderzoeksvragen:

- 1) In hoeverre lijken muizengastruloïden op muizenembryo's? Zijn alle embryonale celtypes aanwezig in gastruloïden, en zo ja, zitten die celtypes allemaal op de juiste plek langs de kop-staart as van de gastruloïden?
- 2) Kunnen we de kweekcondities van de muizengastruloïden verbeteren en daarmee structuren maken die de embryonale ontwikkeling van muizen nauwkeuriger nabootsen?
- 3) Is het mogelijk om een humane versie van dit systeem te ontwikkelen, waarmee de embryonale ontwikkeling van mensen bestudeerd kan worden?

Voor het beantwoorden van al deze vragen hebben we gebruik gemaakt van verschillende laboratoriumtechnieken, die hieronder kort worden uitgelegd.

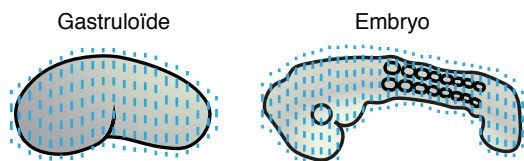
DNA-activiteit en RNA meten met microscopie, single-cell RNA sequencing en tomo-sequencing

De verschillende celtypes die ontstaan tijdens de embryonale ontwikkeling hebben allemaal hetzelfde DNA, maar verschillen ondanks dat toch van elkaar in vorm en functie. De verschillen tussen celtypes worden veroorzaakt door verschillen in hun DNA-activiteit: in elk celttype staan andere delen van het DNA aan of juist uit. Een voorbeeld: het DNA dat codeert voor spier-moleculen zijn in alle cellen van het menselijk lichaam aanwezig, maar staat alleen aan in spiercellen, en staat uit in bijvoorbeeld hersencellen. De actieve delen van het DNA worden door de cel uitgelezen en gekopieerd naar RNA. Deze RNA-moleculen bepalen vervolgens de vorm en functie van de cel. Om terug te komen op het voorbeeld van de spiercellen: in deze cellen is het spier-DNA actief, waardoor er spier-RNA gemaakt wordt. Dit spier-RNA zorgt er vervolgens voor dat deze cel de vorm van een spiercel en niet de vorm van een hersencel heeft.

De onderzoeksgroep waarin ik mijn promotietraject heb doorlopen is gespecialiseerd in het meten van de RNA-inhoud van individuele cellen. Met behulp van zulke RNA-metingen kunnen we meer te weten komen over de eigenschappen van cellen. Zo kunnen we bijvoorbeeld aan de hand van de RNA-inhoud van een cel bepalen wat het celttype is, en kunnen we aan de hand van de hoeveelheid gedetecteerde stress-RNA-moleculen bepalen hoe gezond of gestrest een cel is. Omdat de RNA-inhoud van cellen zoveel interessante informatie bevat, zijn er in de afgelopen jaren veel verschillende laboratoriumtechnieken ontwikkeld waarmee de RNA-inhoud van cellen en weefsels gemeten kan worden. Bij sommige van deze technieken wordt gebruik gemaakt van microscopie: een specifiek type RNA-molecuul krijgt een fluorescente label, waarna de locatie van dit RNA-molecuul in een weefsel bepaald kan worden door met een fluorescentie-microscoop naar dat weefsel te kijken. Een nadeel van dit soort microscopie-technieken is dat we daarmee maar naar een beperkt aantal soorten

RNA-moleculen tegelijkertijd kunnen kijken. Bij andere technieken, zoals ‘single-cell RNA sequencing’, kunnen we de totale set van RNA-moleculen van elke individuele cel bekijken. Een nadeel van single-cell RNA sequencing is wel dat met deze techniek niet bepaald kan worden waar in het weefsel deze cellen zich bevinden. Met een andere techniek, genaamd ‘tomo-sequencing’, kan van alle soorten RNA-moleculen gelijktijdig bepaald worden waar in het weefsel deze zich bevinden. Bij tomo-sequencing wordt de structuur waar we in geïnteresseerd zijn, bijvoorbeeld een embryo, van kop tot staart in hele dunne plakjes gesneden (zie Figuur 2). Vervolgens kunnen we in elk plakje meten welke RNA-moleculen er in dat plakje aanwezig zijn. Deze techniek geeft veel informatie over welke celtypes zich waar in het embryo bevinden.

Figuur 2 | Met tomo-sequencing kan de DNA-activiteit in verschillende locaties gemeten worden. Bij tomo-sequencing wordt een biologisch weefsel, zoals een spier of een embryo, in hele dunne plakjes gesneden (blauwe stippellijntjes). Vervolgens kan precies gemeten worden welke RNA-moleculen aanwezig zijn in welk plakje, wat informatie geeft over welke genen (stukken DNA) actief zijn in welk plakje. Deze techniek kan bijvoorbeeld gebruikt worden om gastruloïden en muizenembryo's in detail met elkaar te vergelijken, zoals is gedaan in Hoofdstuk 3 van dit proefschrift, of om humane gastruloïden met muizengastruloïden te vergelijken, zoals gedaan in Hoofdstuk 4 van dit proefschrift. Credit: Vincent van Batenburg.



Toepassingen van deze technieken in onderzoek naar spierstamcellen en gastruloïden

In dit proefschrift hebben we de hierboven beschreven RNA-technieken gebruikt om muizengastruloïden in detail met muizenembryo's te vergelijken. Op basis van de gevonden overeenkomsten en verschillen tussen embryo's en gastruloïden hebben we een verbeterde versie van het muizengastruloïde systeem ontwikkeld. Daarnaast hebben we in dit proefschrift ook een eerste versie van een humaan gastruloïde systeem ontwikkeld en hebben we de hierboven beschreven RNA-technieken ook gebruikt om onderzoek te doen naar spierstamcellen in de spieren van volwassen muizen. De hoofdstukken van dit proefschrift laten zich als volgt samenvatten:

Hoofdstuk 1 is een introductie. In deze introductie worden de verschillende technieken die in dit proefschrift gebruikt worden in detail uitgelegd. Daarnaast wordt de biologische achtergrond van de verschillende vraagstukken die in hoofdstukken 2, 3 en 4 worden bestudeerd uitgebreid geïntroduceerd.

In **Hoofdstuk 2** hebben we aangetoond aan dat een veelgebruikte onderzoeksmethode waarmee cellen uit organen geïsoleerd worden een stress-reactie kan veroorzaken in een deel van deze cellen. We ontdekten deze stress-reactie per toeval toen we single-cell RNA sequencing toepasten op spierstamcellen. Om de RNA-inhoud in spierstamcellen te kunnen meten, moeten de individuele spierstamcellen eerst uit de spier worden geïsoleerd. De spierstamcellen zitten echter heel erg goed vast aan de spier en daarom is het niet eenvoudig om de spierstamcellen uit te spier te krijgen. De procedure die gevolgd moet worden om de

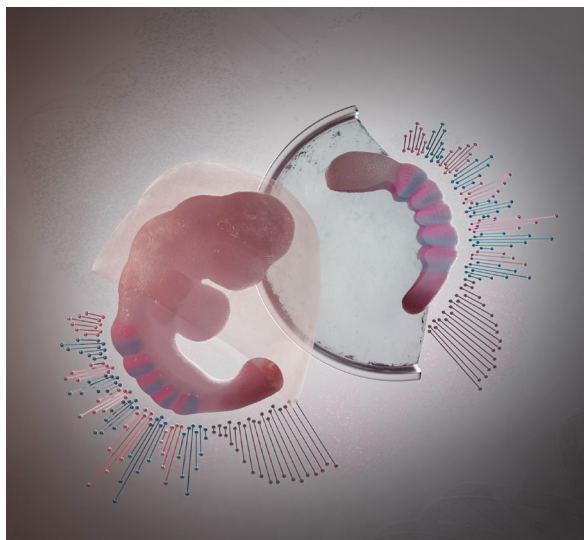
spierstamcellen uit een spier te halen duurt ongeveer 3 uur. Tijdens deze procedure wordt de spier eerst met een mes in kleine stukjes gesneden. Vervolgens worden chemicaliën toegevoegd die de bindingen tussen cellen verbreken en wordt de spier verder uit elkaar gehaald door het spier-chemicaliën-mengsel meerdere malen door een dunne naald te persen. Nadat de spier volledig uit elkaar gehaald is kunnen we de spierstamcellen van de spiercellen scheiden met behulp van een cel-sorteer-apparaat en pas daarna kan de RNA-inhoud van de individuele spierstamcellen gemeten worden. Uit onze metingen op spierstamcellen die met deze standaardprocedure uit spieren van muizen waren gehaald bleek echter dat in een deel van de cellen heel veel stress-RNA-moleculen aanwezig waren. Na vervolgonderzoek met microscopie bleek dat deze stress-RNA-moleculen niet aanwezig waren in spierstamcellen die in intacte spieren zaten en dat deze RNA-moleculen alleen maar aanwezig waren in spierstamcellen die uit een spier waren geïsoleerd. Hiermee toonden we voor het eerst aan dat deze standaard spierstamcel-isolatiemethode de aanmaak van stress-RNA-moleculen veroorzaakt en daarmee RNA-metingen in spierstamcellen kan verstoren. Een belangrijk gevolg van deze ontdekking is dat een deel van de RNA-metingen die in het verleden op uit spieren geïsoleerde spierstamcellen gedaan zijn, gecorrigeerd moet worden. In het laatste deel van Hoofdstuk 2 hebben we twee verschillende methodes ontwikkeld waarmee de gestreste cellen verwijderd kunnen worden en waarmee het door ons ontdekte stress-reactie probleem deels opgelost kan worden.

In Hoofdstuk 2 hebben we ook aangetoond dat onze resultaten niet alleen relevant zijn voor onderzoek naar spieren, maar ook voor allerlei andere onderzoeken waarbij vergelijkbare cel-isolatie procedures gebruikt worden. We hebben namelijk vergelijkbare cel-populaties waarin de stress-genen 'aan' staan gevonden in onder andere de alvleesklier van muizen en in de staart van zebravissen. Dit betekent dat we tijdens onze experimenten met spierstamcellen op een algemeen effect zijn gestuit en dat onze resultaten daarmee belangrijk zijn voor alle wetenschappers die RNA-metingen doen.

Hoofdstuk 3 bestaat uit 3 delen. In het eerste deel van Hoofdstuk 3 hebben we onderzocht in hoeverre muizengastruloïden lijken op muizenembryo's. Om deze vraag te beantwoorden hebben we zowel single-cell RNA sequencing als tomo-sequencing toegepast op muizenembryo's en muizengastruloïden. Met behulp van deze twee technieken konden we precies bepalen welke celtypes in embryo's en gastruloïden aanwezig zijn en waar deze celtypes zich bevinden langs de kop-staart as. Uit deze experimenten bleek dat alle embryonale celtypes, met uitzondering van de hersenen en de placenta, aanwezig zijn in gastruloïden. Zo bleken onder andere bloedvaten en voorlopers van bloedcellen aanwezig te zijn in gastruloïden, wat betekent dat dit modelsysteem gebruikt kan worden om de vorming van bloed te bestuderen. Uit deze experimenten bleek ook dat alle embryonale celtypes in gastruloïden op de juiste plek langs de kop-staart as zitten. Met behulp van deze twee technieken hebben we dus ontdekt dat muizengastruloïden op muizenembryo's lijken, waardoor ze een geschikt model zijn om de embryonale ontwikkeling van muizen te bestuderen in een petrischaal.

In het tweede deel van Hoofdstuk 3 hebben we met behulp van microscopie laten zien dat de moleculaire klok, die de vorming van somieten regelt in embryo's, aan staat en actief is in gastruloïden. Omdat gastruloïden zo makkelijk in grote aantallen verkregen kunnen worden, konden we vervolgens een groot aantal experimenten doen waarin de effecten van veel verschillende soorten chemicaliën op de snelheid van de klok tegelijkertijd gemeten kon worden. Tijdens deze experimenten ontdekten we dat het toevoegen van bepaalde chemicaliën de snelheid van de somiet-specialisatie versnelt. Deze resultaten laten zien dat gastruloïden inderdaad gebruikt kunnen worden om de embryonale ontwikkeling op grote schaal te bestuderen en dat dit tot nieuwe inzichten kan leiden die we niet makkelijk met muizenembryo's hadden kunnen verkrijgen.

In het laatste deel van Hoofdstuk 3 laten we zien dat het mogelijk is om de kweekcondities van gastruloïden te verbeteren en om zo structuren te maken die de embryonale ontwikkeling van muizen nog nauwkeuriger nabootsen. In dit deel van hoofdstuk beschrijven we onze ontdekking dat het toevoegen van tumor-extract ('Matrigel', een gel-achtige substantie) aan gastruloïden de vorming van somieten induceert. Een spannende ontdekking, aangezien het nog nooit eerder iemand was gelukt om somiet-achtige structuren te maken van stamcellen. Daarnaast was het nog nooit eerder gelukt was om zulke complexe embryo-achtige structuren te maken die dit stadium van de ontwikkeling zo nauwkeurig nabootsen (zie illustratie in Figuur 3). Met dit onderzoek laten we dus zien dat gastruloïden ook gebruikt kunnen worden om complexere processen die plaatsvinden in embryo's, zoals de processen die de vorming van somieten reguleren, te bestuderen. Op de kaft van dit proefschrift is een microscopische foto van zo'n in Matrigel gekweekte gastruloïde te zien. In deze gastruloïde is het somiet-RNA blauw aangekleurd; de blauwe delen van de gastruloïde zijn dus de delen waar de somiet-cellen zich bevinden. In de microscopie-foto op de kaft zijn de blokjes en de 'embryonale ruggengraat' van deze muizengastruloïde goed zichtbaar.



Figuur 3 | Illustratie van een muizenembryo (links) en een verbeterde muizengastruloïde (van stamcellen gemaakte embryo-achtige structuur - rechts). De roze-blauw gestreepte blokjes zijn somieten, blokjes weefsel die de voorlopercellen van de ruggenwervels en spieren bevatten. Credit: Núria Taberner.

Hoofdstuk 4 laat zien dat het mogelijk is om humane gastruloïden te maken van menselijke stamcellen. Deze ontdekking heeft mogelijk belangrijke gevolgen, aangezien het niet mogelijk is om dit ontwikkelingsstadium met echte menselijke embryo's te bestuderen, waardoor er heel erg weinig bekend is over de gastrulatie bij mensen. Net als de muizengastruloïden zijn de humane gastruloïden eerst rond en veranderen ze daarna in langwerpige structuren. Een interessant detail is dat de kweekcondities die de humane gastruloïden nodig hebben anders zijn dan de kweekcondities die bij muizengastruloïden nodig zijn. Dit heeft mogelijk te maken met diersoort-specifieke verschillen tussen mensen en muizen. Omdat het niet mogelijk is om deze humane gastruloïden met mensenembryo's te vergelijken, hebben we de humane gastruloïden in dit hoofdstuk vergeleken met muizengastruloïden met behulp van microscopie en tomo-sequencing. Uit deze experimenten bleek dat deze humane gastruloïden net zo georganiseerd zijn als de oorspronkelijke muizengastruloïden uit 2014. Gebaseerd op een vergelijking met afbeeldingen van humane embryo's konden we inschatten dat deze humane gastruloïden op humane embryo's lijken die ongeveer 19-20 dagen oud zijn. Net als de muizengastruloïden maken de humane gastruloïden geen hersenen en is de placenta afwezig, wat betekent dat deze structuren niet levensvatbaar zijn.

In het tweede deel van Hoofdstuk 4 hebben we het effect van verschillende giftige stoffen waarvan bekend is dat ze tot geboortedefecten kunnen leiden op humane gastruloïden bekeken. Tijdens deze experimenten hebben we onder andere Retinoic Acid toegevoegd aan deze humane gastruloïden. Retinoic Acid wordt in het lichaam gemaakt uit Vitamine A en het is bekend dat blootstelling aan een te hoge dosis van Retinoic Acid, bijvoorbeeld door te veel inname van Vitamine A tijdens de zwangerschap, geboortedefecten kan veroorzaken. En inderdaad: ook bij de gastruloïden bleek het toevoegen van een overdosis Retinoic Acid te leiden tot defecten in onder andere de vorming van de kop-staart as. Hiermee hebben we aangetoond dat het mogelijk lijkt te zijn om de effecten van giftige stoffen op de menselijke embryonale ontwikkeling te bestuderen met dit nieuwe humane gastruloïde-systeem.

In **Hoofdstuk 5** worden de resultaten uit de Hoofdstukken 2-4 uitgebreid bediscussieerd en in een bredere context geplaatst. In dit hoofdstuk leg ik uit dat de stress-reactie die wij in Hoofdstuk 2 voor het eerst hebben gevonden, inmiddels door veel meer wetenschappers uit allerlei verschillende vakgebieden is waargenomen. In de jaren na onze publicatie hierover (in 2017) zijn dan ook meerdere wetenschappers aan de slag gegaan met het ontwikkelen van oplossingen voor dit probleem. Hierdoor bestaan er inmiddels verbeterde versies van het cel-isolatie protocol die minder stressvol zijn voor de cellen en die de RNA-metingen niet verstoren. Verder speculeer ik in Hoofdstuk 5 over de mogelijke medische toepassingen van het gastruloïde-vakgebied. Het is daarbij echter wel belangrijk om niet te vergeten dat dit vakgebied momenteel nog in de kinderschoenen staat en dat de huidige versies van de gastruloïde modellen nog verder verbeterd en doorontwikkeld moeten worden voordat het vakgebied kan beginnen aan het ontwikkelen van zulke medische toepassingen. De door ons in Hoofdstuk 3 ontwikkelde muizengastruloïden bijvoorbeeld, lijken slechts één rij somieten te maken, terwijl er in muizenembryo's twee rijen somieten aanwezig zijn. Daarnaast is het

nog niet gelukt om humane gastruloïden met somieten te maken en is het nog niet gelukt om humane gastruloïden te maken van geïnduceerde pluripotente stamcellen*. Daarnaast is reproduceerbaarheid momenteel een belangrijke uitdaging en is er nog grote variatie tussen de verschillende individuele gastruloïden die in een experiment gemaakt worden. Ook een ander belangrijk aspect van dit soort embryo modelsystemen, namelijk het ethische, maatschappelijke en politieke debat omtrent experimenten met humane embryomodellen, wordt besproken in Hoofdstuk 5. De uitkomsten van deze discussies zullen invloed hebben op hoe dit spannende vakgebied zich in de komende jaren gaat ontwikkelen.

** Geïnduceerde pluripotente stamcellen: deze stamcellen komen niet uit IVF-embryo's, zoals bij embryonale stamcellen het geval is, maar worden in plaats daarvan gemaakt door cellen uit volwassen mensen te herprogrammeren naar embryonale stamcellen.*

Dankwoord

During early embryonic development, cellular interactions coordinate the transformation of a small, uniform cluster of cells into a complex 3-dimensional multicellular organism.

During a PhD trajectory, interactions with friends, family, teachers, mentors and scientists from many different backgrounds and institutions coordinate the transformation of a young, immature scientist into a grown-up scientist that is ready to graduate.

I would hereby like to thank everyone who has, directly or indirectly, contributed to my PhD trajectory, and to the work described in this thesis.

De eerste persoon die ik wil bedanken: **Alexander!!!** Dankjewel dat je mij de mogelijkheid wilde geven om in jouw lab en in dit mooie instituut te promoveren. En dat je mij de vrijheid hebt gegeven om mijn passie te volgen en aan gastruloids projecten te werken, ondanks dat dit niet jouw expertise was. Dankjewel dat je bereid bent geweest om mij zo ontzettend veel dingen te leren. Jouw training heeft onder andere mijn presentatie-skills verhoogd en heeft geleid tot belangrijke nieuwe inzichten over welke politiek incorrecte dingen misschien beter niet hardop gezegd kunnen worden tijdens presentaties ;-). Dank ook voor de beursaanvragen waarmee de experimenten van dit promotietraject gefinancierd konden worden. En niet te vergeten: voor de vele gezellige muzikale avonden en drum-gitaar-zang-piano sessies in de kantine van het Hubrecht! Zelfs nu het Hubrecht tijdelijk dicht is gaan deze muzikale activiteiten – in digitale vorm – door via Zoom. Ik heb er absoluut geen spijt van dat ik er destijds voor gekozen heb om mijn PhD in jouw lab te doen (en hoop maar dat jij er ook geen spijt van hebt dat je mij destijds hebt aangenomen ;-)) en zal het Hubrecht, dat inmiddels als een thuis is gaan voelen, ontzettend gaan missen.

And then, **Alfonso!!!** I don't know whether I would have managed to finish this thesis without your endless support. I am very, very grateful that I met you, back in 2013, and that I had the opportunity to perform an adventurous internship in your laboratory in Cambridge that changed so many things in my life (and perhaps also in your life ;-)). I don't think that either of us could ever have foreseen that what started as "Hmm Alfonso, my stem cells are doing something strange" and "Could it perhaps be that these cells are trying to make an embryo?" would so quickly develop into a new and very exciting field. Thank you for being willing to read all the long (loooooong) emails that I have send you over the last few years, about both scientific and personal matters, and thank you for teaching me to trust my scientific intuition. Thank you for being willing to listen to me when I was complaining about my thesis and other things, and thank you for all support and creative ideas. Looking forward to see what additional unexpected discoveries the coming years will bring!

I am also very grateful that the members of my thesis reading committee were willing to read and assess my thesis. **Niels Geijsen, Ina Sonnen, Christine Mummery, Alfonso Martinez Arias**

and **Jeroen Bakkers**: Thank you all for being willing to read and discuss my work, and thank you for all your input and creative ideas for follow-up experiments! **Niels** wil ik daarnaast ook graag bedanken voor alle support in de afgelopen jaren, voor je enthousiasme over gastruloids, voor de tips over communicatie met journalisten, de koffiepauze-momenten, het oprichten van ons consortium (het allereerste consortium waar ik deel van uit maak! De eerste zin uit dit dankwoord komt trouwens overeen met de eerste zin van mijn persoonlijke pagina op onze consortium-website :-)), voor je bijdrage aan de uitbreiding van mijn netwerk – want via jou heb ik ontzettend veel nieuwe mensen heb leren kennen – en voor alle andere dingen die ik hier mogelijk vergeet te benoemen! **Ina**, thank you so much for all your input in the somitogenesis-part of our work. I very much enjoyed the brainstorm sessions during our somitogenesis project, and am very happy that we could work together to explore to what extent gastruloids can be used to study the segmentation clock and somitogenesis in vitro. Thank you for all your support, and for being willing to carefully read and give detailed feedback on particularly the somitogenesis parts of the drafts of our manuscript. In addition, I would like to thank you, **Christine**, for your enthusiasm about this new field, and for your ideas and suggestions for future directions and potential applications of gastruloids. I did actually incorporate some of the ideas that we discussed in Den Haag back in 2018 in the introduction and discussion of this thesis! **Jeroen**, thank you for teaching me about left-right asymmetry during embryonic development during my first master’s internship back in 2012, and for being willing to be part of my thesis assessment committee as well.

Now, I would like to thank all the current and previous members of the Van Oudenaarden lab who contributed to the projects described in this thesis. And for that I should start with: **Anna Catalana!!!** None of the aspects of my PhD would have been the same without you. There are so many things I have to thank you for, that I honestly don’t know where to start! I’m very grateful that you are willing to be my Paranimf during my graduation ceremony (my “wedding with the university”), and thank you for somehow managing to motivate me to finish my thesis. But perhaps more important is that you also taught me how to swear at my “kakka de la thesis” in Catalan – without this essential skill I would NEVER have managed to finish this work ;-). Another thank you for all the essential data analysis work that you have been doing for our two gastruloids manuscripts, your patience with my perfectionism, all the many many gezellige avonden in restaurants, or with sushi in Alexander’s office (sorry Alexander) during late-night paper (re)submission deadline moments. Thank you also for being willing to proofread all parts of my thesis, for allowing me to visit your place and eat sushi there when all restaurant suddenly closed a few weeks ago, for throwing snowballs indoors, and for etc. etc. – I probably missed many things, no? Thank you for creating such amazing memories that will stay with me forever!

Vincent, eerst masterstudent, later PhD student in het Hubrecht gastruloids team: dank voor de ongelofelijk grote hoeveelheid werk die je hebt verzet in korte tijd, resulterend in een ontzettend mooie gezamenlijke publicatie! Al die weekenden, al die vooral aan het eind wel heel erg saaie en repetitieve celweek-experimenten, en dan daarna een oneindige

hoeveelheid revisie-rondes waarbij figuren telkens weer aangepast en daarna opnieuw aligned moesten worden. Ik weet dat het niet makkelijk is geweest, maar gelukkig bleek dit werk achteraf gezien allemaal goed uit te pakken en is er een publicatie uit voortgekomen waar we trots op kunnen zijn! Overigens heb ik je nog niet durven vertellen dat er ook in de door de publisher gecorrigeerde versie van ons gepubliceerde paper, ondanks al ons perfectionistische gepriegel, toch nog een rare spelfout in het main figure staat ;-P.

And there are so many more amazing members of the Van Oudenaarden lab that I want to thank for all their contributions! **Dimitrios**: thank you for your enthusiasm and positivity, and for your awesome musical skills! I am very curious to see where you will end up next. **Anniek**, de eerste masterstudent die ik begeleid heb: dankjewel voor je enthousiasme en voor je latere input op ons somitogenesis-waves-in-gastruloids verhaal. **Marloes, Helena** and **Peter**, thank you for all feedback on the various versions of our manuscripts and figures, and together with **Jörg** and **Kim, Annabel**, and many others for the many gezellige diners. And **Peter**, thank you for being willing to help me to make a “snow-gastruloid” in winter 2017. **Vivek**, thank you so much for your input and suggestions, and for setting up the interactive website associated with our mouse gastruloid publication. In addition, I would like to thank you for all your brilliant, hilarious title suggestions – I still think that “*We applied these cool new technologies to stem cells doing fancy stuff – reviewers won’t believe wat happened next!!!*” would have been a way better title for this thesis! **Mike**, thank you as well for being willing to help with the website, and for helping so many people in the lab with so many things. **Reinier**: dankjewel, dankjewel, dankjewel voor al die vele celsorteerexperimenten!! Onder andere bedankt voor dat ene late avond/nacht-experiment wat last-minute halsoverkop ingepland moest worden zodat we nog net, een week voor de resubmission deadline van het satellite cell paper, een laatste en essentiële dataset konden genereren. En **Stefan**: dankjewel voor de spierstamcellen-sorts! **Nune**, thank you for your enthusiasm, and for patiently waiting till I finally managed to find time to talk to you when you started here. **Christoph**, thank you for your quietness when sitting next to me in the lab – very much appreciated as I am somehow, unlike most people in this lab, unable to pipette and talk simultaneously. **Anna L!!** Thank you for alle gezelligheid, for essential experimental advice during smFISH experiments in my satellite cells project, and for all support on a more personal level. I will truly miss you, and hope that we will stay in touch! **Josi**, dankjewel voor de vele gesprekken, feedback, en dankjewel dat ik af en toe even lekker kon zeuren over de dingen die een PhD student soms dwars zitten tijdens een PhD traject ;-). En natuurlijk voor alle bestellingen – wat een werk was dat altijd... Ik beloof dat ik zal proberen om nooit meer te rennen in het lab (is moeilijk, ik heb nou eenmaal veel energie...) en dat ik me de volgende keer als het sneeuwt in zal houden en geen sneeuwballen in de vriezers van het lab zal bewaren.

Nico, thank you for being Nico, for your excellent and critical feedback on my work, and for accepting my craziness. And **Freddie** thank you for being Freddie. I hope that you will soon be able to admit that you are in fact very (VERY) much creeped out by me, especially when I’m “sneaking around” in the corridors again. **Jake**, thank you for the late-night conversations,

for keeping me company during dinners in the Hubrecht, for playing keyboard in Alexander's office almost daily in the evenings, and for your company on our adventurous flight from Stockholm to Amsterdam during a storm a few months ago. **Buys**, dankjewel voor je droge humor, en voor je bijdragen aan mijn "opvoeding" die Alexander niet alleen aan bleek te kunnen – dankzij jou weet ik nu dat het niet gepast is om naar Frankenstein te refereren tijdens werkbesprekingen. Helaas moet ik bekennen dat jouw opvoedpogingen niet helemaal geslaagd zijn en er om een of andere vreemde reden toch ergens een quote uit Frankenstein terecht gekomen is in dit proefschrift – helemaal per ongeluk natuurlijk! Heb je hem al kunnen vinden? **Maria**, thank you for your quiet kindness, and good luck with the laatste loodjes of your PhD! **Joe**, **Jeroen** and **Francis**: thank you for all long conversations about so many different topics during lunch, and **Joe**, thank you for not making too much fun of me when you figured out that I don't know what a "halogen" is ;-). **Iris**, dankjewel voor de knuffels en voor de mooie foto van een regenboog die precies op mijn huis eindigde! En **Marijn** en **Floris**, vielen dank voor de geweldige zeil-uitjes, die me altijd bij zullen blijven. **Annemiek**, dankjewel voor je hulp met zo ontzettend veel verschillende dingen! Dankjewel voor je hulp met het inplannen van vergaderingen, het samenstellen van mijn promotiecommissie, en voor de telefoongesprekken op de momenten dat ik het even niet meer zag zitten toen vlak voor mijn promotie wereldwijd de pleuris (of was het de corona?) uit brak. Dankjewel voor je geduld met mijn ongeduld met formulierwerk en promotiecommissies. Maar bovenal: dankjewel voor de gezelligheid en leuke spontane gesprekken over allerlei verschillende onderwerpen!

En dan alle "ex-members" van het Van Oudenaarden lab die bijgedragen hebben aan dit traject! Te beginnen met **Mauro**! Zonder jou zou ik nu nog niet geweten hebben hoe ik single-cell RNA sequencing experimenten uit moet voeren. Je hebt mij zowel het handmatige CEL-seq1 als het gerobotiseerde CEL-seq2 protocol geleerd – wat een opluchting dat jij het op een gegeven moment voor elkaar kreeg om een deel van dit protocol te optimaliseren en we niet meer handmatig en met handen vol pipetteer-blaren honderden TRIzol-extracties per dag hoefden uit te voeren! Daarnaast was het echt ontzettend fijn om jou als collega te hebben – ik weet niet of je wel door hebt hoe ontzettend veel positieve invloed jij op de sfeer in een groep mensen hebt! **Kay** – ik mis je, want ik heb al ruim een jaar lang niemand om te out-Kayen... Jij was een van de weinigen die in ieder geval nog een klein beetje tegen mijn niet heel standaard humor in durfde te gaan – al denk ik met vrij grote zekerheid te kunnen zeggen dat zelfs jij niet 100% tegen mijn opmerkingen op kon – en daar ben ik nog steeds HEEL erg trots op ;-). **Chloé**!!! Thank you so much for organizing all those amazing social activities, and sorry that I was somehow not able to take initiative in organizing such events myself. I hope you can forgive me, and I hope that you are doing relatively well in Boston during these crazy times... **Adi**, thank you for being you, and thank you for your musical and vrolijke positive input on the lab. **Abel**! It was so great to share the office with you, and to briefly collaborate in the satellite cells project – you are such an awesome and sweet person! I hope you have by now forgiven me about receiving the blame for the fly infection in the plants in our office – I just didn't dare to admit that this was in fact not your, but my fault. **Lennart**, **Magda**, **Nicola**, **Bastiaan**, **Philipp**, **Maya**, **Sid** and **Dominic**: thank you all for creating such a gezellige

atmosphere during (the first years of) my PhD, and for all your input, ideas and contributions to the scientific chapters of this thesis. **Dylan!** De persoon die mij, na de publicatie over spierstamcellen, met één opmerking deed realiseren dat het zonde zou zijn als ik niet terug zou switchen naar het gastruloids vakgebied. Dankjewel hiervoor! **Jean-Charles:** thank you for your inspirational violin music and critical scientific questions, en **Judith,** dankjewel voor de 10x Genomics experimenten en voor het maken van creatieve posters voor AvO-borrels waar we allemaal trotser op zijn dan we toe durven te geven!

Now, I want to switch to thanking the very (VERY!) important collaborators on the other side of the great ocean. It is unfortunate that none of you will probably be able to be here in June to attend the graduation, but I will definitely send copies of this thesis overseas. I sincerely hope that we will soon be able to finally celebrate the thesis and the acceptance of both publications, and be able to have real-life tea breaks together again. **Alfonso** is already thanked above, and therefore I would like to start with Naomi here. **Naomi,** thank you for all your input, suggestions, discussions, and for the huge amount of work you have done to put an amazing first human gastruloids paper together! Thank you for your Utrecht visits, and for the late-night dinners during human gastruloid and zebrafish pescoid tomo-seq experiments in Cambridge, together with **Vikas** and **Kerim.** Wishing you all the best of luck in your new position – I am sure you will do great! **Kerim, Tina, Julia** and **Sabitri** – thank you all for this amazing collaboration, and for allowing Anna and me to join your team and your wonderful work with human stem cells! And then of course I should not forget to also thank **David** and **Peter,** both also part of the 2013-2014 gastruloids team in Cambridge, without whom the very first gastruloids publication from 2014 that has had such a huge impact on my life would not have been possible. I would also like to thank both **Peter** and **Jenny** for embedded mouse embryos for tomo-seq, and **Peter** for performing the pilot Matrigel-embedding experiments that motivated us to try to embed mouse gastruloids in Matrigel in Utrecht.

In addition to the people in our lab, there are also many other people in the Hubrecht that I would like to thank for their scientific or non-scientific contributions, of gewoon omdat ze het Hubrecht een fantastisch gezellige en inspirerende plek maken. Te beginnen met **Bas!!** FOS!!!! AAAAHHHH!!!! Gelukkig hoef ik jou niet echt te missen als ik straks gepromoveerd en oud ben en het Hubrecht niet meer zomaar in mag – ik heb je immers jaren geleden al gekloond. **Wouter** en **Yasmine,** dank voor jullie tips en ideeën over het versimpelen van de Matrigel-embedding van gastruloids, voor het delen van reagentia en plasmiden, en voor de gezelligheid in de wandelgangen. **Mariëtte:** dank voor de “mini-mediatraining” waarmee je mij zelfvertrouwen over communicatie met de media hebt weten te vergroten. **Stieneke,** dank voor je advies over stamcellen en FBS, maar vooral ook voor het geduld waarmee je steeds weer alle e-mails, post en pakketjes die regelmatig bij de verkeerde “van den Brink” terecht kwamen naar mij doorstuurde. **Jeroen** en **Harry:** dank voor hulp en tips voor de urenlange tomo-seq cryotoom sessies, en voor hulp met het meten van de grootte van somieten in muizenembryo's. **Nicolas,** thank you for the short but successful collaboration that resulted in our ethics comment publication in *Nature*, and **Javier, Pascale** and all other members of

the Geijsen lab for their input and support during our experiments. **Annabel** en **Marco**: veel dank voor de vele gezellige gesprekken en voor het gerobotiseerde tomo-seq protocol. **Erica, Geert, Else, Jens, Erik** and all other people that contributed to our musical borrels, thank you for being there and for not being afraid to show your talents! **Amanda** and **Sanne**: thank you for the much-appreciated late-night experiments chats. I also would like to thank EVERYONE who ever replied to the many labhelp-emails that our gastruloid team sent out to the whole institute when we were in urgent need for many different non-standard reagents during our strict paper (re)submission deadlines; in particular **Jens, Juri** and **Joep**! And then, of course, very importantly: **Catherine Robin, Fanny** and **Carla** and all other members of the Robin laboratory, with who I have had a successful collaboration in 2014-2017: thank you! Dan wil ik daarnaast ook alle **stamcellen** van het Hubrecht bedanken dat ze zo bereidwillig waren om zulke mooie structuren voor ons te maken.

Next, importantly, I want to thank our “neighbours” from the **Jop Kind** lab, with which we have been sharing the cell culture room, and thereby the many ups and downs that we experienced in this tiny room, from sad gastruloids with a bacterial (fungal? We actually still don’t know what it was...) infection to huge eureka-moments with very happy gastruloids that for the first time started to generate somite-like structures. **Sandra, Kim, Corina, Ellen, Samy, Silke, Koos** and **Isabel** (who also helped with setting up in situ gastruloids hybridization protocol from Switzerland here, together with **Josi** and **Jelmer**): thank you voor alle gezelligheid en de vele mooie herinneringen!

En dan natuurlijk **Melanie**! Zo fijn dat je de vormgeving van mijn proefschrift wilde doen toen dat mij door RSI-klachten zelf niet meer lukte aan het eind van een lange PhD met iets te veel computer- en schrijfwerk. Dankjewel voor alle input en feedback op de lay-out! Daarnaast ben ik ontzettend blij dat het Hubrecht zo’n fijne communications-officer heeft, en dat je bereid was om mij te ondersteunen op de momenten dat de media-aandacht en alle andere dingen die kwamen kijken bij onze publicaties over verschillende soorten “knutsel-embryo’s” mij even teveel werden.

Daarnaast ben ik alle andere medewerkers van het Hubrecht die alle belangrijke processen regelen ontzettend dankbaar: **Rob** (dank voor alle gezellige mini-pauzes!) en alle andere proefdierversorgers, de medewerkers van de **bestelafdeling, personeelszaken, financiën** en **administratie**, de medewerkers van de **technische dienst** (die ik wel eens ‘s nachts gebeld heb toen er een probleem was met een van onze vriezers) en de mensen van de **beveiliging** die mij een keer moesten komen “redden” toen het brandalarm van het Hubrecht om 4 uur ‘s nachts afging. Daarnaast ook veel lof voor alle medewerkers van de **kantine**, waaronder **Bianca** en **Mike**. Dank voor het vele lekkere eten, en daarnaast was het ook heel erg fijn om regelmatig gezellig met jullie te kunnen kletsen over Oostenrijk en allerlei andere dingen. **Peter-Erik** en alle andere medewerkers van de **IT-afdeling**: dank voor vele hulp met al mijn (vele) IT-gerelateerde vragen! En de medewerkers van het **HPC cluster** en de **Utrecht Sequencing Facility** in het **UMC Utrecht**: heel erg bedankt voor het runnen van onze regelmatig erg last-

minute submission-deadline-paniek sequencing runs. **John**, dankjewel voor het redden van de -180 vriezer op kerstavond in 2018 en voor alle andere hulp met de vele apparaten en vriezers in het Hubrecht. **Litha**, dank voor de vele tips en alle gezelligheid. En dan mag ik natuurlijk ook niet vergeten om alle facilities en bedrijven, waaronder **Single-Cell Discoveries**, de **Hubrecht FACS facility** en de **Hubrecht Imaging facility** (alias **Anko**), te bedanken voor al hun in put in de vele experimenten die gedaan zijn in het proces wat tot dit proefschrift heeft geleid! Next, I am also very happy that the Hubrecht has a PV, and I hereby want to thank all **members of this PV** for organizing so many awesome activities! En natuurlijk niet te vergeten alle medewerkers van de receptie, waaronder **Thea**, **Esta** en **John**: bedankt voor alle hulp met de vele kleine dingen die ik de afgelopen jaren aan jullie gevraagd heb!

Besides all people in Cambridge and the Hubrecht Institute, we also received a lot of input from people outside of these two institutes. I would for example like to thank **Ana** and all the other ethicists that have been directly or indirectly involved in our work for discussions and thoughts about the ethical aspects of our work. **Sarah**, thank you for being willing to join our borrels and play bass guitar for hours! **Jianping Fu** and all other anonymous reviewers of our manuscripts: thank you all for your dedication, ideas, suggestions and input during the many revision rounds that we have been through with both of our gastruloid publications in 2019. En heel belangrijk **Maarten**: dank dat je ons onderzoek zo goed aan een groter publiek uit kan leggen!

Dan, kort even een klein beetje verder terug in de tijd. Mijn passie voor wetenschap begon namelijk al vroeg en werd versterkt door verschillende fantastische docenten op de basisschool en middelbare school, waaronder **Wim Broekhuizen**, **Rob Burer** en **Peter Moelker**: dank voor jullie positieve invloed op mijn carrièrepad! Daarnaast zijn er ook tijdens mijn bachelorstudie Biologie aan de Universiteit Utrecht meerdere docenten geweest die ontzettend belangrijk zijn geweest, waaronder **Astrid**, **Wim**, **Adri** en **Rebecca**, die ik hierbij wil bedanken voor hun enthousiasme en hun support tijdens mijn bachelor en daarna. En dan natuurlijk niet te vergeten meerdere mensen van het IRAS, waaronder **Gert**, **Siegfried** en **Jack**: dank voor alle ondersteuning in die destijds voor mij niet heel makkelijke periode. Jullie maakten het medemogelijk dat ik ondanks ingewikkelde omstandigheden toch door kon studeren!

Daarnaast ben ik heel veel mensen uit mijn gezin en familie heel veel dank verschuldigd. Te beginnen met **mam**! Dankjewel dat ik je altijd mocht bellen als de spanning, stress en aandacht me even te veel werden. Dankjewel voor de idioterie en hilariteit tijdens het maken van oneindig veel legpuzzels. Dankjewel voor al je proefschrift-kaft-ideeën, gezelligheid en de knuffels, en dankjewel dat ik af en toe eens even lekker bij jou mocht uitzuren op de momenten waarop ik het niet meer zag zitten. En dan natuurlijk **Jaap**: wat ben ik blij dat we jou een aantal jaren geleden hebben mogen leren kennen! Dankjewel dat je altijd bereid bent om me op te halen of weg te brengen, en dankjewel dat je de kruipruimte vol spinnen onder je huis aan wilde bieden als schuilkelder tijdens enge “media-stormen”. **Joost**: dankjewel voor je Joost-zijn en voor de barbecues en telefoongesprekken, en **Nikki**,

dankjewel voor alle gezelligheid en voor het (meestal) geduldig met mij zijn als ik weer eens zo diep verzonken ben in mijn wetenschappelijke gedachten dat het niet mogelijk meer is om een normaal gesprek met me te voeren. **Bart**: dankjewel voor je functie als Paranimf tijdens mijn promotieceremonie, voor het maken van de website van het allereerste consortium waar ik onderdeel van uitmaak, maar vooral ook voor de knuffels, serieuze gesprekken en idiote gesprekken over – eeh – tja, waar gingen die gesprekken eigenlijk over? Weet jij het nog? En niet te vergeten **Margret, Jos, Antoinette, Sander, Rianne, Sjoerd, Celine, Liza**, en alle andere (stief)familieleden en aanhangsel(s) daarvan: bedankt voor de gezellige etentjes, en voor jullie begrip dat het mij niet altijd lukte om aanwezig te zijn bij familiefeesten door congressen en experimenten in het buitenland.

Daarnaast ben ik ook heel veel bedankjes verschuldigd aan al mijn vrienden en vriendinnen, voor al hun gezelligheid, steun, inspiratie en brainstormsessies! **Francine, Tessa, Naomi, Sander, Ingeborg**: dank voor alle gezelligheid, (Skype)gesprekken en muzikale gezelligheid. En **David**, dankjewel voor de ontstress-wandelingen, zwembadbezoeken en flauwe maar altijd leuke woordgrappen (volgende keer moet je er wel meer zout op doen; ze zijn vaak wat flauw, die woordgrappen... ;-P). **Hilje**: dankjewel dat je me af en toe dwingt tot een pauze, voor alle gezelligheid en muziek in de afgelopen jaren, voor de studeer-logeersessies tijdens onze bachelor en voor je vele creatieve brainstormsessie over honderden verschillende onderwerpen! Heel veel succes met de laatste loodjes van de promotie, en wat ontzettend stoer dat je direct na je PhD als UD aan de slag gaat! En daarnaast **Laurien**! Dankjewel voor al die jaren aan gezelligheid en etentjes, je vele fijne adviezen en tips, en voor je mooie post-its en notitieblok Sinterklaascadeautjes (essentieel om een proefschrift te kunnen schrijven – zonder al die kleuren zou mijn quarantaine-huis-kantoor immers maar een saaie, inspiratieloze bedoening zijn geweest). **Daan**: dankjewel voor de fijne wekelijkse pauzes op het drumstel. **Lenka, Meritxell** and **Jen**: thank you for all those beautiful days in Cambridge, with pints, Pims, firework-shows and punting. **Sandra** (Petrus Reurer) and **Sandra** (Segura Bayona): thank you for your friendship here and in Stockholm.

Like most of you know, the last months of my PhD did not go exactly as planned. When I applied for a graduation date in December 2019 I could after all NEVER have predicted that I would end up graduating in the midst of a pandemic. While I am writing this Dankwoord I am in “intelligent lockdown” in a small studio on the campus of the Utrecht University, and I currently do not know exactly when, how and where my graduation ceremony will take place. I am however very lucky that my studio has large windows and that I can see a beautiful sunset view from my desk almost every day. A picture of this view, with in the background the RIVM (Rijksinstituut voor Volksgezondheid en Milieu, the Dutch National Institute for Public Health and Environment), which plays an essential role during this pandemic, is displayed on the title page of this addendum.

Lastly, to all of the people mentioned in this Dankwoord, and also to those who I may have forgotten to mention: thank you so much for all the adventures that we experienced together in the last years. Let us please never forget:

TRI POLOSKI!!!



List of publications

Published

van den Brink, S.C.*, Baillie-Johnson, P.* , Balayo, T., Hadjantonakis, A.K., Nowotschin, S., Turner, D.A. & Martinez Arias, A.[§] Symmetry breaking, germ layer specification and axial organisation in aggregates of mouse embryonic stem cells.

Development **141**, 4231-4242 (2014).

Baillie-Johnson, P., **van den Brink, S.C.**, Balayo, T., Turner, D.A., Martinez Arias, A.[§] Generation of aggregates of mouse embryonic stem cells that show symmetry breaking, polarization and emergent collective behaviour in vitro.

Journal of Visualized Experiments **105**, e53252 (2015).

Rivron, N.*[§], Pera, M.*[§], Rossant, J., Martinez Arias, A., Zernicka-Goetz, M., Fu, J., **van den Brink, S.C.**, Bredenoord, A., Dondorp, W., de Wert, G., Hyun, I., Munsie, M. & Isasi, R. Debate ethics of embryo models from stem cells.

Nature **564**, 183-185 (2018).

van den Brink, S.C.*, Sage, F.* , Vértesy, Á., Spanjaard, B., Peterson-Maduro, J., Baron, C.S., Robin, C. & van Oudenaarden, A.[§] Single-cell sequencing reveals dissociation-induced gene expression in tissue subpopulations.

Nature Methods **14**, 935-936 (2017).

van Batenburg, V., **van den Brink, S.C.[§]**, Blotenburg, M., Alemany, A., Moris, N., Baillie-Johnson, P., el Azhar, Y., Sonnen, K.F., Martinez Arias, A. & van Oudenaarden, A.[§] Generating gastruloids with somite-like structures from mouse embryonic stem cells.

Protocol Exchange <https://doi.org/10.21203/rs.2.18203/v1> (2020).

van den Brink, S.C.*[§], Alemany, A.* , van Batenburg, V.* , Moris, N., Blotenburg, M., Vivié, J., Baillie-Johnson, P., Nichols, J., Sonnen, K.F., Martinez Arias, A. & van Oudenaarden, A.[§] Single-cell and spatial transcriptomics reveal somitogenesis in gastruloids.

Nature (2020).

Moris, N.[§], Anlas, K., Ghimire, S., Balayo, T., **van den Brink, S.C.**, Alemany, A., van Oudenaarden, A. & Martinez Arias, A.[§] Generating human gastruloids from human embryonic stem cells.

Protocol Exchange <https://doi.org/10.21203/rs.3.pex-812/v1> (2020).

Moris, N.*[§], Anlas, K.* , **van den Brink, S.C.***, Alemany, A.* , Schröder, J., Ghimire, S., Balayo, T., van Oudenaarden, A.[§] & Martinez Arias, A.[§] An in vitro model for early anteroposterior organisation during human development.

Nature (2020).



Submitted

Pereira Daoud, A.* , Popovic, M.* , Dondorp, W., Trani Bustos, M., Bredenoord, A., Chuva de Sousa Lopes, S.M., van den Brink, S.C., Roelen, B.A.J., de Wert, G., Heindryckx, B.[§] Modelling human embryogenesis: embryo-like structures spark ethical and policy debate.

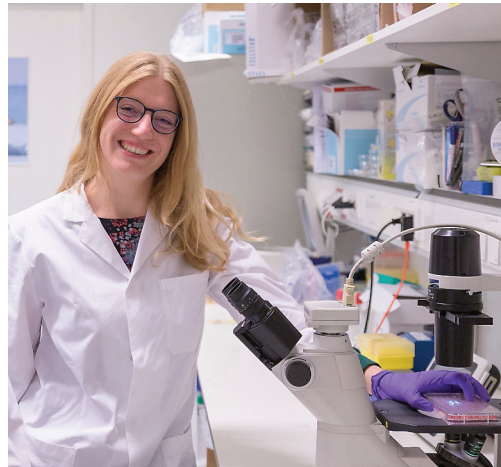
Under review at *Human Reproduction Update*.

* Equal contribution

§ Corresponding authors

Curriculum Vitae

Susanne C. van den Brink was born in Vleuten-De Meern on 3 July 1989. She attended the Drie Koningen primary school, and for her secondary school attended the Sint Gregorius College in Utrecht. She then obtained a Bachelor's degree in Biology cum laude from the Utrecht University in 2011 and a cum laude Masters of Sciences degree in the Cancer Genomics and Developmental Biology programme of the Utrecht University in 2014. During this Master's programme, she performed an internship in the lab of Prof. Jeroen Bakkers, in the Hubrecht



Institute, where she applied microscopy to study left-right asymmetry establishment during heart development in zebrafish embryos. She performed her second internship in the laboratory of Prof. Alfonso Martinez Arias, in the University of Cambridge, in 2013. During this internship, she developed the first version of the mouse gastruloids protocol. In 2014 she started a PhD with Prof. Alexander van Oudenaarden, director of the Hubrecht Institute and at the time one of the first groups to work on single-cell RNA sequencing. During the first part of her PhD, she discovered that widely-used tissue dissociation protocols can influence the experimental outcome of transcriptomics studies. In the second part of her PhD, she applied single-cell RNA sequencing and spatial transcriptomics to mouse gastruloids, used mouse gastruloids to study the segmentation clock in vitro, and developed an improved version of the mouse gastruloids protocol which resulted in gastruloids that generate somite-like structures in vitro. In addition, she was involved in the characterization of a first version of the human gastruloids system, and in discussions regarding the ethical and societal implications of this work. The results of her PhD are described in this thesis.

